The development of low-cost ground-based remote sensing instruments and their application in volcanology

Thomas Charles Wilkes

A dissertation submitted to the University of Sheffield in accordance with the requirements for award of the degree of Doctor of Philosophy

Department of Geography
June 2019

Abstract

Volcanic eruptions pose significant risk to local populations, as well as having the potential to cause global-scale atmospheric impacts. A range of tools are used to research and monitor volcanoes, to better understand the phenomena and, ultimately, to attempt to forecast volcanic eruptions. Remote sensing techniques are critically important to these efforts, providing invaluable data on a range of volcanic manifestations whilst mitigating the risk to volcanologists gathering the data.

This thesis presents on the development and testing of three novel low-cost instruments for ultraviolet (UV) and near-infrared (NIR) remote sensing applications in volcanology. The instruments were all based on the Raspberry Pi Camera Module (v1.3), which houses a sensor primarily designed for the smartphone market. Firstly, this work details the modification of this sensor, by chemical removal of its Bayer filter, to attain an improved UV/NIR sensitivity. From this modified sensor, three instruments were designed and built: the PiCam, a UV imaging camera for SO_2 camera retrievals; the PiSpec, a UV spectrometer for differential optical absorption spectroscopy retrievals of SO_2; a NIR PiCam, for thermal imaging of high-temperature sources. Each instrument was built from the modified sensor, 3D-printed optical mounts, and off-the-shelf optical components. All instruments were rigorously tested, through laboratory and field tests, to evaluate their performances. This included data acquired from deployments on a number of active volcanoes: Mount Etna (Italy), Masaya volcano (Nicaragua), Kīlauea (Hawai'i, US). In general, the instruments were found to perform at least adequately for their desired applications.

These low-cost instruments could promote widespread dissemination of important scientific equipment, facilitating the expansion of data acquisition for volcano monitoring and research. This could be of particular importance in developing countries, where a large proportion of the world's active volcanoes are located, but where volcanology funding is often quite limited.

Author's Declaration

I declare that the work in this dissertation was carried out in accordance with the requirements of the University's Regulations and Code of Practice for Research Degree Programmes and that it has not been submitted for any other academic award. Except where indicated by specific reference in the text, the work is the candidate's own work. Work done in collaboration with, or with the assistance of, others, is indicated as such. Any views expressed in the dissertation are those of the author.

Thomas C. Wilkes

Acknowledgements

I would like to thank Andrew McGonigle, Robert Bryant, Tom Pering and Jon Willmott for their considerable contributions to this thesis. To my friends and colleagues in Electronic Engineering, in particular Ben White, Leigh Stanger, and Nicholas Boone, I am extremely grateful for your support and help with my work. Thank you to all of the colleagues overseas whom I have met and worked with along the way; in particular: Alessandro Aiuppa, Forrest Mims III, Wilfreid Strauch, Giancarlo Tamburello. I would like to thank the Department of Geography staff, in particular Rob, Alan, Mike, David and Joe, who have been extremely accommodating in their help with work which is not quite typical for a Geography department. Thanks to my office friends, in particular Hannah, Kate, Rob and Will, for helping to keep me sane along the way. Thanks to my family, in particular Mum, Dad, Louisa and Kev, for always supporting me, and for motivating me with words such as "Have you finished your thesis yet?", "Haven't you finished your thesis yet!?" and "Get on with your thesis!". Thank you to the UoS Futsal Club, especially FNC, who have made my time in Sheffield a very enjoyable one. To anyone that I have missed out, thank you too.

Contents

List of Figures

List of Tables

List of common acronyms

CAD	Computer Aided Design
CCD	Charge-Coupled Device
CMOS	Complementary Metal-Oxide Semiconductor
COSPEC	COrrelation SPECtrometer
DN	Digital Number
DOAS	Differential Optical Absorption Spectroscopy
FOV	Field Of View
FPA	Focal-Plane Array
FPN	Fixed Pattern Noise
FWHM	Full Width at Half Maximum
GUI	Graphical User Interface
ICA	Integrated Column Amount
IDOAS	Imaging Differential Optical Absorption Spectroscopy
IFOV	Instantaneous Field Of View
ILS	Instrument Line Shape
IR	InfraRed
LWIR	Long Wavelength InfraRed
MWIR	Medium Wavelength InfraRed
NIR	Near-InfraRed
NOVAC	Network for Observation of Volcanic and Atmospheric Change
RGB	Red-Green-Blue
R-Pi	Raspberry Pi
ROI	Region Of Interest
SLS	Selective Laser Sintering
SNR	Signal-to-Noise Ratio
UTC	Universal Time Coordinated
UV	Ultraviolet

"All we have to decide is

what to do with the time that is given to us."

Gandalf

The Lord of the Rings: The Fellowship of the Ring

J. R. R. Tolkien

Chapter 1

Introduction

This chapter provides a brief overview of volcanic phenomena, the hazards posed by such activity and the range of monitoring and research techniques volcanologists employ on active volcanoes. Following from this, I outline the aims and objectives of my thesis.

1.1 A brief history of volcanology

Approximately one tenth of the world's population live within 100 km of an active volcano, a proximity which can potentially expose them to volcanic hazards (Brown et al., 2017). Furthermore, large-scale eruptions have the potential to not only devastate local regions, but also produce climate forcings on a global scale. Most notably in recent historical times, the eruption of Mount Tambora (Sumbawa Island, Indonesia) is believed to have had significant global impacts, with it being attributed as the likely cause of "the year without a summer" across the Northern Hemisphere in 1816 (e.g., Oppenheimer, 2003). It is suggested that a number of significant cultural pieces, such as Mary Shelley's book "Frankenstein" and Lord Byron's poem "Darkness" were inspired by these dire conditions. However, more poignant effects, such as widespread famine and the severity of a typhus epidemic in south-east Europe, have also been linked to the climatic anomaly in the years following the eruption of Tambora. More recently, in the satellite era, climatic forcings resulting from atmospheric loading of volcanogenic aerosols have been directly tracked and modelled, most prominently related to the eruption of Mt. Pinatubo in 1991 (McCormick et al., 1995; Stenchikov et al., 1998; Robock, 2000). The globally averaged temperature anomaly in 1992, resulting from the eruption of Pinatubo, was estimated to be -0.4 °C (McCormick et al., 1995). To this end, some volcanoes have the potential to significantly impact all life on Earth, not just communities living on their flanks.

In relatively proximal volcanic settings, numerous volcanic phenomena pose significant hazard to humans. Such events are much more common than those with globally reach-

ing effects and, thus, monitoring and forecasting these hazards is arguably the most prominent area of research in volcanology (e.g., Sparks, 2003; Sparks et al., 2012). Volcanic hazards include, but are not limited to: pyroclastic flows, lahars, ballistics and ash fallout, lava flows, volcanic gases, debris flows. Doocy et al. (2013) rank the eruptions of Mount Pelée (Martinique, 1902) and Nevado del Ruiz (Colombia, 1985) as the two most fatal eruptions in the period 1900-2009, killing approximately 30,000 and 23,080 people, respectively. The former event involved a series of pyroclastic flows (e.g., Walker and McBroome, 1983), whilst in the latter case fatalities were caused by a lahar (Voight, 1990); as such, no single volcanic phenomenon can be isolated as the main threat to communities living close to volcanoes. This highlights the great complexity faced when attempting to forecast and mitigate volcanic hazards.

At the current level of understanding, it is difficult for scientists to confidently predict the size of an eruption, the timing of eruption onset, or indeed whether or not an eruption will occur at all; however, in recent decades the scientific community have made great leaps forward with respect to volcano monitoring and research. It is of paramount importance for scientists to gather as much pertinent geophysical and geochemical data from a volcano, which will help to inform their forecasts. Indeed, on a number of occasions in recent history the importance of volcano monitoring has been emphasized. For example, evacuations of areas surrounding Mount Pinatubo prior to its eruption in 1991 are estimated to have saved thousands of lives (Newhall and Punongbayan, 1996). More recently, prior to the 2010 eruption of Mount Merapi volcano, Indonesia, precursory signals of seismicity, ground deformation, and gas emissions prompted a large scale evacuation. In places the exclusion zone reached 20 km from Merapi's summit, an action which saved an estimated 10,000-20,000 lives (Surono et al., 2012).

However, contrary episodes, where the link between science and decision-making has strained somewhat, have also occurred. For example, the 1976 volcanic crisis of La Soufrière volcano, Guadeloupe, highlighted the extreme socio-economic consequences of false positive forecasting (Fiske, 1984; Feuillard et al., 1983). Amidst growing concern due to unrest of La Soufrière, and on the advice of one group of scientists, 72,000 people living near to the volcano were evacuated. Ultimately, a hazardous explosive eruption did not occur. As a result, the 6 month long evacuation is estimated to have cost Guadeloupe 60 % of its total annual per capita Gross Domestic Product (GDP). However, had an eruption occurred and lives been saved, no question of this evacuation and its monetary cost would have been raised. Here, the precarious grounds of volcano forecasting, which many volcanologists tread, are starkly illustrated. Nevertheless, it is argued that in this case scientists and authorities could have been better prepared; more informed decisions may then have been made. Learning from this crisis, both Feuillard et al. (1983) and Fiske (1984) stress that long-term monitoring of volcanoes, to obtain a knowledge of baseline activity and therefore a reference for comparison when activity changes dramatically, is crucial to the forecasting process.

1.2 Volcano monitoring and research

Whilst monitoring and research could be thought of as two separate branches of volcanology, the two are intrinsically connected: a better understanding of volcanic processes helps monitoring attempts and, inversely, monitoring networks often lead to a better understanding of volcanic processes through the data they gather. A wide range of disciplines and instrumentation can be applied in volcanology, owing to the complexity of volcanic systems and the myriad ways in which activity is manifested at the surface. However, the use of equipment is also often limited by costs and the practicality of deploying an instrument on, or close to, a volcano (e.g., Sparks et al., 2012). These two factors underpin the work presented in this thesis, as outlined in the objectives (Section 1.3). These factors have also led volcanologists to experiment with developing their own instruments, rather than relying on commercial products; Section 1.2.3 discusses some such instruments, all based on the same low-cost computer board (Raspberry Pi).

Some of the most common techniques for both monitoring and researching volcanic activity include: seismology, gas observations, geodesy/ground deformation, thermal imaging (Sparks et al., 2012). Within these fields, a number of techniques/technologies exist to investigate pertinent phenomena. Many of these techniques, omitting the study of seismicity, can involve remote sensing, a process of acquiring information about an object without coming into physical contact with it. Such technologies are of great importance in volcanology and form the focus of this thesis; therefore, the following paragraphs introduce remote sensing, before subsequent sections/chapters provide more details on pertinent aspects of the field.

As has been emphasized in Section 1.1, volcanoes pose huge threats to people in close proximity. Naturally, as volcanologists strive to understand more about volcanic processes they will often put their own lives at risk, by entering hazardous areas in pursuit of data. Indeed, sadly a number of volcanologists have lost their lives in this manner (Brown et al., 2017). Where possible, it is therefore advantageous to be able to retrieve information from the volcano at a safer distance. Remote sensing techniques allow just this: ground based systems may be installed many kilometres from a volcano, where not only is the volcanologist relatively safe, but the instrument is also less likely to be damaged by eruptions; satellite platforms also house a number of instruments utilised in volcanology, clearly eradicating all risk to the volcanologist posed by the volcano; airborne systems provide something of a bridge between the aforementioned two techniques, allowing high spatial resolution data acquisition that can cover considerable areas.

Remote sensing covers an extremely broad range of techniques and instrumentation, all sharing the common foundation of retrieving information from a target without coming into physical contact with it. Most prominently, remote sensing involves the detection of electromagnetic (EM) radiation which has interacted with, or been emitted from, a target. Examples of some such techniques include: thermal imaging (e.g., Spampinato

et al., 2011; Patrick et al., 2014); interferometric synthetic aperture radar (InSAR) for investigating inflation and deflation (deformation) of volcanic edifices (e.g., Pritchard and Simons, 2004; Sparks et al., 2012); satellite remote sensing of SO_2 (e.g., Carn et al., 2017); differential optical absorption spectroscopy (DOAS) of gas emissions (e.g., Galle et al., 2003; Platt and Stutz, 2008; Galle et al., 2010; Kern et al., 2017); Fourier transform infrared (FTIR) spectroscopy for measuring chemical composition of magmatic gas (e.g., Burton et al., 2007; Oppenheimer and Kyle, 2008; La Spina et al., 2015); ultraviolet (UV) SO_2 imagery (e.g., Mori and Burton, 2006; Bluth et al., 2007; McGonigle et al., 2017; Platt et al., 2018); ash imagery using polarized light (Esse et al., 2018). Beyond EM radiation remote sensing, muography, which involves the detection of muons, is an exciting new technique for viewing the internal structure density of a volcanic edifice (Oláh et al., 2018). Infrasound detection is another, more common, example of non-EM radiation-based remote sensing (e.g., Johnson, 2004; Delle Donne et al., 2016).

Notwithstanding the improved safety aspect introduced by these instruments, remote sensing can also often provide a more comprehensive overview of volcanic parameters where in-situ measurements may provide only isolated snapshots. For instance, a thermocouple can measure the temperature of a single fumarole, whilst a thermal imaging system may capture the temperature of an entire fumarole field in a single image or image mosaic (Harris et al., 2009). Of course, it should be acknowledged that there are a number of reasons for making in-situ measurements, which are very much a critical aspect of volcanology. Indeed, with present technology, in-situ and remotely sensed datasets can often be extremely complementary (e.g., Aiuppa et al., 2008; Aiuppa et al., 2010; Pering et al., 2014; Coppola et al., 2017).

1.2.1 Remote sensing of volcanogenic SO_2

The main volcanic gas constituents are typically H_2O and CO_2, with SO_2 and HCl generally forming the next most abundant species (e.g., Burton et al., 2007). These emissions are the manifestation of magmatic degassing in the subsurface, and can therefore provide insight into the state of a volcanic system (Edmonds, 2008; Aiuppa et al., 2009). Due to the high atmospheric background concentrations of H_2O and CO_2, however, accurately quantifying their emission from a volcano, especially through remote sensing techniques, can be difficult, although not impossible (e.g., Mori and Notsu, 1997; Allard et al., 2005; Kern et al., 2015b; Aiuppa et al., 2015; Kern et al., 2017). Conversely, SO_2 can be detected by a number of relatively straightforward remote sensing techniques, owing to its low background concentration and relatively strong and distinctive absorption cross-section in UV and thermal IR wavelengths (Moffat and Millan, 1971; Galle et al., 2003; Mori and Burton, 2006; Bluth et al., 2007; Prata and Bernardo, 2014).

In addition to the relative ease of detecting SO_2 in volcanic plumes, the species has other importance which makes it a crucial constituent to monitor. Firstly, SO_2 can form

sulphate aerosol (H_2SO_4) through photo-oxidation and hydration in the atmosphere (Pinto et al., 1989; McGonigle et al., 2004b). This can pose the hazard of acid rain (along with a significant contribution from HCl) to surrounding communities (Balagizi et al., 2017). In the case of large-scale volcanic eruptions, sulphate aerosols also induce significant radiative forcings, through backscatter of downwelling solar radiation, which can ultimately have dramatic effects on the climate (McCormick et al., 1995; Stenchikov et al., 1998; Robock, 2000; Langmann, 2014).

Since sulphur has quite a high solubility in magma, and thus exsolves at relatively shallow depths, monitoring SO_2 emissions can give key insights into the movement of magma in the relativity shallow volcanic conduit (Oppenheimer et al., 2011). Indeed, SO_2 monitoring can play a crucial role in volcano monitoring, as was realised during the 1991 eruption of Pinatubo, where elevated SO_2 levels contributed to the evacuation decision which saved thousands of lives (Newhall and Punongbayan, 1996). In combination with detection of other species, such as CO_2 which is less soluble in magma, SO_2 monitoring can also provide some indication of gas source depths (Burton et al., 2007), therefore potentially providing a more robust hazard assessment (Aiuppa et al., 2007; Aiuppa et al., 2009).

A number of instruments have been used to remotely detect SO_2 in volcanic plumes over the last few decades. Early work used the Correlation Spectrometer (COSPEC), which was primarily designed with power station stack plumes in mind (Moffat and Millan, 1971). Whilst it may still be possible to see these instruments in use on some volcanoes, they have almost entirely been superseded by differential optical absorption spectroscopy (DOAS) instruments (see Section 2.3), which typically are considerably cheaper and smaller and, therefore, much more practical for field campaigns (Galle et al., 2003). Both of these instruments provide a single datum SO_2 column density per acquisition, i.e. they acquire information from a single spatially integrated area related to the instrument's field of view (FOV). To estimate an emission rate of SO_2, the instruments must traverse or scan across the width of the plume, to obtain an integrated column amount which can then be multiplied by a plume speed. The COSPEC has been used almost exclusively in the traversing mode, therefore requiring human interaction and not facilitating an automated setup. Furthermore, both the scanning and traverse procedures take time, therefore, the temporal resolution of COSPEC and DOAS instruments is typically on the order of minutes to tens of minutes. McGonigle et al. (2009) has proposed using a wide angle field of view for DOAS instruments, such that a single acquisition spatially integrates across the entire plume width, therefore allowing 1 Hz capture of emission rates; however, this comes at a loss of spatial resolution, and it is not clear whether this may introduce errors into the DOAS retrieval. Indeed, the majority of DOAS instruments currently installed on volcanoes still employ a scanning procedure. The IDOAS (Imaging DOAS) instrument presented by Bobrowski et al. (2006) could also present a means of integrating across the entire plume width in one acquisition, through

hyperspectral imaging. This can produce a high temporal resolution of emission rates (although it is not used to this end in the article), and improved spatial resolution relative to McGonigle et al. (2009); however, this instrument is somewhat more complex than a standard spectrometer, and is therefore not currently a commonly used tool in volcanology.

Recently, the SO_2 camera, which acquires SO_2 images of a volcanic plume, was developed independently by two separate research groups (Mori and Burton, 2006; Bluth et al., 2007), although a similar system was presented decades earlier by McElhoe and Conner (1986) for measuring power station stack SO_2 emissions. It is fast becoming one of the most popular options for remote volcanic SO_2 measurements, as evidenced by the large number of reviews recently published on these systems (Kern et al., 2015b; Platt et al., 2015; Burton et al., 2015; McGonigle et al., 2017), as well as a 2015 special edition in the Journal of Volcanology and Geothermal Research (vol. 300) which focussed almost entirely on SO_2 cameras. The instrument's prevalence stems from a number of benefits it provides relative to the aforementioned spectroscopic approaches: nominally relatively low-cost (1000s-10000s USD), provision of high time-resolution emission rates (can be $>>$ 1 Hz), the ability to resolve more than one source within an image (e.g., Tamburello et al., 2011b; D'Aleo et al., 2016), and providing tangible image representation of a volcanic plume.

Prata and Bernardo (2014) have developed a similar camera system, but based on detection at thermal infrared (TIR) wavelengths. Whilst this and similar instruments have the advantage of working during both day and night, and have been used to retrieve both SO_2 and particulate information (Prata and Bernardo, 2009; Lopez et al., 2015), in general they are utilised less frequently than UV SO_2 cameras (e.g., Platt et al., 2018). Smekens and Gouhier (2018) have recently presented the use of a hyperspectral thermal infrared imager for SO_2 retrievals, which may also grow in popularity in future years; however, the cost and weight (31 kg) of this instrument will be somewhat prohibitive to their proliferation in volcanology.

1.2.2 Thermal imaging

It may be no surprise that thermal imaging can provide great insight into a number of volcanic phenomena, which are sourced from magmas that can reach temperatures in excess 1000 °C (e.g., Ball and Pinkerton, 2006; Lee et al., 2009). Indeed, in volcanology thermal imaging systems have provided vital information on the state of volcanic systems, ultimately aiding monitoring efforts and volcanic research (e.g., Spampinato et al., 2011; Patrick et al., 2014).

Ramsey and Harris (2013) draw attention to the rise of thermal remote sensing in volcanology since the "pivotal" year of 2000, suggesting that as technologies advance

their use will further proliferate and grow ever more important. Prior to 2000, ground based techniques were confined primarily to point measurements using radiometers (e.g., Wright et al., 1968; Birnie, 1973), lacking any detailed spatial information. These measurements were, however, still useful for highly accurate single point remote temperature retrievals, since it is easier to optimise the optical system and calibrate the instrument for a single detector. Around the year 2000, thermal imaging systems began to become affordable for some researchers, although still with quite a large price tag of 10,000s USD. Since then, prices of thermal cameras have steadily decreased, along with their size and weight, making them increasingly more useful field instruments that are used in a variety of ways in volcanology (Spampinato et al., 2011).

Satellite retrievals of thermal properties have been possible since the 1960s (Ramsey and Harris, 2013), and are an omnipresent tool in volcano monitoring and research. As with ground-based instruments, the quality of available data is continually improving, as novel instrumentation and retrieval algorithms are developed (Ramsey and Harris, 2013). Since they can provide global coverage, these instruments are extremely useful for identifying new areas of unrest and monitoring ongoing eruptions (e.g., Wright et al., 2004; Coppola et al., 2016; Wright, 2016). The ability to perform detailed investigations into eruptions with satellite data is, however, limited by generally low spatial resolutions; this is especially the case for IR wavelengths, since the optics required at these wavelengths are more complex than visible remote sensing (e.g., Blackett, 2017).

1.2.3 Raspberry Pi instruments in volcanology

The Raspberry Pi (R-Pi; Raspberry Pi Foundation) is a single board computer, typically with a credit card-sized footprint, the first version of which was released in 2012. The current model, R-Pi 3 Model B+ (released in March 2018), boasts a quad-core Broadcom processor, 1GB RAM and built-in wireless LAN capabilities, amongst other things (https://www.raspberrypi.org/). It costs approximately £35, therefore providing a brilliant low-cost processing platform from which various hardware peripherals (sensors) can be attached via the broad range of communication ports, e.g., general purpose input/output (GPIO) pins, USB 2.0, ethernet, CSI camera port.

The R-Pi has led to the expansion of portable sensors deployed on volcanoes for monitoring and research purposes. Moure et al. (2015) highlight the utility of the R-Pi in this setting, presenting a system capable of monitoring gravity and ground deformation, as well as providing visual imagery. Therein, they also highlight that there are a number of alternative single board computers available, providing a summary table. As the technology has moved forwards quite considerably in the few years since their publication, Table 1.1 represents an updated comparison of currently available single-board computers. Many other boards are available today, as the market has expanded quite considerably; therefore, this table attempts to give a summary of some of the more

popular boards based on internet searches. Of these, the R-Pi is one of the cheapest, as well as having a very large and active user community; the latter factor is particularly important when developing new instrumentation and associated software, providing a considerable aid for troubleshooting. Generally, the other boards are, however, more powerful in some respects, with larger RAM and many having incorporated non-volatile storage. Without detailed studies into the CPUs and GPUs, however, it is difficult to assess their relative performances.

The R-Pi camera module has been used on a number of volcanoes, to provide imagery in a range of formats. Both visible and visible-near-infrared imagery and video were captured by Patrick et al. (2015) to monitor Kīlauea and its associated lava lake. Here, the instrument was particularly useful due the versatility and customisation capacity of both the hardware and software, which many other commercial instruments don't provide. Radebaugh et al. (2016) also monitored a lava lake with the R-Pi camera module, therein developing a low-cost thermal camera by mounting near-infrared bandpass filters to the fore of the lens system.

The R-Pi has also been used as part of cutting-edge technical projects, such as Muon radiography for mapping the internal structure of volcanoes (Ambrosino et al., 2014; Oláh et al., 2018) and robotic mapping of post-eruptive fissure conduits (Parcheta et al., 2016). Furthermore, due to its light weight, it has been possible to mount the R-Pi to an unmanned aerial vehicle as a controller for a spectrometer, enabling SO_2 traverse measurements to be made (Mori et al., 2016).

In a world where the public is becoming more technologically literate and maker communities are on the rise, the R-Pi appears to be a front-runner in low-cost, light-weight computing. It therefore lends itself well to further development of instrumentation in volcanology.

1.3 Objectives

The overarching goal of this thesis was to develop a range of low-cost remote sensing instruments, capitalising on the diverse functionality and benefits granted by the R-Pi computer board and associated peripherals. This work was motivated by the reality that funding in volcanology, particularly in developing countries, can often be restrictive to the amount and type of instrumentation available to both researchers and, possibly to a larger extent, monitoring networks (e.g., Sparks et al., 2012). If the cost of instrumentation can be reduced, it will be possible to monitor and research a greater number of active volcanoes and in more detail. This could lead to a better understanding of volcanic hazards, and ultimately save lives and money in the future.

Table 1.1: Single-board computers

	Raspberry Pi 3 Model B+	**Pine A64-LTS**	**Banana Pi M64**	**Odroid-XU4**	**LattePanda**
System chip (SoC)	Broadcom BCM2837B0	Allwinner R18	Allwinner A64	Samsung Exynos5422	Intel Atom Cherry Trail
CPU	ARM Cortex-A53	ARM Cortex-A53	ARM Cortex-A53	ARM Cortex-A15 + ARM Cortex A7	Intel Z8350
GPU	Broadcom Videocore-IV	Mali-400 MP2	Mali-400 MP2	Mali-T628 MP6	Intel HD Graphics
RAM	1 GB	2 GB	2 GB	2 GB	2-4 GB
Non-volatile Memory	None built in	$\leq$ 128 GB (Optional)	8-64 GB	$\leq$ 64 GB (Optional)	None built in
Interfaces	USB 2.0, Ethernet, WiFi, Bluetooth 4.2, I2C, SPI, UART	USB 2.0, Ethernet, WiFi[1], Bluetooth 4.0[1], I2C, SPI, UART	USB 2.0, Ethernet, WiFi, Bluetooth 4.0, I2C, SPI, UART	USB 2.0/3.0, Ethernet, I2C, SPI, UART	USB 2.0/3.0, Ethernet, WiFi, Bluetooth 4.0, I2C, SPI, UART
Camera interface	Yes	Yes	Yes	No	No
Video output	HDMI, MIPI-DSI	HDMI, MIPI-DSI	HDMI, MIPI-DSI	HDMI	HDMI, MIPI-DSI
Power supply	5 V	5 V	5 V	5 V	5 V
Power consumption[2]	2-10 W	2-10 W	5-10 W	5-20 W	2-12 W
Dimensions [mm]	82 $\times$ 56	133 $\times$ 80	92 $\times$ 60	83 $\times$ 58	88 $\times$ 70
Price	£34	$42[3]	£75	£70	£70

[1] Requires the WiFi and Bluetooth module.
[2] Values are rough estimations based on a range of online sources. Lower values are typical idle consumption whilst peak draw may be during start-up.
[3] Difficult to source in the UK. Price includes WiFi/Bluetooth module ($10).

1.3.1 Objective 1

The first objective of this thesis was to modify a commercial, low-cost camera (the R-Pi camera module), such that it may be used in applications other than simply visible imaging. This involved removal of its Bayer filter, to produce a sensor with heightened ultraviolet (UV) and near-infrared (NIR) sensitivity and a uniform sensor response.

1.3.2 Objective 2

The second objective of this thesis was to build and test an ultraviolet SO_2 camera based on the modified R-Pi camera module. Due to the current popularity of the SO_2 camera for making volcanic SO_2 measurements, such an instrument could be extremely beneficial to researchers and volcano monitoring groups across the globe.

1.3.3 Objective 3

The third objective of this thesis was to design and build a custom ultraviolet spectrometer capable of performing differential optical absorption spectroscopy retrievals of volcanogenic sulphur dioxide. The spectrometer makes use of the modified R-Pi camera module detector.

1.3.4 Objective 4

The fourth objective of this thesis was to develop a near-infrared thermal camera capable of performing accurate temperature retrievals of high-temperature objects. Again, this camera was based on the R-Pi camera module. This work builds upon that of Radebaugh et al. (2016), who have previously developed a low-cost thermal camera based on the R-Pi camera module; however, in general their calibration procedure and use of the detector lacked scientific rigour and is unlikely to be very accurate.

1.4 Thesis Structure

Below is an overview of the layout of this thesis, with particular regard to the discussion and achievement of the objectives outlined in Section 1.3. Furthermore, a number of publications have emanated from the work discussed herein, therefore, where these pieces fit into the presented body of work is also outlined below.

Chapter 2 provides a review of pertinent theory and literature related to ground-based remote sensing of both volcanogenic SO_2 and of high temperature objects. Specifically, this involves discussion on the SO_2 camera, differential optical absorption spectroscopy

(DOAS) for retrieval of volcanic gas emissions, and thermal imaging. The application and utility of these techniques in volcanology is also highlighted.

Chapter 3 addresses both objectives 1 and 2. It first presents the modification of the R-Pi camera module to improve its utility in scientific research. Bodies of this work have been published in Wilkes et al. (2016), where the development of a UV SO_2 camera was discussed. Subsequently, the chapter presents an assessment of this instrument's performance during tests on Mount Etna in Italy. This involves a side-by-side comparison with a commercial SO_2 camera unit, which is published in Wilkes et al. (2017a).

Chapter 4 addresses objective 3. It presents the development of a 3D-printed UV spectrometer, utilising the modified sensor discussed in Chapter 3; this work is an elaboration of an article published as Wilkes et al. (2017b). Subsequently, the spectrometer was tested in volcanic settings, namely Masaya volcano and a fissure eruption on Hawai'i. Work on the former volcano was published as Wilkes et al. (2019).

Chapter 5 addresses objective 4. It discusses the development of a low-cost thermal imaging system for the remote retrieval of temperatures from high-temperature sources. The work discusses the calibration of a near-infrared camera, and a detailed consideration of uncertainties in temperature retrievals. It then presents the deployment of the instrument on Masaya volcano, to image an active lava lake. This chapter is a version of the work published as Wilkes et al. (2018).

Chapter 6 summarises the work presented in this thesis. Additionally, it presents future avenues of work and alternative applications of the instruments developed and discussed herein. Specifically, it presents the results of preliminary tests into the potential use of the UV spectrometer for atmospheric ozone retrievals and as a hyperspectral imager, as well as the use of the UV camera for assessing human exposure to UV radiation.

Chapter 2

Ground-based remote sensing in volcanology

This chapter reviews a number of ground-based remote sensing techniques that are utilised in volcanology. It aims to provide a background of the theory upon which much of the subsequent chapters are based. Specifically, this chapter focuses on SO_2 cameras, differential optical absorption spectroscopy, and thermal imaging systems. Later chapters will present the development and application of new low-cost alternatives to the equipment discussed here, for all three of these applications.

2.1 Introduction

As Chapter 1 highlighted, remote sensing is an integral part of volcanology, not least because it limits the risk attached to volcanologists when attempting to gather data from a volcanic system. Remote sensing systems can be deployed in a number of modes: satellite-based, aerial, and ground-based. In many ways, aerial is an extension of ground-based techniques, since similar instruments can be used for both; furthermore, both typically require considerable human interaction in order to acquire a dataset. Conversely, satellites acquire data autonomously, without requiring the researcher to interact with the instrument; in addition, retrievals are often more complex due to complicated radiative transfer through the atmosphere that must be considered. Finally, satellite remote sensing is less accessible in terms of the development of new technologies by an average researcher, since it requires the ability to put the instrument into orbit; therefore, in general these technologies are delivered by large organisations such as the National Aeronautics and Space Administration (NASA) and the European Space Agency (ESA). All modes are of great worth to volcanology, each providing specific strengths and weaknesses; therefore, the full suite of remote sensing technologies can often be quite complementary (e.g., Pyle et al., 2013).

Here, focus is placed on ground-based instruments, which have the advantage of being located relatively close to the target object, therefore generally providing high spatial-resolution data. Their close proximity also often means that radiative transfer is significantly less complex than for satellite-based remote sensing. Furthermore, these instruments can usually be deployed rapidly, allowing new targets to be investigated at relatively short-notice; for example, if a previously inactive volcano begins to show signs of unrest, volcanologists can quickly deploy an array of ground-based instruments to monitor its activity in detail.

It should be noted that all of the techniques/instruments discussed below have applications outside of volcanology, and in most cases were not principally developed for volcanological applications. Rather, often volcanologists take techniques which have already been developed and rigorously applied elsewhere and apply them in a volcanic setting. As such, it is worthwhile to acknowledge that the new instruments developed and presented within this thesis may have far reaching applications outside of volcanology, regardless of their principle design purpose in volcanology.

2.2 SO_2 camera

2.2.1 Principles of the SO_2 camera

This section provides a theoretical description of the SO_2 camera, outlining how UV cameras can be used to make relatively accurate retrievals of SO_2 emission rates. In Chapter 3, some of the methods outlined here will be used. It is important to note that there are a number of proposed methods for SO_2 camera processing, most of which are well covered by Gliß et al. (2017). The software presented therein is extremely powerful, however, it was released only quite recently, and was therefore not available for use throughout this thesis. All SO_2 camera work presented in this thesis therefore used custom code written in MATLAB® and/or Python, with a number of the protocols outlined below. This section will briefly discuss the range of different processing protocols for SO_2 cameras, highlighting those which were used for the work presented in Chapter 3.

The SO_2 camera exploits the fact that SO_2 exhibits strong absorption within the band $\approx$ 300 - 320 nm, due to electronic excitation (e.g., Platt and Stutz, 2008). Imaging at these wavelengths therefore provides a contrast between the background sky illumination and the SO_2-laden plume, which attenuates incident UV light. The attenuation is described by the Beer-Lambert law (also referred to as the Bouguer-Lambert law, Lambert-Beer law, Beer-Lambert-Bouguer law), which states that the intensity of radiation after passing through a medium, $I(\lambda)$, is dependent on the initial beam intensity, $I_0(\lambda)$, and an exponential function of the light path, L, the concentration of the absorbing medium, c,

and the absorption cross-section of that absorber, $\sigma(\lambda)$ (Platt and Stutz, 2008):

$$I(\lambda) = I_0(\lambda) \cdot \exp(-\sigma(\lambda) \cdot c \cdot L) \tag{2.1}$$

This assumes that the medium is homogeneous/well-mixed, and thus, c accurately represents the concentration in any sub-volume of the total layer. The quantity $c \cdot L$ is referred to as the column density, S, which is commonly reported in ppm·m; it may be defined more specifically as the integral of SO_2 concentrations along the effective light path (Kern et al., 2010b).

The optical density, $\tau(\lambda)$, may now be defined as the negative logarithm of the ratio $\frac{I(\lambda)}{I_0(\lambda)}$.

$$\tau(\lambda) = -\ln\left(\frac{I(\lambda)}{I_0(\lambda)}\right) = \sigma(\lambda) \cdot S \tag{2.2}$$

In reality, S is wavelength dependent, since the effective light path L deviates from a straight line through the plume due to wavelength-dependent radiative transfer effects (Kern et al., 2010a). Here, however, for simplicity it is acceptable to assume that S is not a function of wavelength.

In a simple case, by capturing images in a spectral band where SO_2 absorbs ("on-band"), $\approx$ 310 nm, and using the background sky intensity as I_0, a wavelength-weighted-average optical density $\hat{\tau}$ in the plume may be calculated and later calibrated; this approach was proposed by Bluth et al. (2007). Of course, volcanic plumes do not contain only SO_2, and thus, there are other species which can cause attenuation of radiation as it passes through the plume. In particular, aerosols cause significant effects at UV wavelengths, through both scattering and absorption. Whilst the SO_2 absorption cross-section diminishes significantly towards longer wavelengths, aerosol extinctions are less wavelength dependent, therefore, by introducing a second band ("off-band") typically centred at $\approx$ 330 nm, the majority of aerosol extinction can be corrected for; Section 2.2.3 discusses why this is not a strictly perfect correction. Including this aerosol correction, Mori and Burton (2006), presented a method for determining the weighted-average optical density of SO_2, $\hat{\tau}_{SO_2}$ (often referred to as the apparent absorbance, AA), by using a two-filter system:

$$\hat{\tau}_{SO_2} = AA = -\ln\left[\frac{\left(V_{on}^{plume}/V_{on}^{sky}\right)}{\left(V_{off}^{plume}/V_{off}^{sky}\right)}\right] \tag{2.3}$$

where V^{plume} is the in-plume pixel intensity, and V^{sky} is the background pixel intensity; the subscript then specifies on-/off-band wavelengths. Here, V represents a digitisation of beam intensity I by a UV camera, under the assumption that $V \propto I$. To capture the on-/off-band images, filters are used, which typically have a bandpass of ≈ 10 nm full-width-at-half-maximum (FWHM); these are discussed in more detail later.

Since there is not a sufficient spectral resolution in an SO_2 camera system, the column density of SO_2 cannot be directly determined from AA. This is because the intensity of incident radiation, filter transmission, $T(\lambda)$, and quantum efficiency of the detector, $Q(\lambda)$, all of which are wavelength dependent, are not well known (Kern et al., 2010b):

$$V = \alpha t \int Q(\lambda) \cdot T(\lambda) \cdot I_{\gamma}(\lambda) \cdot d\lambda + \beta(t) \tag{2.4}$$

where α is the detector's gain setting, $\beta(t)$ is the electronic offset, and t is the integration time of the detector; this simplified equation omits noise sources which will also be present. Here, $I(\lambda)$ takes the form of $I_{\gamma}(\lambda)$, which is the photon flux (number of photons per second) arriving at the instrument. In a practical application, to correct for β all images are first dark current subtracted by placing the lens cap on the lens and acquiring an image at the shutter speed used for subsequent plume acquisitions.

Calibrating AA to a column density of SO_2 must therefore be performed by using either quartz cells filled with known amounts of SO_2 (Mori and Burton, 2006; Bluth et al., 2007), or a co-aligned DOAS instrument (Kern et al., 2010b; Lübcke et al., 2013). The latter provides more spectral information, which is lacking from the SO_2 camera, combining the advantages of DOAS retrievals (presented in Section 2.3) with the imaging and high-frame rate capabilities of the SO_2 camera.

Whilst DOAS calibrations are becoming more prominent, gas cells were the first method of calibrating the SO_2 camera, and are still commonly used today. It is this method which is used throughout this thesis. The calibration involves using a number of cells containing different column densities of SO_2. By imaging the cells and calculating their apparent absorbance, AA, from Equation 2.3, a linear relationship between AA and the SO_2 column densities can be determined. All subsequent measurements of AA in the volcanic plume are fitted to this regression. The calibration will change throughout the day, as the spectral radiance of the clear sky changes; therefore, cell calibration should be performed regularly, typically every hour or so.

From Equation 2.3, there are a number of arrangements in which the filters may be mounted to the UV camera(s). Due to the cost of UV scientific-grade cameras, some research groups have opted to buy a single camera and mount a filter wheel, such that consecutive on-/off-band images may be taken by rotating the wheel (e.g., Lübcke et al., 2013; Kern et al., 2015b; Stebel et al., 2015). Whilst this does ensure that the images

are registered with respect to stationary parts of the image, under conditions of rapid plume motion the on-/off-band image pair can have offsets in plume position, as the plume moves between the acquisition of the two images. Furthermore, it is preferable to avoid moving parts in the system, since they are prone to malfunctioning. Finally, the use of a filter wheel limits the time resolution of the system, since on-/off-band images must be taken sequentially by the same instrument. In general, therefore, it is preferable to use two cameras, with the on-band filter mounted to one and the off-band filter to the other (e.g., Kantzas et al., 2010; Kern et al., 2015b; Kern et al., 2015a; Campion et al., 2018); however, this comes with the added cost of requiring two cameras. Issues with a two camera setup arise from image registration, since both the physical offset in optical system location and slight differences in their orientations results in the image pairs not being perfectly aligned. With software, the images can be quite accurately registered, such that the scenes in the two images are well matched. The location of the filters in the optical system also affects the instrument's performance and must be considered; this is discussed in Section 2.2.3.

Also from Equation 2.3, there have been a number of methods for estimating background sky intensity, V^{sky}, suggested in the literature (see Gliß et al., 2017, for an overview). Estimating this intensity can be particularly problematic for inhomogeneous backgrounds, i.e., on cloudy days; however, Osorio et al. (2017) have proposed a method to deal with such conditions, by using an automatic plume segmentation procedure, followed by polynomial interpolation of the background sky intensity. Unless otherwise stated, in this thesis the simple method of averaging the intensity of a region of clear sky adjacent to the plume in each image is used to estimate V^{sky}. This intensity is extracted after correcting the plume image with a vignette mask generated by normalising a clear-sky image (Kantzas et al., 2010). This mask corrects for filter vignetting effects caused by deviation from perpendicular filter illumination (see Section 2.2.3), as well as any non-uniform sensor response; the latter issue is particularly pertinent to the work presented in Chapter 3, where the sensor response is not perfectly uniform across the array.

Once the images have been calibrated, SO_2 emission rates are extracted by integrating across a cross-section through the plume, and multiplying this integrated column amount (ICA) by the plume speed. There are two common techniques for plume speed estimation: cross correlation and motion estimation algorithms. The former is a long-standing technique which was used in spectroscopic measurements prior to work with the SO_2 camera (McGonigle et al., 2005b; McGonigle et al., 2005a), and was proposed in the first paper on the SO_2 camera (Mori and Burton, 2006). This relatively simple method assumes that the plume moves at a single velocity at all points in space, and therefore parcels of SO_2 can be tracked from one plume cross-section to another located further downwind. Two ICA time series can therefore be cross-correlated and their lag in frames converted to a plume speed with a knowledge of the camera frame rate and distance between the two ICAs. In recent years, motion estimation algorithms have been proposed,

which use more sophisticated computer-vision techniques to estimate the motions of individual pixels. Theoretically, such techniques can much more accurately represent the motion of more complex systems, such as turbulence in a volcanic plume (Thomas and Prata, 2018; Peters et al., 2015). However, from experience, at times it can be difficult to find the correct input parameter values for the algorithms, which can lead to quite significant errors. Therefore, for simplicity, in work presented herein cross-correlation is used throughout.

2.2.2 Utility of the SO_2 camera in volcanology

The SO_2 camera, still a relatively nascent instrument, has spawned a swathe of new volcanological research, primarily due to the high time-resolution emission rates it provides. This makes integration of SO_2 datasets with other geophysical parameters much more plausible than previously, as well as allowing the study of more transient degassing phenomena, such as explosive plumes. Below, a number of such articles are introduced, to highlight the utility of this instrument in volcanology.

The high time-resolution emission rates provided by the SO_2 camera have facilitated a number of ground-breaking studies into volcanic phenomena, by capturing transient events and allowing a more detailed comparison with other geophysical parameters which are recorded with data frequencies of at least 1 Hz (e.g, seismics). Although this has previously been shown to be possible using specialised DOAS instruments (McGonigle et al., 2009), recent research has preferred the SO_2 camera for acquiring high time-resolution SO_2 emission rates (e.g., Nadeau et al., 2011; Tamburello et al., 2012; Tamburello et al., 2013; D'Aleo et al., 2016; Pering et al., 2016; Delle Donne et al., 2017). Such works have greatly improved our understanding of conduit processes and their manifestation at the surface. The multi-parametric study by Tamburello et al. (2012) found a correlation between SO_2 emissions, thermal magnitude and seismic very long period (VLP) displacements during Strombolian explosions on Stromboli, Italy. This suggested that the three are linked to a single phenomenon: a larger gas slug rising through the conduit causes a larger volumetric change, and thus greater VLP displacement; the larger slug therefore manifests as a larger emission of SO_2 at the surface, where the explosive volume causes a greater fragmentation of magma which is entrained into the eruptive column (a higher thermal signal). This latter relationship between SO_2 eruptive mass and thermal signal has more recently been contradicted by Barnie et al. (2015), who found no such link between explosive SO_2 mass and solid ejecta mass, suggesting that, for slug generated explosions, the mass of ejected solids is dependent on the rheology and geometry of a magma surface film, rather than the size of the slug which ruptures it. Similar correlations between SO_2 emissions data and VLP displacements have, however, been made on Mt. Asama (Kazahaya et al., 2011) and Fuego volcano (Waite et al., 2013).

SO_2 camera data can also be integrated into research on fluid dynamics within volcanic conduits. Pering et al. (2016) used computational fluid dynamics (CFDs) to model slug behaviour in a volcanic conduit, showing that codas in SO_2 emission rates following a slug-generated explosion can be produced by daughter bubble production at the base of the slug as it ascends the volcanic conduit. This should pave the way for further research linking gas data to CFD models, which is, thus far, a relatively unexplored research methodology.

Gas release from Strombolian-style explosive volcanism has been investigated on a number of occasions with SO_2 cameras. Mori and Burton (2009) found that on Stromboli explosive phases contributed 3-8 % of the total SO_2 flux, therefore, highlighting that continuous quiescent degassing is the main source of SO_2. Tamburello et al. (2012) extended this work, measuring many more explosions on Stromboli (133 events vs just 5 events from Mori and Burton). Their work corroborated Mori and Burton's earlier study, finding that explosive activity contributed ≈ 7 % of the total SO_2 emissions. These works, which were performed 4-5 years apart, also indicate that Stromboli's typical activity displays quite stable characteristics.

Nadeau et al. (2015) used SO_2 cameras and contemporaneous seismic measurements to investigate gas pistoning in the lava lake of Kīlauea Volcano, on the island of Hawai'i. They found that as the lava lake level rose SO_2 emissions and seismicity both decreased; a subsequent drop in the lake's level was accompanied by a concomitant increase in SO_2 emissions and seismicity. The heightened emissions were found to compensate for the deficit during lava lake rise, indicating that the lake's rise and fall was caused by an accumulation of gas beneath the surface. Gas accumulation was suggested to occur beneath some form of viscous cap, as also proposed by Patrick et al. (2010).

Recently, Campion et al. (2018) investigated degassing at Popocatépetl, an andesitic stratovolcano. They used the high temporal resolution afforded by the SO_2 camera (1 image every 5-15 seconds) to track emission rates prior to and after explosive events. From this, they categorised explosions into two classes. The first type occurred in the middle of "normal" degassing, with SO_2 emissions quickly returning to the pre-explosive level following the eruptive pulse. The second type, which incorporated the largest explosive events, was preceded by a significant decrease in SO_2 emissions and subsequent return to the typical state after the explosion. They therefore suggested a mechanism for degassing at Popocatépetl, and possibly other andesitic lava domes, proposing that the latter explosive phenomena resulted from gas accumulation following rapid blocking of degassing pathways, by partial internal collapse of the viscous lava dome. The former, less severe explosions may have been caused by rising gas slugs, or they represent more extreme gas puffs.

The transition to explosive volcanism on an andesitic volcano was also investigated by Kazahaya et al. (2016) on Sakurajima volcano, Japan. They found a positive correlation

between inflation (quantified by tangential strain) and the amount of SO_2 accumulated prior to eruption. The latter was estimated by integrating the decrease in SO_2 emission rate prior to eruption from the point of accelerated inflation; indeed, the eruptions were predominantly preceded by a decrease in SO_2 flux, suggesting accumulation beneath a layer of reduced permeability in the conduit, much like that observed by Campion et al. (2018) on Popocatépetl.

2.2.3 Limitations

Although the SO_2 camera has resulted in a marked improvement to many aspects of volcanological monitoring and research, the system has a number of limitations. Many of these stem from the significant compromise in spectral resolution which has to be made in these systems, relative to a spectrometer. The SO_2 camera's ≈ 10 nm bandpass filters are too coarse to enable DOAS retrievals, which exploit the high frequency electronic absorption structures of the SO_2 molecule (discussed further in Section 2.3.1 and Chapter 4); for such measurements, a spectral resolution of at least ≈ 1 nm is required.

As a result of the broader spectral bands used in the SO_2 camera, calibration must be performed either with the use of SO_2-filled quartz cells or a collocated DOAS instrument (see Section 2.2.1). The former method results in issues with light dilution, which is the process of light being scattered into the instrument's field of view between the plume and the observer. Since this light has not passed through the plume, but is contributing to the signal produced at the detector, the final quantity of SO_2 measured by the system will be an underestimation of the true amount. Campion et al. (2015) have, however, proposed a method for correction of this error by using the changing intensity of land surfaces within the camera images; that is, surfaces further from the instrument will appear brighter than those nearby due to more light scattered into the instrument's field of view along the light path. This can be used to deduce atmospheric scattering coefficients, which enables correction of SO_2 retrievals for light dilution. When calibrating the SO_2 camera with a DOAS instrument, light dilution can be corrected for by making use of the gathered DOAS spectra (Kern et al., 2012; Kern et al., 2013).

The SO_2 camera uses bandpass filters to acquire images at nominally on- and off-band wavelengths (typically ≈ 310 and ≈ 330 nm, respectively). However, the interference filters commonly used for this application have limitations themselves, which subsequently affect SO_2 retrievals. Kern et al. (2010b) highlight that with increasing incidence angle on the filter the transmission window shifts towards shorter wavelengths; furthermore, the peak transmission decreases and the bandwidth increases. These effects work to increase the sensitivity of a specific camera system to SO_2 (Kern et al., 2015b), such that at the edges of the field-of-view of a camera system with filters mounted to the fore of the object lens retrieved SO_2 column densities will be systematically overestimated relative to the centre of the image, unless this effect is suitably corrected for. This issue can be

mitigated by one of two approaches (Kern et al., 2010b; Kern et al., 2013; Kern et al., 2015b): mounting the filter between the object lens and the detector, or between two lenses in a more complex setup, thus ensuring that light striking each pixel has passed through the filter at a range of different angles, making the resulting sensitivity notably less dependent on the distance of a pixel from the centre of the image; alternatively, employing a 2D calibration that is dependent on the distance of each pixel from the centre of the image (i.e., dependent on the illumination angle of the filter).

Aerosols in the volcanic plume cause significant problems for SO_2 cameras. Although a longer wavelength (off-band) image is used for correction of aerosol effects, which are generally broad-band in nature, aerosol scattering is still wavelength-dependent and, thus, some error is introduced here (Kern et al., 2010b; Lübcke et al., 2013). Furthermore, aerosols cause multiple scattering within a volcanic plume, which can increase the effective light path by possibly >70 % (Kern et al., 2010a). This would lead to a dramatic overestimation in SO_2 due to much greater attenuation of radiation following from the increased effective light path. It is possible for ash and aerosols to become so thick that light cannot pass through the plume and the majority of the signal is then sourced from light reflected by the plume edges; in such cases, the SO_2 camera will give highly erroneous retrievals. This is especially the case in explosive plumes.

Finally, although SO_2 cameras are nominally cheap (1000s-10000s USD), their cost still precludes widespread proliferation of the devices throughout the volcanology community. This issue is exacerbated by the fact that a large number of active volcanoes across the globe are situated in developing countries, where funding is limited. It is primarily this concern which prompted the work presented in Chapter 3, aimed at developing a camera system based on consumer electronics which, as such, is considerably cheaper than the scientific-grade instruments currently available.

2.3 Differential Optical Absorption Spectroscopy (DOAS)

2.3.1 Principles of DOAS

Differential optical absorption spectroscopy (DOAS) is a method for analysing trace gas concentrations in a medium. It has a broad range of applications, as well as a large number of distinct deployment modes (Platt and Stutz, 2008). Of pertinence here, passive scattered-light DOAS provides an accurate means of retrieving column amounts of SO_2 (and other species) in volcanic plumes. It follows the Beer-Lambert law presented in Equation 2.1, but further exploits a principle that the target species, in this case SO_2, has a unique high-frequency absorption cross-section trace in the wavelength domain. These absorption features can be isolated, and a reference spectrum fitted to them, to quantify the column density of gas in the light path. This removes the effects of

other processes in the atmosphere, predominantly Rayleigh and Mie scattering, which are relatively broad-band in nature. The critical difference here between the SO_2 camera and DOAS retrievals is that the use of a spectrometer with the latter, rather than bandpass filters, allows for the detection of more detailed spectral characteristics; therefore, a more comprehensive consideration of radiative transfer effects is possible.

DOAS works by separating absorption cross-section features which vary rapidly with wavelength, $\sigma_j^{'}(\lambda)$, from those which are more broad-band in nature, $\sigma_{j0}(\lambda)$, (Platt and Stutz, 2008).

$$\sigma_j(\lambda) = \sigma_{j0}(\lambda) + \sigma_j^{'}(\lambda) \tag{2.5}$$

Where the subscript j denotes any absorbing species in which these slow and rapid variations in the absorption cross-section are both present. These rapid changes will manifest in the medium's optical density and, thus, by isolating the rapid variations in optical density, $\tau(\lambda)$, from Equation 2.2, we may define a differential optical density $\tau^{'}(\lambda)$:

$$\tau^{'}(\lambda) = -\lfloor \ln\left(\frac{I(\lambda)}{I_0(\lambda)}\right) \rfloor = L \cdot \sum_j \sigma_j^{'}(\lambda) \cdot c_j = \sum_j \sigma_j^{'}(\lambda) \cdot S_j \tag{2.6}$$

Here, $\lfloor \cdot \rfloor$ denotes a high-pass filtering process which removes the broad-band structures of $\tau(\lambda)$. Similarly, the differential optical density, $\sigma_j^{'}(\lambda)$, may be obtained by applying the same high-pass filter to the absorption cross-section, $\sigma_j(\lambda)$: $\sigma_j^{'}(\lambda) = \lfloor \sigma_j(\lambda) \rfloor$. High-resolution absorption cross-sections for most common species, including SO_2 (e.g., Vandaele et al., 2009), have been well defined through laboratory experiments; therefore, by fitting $\sigma_j^{'}(\lambda)$ to $\tau^{'}(\lambda)$, through a least-squares method, the column density, S_j, of a molecular species can be retrieved.

Commonly in volcanology, along with SO_2, there are other differential absorption cross-sections $\sigma_j^{'}(\lambda)$ that need to be considered in the DOAS retrieval. Specifically, O_3 has a similar high frequency absorption cross-section within the typical SO_2 DOAS fit window ($\approx$ 300 - 330 nm), therefore fitting of this spectrum should be included too. Additionally, a ring spectrum is usually used as a further absorption cross-section to be fitted to $\tau^{'}(\lambda)$. This spectrum, stemming from the ring effect, is generally accepted to be a result of rotational Raman scattering in the atmosphere (Fish and Jones, 1995; Platt and Stutz, 2008), and results in partially reduced optical densities of Fraunhofer lines at high solar zenith angles.

2.3.2 Spectrometers

Spectrometers are fundamental to DOAS systems. They can come in a range of formats, therefore, it is important here to understand the core principles of such instruments before attempting to apply DOAS retrievals to real-word scenarios. In general, DOAS systems incorporate dispersive spectrometers, which separate incident electromagnetic radiation such that different wavelengths can be spatially resolved. Dispersion can be performed either through refraction (e.g., from a prism) or diffraction (e.g., by a diffraction grating). In general, the latter are now more common, possibly owing to their greater dispersion potential and improved manufacturing techniques in recent years.

A diffraction grating is essentially a series of equally spaced slits which result in a wavelength-dependent angular dispersion, either through transmission or reflection of incident light. The diffraction grating equation (e.g., Platt and Stutz, 2008), which describes the angle, β, at which rays exit the slit under incident angle, α, is :

$$d(\sin\alpha + \sin\beta) = N\lambda \tag{2.7}$$

where d is the spacing between slits, N is the order the spectrum, and λ is the wavelength of light. This equation identifies the angles at which interference maxima are located.

In a spectrometer, the diffraction grating is positioned between lenses or mirrors which control the geometry of rays both incident on and exiting from the grating. They collimate light onto the grating and then refocus it, after diffraction, onto a detector or slit. These optical elements can be arranged in a number of different configurations, e.g., Czerny-Turner, Littrow, Fastie-Ebert (Fig. 2.1). The crossed Czerny-Turner design, which produces compact spectrometers due to its folded optical system, is popular for miniature spectrometers (e.g., Tang et al., 2015), with it being used in commercial instruments such as the Ocean Optics USB2000 and Flame-S models.

A critical part of the spectrometer is the entrance slit. Whilst controlling the light throughput of the system, the slit also affects the spectral resolution of the instrument, with a smaller slit providing a higher spectral resolution for a given instrument design (e.g., Tang et al., 2015). There is therefore a trade-off between spectrometer sensitivity, related to light throughput, and spectral resolution, which must be considered. This is particularly important when the spectrometer is working in a spectral band at which the detector has a low quantum efficiency, for instance, a typical silicon photodiode working at UV wavelengths. If a highly dispersive element is in use this will also decrease the irradiance at the sensor, so this must also be considered here.

The dispersed radiation is detected by a sensor which is typically a linear array of pixels. This discretises the dispersed spectrum and, thus, in order to avoid aliasing, or simply

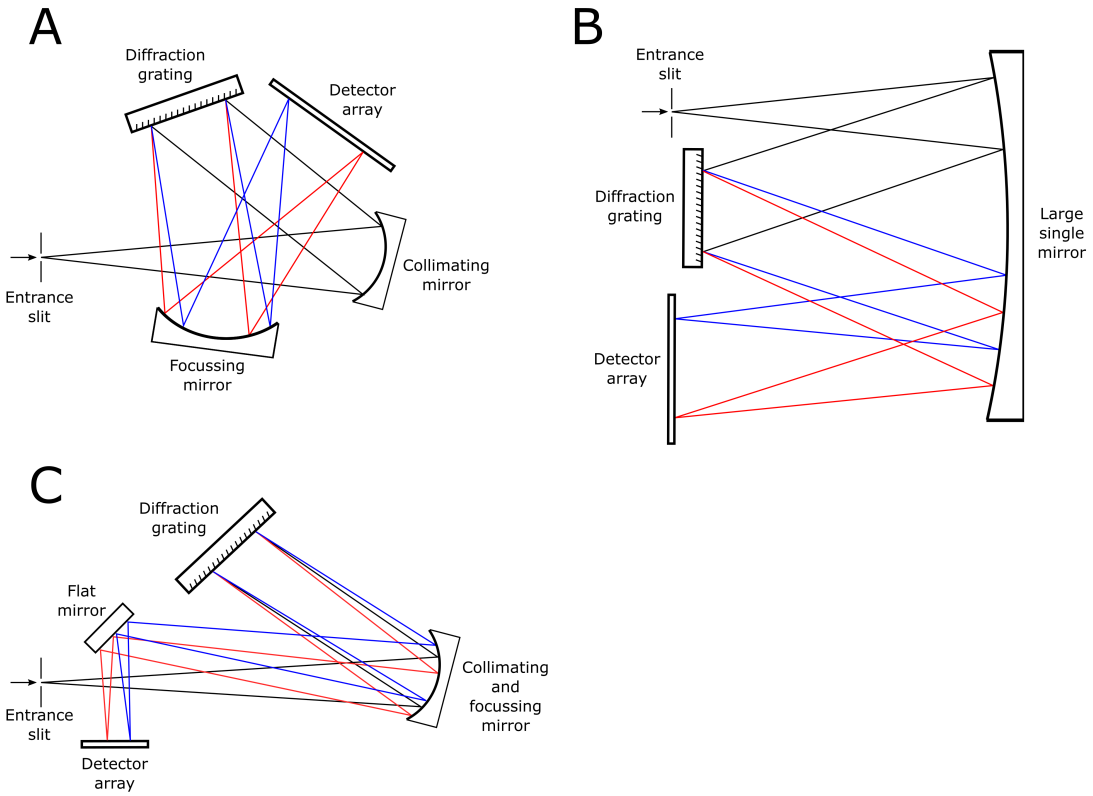

Figure 2.1: Schematic drawings of common spectrometer formats. A) Crossed Czerny-Turner; B) Fastie-Ebert; C) Littrow. Black rays represent white light, whilst the coloured rays represent constituent wavelengths of light that have been isolated by the diffraction grating's dispersion.

ensure that lines are adequately resolved, it is important that the width of each pixel is sufficiently small that the wavelength interval of each pixel is markedly less than ($\approx$ 10-20 % of) the linewidth of the spectrometer (e.g., Platt and Stutz, 2008). This ensures that the spectrometer's spectral resolution is limited by its fundamental ability to separate wavelengths of light, rather than the performance of its detector. Figure 2.2 shows how inadequate pixel sampling could result in significant errors in retrievals.

2.3.3 DOAS in volcanology

In volcanology, a wide range of instrument designs and deployment modes have been proposed and implemented for DOAS systems: Multi-AXis DOAS (MAX-DOAS; e.g., Hönninger et al., 2004; Bobrowski et al., 2007; Galle et al., 2010), walking traverses (e.g., McGonigle et al., 2002), road traverses (McGonigle et al., 2002; Galle et al., 2003; Salerno et al., 2009), airborne traverses (Galle et al., 2003; McGonigle et al., 2004c; Grutter et al., 2008), high time resolution fixed field of view deployment (McGonigle et al., 2009; Boichu et al., 2010; Tamburello et al., 2011a), satellite remote sensing (Khokhar et al., 2005; Rix et al., 2009; Theys et al., 2015), and collocated with SO_2

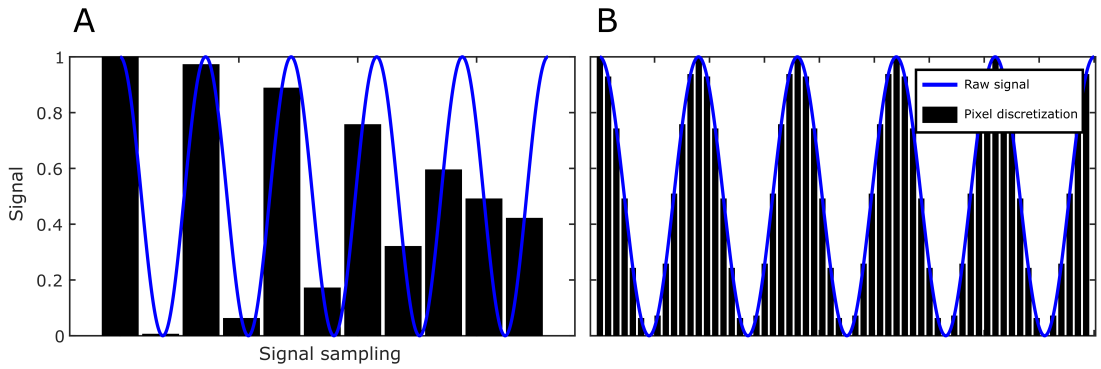

Figure 2.2: Example plots of signal sampling, here pertinent to a spectrometer detector's pixel discretisation of spectra. (A) Too low a sampling frequency results in poor representation of the form of the original signal. (B) An adequate sampling rate discretises the signal in a manner which quite accurately represents the true signal's form.

camera for calibration (e.g., Kern et al., 2013; Lübcke et al., 2013; Kern et al., 2015b). Airborne DOAS instruments have also been proposed as a means of improving aviation safety related to volcanic hazard, by providing an early detection system of a volcanic plume when mounted to an aircraft (Vogel et al., 2011).

As outlined in Section 1.2.1, prior to the development of the SO_2 camera by Mori and Burton (2006) and Bluth et al. (2007), DOAS instruments were the primary means of quantifying volcanic emission rates of SO_2. Whilst the SO_2 camera has shown great utility in providing unprecedented high time- and spatial-resolution SO_2 emission rates, DOAS instruments remain an important component of monitoring and research inventories. This is in part due to the higher spectral resolution of DOAS instruments relative to SO_2 cameras, which allows more accurate/complex retrievals of SO_2 column densities to be performed (Kern et al., 2010a; Kern et al., 2010b; Kern et al., 2013; Platt et al., 2018). For instance, DOAS retrievals can better deal with inhomogeneous background sky illumination due to cloud cover, relative to SO_2 camera retrievals. Furthermore, as highlighted above, many SO_2 camera systems are preferring to use a DOAS instrument as a means of calibrating images, as opposed to calibration cells; therefore, the two techniques can be complementary. Incorporation of DOAS calibration is particularly beneficial to permanent cameras for continuous monitoring, since it negates the need for moving parts required for automated cell calibration. Furthermore, cell calibrations cannot take into account complex radiative transfer and can therefore be quite erroneous, particularly for distant plumes and/or those containing high SO_2 and aerosol loadings (Kern et al., 2013; Kern et al., 2015a).

DOAS instruments are well established at a number of volcanoes across the globe, thanks primarily to the NOVAC project (Galle et al., 2010), as well as other smaller projects such as the FLux Automatic MEasurement (FLAME) network in Italy (Burton et al., 2009; Salerno et al., 2009). These permanent installations employ scanning-mode DOAS

retrievals. One advantage of these networks of instruments, over a network of SO_2 cameras for instance, is that they can often be used to determine emissions from more than one volcanic species. For example, Bobrowski et al. (2003) has shown that bromine monoxide (BrO) can readily be retrieved from volcanic plumes in the spectral range $\approx$ 320 - 360 nm, prompting further work investigating BrO/SO_2 ratios (Lübcke et al., 2014) and even their possible correlation with earth tides (Dinger et al., 2018).

Since spectrometers are relatively light, recent work by Stix et al. (2018) has also shown that DOAS instruments can be mounted to unmanned aerial vehicles (UAVs) to perform traverse measurements. In the future, this could allow quantification of emission rates from remote volcanoes which are difficult to access over ground, as well as minimising the effect of light dilution by flying close to the plume. Furthermore, plume speed, which is a critical parameter for computing an emission rate, can be quite accurately estimated using the drone's drift speed when within the plume.

2.3.4 Limitations

In general, the retrievals which can be performed by a spectrometer are more accurate than SO_2 cameras in terms of quantifying the column density of SO_2 (as discussed in Section 2.3.3), since the higher spectral resolution allows more sophisticated consideration of radiative transfer effects (e.g., Kern et al., 2010b; Kern et al., 2010a; Kern et al., 2013; Platt et al., 2018). However, since most spectrometers only gather a single spatial data point for each acquisition, the time taken to acquire an integrated column cross-section through the plume can be significantly longer than the single acquisition required for a SO_2 camera ($\approx$ 5-10 minutes vs $\approx$ 1 second); as such, the resulting emission rate time series have relatively poor time-resolution, and are unable to resolve transient volcanic phenomena. As mentioned in Section 1.2.1, McGonigle et al. (2009) and Boichu et al. (2010) have proposed a solution to this problem, by using cylindrical lenses which provide a quasi-rectangular field of view for the gathered spectra. When oriented correctly, this allows the entire width of a volcanic plume to be incorporated into a single spectral acquisition. As a result, $\approx$ 1 Hz data has been gathered using a DOAS system. Although this shows great promise for DOAS systems, it has not become a common practice retrieval mechanism for the volcanology community, and it is not clear whether the significant decrease in spatial resolution of this device will negatively affect the quality of DOAS retrievals.

Related to the above discussion, DOAS instruments suffer from a lack of spatial information, since each spectral acquisition represents a single integrated area. Whilst it has been shown that the SO_2 camera can rapidly and easily distinguish between different degassing sources (e.g., D'Aleo et al., 2016), since it forms an image of the scene, traditional DOAS systems are unable to provide such detail. As mentioned earlier, IDOAS, introduced by Bobrowski et al. (2006), presents a possible solution to this problem by us-

ing a 2-dimensional sensor, such that spectra are dispersed through one direction whilst the second direction provides spatial information, i.e., a line of spectra are gathered at once. By scanning in the second spatial direction, a hyperspectral image can be built; each pixel in this image therefore has an associated spectrum, rather than only the one or two bands of an SO_2 camera. Whilst this technique shows great promise, the necessity of scanning for multiple acquisitions means that this image takes ≈ 15 minutes to be built, at a resolution in the scanning direction of 100 pixels. Of course, over this time frame the plume structure may have changed quite significantly and, thus, the investigation of short-lived phenomena would not be possible with such an instrument.

Following from the lack of spatial information, DOAS instruments often suffer from an inability to determine a plume speed, which is integral to determining SO_2 flux from a volcano. McGonigle et al. (2005b) presented a method for determining the plume speed, using multiple spectrometers to integrate across the plume at different distances from the volcanic source. Integrated column amounts of SO_2 can then be cross-correlated, much like with SO_2 camera plume speed determination (Section 2.2.1), to derive a plume speed from the lag time. However, this method requires multiple spectrometers or possibly a clever scanning protocol from a single spectrometer (e.g., McGonigle et al., 2005a). Often, however, reanalysis model data from forecasting models are used for wind speed estimation, which can incorporate significant errors into the emission rate values (e.g., Stix et al., 2018). If the plume is persistently condensed at a volcano, a simple visible imaging webcam could be used to determine plume speeds quite accurately; alternatively, a single UV camera imaging at ≈ 310 nm would be able to detect the plume, whether it is condensed or not, and could therefore provide a source of quite accurate wind speed estimations. Again, this highlights the complementary nature of DOAS and SO_2 camera systems.

2.4 Thermal Imaging Systems

The fundamental theory behind thermal imaging differs quite considerably from the two techniques previously discussed (Sections 2.2 and 2.3), which are both based on the same concept of the Beer-Lambert law. However, thermal imaging also plays a crucial role in volcano monitoring and research, and its ability to retrieve data remotely, rather than in-situ, provides a number of the same benefits given by SO_2 cameras and DOAS instruments. Namely, they can all be performed some distance from the volcanic phenomenon of interest, therefore being much safer than in-situ methods; also, they all generally provide more spatial coverage and, thus, a more complete view of the volcanic phenomenon, relative to spot measurements made in-situ. Moreover, all of the techniques have uncertainties associated with the complexity of atmospheric radiative transfer. Of particular pertinence to this thesis, much like SO_2 cameras and DOAS instruments to date, the cost of thermal imaging systems can be prohibitive to their

widespread availability within the volcanology community.

2.4.1 The fundamentals of thermal imaging

Whilst the previously discussed remote sensing techniques have exploited characteristics of the absorption of electromagnetic (EM) radiation, thermal imaging is based upon the emission of EM radiation, which increases with increasing object temperature. The emission from a source is often compared to that of a black body - an ideal radiating surface which is a perfect diffuse emitter (e.g., Dixon, 1988); for a defined temperature and wavelength, no surface is able to emit more thermal radiation than that of a black body. The spectral radiance of a black body is defined by Planck's law:

$$L_{bb}(\lambda, T) = \frac{c_1}{\lambda^5(\exp\left(\frac{c_2}{\lambda T}\right) - 1)} \tag{2.8}$$

where $c_1 = 1.1911 \times 10^8$ W μm^{-4} m^{-2} sr^{-1} is Planck's first radiation constant, and $c_2 = 1.4388 \times 10^4$ μ K is Planck's second radiation constant. Spectral radiance therefore has the units W m^{-2} sr^{-1} μm^{-1}.

From Planck's law, two further important laws can be derived; these are also evident from the black body curves shown in Figure 2.3. Firstly, Wien's displacement law indicates that with increasing temperature of a black body the wavelength of peak emission shifts to shorter wavelengths, i.e., to EM radiation of a higher energy. Secondly, the Stefan-Boltzmann law shows that the radiant exitance M (W m^{-2}) for a black body increases proportionally to the fourth power of temperature.

$$\lambda_{max} = \frac{2898}{T} \tag{2.9}$$

$$M = \sigma T^4 \tag{2.10}$$

In Wein's law (Equation 2.9), the wavelength λ_{max} is expressed in micrometres (μm). In the Stefan-Boltzmann law (Equation 2.10), $\sigma = 5.67 \times 10^{-8}$ W m^{-2} K^{-4} is the Stefan-Boltzmann constant.

Since no real object behaves as a perfect black body, the parameter emissivity, ε, can be used to describe the departure of an object from a theoretical black body's spectral radiance:

$$L(\lambda, T) = \varepsilon(\lambda, T) \cdot L_{bb}(\lambda, T) \tag{2.11}$$

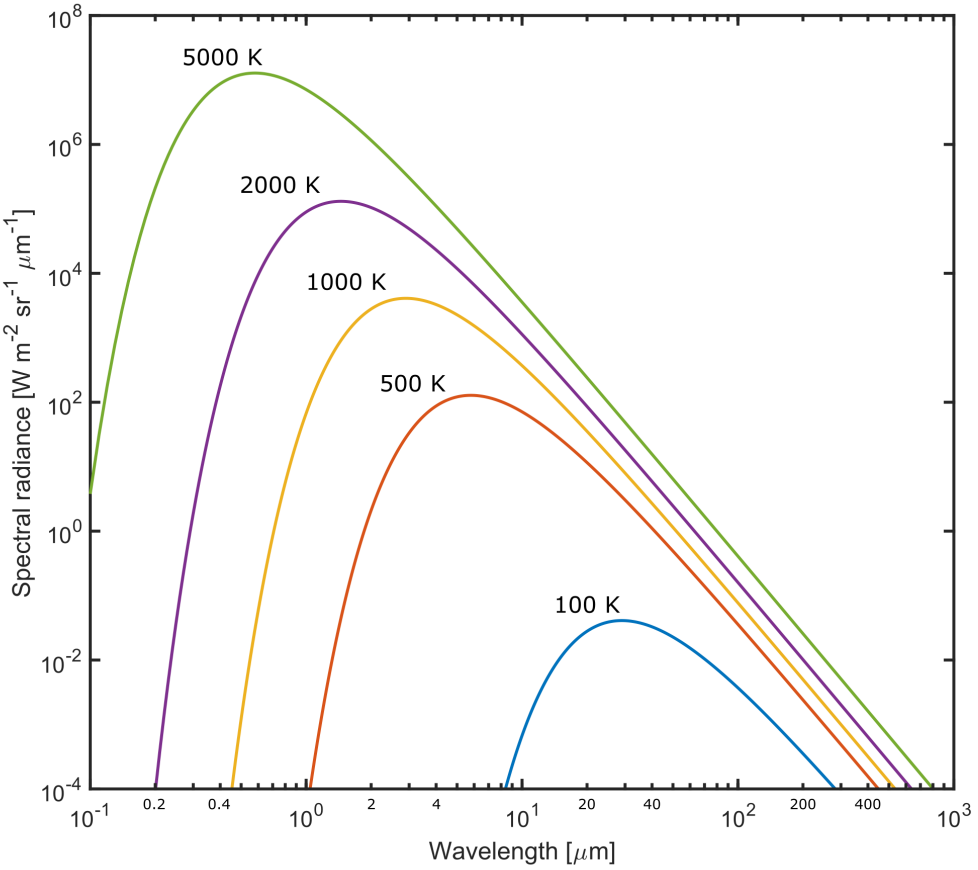

Figure 2.3: Black body spectral radiances between the wavelengths 0.1 - 1000 μm. Five black body curves are shown for distinct temperatures (labelled on the curves). Note that with increasing temperature the peak emission shifts to shorter wavelengths and the radiant flux increases.

where $L(\lambda)$ is the object's spectral radiance at temperature T, whilst $L_{bb}(\lambda)$ is the spectral radiance of a perfect black body at the same temperature. As well as being wavelength dependent, the emissivity itself is somewhat dependent on temperature, which can be problematic when attempting to make highly accurate remote measurements of a surface's temperature (Saunders, 2001). For most applications, however, this detail is neglected.

In reality, there are often other sources of radiation which are reflected from the emitting surface and, thus, Equation 2.11 becomes:

$$L(\lambda, T) = \varepsilon(\lambda, T) \cdot L_{bb}(\lambda, T) - (1 - \varepsilon(\lambda, T)) \cdot L_S(\lambda, T) \tag{2.12}$$

where $L_S(\lambda, T)$ is the spectral radiance of all surrounding objects incident on the emitting

surface. $[1 - \varepsilon(\lambda, T)]$ defines the reflectivity of the surface.

An imaging system is used to quantify the radiant flux incident on the detector, therefore allowing the temperature of the observed object to be inferred (more details on this, including calibration, are presented in Chapter 5). From Figure 2.3, it can be seen that the type of sensor used for this measurement will depend on the temperature of the object. A cooler object will require longer wavelength sensitivity, to ensure adequate emitted radiant flux across the sensor's response waveband. As a result, the majority of thermal imaging systems used in science and industry are based on Mid-Wavelength InfraRed (MWIR) and Long-Wavelength InfraRed (LWIR) detectors. Specifically, these are generally located in two wavebands, 3-5 μm and 8-14 μm, which have good atmospheric windows, i.e., important atmospheric species such as water vapour and CO_2 have relatively weak absorption features at these wavelengths (Dixon, 1988; Ball and Pinkerton, 2006; Sawyer and Burton, 2006; Spampinato et al., 2011). Often, such instruments can be sensitive down to ambient temperatures, or even below freezing; therefore, they have a broad range of applications.

MWIR/LWIR instruments are, however, generally expensive (1000s-10000s USD), since they have not benefited from the high consumer demand of cameras based on visible-band silicon photodetectors. The focal plane arrays (FPAs) used for a MWIR/LWIR instruments are often thermal detectors rather than photon detectors, since the energy at these wavelengths is not enough to exceed the band gap of most common semiconductors (e.g., Dixon, 1988). For instance, many FLIR (a company that produces popular instruments for thermal detection) cameras use microbolometer FPAs, which will contain an array of resistor elements that are sensitive to changes in internal temperature. The incident radiation from an object induces such temperature changes; therefore, an electrical circuit can be used to detect and record changes in resistivity across the FPA. Further complexity in MWIR/LWIR systems comes from the optics, which require materials that are less common than the glass or plastics used in visible imaging; materials such as sapphire and germanium have good transmissivity in the MWIR and LWIR spectral bands, respectively, and are therefore often used in these instruments (e.g., Dixon, 1988).

In certain scenarios there can be further advantages to using instruments with an operational waveband at shorter wavelengths, such as the Near-InfraRed (NIR). Dixon (1988) shows that the precision at which a measurement of spectral radiance needs to be made to achieve a certain precision in the temperature measurement decreases with decreasing operational wavelength. However, here there is a trade-off, since their must also be a large enough integrated spectral radiance within the instrument's operational waveband such that the signal produced by the detector far exceeds the system noise. Planck's law (Fig. 2.3) indicates that for shorter operational wavebands (NIR), this criterion will generally only be achieved for high temperature (≈ 500 °C) objects.

A NIR system can also provide benefits associated with the transmission of radiation through the instrument's sight path. The effect at a given wavelength is dependent primarily on three factors: the magnitude of the absorption cross-sections of all pertinent absorbing species within the instrument's operational waveband, the abundance of those species in the instrument's sight path, and the rate of change of spectral radiance with respect to changing object temperature. Of the common/abundant atmospheric species, only H_2O absorbs strongly at NIR wavelengths, whilst at longer wavelengths CO_2 also absorbs strongly. The effect of H_2O and a correction for this is discussed further in Chapter 5. For the latter factor, Furukawa (2010) highlights that at 10 μm, the difference in radiant intensity between 200 °C and 400 °C is just one order of magnitude, whilst at 1 μm this difference is approximately four orders of magnitude. Therefore, at 1 μm the absorption of 50 % of an object's emitted radiation has a considerably smaller effect on the retrieved temperature than it would have at 10 μm. This result is closely linked to the measurement precision factor which was discussed in the previous paragraph.

In general, each application and scenario can require a different optimal instrument design, i.e., there is not one instrument which is suitable for all applications. In volcanology, high temperatures are often encountered, when exposed lava is the target object; therefore, silicon photodetectors working in the NIR may often be suitable (e.g., Saito et al., 2005; Furukawa, 2010; Radebaugh et al., 2016). Furthermore, the limited funding often available for volcano monitoring networks means that low-cost solutions are always desirable.

2.4.2 Thermal imaging in volcanology

The general applicability of thermal imaging systems to volcanology was highlighted in Section 1.2.2. The following sub-sections provide more detail into a number of thermal imaging applications in this field; however, this review is not exhaustive, and it should be acknowledged that there may be a number of further applications which are not presented here.

Explosive plumes

Explosive volcanic plumes and their dynamics are often investigated using thermal imagers. Even many hundreds of metres from the vent, these plumes still have a temperature above the ambient background, therefore, they can easily be detected with thermal cameras. For Strombolian explosions on the eponymous volcano, Patrick (2007) identified the gas thrust and buoyant phases of an explosive plume, finding that entrainment of ambient air is much greater in the latter. Furthermore, they highlighted the transient (significant changes to the plume's state occurring on the order of seconds) and inhomogeneous nature of explosive volcanic plumes. Patrick et al. (2007) categorised these

explosive phenomena, and found that a particular vent would maintain similar explosive characteristics for many days/weeks. This indicated that the upper conduit is relatively stable over these timescales.

High-frame rate cameras have utility in capturing transient volcanic phenomena such as explosions. Delle Donne and Ripepe (2012) investigated the dynamics of Strombolian explosions with a 50 Hz thermal imaging system along with differential pressure transducers. They demonstrated that the thermal energy emitted by an explosion is related to the eruptive ash volume; thus, thermal cameras can be used to estimate the volumetric eruptive flux in real-time. The authors highlight that the ability to make such retrievals rapidly could be particularly beneficial to monitoring and risk assessment on Stromboli and any other volcanoes that exhibit this relationship. Furthermore, from the delay between thermal and acoustic signals, they showed that explosive source dynamics are primarily responsible for generating infrasound, rather than expansion of the eruptive cloud once it has exited the conduit.

Lava flows and lava lakes

As previously mentioned, exposed molten lava can reach temperatures in excess of 1000 °C. Lavas are therefore prime targets for thermal imaging systems, and have been probed by a number of studies. Thermal cameras can be used to track the evolution of lava flows through time, mapping their spatial extent, level of activity, heat and mass fluxes, and flow dynamics (e.g., James et al., 2006; Ganci et al., 2013; Ramsey and Harris, 2013; Patrick et al., 2017; Calvari et al., 2018). Ultimately, this has the potential to aid in hazard assessments, as well as further scientific understanding of these phenomena.

Patrick et al. (2017) used airborne thermal imagery to map the expanse of pāhoehoe lava flow fields during an episode of activity from Kīlauea volcano, Hawaii, in 2014-2015. This volcano's effusive eruptions are renowned for causing significant threat to property and infrastructure on Hawai'i's big island; therefore, monitoring flow evolution and gaining a better understanding of the driving forces behind a flow's expansion are critical. With thermal imagery the authors were able to identify the formation of a lava tube system, which exhibited surface temperatures of $\approx$ 15-50 °C above the surrounding cooled lava surfaces. Furthermore, they found that new up-slope flow breakouts, often associated with an abrupt change in lava supply rate, can lead to cessation of activity at the flow front. Of course, new hazards are then posed by the young breakout regions (Orr et al., 2015).

Lava lakes are a relatively rare phenomenon, with fewer than ten persistent lakes currently present on earth. They give a rare glimpse into the top of a volcanic plumbing system, with thermal cameras providing one of the best means for investigating this phenomenon (Oppenheimer, 2003; Calkins et al., 2008; Patrick et al., 2014; Radebaugh et al., 2016). From a hazard assessment point of view, thermal cameras can also be used

to track the surface level of lava lakes in near-real-time, providing an indication of the level of activity and associated hazard (Patrick et al., 2016). More discussion of lava lakes is provided in Chapter 5, where Masaya's lava lake is investigated in some detail.

Fumaroles and hydrothermal systems

The activity and spatial distribution of fumaroles and associated hydrothermal systems can provide important insights into the activity of a volcano and interactions between magmatic and hydrothermal systems (e.g., Harris and Stevenson, 1997; Harris and Maciejewski, 2000; Chiodini et al., 2015; Gaudin et al., 2016). However, in-situ thermocouple measurements can be difficult, due to the presence of corrosive gases, as well as being potentially dangerous; furthermore, with this technique the fumarole sampling rate is quite limited. Thermal cameras can allow mapping of an entire fumarole field quite rapidly, and from a remote location, providing a synoptic overview of an environment (Harris et al., 2009). As with mapping of lava flows, often it can be useful to perform such measurements with airborne instruments, which achieves good spatial coverage whilst providing a higher spatial resolution than satellite-borne instruments (Gaudin et al., 2016).

Investigating fundamental subsurface volcanic processes

The fundamental driving forces involved in volcanism often need to be inferred from measurements made at the surface. A range of different parameters can be studied at the surface to facilitate such inferences, and surficial thermal properties often provide critical insights.

In some of the earliest work with hand-held thermal cameras on volcanoes, Oppenheimer and Yirgu (2002) quantified the power output from Erta 'Ale's lava lake in Ethiopia, finding radiative heat losses of 70-150 MW. They used these data to identify magma crystallisation as potentially a significant driver of convection, whilst previous models had focussed on degassing being the principal driver of this process.

Multi-parametric studies involving thermal data have proved extremely insightful. Peters et al. (2014) examined the radiant heat output, surface motion and gas composition of Erebus's Ray lava lake, finding a common cyclicity of $\approx$ 10 minutes in each. This cycle was not found to correlate with bubble bursts at the surface, suggesting that the lava lake behaviour was principally controlled by magma exchange in the conduit, rather than the flow of gases. This work corroborates that of Oppenheimer et al. (2009), who also used thermal observations, along with gas ratios, to explore Erebus's plumbing system. Both studies concluded that pulsatory behaviour in the Ray lake was a result of intermittent perturbations of the bi-directional magma flow within the conduit.

2.4.3 Limitations

Retrieving a truly accurate temperature of a source through remote sensing is extremely difficult. A good summary of the most prominent issues in volcanology is provided by Ball and Pinkerton (2006), whilst Lane et al. (2013) also give a detailed discussion of uncertainties in thermal imaging more generally. Here, some common and pertinent issues are briefly outlined, some of which have been touched on in previous sections.

As highlighted in Section 2.4.1, transmission of radiation from source to detector can cause errors, primarily due to absorption and scattering of radiation. This can be particularly problematic in volcanology, since emissions of hot gases and particles can often obscure the intended source. Indeed, this has been addressed by a number of studies (Sawyer and Burton, 2006; Ball and Pinkerton, 2006; Harris et al., 2009; Radebaugh et al., 2016). Careful selection of wavelengths can reduce the effect of gases, by imaging in spectral windows where transmission is higher (e.g., Sawyer and Burton, 2006; Radebaugh et al., 2016). Furthermore, attenuation of radiation can be modelled, if the path conditions are known (or can be estimated), allowing a correction to be made to the retrieved signals (see Section 5.2.4).

The emissivity of an object is difficult to determine and can have quite large effects on the retrieved temperature, since an object's radiance is directly proportional to its emissivity (Equation 2.11). Furthermore, emissivity is dependent on both wavelength and to some extent temperature itself (Saunders, 2001), adding extra complexity to its estimation; for simplicity, in general both dependencies are neglected, therefore emissivity is assumed to be a single value. This emissivity value is further dependent on other factors, such as viewing angle and composition of the object (Ball and Pinkerton, 2006). Emissivity can typically be measured indirectly by quantifying the reflectivity of a surface (since reflectivity and emissivity sum to unity), or directly using a furnace.

As with any imaging system, thermal imagery is also limited by the instrumental performance in a number of ways. Detectors will introduce various sources of noise (e.g., Dixon, 1988; Grgić and Pušnik, 2011), and in some cases their response can drift through time (Whittam et al., 2014). Furthermore, issues associated with the quality of the optical system can be significant. The optics, along with a contribution from pixel cross-talk in the detector, result in a point spread function, which corresponds to the spatial distribution of measured signal induced by radiation originating from a point source i.e., it quantifies the inability of a camera to perfectly resolve a small object (Du and Voss, 2004). This gives rise to the size of source effect, which indicates that high spatial-frequency temperature variations across an image will result in inaccurate temperature measurements (e.g., Lane et al., 2013; Stanger et al., 2018).

2.5 Summary

This chapter has provided the details of three ground-based remote sensing techniques which are commonly used in volcanology: the SO_2 camera, differential optical absorption spectroscopy (DOAS), and thermal imagery. Such instruments provide a number of benefits relative to in-situ measurement methods, including the ability to acquire data at safer distances from volcanic hazards and the potential to retrieve a greater spatial coverage of data with a single acquisition. All three techniques also currently suffer from one main drawback in their usage: the cost of instrumentation. Scientific grade equipment can be expensive, however, its use is not always necessary. Indeed, for each of these three techniques the upcoming chapters present on the development of low-cost alternatives to the current instrumentation.

Chapter 3

Development of a low-cost ultraviolet camera for the remote sensing of volcanic SO_2

This chapter is associated with two bodies of published work (Wilkes et al., 2016; Wilkes et al., 2017a). It presents the development of a low-cost UV camera, based on a sensor primarily designed for the smartphone market. This UV camera was incorporated into an SO_2 camera system, of the format which is routinely used in volcanology for quantification of volcanic SO_2 emission rates. The system is presented with tests both at a power station in the United Kingdom and on Mount Etna in Italy; throughout the latter deployment, a side-by-side comparison with a commercial UV camera was performed.

3.1 Introduction

Since its advent over a decade ago (Mori and Burton, 2006; Bluth et al., 2007), the SO_2 camera has become an extremely popular instrument for remote sensing of SO_2 emissions on volcanoes. Until now, the units have involved the use of scientific-grade UV cameras that are utilised across a broad range of applications, for example in forensics (Krauss and Warlen, 1985), industrial fault inspection (Chen et al., 2008), astronomy, monitoring skin conditions (Fulton, 1997a), and SO_2 measurements of ship (Prata, 2014), power station (Smekens et al., 2015) and volcanic emissions (Kern et al., 2015b).

Whilst nominally low-cost (1000s - 10000s USD per unit), the price of these UV cameras is still relatively high, as they are quite specialist pieces of a equipment. Indeed, their price-tag can still be inhibitive in science, which is often limited by available research budgets. Within the consumer market, imaging systems are becoming increasingly affordable, to the point that almost every mobile phone now incorporates at least one camera; many

have more than one. In this chapter, a description is given of the utilisation of these extremely low-cost technologies to develop a UV camera that is at least an order of magnitude cheaper than scientific-grade systems. Based on a camera module which costs just ≈25 USD, the work details the modification of a sensor primarily designed for the smartphone market, rebuilding of the optical system for good UV transmissivity, and a number of tests to assess the performance of this low-cost UV camera. In particular, the chapter discusses deployment of the camera as an SO_2 camera to measure emissions from both Drax power station (UK) and Mt. Etna volcano (Italy).

3.2 Development of a low-cost UV camera

3.2.1 Silicon photodetectors

Imaging systems at visible, near-infrared (NIR) and ultraviolet (UV) wavelengths are almost universally built using 2D arrays of silicon photodetectors. Silicon is a semiconductor with a band gap of 1.1 eV, which relates to the energy of electromagnetic (EM) radiation at a wavelength of ≈ 1125 nm (e.g., Darmont, 2009). Theoretically, therefore, all EM radiation of shorter wavelength (higher frequency and thus energy) has enough energy to free an electron from silicon's energy band. This electron can subsequently become part of a photo-current. The detection of these free electrons is often performed by a PN junction diode. Since this PN junction must be located at a specific depth in the silicon material, in general photons will only be detected if they are absorbed within the PN junction; in reality, current leakage from outside of the PN junction can contribute to the final signal (e.g Murakami and Shingyouji, 1994). The depth at which a photon is absorbed is dependent on its energy/wavelength; photons of higher energy (shorter wavelength) have a larger absorption coefficient, and are therefore absorbed closer to the surface of the silicon (Darmont, 2009). Therefore, silicon detectors designed primarily for visible applications, have a relatively poor quantum efficiency in the UV, since the PN junction location is optimised for absorption of visible wavelength photons.

There are two main silicon photodiode architectures available for manufacturing a focal-plane array (FPA): Charge-Coupled Device (CCD) and Complimentary Metal-Oxide-Semiconductor (CMOS). In simple terms, the two differ in their handling of the freed photoelectrons. CCDs transfer charge through rows or columns of pixels to a single readout node which performs the charge-to-voltage conversion. Conversely, in a CMOS detector the charge-to-voltage conversion is performed individually at each pixel (Magnan, 2003). As a result of the added pixel complexity, the typical CMOS sensor has a smaller fill factor (photosensitive region) than a CCD, which can result in lower quantum efficiency. Advantages of the CMOS sensor include: low power consumption, lower cost, capability of integrating peripheral functions, and high readout rate.

Recently, the development of back-illuminated CMOS sensors has improved the fill factor, and thus, the quantum efficiency of the CMOS architecture. Whilst on the traditional front-illuminated sensor the metal wiring is located above the photodiode, therefore attenuating incident radiation and reducing fill factor, back-illuminated technology flips the sensor such that the metal wiring is located beneath the photodiode (Iwabuchi et al., 2006). Indeed, specialist back-illuminated sensors have previously been used in UV applications for this reason (Waltham et al., 2007). For heightened UV sensitivity, Waltham et al. (2007) also back-thinned the sensor, etching oxide layers from the surface of the sensor; since UV photons are absorbed at a relatively shallow depth, this ensured that they were not absorbed prior to reaching the photodiode.

3.2.2 Enhancing detector UV sensitivity

The first and most critical step to developing a UV camera is ensuring that the applied sensor has UV sensitivity: this is quite clear. However, for a number of reasons, some of which were discussed in Section 3.2.1, the majority of consumer cameras do not have the sensitivity to produce good quality UV images, especially at wavelengths of $\approx$ 310-330 nm, the band in which SO_2 cameras typically function. Firstly, it is likely that standard cameras, which are designed for visible imagery, contain optical systems which are not UV transmissive. Secondly, the sensor will, unless monochrome, be coated in a colour filter array (often in the Bayer configuration) which not only attenuates incident UV radiation but also creates an inhomogeneous mosaic response on the detector (e.g., Garcia et al., 2013; Wilkes et al., 2016). Finally, the P-N junction, which is responsible for reading off photoelectrons, may be located deeper in the silicon photodiode than the depth at which UV photons are absorbed (e.g., Magnan, 2003; Darmont, 2009). A combination of these effects results in UV imaging with an unmodified visible imaging camera being either difficult or impossible. For the work herein, modification of the chosen camera system was evidently necessary.

Here, the Raspberry Pi (R-Pi) Camera Module v1.3 (Fig. 3.1) was selected as a strong candidate for sourcing a low-cost UV sensor; the UV camera system will be referred to as 'PiCam' throughout this thesis. The camera module houses a 1/4″ Omnivision OV5647 detector which was primarily designed for the smartphone market; it therefore benefits from the large consumer market making costs considerably lower. The entire R-Pi Camera Module costs $\approx$ 25 USD. Perhaps most importantly, it is a backlit-CMOS sensor, which provides higher sensitivity than conventional CMOS detectors due to the absence of metal wiring obstructions between the sensor surface and the photodiode (as discussed in Section 3.2.1); this makes the sensor perfect for application in UV imaging. The sensor is 5 megapixels (1944 $\times$ 2592) with 8-bit standard JPEG output or 10-bit RAW pixel output.

To improve the camera's sensitivity to UV radiation it is clear that removal of the Bayer

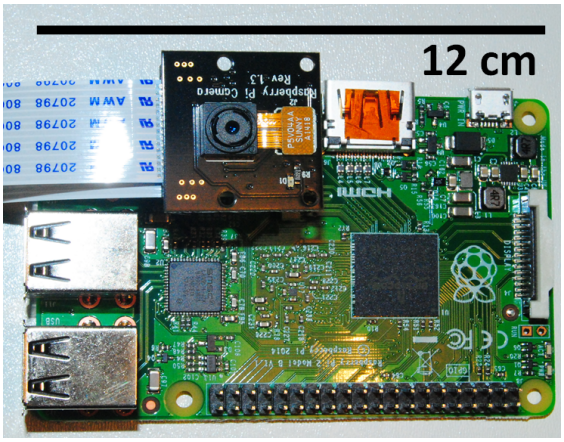

Figure 3.1: The R-Pi camera module (black board) attached to a R-Pi computer.

filter, which has very low transmission at UV wavelengths, is critical. Initial tests showed that this can simply be abraded using a sharp plastic or wooden utensil (Fig. 3.2). Using this method, however, it is extremely difficult to achieve a clean, homogeneous finish to the sensor surface. This degrades the quality of the image, as parts of the image may appear dirty or have streaks of filter still intact after the scratching procedure. Nevertheless, results from this method quickly provided a proof of concept for the utility of this sensor within a UV camera. As can be seen from Figure 3.2, which was taken of clear sky with a 310 nm bandpass filter (10 nm full-width-at-half-maximum; FWHM) to the fore of the sensor, regions where the Bayer filter had been removed provided considerably higher sensitivity to UV radiation; in these regions the signal was 6 times that of where the Bayer filter remained intact.

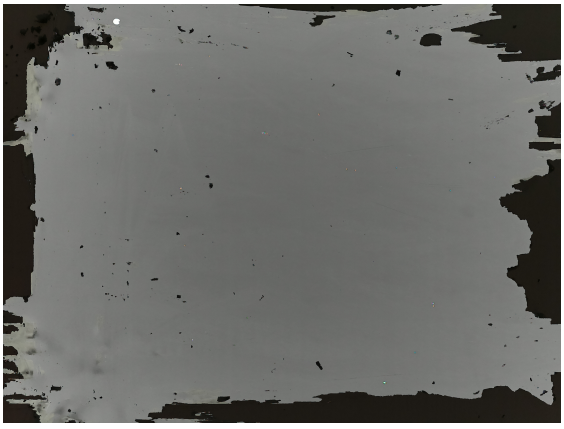

Figure 3.2: Image of clear sky taken with the R-Pi Camera Module v1.3, through a 310 nm bandpass filter (10 nm FWHM); a lens was used to form an image. The Omnivision OV5647 sensor was scratched to remove the Bayer filter in the centre of the image. A clear improvement in UV sensitivity can be seen in this region, which has 6 times the signal of regions where the Bayer filter remains intact (around the edges of the image).

To improve the Bayer filter removal process, achieving a cleaner finish, chemicals must be used. Since the filter is almost certainly composed of photoresist, a photoresist strip-

per was used to remove the filter. There are a broad range of photoresist strippers commercially available, designed for either positive or negative photoresist. Simply due to having easy access to the chemical, Posistrip® EKC830™was tested and found to remove Bayer filter efficiently. The sensor was submerged in a Posistrip bath, which was heated to ≈ 60-70°C. After ≈ 20-30 minutes, with some agitation the Bayer filter detached from the sensor, floating into the solution. The Posistrip was then washed from the sensor using a 3-stage cleaning procedure commonly used in semi-conductor fabrication laboratories: the sensor was submerged sequentially in n-butyl acetate, acetone and finally isopropyl alcohol. The chemicals were gently warmed (≈ 40-50 °C) to improve the cleaning process. Through trial and error, it is apparent that the sensor should be submerged in each stage for approximately one minute; however, if the procedure is unsuccessful, it can be repeated for longer periods of time, until the sensor is free from residue when removed from the isopropyl alcohol. A nitrogen gun may be used on the sensor upon removal from the alcohol, to prevent the appearance of drying marks. When performed well, this procedure results in a uniformly responding sensor with greatly heightened UV sensitivity. Figure 3.3 shows microscope images of the sensor appearance before and after this process, confirming the removal of the Bayer filter and microlenses which overlay the silicon detector.

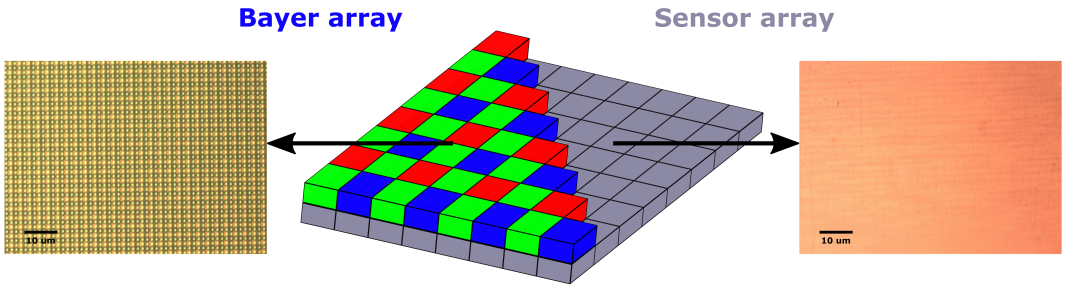

Figure 3.3: A schematic (centre) of the Bayer filter array and how it lies on top of the silicon photodiode. Also shown are microscope images of the OV5647 sensor pre- (left) and post- (right) Bayer removal. The different red, green and blue filters overlying each pixel can just be seen pre-removal, along with the circular microlenses.

3.2.3 Building the UV camera

Once the sensor had been modified, the camera was rebuilt with a new optical system to form a UV image on the detector. To keep costs low, a simple singlet plano-convex lens was used here. This resulted in some spherical aberrations in the images formed, with perfect focus being lost towards the edge of the image; however, the quality has been found to be sufficient for SO_2 camera applications when a relatively small aperture is used (1.5 mm diameter). A 6 mm diameter fused silica lens with a focal length of 9 mm (Edmund Optics Ltd.; ≈ 100 USD) was used for this design. To increase UV transmission

it comes coated with an anti-reflective layer (280-425 nm). When mounted to the sensor this lens provided a field-of-view (FOV) of $\approx 23.1^\circ \times 17.3^\circ$ (width $\times$ height).

The lens was mounted to the R-Pi camera sensor using 3D prints. This fast-growing technology has opened up a wide range of possibilities for amateur makers, and allows rapid prototyping of designs (e.g., Zhang et al., 2013). The lens holder model was designed in Solidworks®, a computer aided design (CAD) software. The design allows the user to focus the image by turning the threaded lens mount (Fig. 3.4). This was preferred to a fixed focus system, since it is possible that changes in both sensor height on the R-Pi board and 3D print accuracy could affect the quality of focus in a fixed setup. Preliminary tests showed that the commonly used fused filament fabrication process did not provide enough precision to produce the fine threading mechanism used in the lens holder model. The much more precise method of selective laser sintering (SLS), however, was found to work extremely well (https://3dprintdirect.co.uk/), and is still very affordable for prints of this size (<25 USD for a pair of UV cameras). This company quote an accuracy of ± 0.2 mm and a layer thickness of 0.1 mm in their SLS prints.

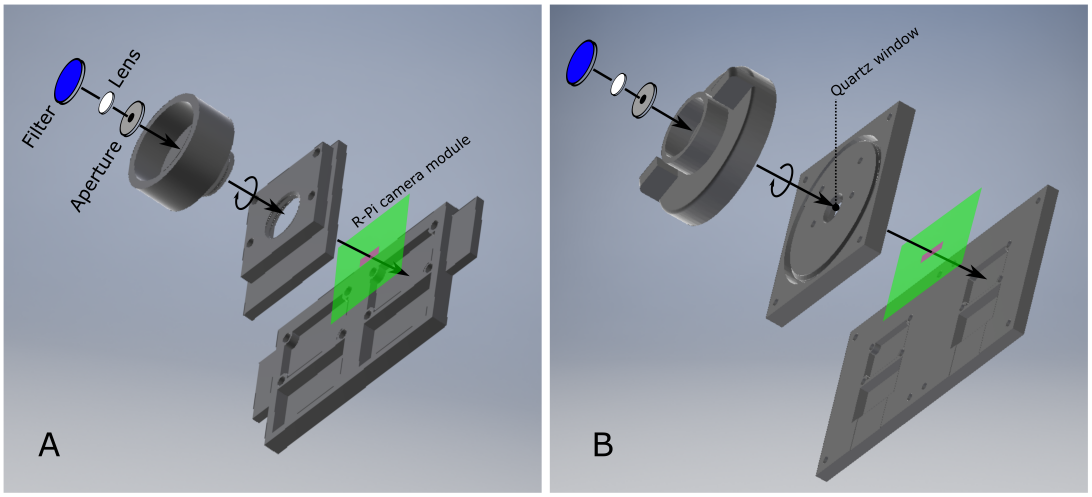

Figure 3.4: Iterations of the PiCam lens holder design (A) c. 2016 (B) c. 2017 (current design). Both designs have a backing plate to hold two cameras in an approximately coaligned format, as is required for SO_2 camera systems. The latter design (B) minimises stray light (without the need for additional measures such as the use of blu-tack, as was frequently adopted in design (A)) by locating the lens holder thread outside of the central optical cavity.

A number of iterations of the lens holder design have been worked with over the course of this thesis. Most notably, the first design (Fig. 3.4A), which incorporated a thread very close to the sensor, resulted in dust from the SLS print being deposited onto the sensor as the thread was turned. To prevent this, the thread was moved away from the sensor and a quartz window (product code WHQ1600; Knight Optical ltd.) was added to the design to provide better protection for the sensor. A laser cut aperture is now also used in the camera build, where initial iterations relied solely on the 3D print to

provide the aperture for the system; clearly, this earlier design was sub-optimal as the aperture edge is not precise.

3.2.4 Data extraction and sensor linearity

Once the UV camera was built, a number of software developments needed to be made. The camera was controlled via Python's (Python 3.x) `picamera` module, from which a range of camera attributes can be accessed and controlled. The standard data output are 3-channel (Red-Green-Blue; RGB) 8-bit JPEGs; however, since the Bayer filter has been removed from the sensor, the RGB information is lost, making this data format somewhat redundant. The camera module also allows users access to the RAW 10-bit Bayer data, which is simply a single channel array of pixel digital numbers (DNs). This is often referred to as RAW Bayer data, since on a typical sensor the data will be mosaicked from the varying responses caused by the Bayer filter array; demosaicking algorithms, as well as other image processing algorithms, are then applied to form a typical RGB JPEG image. However, in this work, since the Bayer filter has been removed, the RAW data is exactly what is needed, as it has not had any post-processing applied to the pixel DNs. At the beginning of this work, custom Python code was required to extract the RAW 10-bit data, which is saved in the meta-data of a standard JPEG image on request. However, recently the `picamera` module has been updated to include a `PiBayerArray` class, which makes RAW data extraction simpler for the end-user.

It was first critical to test the linearity of the sensor's response to incident UV radiation, since SO_2 camera retrievals depend on instrument linearity (e.g., see Section 2.2.1). Images of uniformly illuminated clear-sky were taken through a 310 nm filter at varying shutter speeds; these experiments were performed in Sheffield, UK, during February 2016. Using initial simple recipes from the `picamera` documentation, the images showed a non-linear response to incident radiation (Fig. 3.5). However, further examination found that, unless specified, the camera automatically adjusts gains for each image; this compromises the linearity. From Figure 3.5, up to 400 ms, the system performed somewhat as expected, with a quite linear increase in signal relative to the shutter speed; the SO_2 gas cells also showed greater attenuation resulting from the 1600 ppm·m cell relative to the 400 ppm·m cell, as would be expected. However, at >400 ms the system began to respond unpredictably, as a result of automatic gain adjustments which the camera board applies to the signal. When gain was subsequently fixed, by setting `exposure_mode = 'off'`, the camera response was extremely linear (Fig. 3.6A). Furthermore, Fig 3.6B highlights that post-processing involved in forming the standard JPEG images also introduces non-linearity; it is therefore crucial that the 10-bit RAW data is used for any scientific application. These results also highlight the quite reasonable sensitivity of the OV5647 detector to UV radiation, since saturation was almost achieved at 400 ms, even though irradiance is quite restricted at 310 nm in the winter months of a high-latitude

country. It should be noted, however, that although the gain for these initial tests was not known/recorded, it may have been substantially higher than is preferable to use for good signal-to-noise ratios; therefore, this level of saturation may have been a result of a high analog gain applied to the signal.

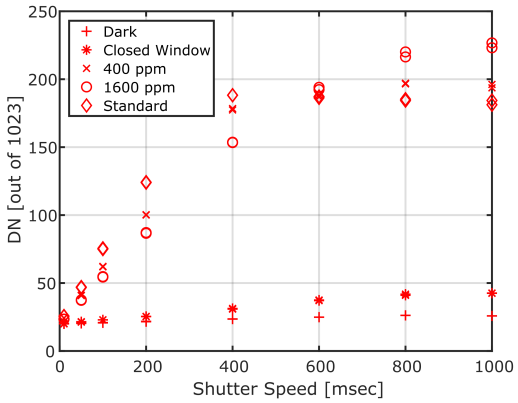

Figure 3.5: Preliminary tests of the PiCam using rudimentary software which did not fix analog gain. Images were taken through a 310 nm filter, pointing to clear sky. This plot shows the average pixel digital number (DN) of a cropped region (800 × 600 pixels) for different shutter speeds (ms). Dark denotes image taken with a lens cap on, which, helped to confirm that there was not significant stray light arriving at the sensor. The closed window denotes images which were taken through a window pane, and hence the UV radiation has been attenuated substantially. This was also used to confirm that the optical system was imaging through the filter correctly, and not leaking light. The 400 and 1600 ppm·m denote images taken with a quartz cell containing the quoted column density of SO_2 placed in front of the camera optics. The standard was through an open window imaging the clear sky.

3.2.5 Dark Current

Noise in images stems from a number of sources, some of which follow random Poisson statistics (shot noise) or are stochastic and therefore are difficult to perfectly correct; however, fixed-pattern noise (FPN), which results in a gain and offset that varies pixel-to-pixel, can be corrected for via a number of proposed methods (Choubey and Collins, 2007; Schoberl et al., 2009; Mohammadnejad et al., 2012; Liu et al., 2015; Xu et al., 2017). Most simply, if exposure time remains constant, a dark image can be captured and subsequently subtracted from all acquired frames (e.g., Porter et al., 2008; Schoberl et al., 2009). In particular, this corrects for dark signal non-uniformity. Due to the architecture of a CMOS sensor and its readout circuit, FPN appears as strips down an image (e.g., Mohammadnejad et al., 2012).

To investigate the FPN and dark current in the PiCam's OV5647 sensor, a series of images were taken with the lens cap on the camera. Images were taken at a number of shutter speeds, whilst at a shutter speed of 50 ms a series of 100 images were taken. This

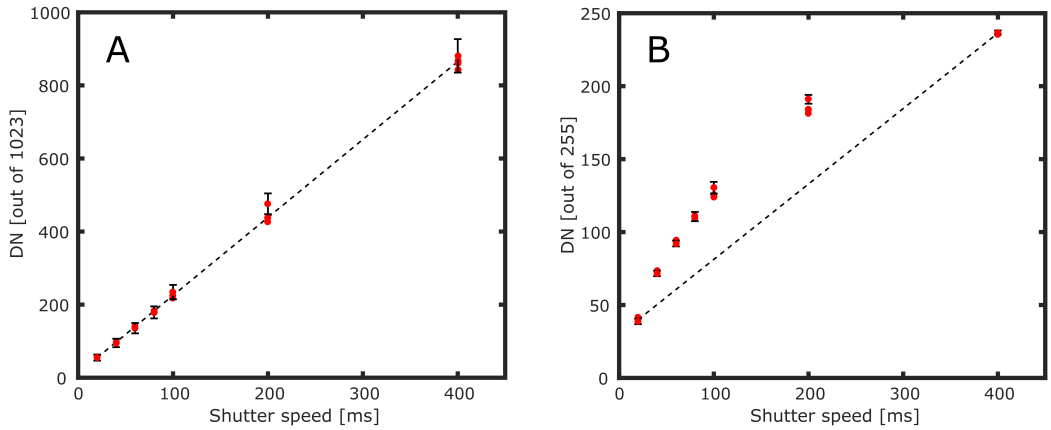

Figure 3.6: Plots of average pixel signal (in digital number; DN) vs. shutter speed (ms) for a cropped region (800 × 600 pixels) of clear-sky images taken at 310 nm. (A) the 10-bit RAW image output shows a linear increase in DN with respect to shutter speed; (B) the 8-bit standard output JPEG image shows a non-linear response in all three of the red-green-blue (RGB) channels (Red-channel DNs are plotted here). An error bar is inserted on one data point per exposure time, indicating the standard deviation of the pixel intensities in the cropped region; the bar heights are approximately the same for all points of equivalent shutter speed, and just one bar is displayed for clarity.

allowed assessment of dark current variability both spatially and temporally. All images were acquired with an analog gain of 1 and were binned to a resolution of 648 × 486, as is suggested for most field acquisitions to maximise signal-to-noise ratio (SNR; see Section 3.4.3). Whilst the noise would be more pronounced in a full resolution image, this test was chosen to asses the PiCam's performance under representative field deployment.

As can be seen in Fig 3.7A, the FPN appears in vertical strips on the image, as would be expected on a CMOS sensor. However, the difference in DN between the dark and light strips is incredibly small, with a maximum and minimum DN of 19 and 12, respectively (just 0.7 % of the sensor's 10-bit range). Furthermore, the temporal variation between images is very small for a single pixel (Fig. 3.8), with each of three randomly selected pixels deviating only periodically from their typical intensity state. In this experiment, the pixels only ever deviated by 1 DN from their modal value. Some pixels appeared to show greater variability than others across the 100 images. Figure 3.7, which displays images from two different PiCam sensors, highlights that each sensor has a different fixed pattern noise. This is to be expected, since the noise results from small inconsistencies in the sensor fabrication process. Whilst the FPN is different, both sensors exhibit a negatively skewed dark current with a modal pixel DN of 16.

A particularly surprising result from these tests was the sensor's dark current response to increasing shutter speeds: no concomitant increase in dark current was observed. This result was similarly found by Pagnutti et al. (2017) who investigated the v2 R-Pi camera module, which house a Sony IMX219 CMOS sensor. The reason for this lack of change in

dark current is not clear; however, Porter et al. (2008) found a similar result in a CMOS sensor when the exposure time is less than the frame time (the inverse of frame rate). They suggested that there are two separate dark current generation rates, one for the photodiode and one for the sense node. It appears that this is the case with the PiCam, which showed no variation of mean dark current with shutter speeds of $\leq$ 500 ms and a frame time of $\geq$ 2000 ms (0.5 Hz). Nevertheless, dark current is also dependent on temperature (Lin et al., 2010), and therefore regular acquisition of dark images during camera use is still important for correction of this drift. Furthermore, it should be noted that, whilst the mean DN does not appear to be linearly dependent on shutter speed, the signal noise (standard deviation of DNs within an image) was found to increase with increasing shutter speed, as would be expected.

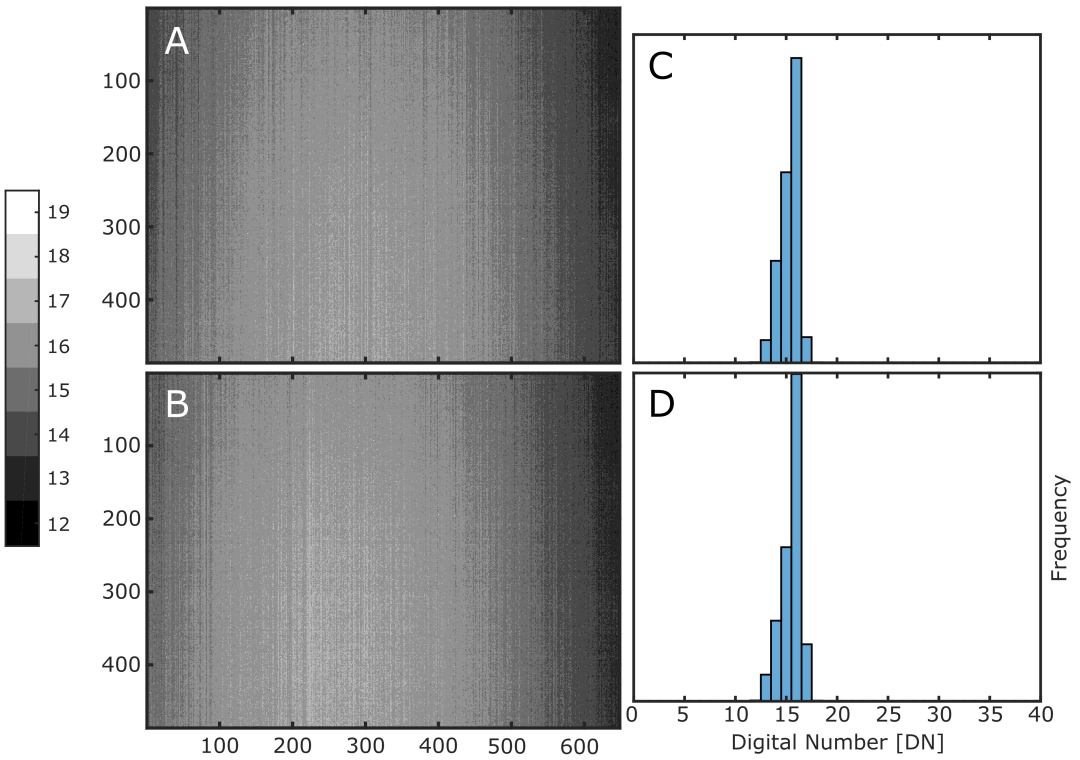

Figure 3.7: Dark images taken with two separate PiCam sensors (A and B), using a shutter speed of 500 ms and an analog gain of 1. The images were binned to 648 $\times$ 486, as is suggested for PiCam use. The colour scale of the image, which displays the digital number (DN), is greatly exaggerated such that the small variations in dark current are clearly visible. Distributions of pixel DNs are displayed in the respective histograms (C and D).

3.3 First measurements of SO_2

Following the initial tests of the PiCam, which highlighted its ability to capture UV imagery with a linear response to irradiance, the system was next tested as an SO_2

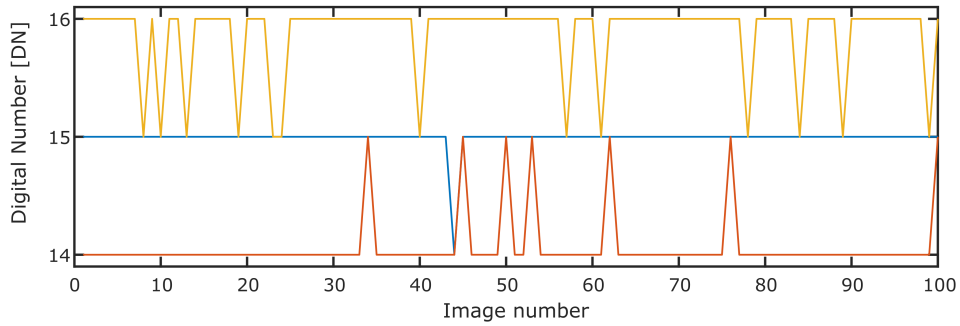

Figure 3.8: The temporal variation in pixel intensities shown by tracking 3 randomly chosen pixels through 100 images. Images were binned to 648 × 486, taken at 50 ms and with an analog gain of 1.

camera. For this application, as described in Section 2.2.2, two filters are used, corresponding on- and off-resonance bands for SO_2 absorption. This can be achieved either using a filter wheel or two separate cameras. The low cost of the PiCam module makes it extremely viable to use a 2 camera system, and the advantages to this approach were highlighted in Section 2.2.2. Therefore, here two cameras, with a 310 nm bandpass filter mounted to the fore of one and a 330 nm to the other, were used. Both filters were 10 nm FWHM, purchased from Edmund Optics (310 nm stock no. #67-752, 135 USD; 330 nm stock no. #67-756, 135 USD). The two cameras were co-aligned using the 3D-printed backing-mount displayed in Figure 3.4.

Preliminary tests were made by imaging quartz cells filled with known column densities of SO_2 (Fig. 3.9). First, the images were registered, by warping the 330 nm image such that it was mapped pixel-to-pixel to the corresponding location on the 310 nm image; this was performed by using control point registration, whereby distinct features were manually matched across the two images. The apparent absorbance of each pixel in the image was then calculated using Equation 2.3. The plot of apparent absorbance vs the cell SO_2 column density showed a linear relationship (Fig. 3.9B), somewhat validating the performance of the PiCam in this application.

Remote sensing of power station stack emissions can be used to ensure compliance with regulations and also to investigate atmospheric effects (McElhoe and Conner, 1986; Smekens et al., 2015; Millan, 1980; McGonigle et al., 2004a). Therefore, following the proof of concept of the PiCam as an SO_2 camera, the system was deployed to measure SO_2 emissions from Drax power station in the UK, on the 15th August 2016. The observation point (53°43′55.30″N, 1°1′7.21″W) was approximately 1500 m from the stack source. Measurements were made using the protocols outlined in Section 2.2.1. The two cameras acquired simultaneously at a rate of 0.25 Hz, with the 310 and 330 nm cameras acquiring at shutter speeds of ≈ 300 and 40 ms, respectively. The longer shutter speed required for the 310 nm camera is a result of both the reduced intensity of diffuse sky radiation at this wavelength and the decrease in quantum efficiency of the sensor at

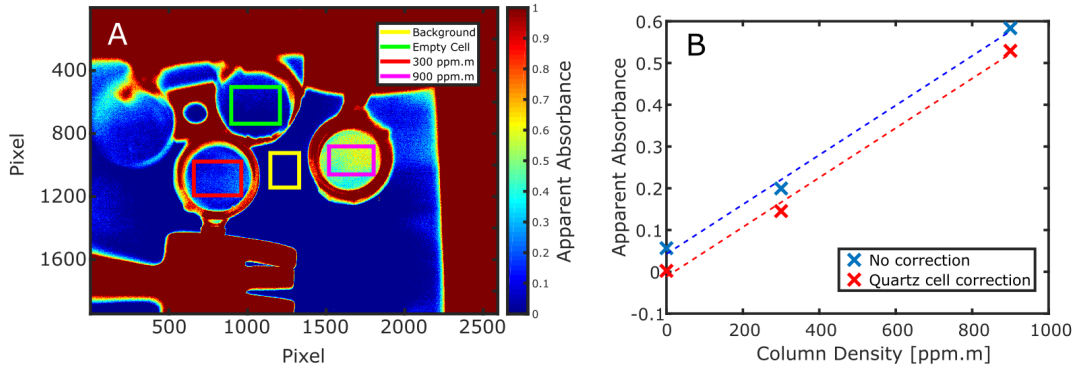

Figure 3.9: (A) Image of apparent absorbance for 3 quartz cells filled with known amounts of SO_2. Regions used to determine mean apparent absorbance are outlined by the coloured rectangles. (B) Plot of apparent absorbance vs cell column density showing a linear fit, as would be expected. The fit passes close to the origin once the absorbance due to the quartz alone (empty cell) is subtracted from the regression line.

shorter UV wavelengths.

Figure 3.10, shows a typical set of images from the two cameras and the resultant calibrated SO_2 image (see Supplementary Video S1 for the full image sequence). Here, pixels were binned to produce 648 × 486 images to improve SNR (as discussed in Section 3.4.3). The background SO_2, assessed by analysing a region upwind of the stack, had a standard deviation of ≈ 25 ppm·m, which can be taken as an assessment of the noise of the measurement. Smekens et al. (2015) similarly found a standard deviation of ≈ 30 ppm·m for a Quantum Scientific Imaging 620 s high sensitivity camera. This relatively simple assessment indicates that the PiCam performs quite well when compared to a commercial UV camera. A more rigorous evaluation of the PiCam's performance is presented later, in Section 3.4.

Following from Section 2.2.1, the plume speed was calculated through cross correlation of two ICAs; it was estimated to be 4.9 m s^{-1}. The resultant SO_2 emission rates between 13:00 and 13:15 UTC are presented in Figure 3.11. The emission rate, with a mean of 0.44 kg s^{-1}, was relatively stable throughout the acquisition period, although notable puffs are visible in both the camera imagery and the time series. The Drax Annual Review of Environmental Performance (Drax, 2013), provides the best available ancillary emissions data for comparison, quoting annual SO_2 loadings ranging 24.5-35.1 kt yr^{-1} for the period 2008-2013; this translates to 0.78-1.1 kg s^{-1}in the units used herein. Since these values are of the same order of magnitude as the measured PiCam mean, these data appear to corroborate the work herein, especially given that Drax's operational output is likely to fall somewhat below the annual average during British summer, when the PiCam measurements were made.

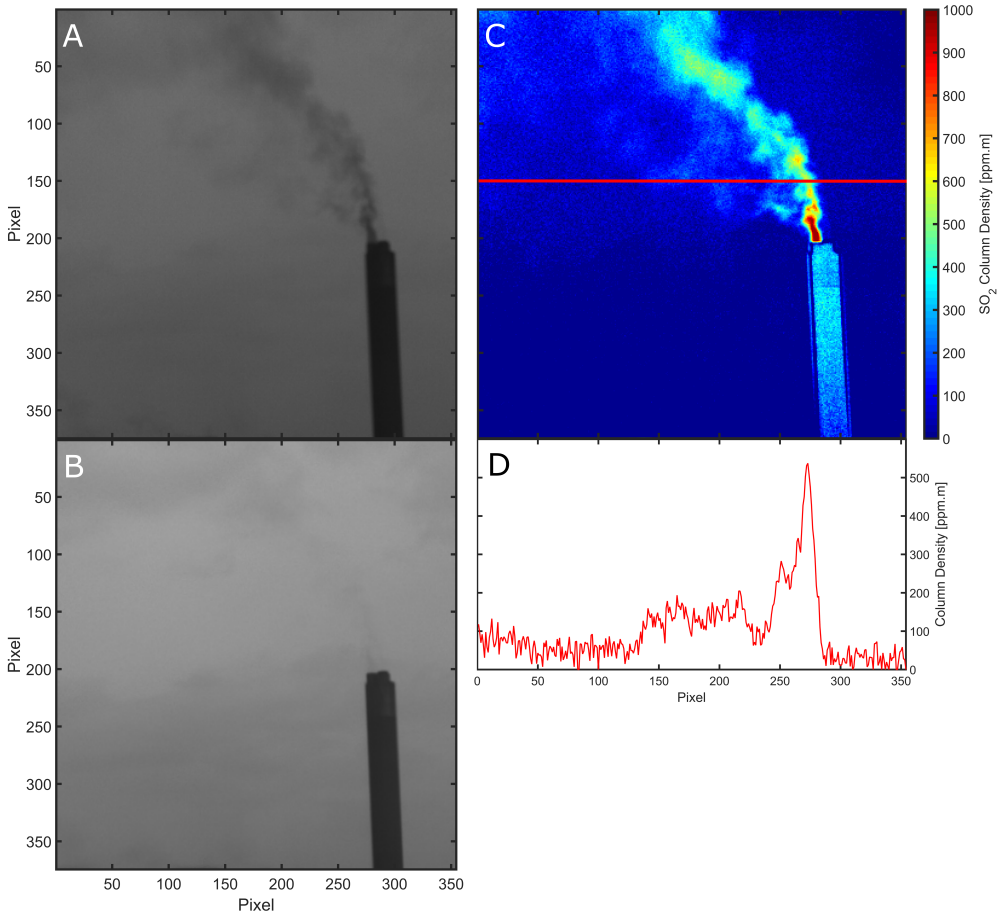

Figure 3.10: (A) A cropped image of the Drax smokestack taken at 310 nm with a shutter speed of 300 ms. The initial image pixels are binned to generate a pixel resolution of 648 × 486, to reduce noise; dark image subtraction and mask corrections have been applied. (B) As in (A) but at 330 nm with a shutter speed of 40 ms. (C) The resulting calibrated SO_2 image of Drax power station stack and plume showing the clear capacity of the system to resolve the plume emissions. (D) A cross-section of (C) showing gas column densities along the row delineated by the red line. The background noise level can be clearly observed between pixels 300 to 350, as SO_2 should be absent upwind of the stack.

3.4 Side-by-side comparison with a commercial unit

The previous sections have validated the use of the PiCam for remote sensing of SO_2. The following section now presents a comparison of the PiCam with a state-of-the-art SO_2 camera system based on scientific-grade UV cameras. These tests were performed in Italy, on Mount Etna, where for the first time the PiCam was deployed under the principle purpose of its design: to retrieve emission rates of SO_2 from an active volcano.

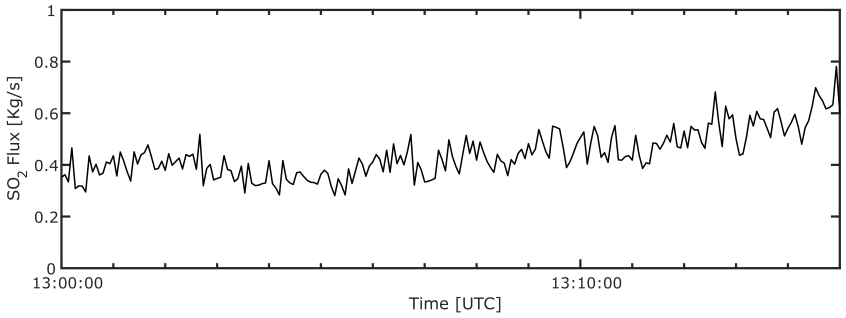

Figure 3.11: Time series of SO_2 emission rates from Drax power station on 15 August 2016, acquired using the UV PiCam.

3.4.1 Site description

Mount Etna is a basaltic stratovolcano located on Sicily, Italy. It has 5 primary degassing craters in the summit region: the north-east crater (NEC), the Bocca Nuova crater (BNC), Voragine crater, the south-east crater (SEC), and the new south-east crater (NSEC) (Aiuppa et al., 2008; D'Aleo et al., 2016). Mt. Etna was the 6^{th} largest passive volcanic emitter of SO_2 on the planet over the period 2005-2015 (Carn et al., 2017); its average emission rate in this period was 23.6 kg s^{-1}.

Due to its high emissions, as well as other factors, such as relative ease of access, Mt. Etna has been the target of a wide range of SO_2 camera studies to date (Tamburello et al., 2013; Pering et al., 2014; D'Aleo et al., 2016). Here, the ability of SO_2 cameras to isolate individual SO_2 sources has been extremely beneficial, due to Etna's large number of emitting craters. From Pizzi Deneri Observatory (37°45′56.54″N, 15°0′59.28″E), SO_2 camera measurements of the NEC emissions can easily be made; it is at this location that the PiCam field work was performed, approximately 2200 m from the degassing NEC.

3.4.2 Quantifying emission rates from Mount Etna

To robustly evaluate the PiCam's performance as an SO_2 camera, side-by-side measurements of Etna's SO_2 emissions were performed using the PiCam and a scientific-grade SO_2 camera system that is routinely used in volcanology for such measurements. The scientific-grade UV camera was a JAI CM-140GE-UV (hereafter referred to as JAI), which contains a Sony ICX407BLA UV-enhanced CCD array. This provides 10-bit images at a resolution of 1392 × 1040; however, through hardware and software binning, the images were reduced to a resolution of 696 × 520 to increase the SNR of the images. As with the PiCam, a two-camera system was assembled, mounting a Pentax B2528-UV lens (focal length = 25 mm) to the fore of each camera. This resulted in a FOV of 14.6° × 11.1° (width × height), somewhat smaller than that of the PiCam (23.1° × 17.3°).

The bandpass filters attached to the JAI were the same as those on the PiCam (310 and 330 nm; Edmund Optics); however, here they were affixed between the object lens and the sensor, to reduce issues caused by the angular dependence of the filter transmission spectrum (Kern et al., 2010b). Each JAI unit was operated through a GigE vision interface (via an Ethernet connection), and the acquisitions were controlled by a single laptop using the Vulcamera software (Tamburello et al., 2011c).

The price of a JAI is $\approx$ 4000 USD per camera, therefore, once optics are considered, a 2 camera unit will be just a little under 10,000 USD. The most recent iteration of the PiCam, excluding the laptop for system control, is $\approx$ 800 USD. The price difference between these two camera systems, an order of magnitude, is substantial. Unlike the JAI system, the most expensive parts of the PiCam are the fore-optics (lenses and filters); however, bulk purchasing these parts (all from Edmund Optics), can significantly reduce their price. For example, the 310 nm bandpass filter, which is priced at 129.00 USD for 1-5 units, reduces to a price of 103.20 USD for an order of 6 (on 4$^{\text{th}}$ September 2018); quotes for larger quantities can also be requested, and presumably lead to further reductions in price.

On 19 July 2016, the PiCam and JAI SO_2 camera systems were deployed side-by-side at Pizzi Deneri, imaging gas release from Mt. Etna's NEC (Fig. 3.12). To replicate possible volcano monitoring deployment conditions for each system, shutter speeds for all four cameras were designated individually (200 and 30 ms for the 310 and 330 nm channels on the PiCam, respectively; for the JAI, auto-exposure adjustment was implemented, with typical speeds of 60 ms and 20 ms for the 310 and 330 nm channels, respectively). An acquisition rate of 0.25 Hz was applied for the PiCams, whilst the JAI images were acquired at 0.5 Hz.

As earlier, the images were processed following the protocols outlined in Kantzas et al. (2010) and Section 2.2.1, in particular, involving dark subtraction, vignette correction, and calibration with three quartz cells containing known column amounts of SO_2 (0, 998 and 1861 ppm·m), to convert the image pixel absorbances to ppm·m values. Plume speeds, estimated using the cross correlation technique, generated from the two camera systems were in good agreement ($< \pm 5$ %); to remove this error from the time series, the same wind speed, defined as the average between the two systems, was used for both systems. In this case, the plume speed was estimated to be 6.2 m s^{-1}. Example imagery from the field acquisitions are shown in Figure 3.13, demonstrating very similar retrieved column densities across the image from the two systems.

To compare the emission rates measured by the two systems, the JAI dataset was first sub-sampled, given the different acquisition frequencies. For every PiCam datum, the corresponding JAI flux was taken to be that acquired within a second of the PiCam value. Where this criterion could not be satisfied the PiCam data point was simply omitted, to maximise the integrity of the comparison. This resulted in quasi-contemporaneous

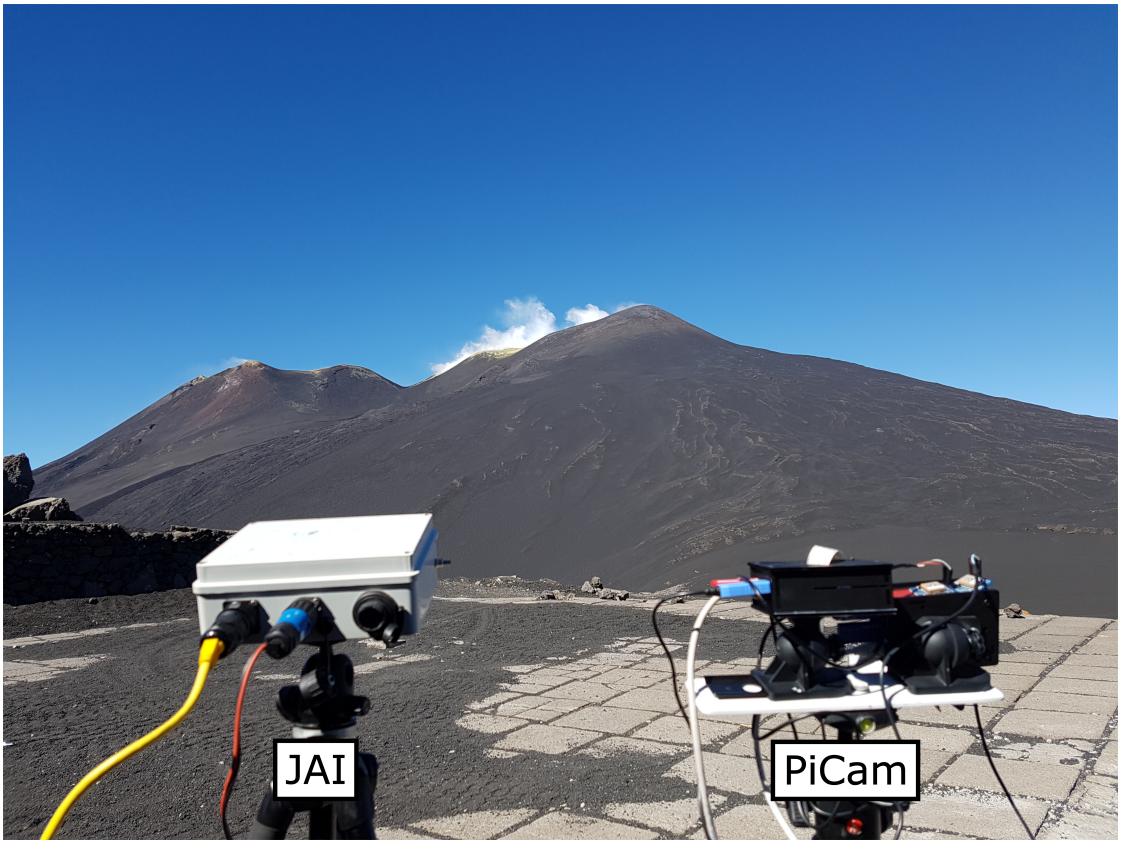

Figure 3.12: Side-by-side deployment of the JAI and PiCam UV cameras on 19 July 2016. The systems are imaging Etna's North East Crater plume at $\approx$ 2.2 km distance.

time series of SO_2 emission rates. The resulting time series of matched JAI-PiCam data pairs, between 07:49:00 and 08:35:08 UTC, are shown in Figure 3.14 (see Supplementary Videos S2 and S3 for the complementary SO_2 image sequences). A remarkably strong agreement between the two time series ($r^2 = 0.92$) was found. In most cases, it is simply the flux trace which is the volcanologist's desired product from an SO_2 camera. Therefore, this relatively simple comparison technique highlights that, in this scenario at least, the PiCam would be a suitable low-cost replacement for the JAI unit. It is, however, important to provide a more detailed comparison of the systems, in terms of their detection limits and SNRs, which should give a more holistic view of how well the instruments are likely to perform in all scenarios, not just the one experienced on Mt. Etna here. In the following section, therefore, more detailed analyses are presented.

3.4.3 Characterising the performance of the PiCam versus JAI

To compare the PiCam and JAI systems in a more rigorous manner, the approach of Kern et al. (2015b) was followed, who performed a detailed intercomparison of seven SO_2 camera systems. On 20th July 2016, at 10:48 UTC, the two systems were set to image the same region of clear sky from a rooftop in Linguaglossa, Sicily; a small outcrop

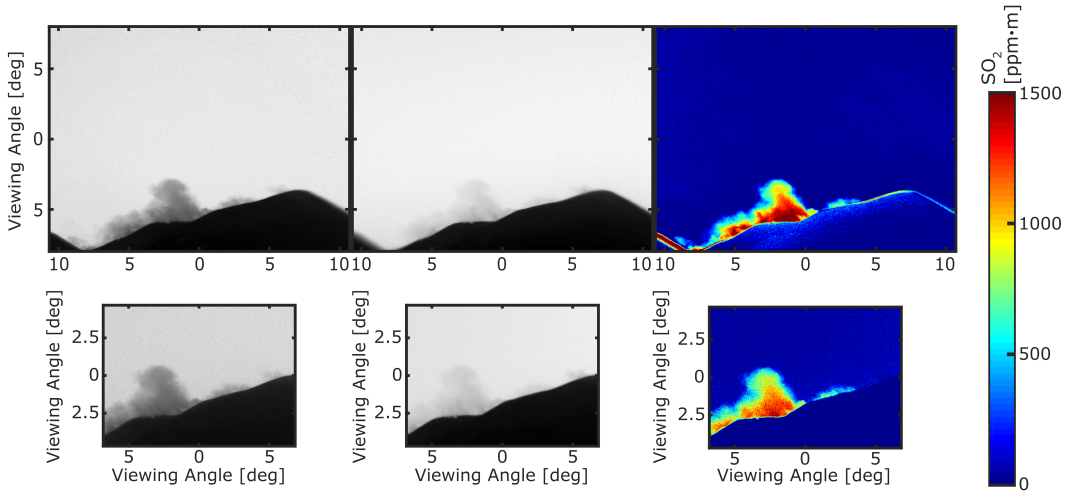

Figure 3.13: Images of Mount Etna's plume taken with the PiCam units (top panels; pixels binned to 648 × 486) and the JAI systems (bottom panels) at 08:22:16 UTC on 19 July 2016. From left to right, the panels display 310 nm images, 330 nm images, and calibrated SO_2 column amounts. The dotted black line in the calibrated SO_2 images displays the profile across which integrated column amounts were retrieved.

of horizon was present at the bottom of the images, to ensure that viewing directions were consistent. Unlike in Section 3.4.2, here the shutter speeds of the two cameras were standardised to times typically used by the JAI system in the field (60 ms at 310 nm and 20 ms at 330 nm). This ensured that comparisons could directly be made between the performances of the two systems, with consideration of the UV sensitivities of the systems being incorporated into the analysis. As a result, PiCam channels were significantly undersaturated, as would be expected from a sensor not specifically designed for UV imagery, with average saturations of $\approx$ 18 % and $\approx$ 19 % for the 310 and 330 nm channels, respectively; JAI images were at $\approx$ 74 % and $\approx$ 75 % saturation for the 310 and 330 nm channels, respectively. Of course, the differing optics will also influence this disparity. For all subsequent analyses, clear sky images were acquired, then dark image subtracted and vignette corrected, as would be the case in standard volcanic field acquisitions.

Firstly, the SNR of the two camera systems was characterised. This was done by finding the inverse of the standard deviation, σ, of the quotient of two successively acquired clear-sky images, with intensities I_1 and I_2:

$$SNR = \frac{1}{\sigma} \tag{3.1}$$

$$\sigma = std\left(\frac{I_1}{I_2}\right) = \sqrt{\frac{1}{N}\sum_{p=1}^{N}\left[\frac{I_1(p)}{I_2(p)} - \left\langle\frac{I_1}{I_2}\right\rangle\right]^2} \tag{3.2}$$

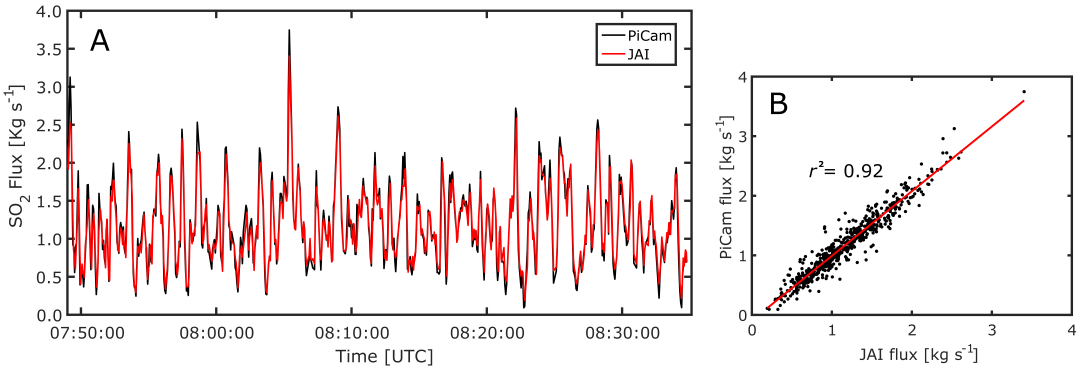

Figure 3.14: (A) Time synchronised SO_2 fluxes calculated from the PiCam (black) and JAI (red) camera systems, between 07:49:00 and 08:35:08 UTC on 19 July 2016. The PiCam retrieved fluxes show excellent concordance with those of the JAI; (B) A scatter plot of contemporaneous fluxes, remarkable correlation ($r^2 = 0.92$).

where p denotes an individual pixel, N is the total number of pixels, and $\left\langle \frac{I_1}{I_2} \right\rangle$ is the average value of the quotient of the two images. If the change in radiance between two successive images is assumed to be negligible, the quotient $\frac{I_1}{I_2}$ would equal unity in an ideal system. Therefore, with an assumed signal of 1, the SNR is equal to the inverse of the standard deviation σ (Kern et al., 2015b).

SNRs for the JAI and PiCam systems were calculated both for single image pairs and for co-added images, where I_1 and I_2 were obtained by co-adding 4 separate images on a pixel-by-pixel basis. The results are shown in Figure 3.15A. For the PiCam, data are presented both for full resolution images, for pixels binned to a similar resolution as the JAI (648 × 486), and for pixels binned such that the instantaneous field of view (IFOV) was roughly equal to the JAI IFOV (0.0178° at 1296 × 972 and 0.021° at 696 × 520, for the PiCam and JAI, respectively); note that since pixel binning can only be performed discretely, binning to achieve exactly equal image resolutions and IFOVs for these comparisons was not possible.

For both the PiCam and the JAI system, the SNR improved when co-adding, as would be expected. Moreover, with the exception of the JAI at 310 nm, all tests followed the theoretical $t^{-1/2}$ proportionality associated with Poisson statistics, where t is the total integration time (Kern et al., 2015b). That is to say that the four co-added images increased the signal to noise ratio by a factor of 2. These results are expected in well designed optical systems, where the SNR is limited by photon (Poisson) noise rather than internal electronic noise. This suggests that increasing the PiCam integration times (shutter speed) to reach a saturation of ≈ 70 % would approximately double the SNRs measured here, as long as the system does not begin to be limited by internal electronic noise (e.g., fixed-pattern noise).

The notable disparity in SNR between the PiCam's 330 and 310 nm images suggest

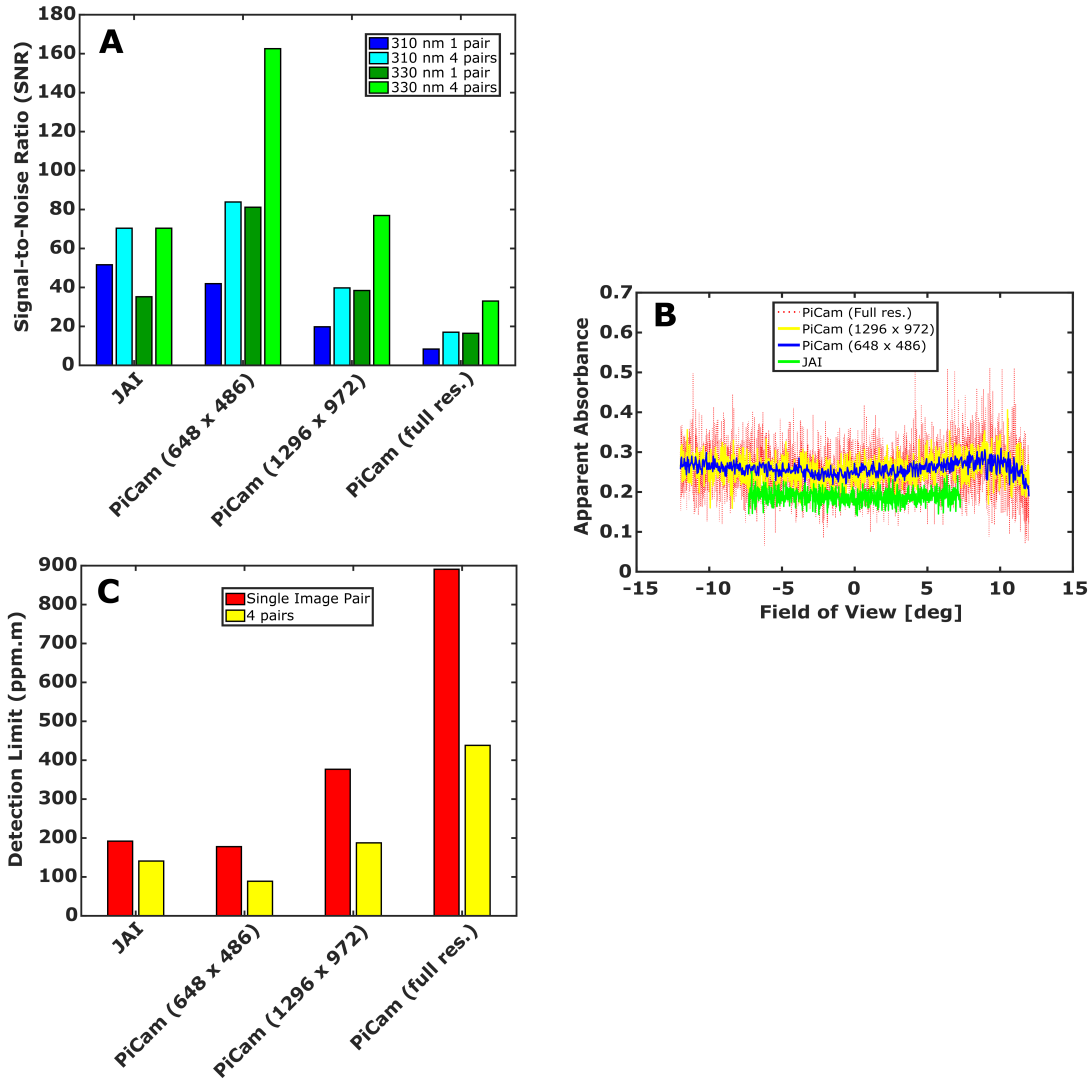

Figure 3.15: (A) Signal-to-noise ratios (SNRs). (B) Cross sections over apparent absorbance images for a SO_2 cell (1861 ppm·m). (C) Detection limits for the JAI and PiCam systems with equal exposure times. For the PiCams, both binned (648 × 486 and 1296 × 972) and full resolution (2592 × 1944) arrays were examined. The former binning scenario provides approximately equal pixel resolutions across both systems (the JAI camera has a narrower FOV); the latter binning scenario provides approximately the same FOV per pixel from both systems. Four images were also co-added to increase SNR in (A) and (C) by summing four successive images on a pixel-by-pixel basis; results from this process are displayed as "4 pairs". The drop in PiCam apparent absorbance at FOV >10° is a manifestation of the gas cell holder entering the edge of the cameras field of view and thus can be neglected. The 648 × 486 binning scenario, which we consider to provide sufficient spatial resolution for volcanic gas monitoring applications, provides comparable performance to the JAI cameras in these experiments.

that this sensor's quantum efficiency diminishes at a faster rate than the JAI system's when moving towards shorter wavelengths; hence the PiCam would present better SNR characteristics with longer shutter speeds than used by the JAI system, especially for the 310 nm images. This is to be expected, since the JAI's SONY CCD is specifically designed for high UV sensitivity.

Post acquisition pixel binning of the PiCam images resulted in a significant improvement in SNR. At 648 × 486, which is a comparable resolution to that of the JAI, the SNR increased approximately by a factor of 5 relative to the full resolution images. Furthermore, at this resolution, which provides enough pixel resolution to adequately capture plumes in the majority of cases, the PiCam outperformed the JAI in all but the single image 310 nm test. For the comparable IFOVs, with PiCam images binned to 1296 × 972, the JAI outperformed the PiCam markedly at 310 nm, as would be expected given the greater expense of the former unit. For many volcanological applications, however, this spatial resolution may be beyond what is required for accurate SO_2 measurements. Kern et al. (2015b) provides a general suggestion that typically a pixel spatial resolution of several meters is adequate. Considering the PiCam's coarse resolution investigated here of 648 × 486 (IFOV = 0.0356°), a spatial resolution of 3 m is reached at a distance of 2.4 km from the plume; binning to 1296 × 972, 3 m spatial resolution is reached at 4.8 km. The term several is, however, quite ambiguous, and in many scenarios spatial resolutions of >5 m may be adequate; in this case, the coarse resolution PiCam images could be used at greater distances than the 2.4 km stated above.

In a second test, a 1861 ppm·m SO_2 filled quartz calibration cell was placed in front of the camera lens, enabling the generation of apparent absorbances across the image with:

$$AA = -\log_{10}\left[\frac{\left(I^{cell}_{310}/I^{sky}_{310}\right)}{\left(I^{cell}_{330}/I^{sky}_{330}\right)}\right] \tag{3.3}$$

Here, I^{cell} denotes the intensity with the cell in place and I^{sky} denotes the intensity of the clear sky; the subscript then specifies the filter. As always, the images were first dark subtracted, and AA calculation is performed on a pixel-by-pixel basis. Results of a cross-section through the resulting AA images are shown in Figure 3.15B. As may be expected, the full resolution PiCam AA has considerable noise in the cross-section; however, the 648 × 486 binning results in greatly dampened noise, which is marginally lower than the JAI image noise for this test. For each image, the standard deviations of AA across the sensor, over the FOV range of ±5°(to mitigate effects from changing sensitivity to SO_2), are: 1.2×10^{-2} (648×486 PiCam), 2.5×10^{-2} (1296×972 PiCam), 5.4×10^{-2} (2592×1944 PiCam), and 1.6×10^{-2} (696×520 JAI). In accordance with previous studies (Kern et al., 2010b; Lübcke et al., 2013; Kern et al., 2013; Kern et al., 2015b), the PiCam displays a

higher sensitivity to SO_2 towards the edges of the image. As described in Section 2.2.3, this is a result of deviation from non-perpendicular illumination angle of the bandpass filter, which causes a shift in the filter transmission spectrum, and thus, a change in SO_2 sensitivity. This effect is exacerbated in filters mounted to the fore of the object lens, therefore, the JAI system, with its filters mounted behind the object lens, shows little change in SO_2 sensitivity across the image. The current lens configuration of the PiCam makes it impossible to mount the filter behind the lens, due to its short focal length; future work could develop a new optical system which makes it possible to mount the filter in an optimised position. Nevertheless, the PiCam sensitivity change across the image, $\approx$ 15 % increase, is quite modest in comparison to other systems which are commonly used in volcanology (up to $\approx$ 40 %; Kern et al., 2015b).

It is evident that the PiCam has a higher sensitivity to SO_2 than the JAI system, leading to larger AA values for a given SO_2 amount, which may in part be a result of differing filter positions and the associated effect discussed above. However, it should be noted that the calibration procedure directly accounts for this disparity, and thus, there will be no systematic differences in SO_2 measurements caused by this effect.

The final assessment of PiCam performance versus the JAI system considered the detection limits of the two units; again, this followed the protocols outlined by Kern et al. (2015b). This was calculated by multiplying the standard deviation of the 310 nm quotient image (Equation 3.2) by the gradient of the calibration line, i.e., that formed by fitting gas column densities to AA during a typical cell calibration. It should be noted that, since the two camera systems have differing SO_2 sensitivities, this detection limit is not solely dependent on the system's SNR. The results are presented in Figure 3.15. As with the previous tests, the PiCam, when binned to 648 $\times$ 486, had comparable performance to the JAI system, with detection limits of $\approx$ 180 ppm·m and $\approx$ 190 ppm·m, respectively, for single images; for four co-added images, the binned PiCam and JAI detection limits were $\approx$ 90 ppm·m and $\approx$ 140 ppm·m, respectively. When binning the PiCam to a similar IFOV as the JAI, the detection limits were somewhat larger, at $\approx$ 380 ppm·m and $\approx$ 190 ppm·m for the single image and co-added images, respectively. Under these test conditions, at this shutter speed, the full resolution PiCam performance is clearly unusable, with a single image pair detection limit of $\approx$ 890 ppm·m. In many scenarios this value will be close to, or even larger than, the maximum column densities present, and thus, much of the plume would be lost in the noise.

3.4.4 Quantification of uncertainties in SO_2 measurements

The detection limits estimated in Section 3.4.3 can also be used to consider the uncertainty, $\triangle C$, in a retrieved SO_2 column amount. Therefore, they can be used along with other uncertainty estimates to quantify the total uncertainty in emission rate measurements made in Section 3.4.2. It should be noted, however, that the PiCam shutter speeds

were somewhat longer during plume imaging, which should improve the detection limit of the system; therefore, the uncertainty calculation presented below is likely an upper limit.

The total uncertainty in the ICA measurements, $\triangle ICA$, can be found from the number of pixels, N, in the ICA and the height of each pixel, h, combined with the detection limit of the system:

$$\triangle ICA = \sqrt{N\left(\triangle C \cdot h\right)^2} \tag{3.4}$$

In the case of Section 3.4.2, the PiCam had 155 pixels of height 1.58 m, and for the JAI units these parameters were 280 and 0.92 m, respectively. Recall that the detection limits, now $\triangle C$, of the binned PiCam and JAI images were $\pm$180 ppm·m and $\pm$190 ppm·m, respectively. This led to an ICA uncertainty of $\pm$3500 ppm·m and $\pm$2900 ppm·m for the PiCam and JAI systems, respectively. Considering average ICA values for the emission rate time series in Figure 3.14, uncertainties of 4 % and 3 %, respectively, were found.

In addition to this, there are a number of further uncertainties which affect the PiCam and JAI measurements (e.g., see Kern et al., 2010b; Holland et al., 2011; Lübcke et al., 2013; Kern et al., 2013; Campion et al., 2015, for further details). Most significantly, these errors include: plume speed determination, cell calibration, and light dilution. Although these errors are dependent on measurement conditions, and therefore specific to each deployment, some general estimates can be made. An uncertainty of ≈10 % is commonly attributed to plume speed estimation by cross-correlation; cell calibration uncertainty may also be ≈ 10 %, although it can far exceed this in certain conditions (Lübcke et al., 2013); light dilution here was neglected due to the close proximity of the cameras to the plume. By adding in quadrature, the total uncertainties were conservatively estimated to be 14.7 % and 14.5 % for the PiCam and JAI, respectively. Here, it is now apparent that the contribution to total uncertainty from the performance of the two systems, i.e., their detection limits, was relatively small. Furthermore, the disparity in their relative uncertainty related to camera performance was quite modest (≈ 1 %). Overall, this shows that a broadly similar performance of these two systems is achievable in terms of total uncertainties in emission rate measurements, complimenting the good agreement found in the measurements themselves (Fig. 3.14). When considering the difference in cost of the two systems, these results are quite significant.

3.5 Recent updates to the PiCam

As is the case with any development of new equipment, the PiCam has been subject to a number of iterations through its current lifetime. The first deployment, at Drax

power station (Section 3.4.3), involved a very rudimentary design in the field, simply to test the utility of this device. For the work on Mt. Etna, the PiCam had been further developed, although it still lacked a single, simple packaging for the two cameras, and its software was not very user friendly. Furthermore, at this time, a number of bugs were still persistent in the interfacing codes. More recently, work has been done to develop a system which can be more easily disseminated and used by other research groups, to promote the use of SO_2 cameras where they may previously have been precluded by the high system costs. In particular, the two camera system is now housed inside a single Peli Case (Figure 3.16), powered by a single Lithium polymer power bank which, can sustain operation for an entire day in the field.

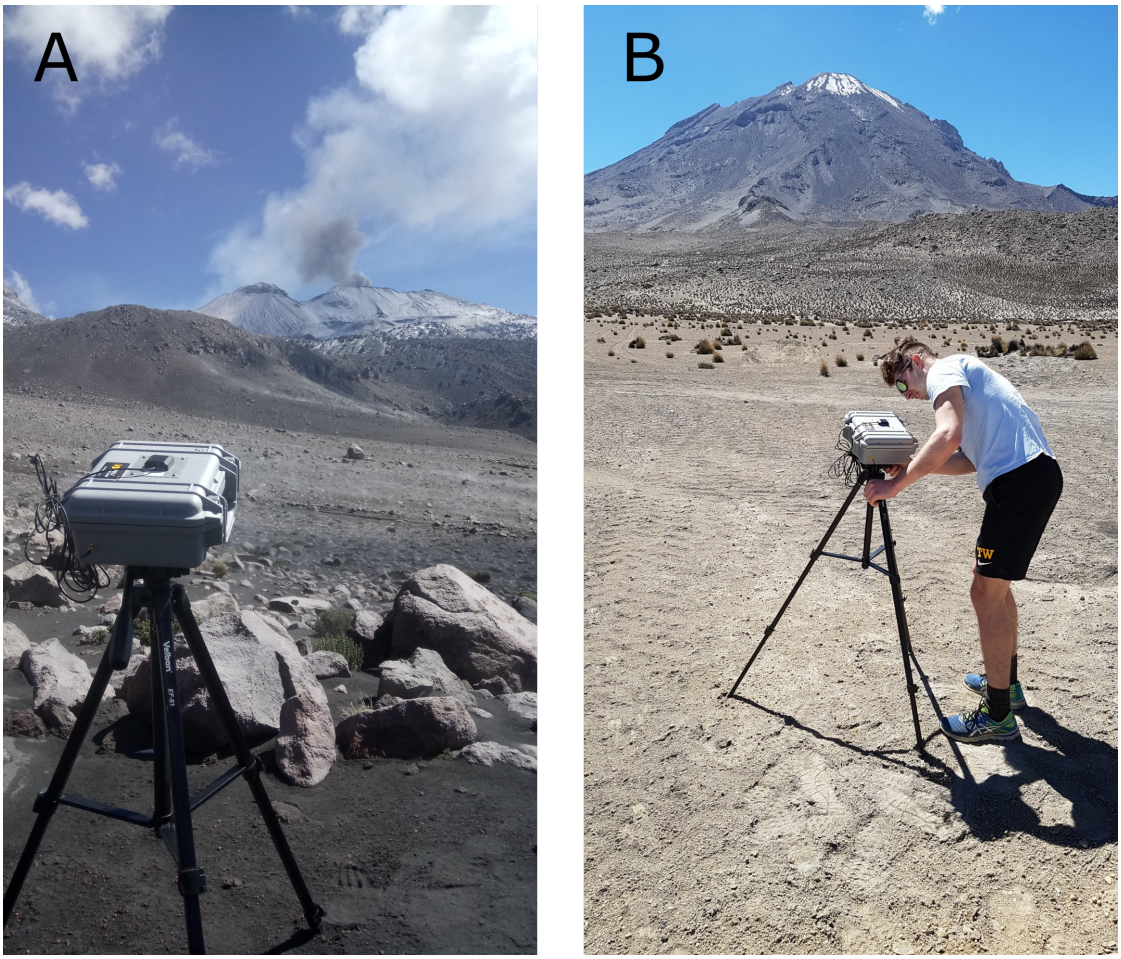

Figure 3.16: (A) The PiCam deployed on Sabancaya, Peru, during a small explosion. (B) Deploying the PiCam on Ubinas, Peru: proof that I did do some work in the field. Photo credit: Dr Tom Pering.

In addition to the hardware, the software, which was written in Python 3, has iteratively been improved over the last couple of years. Further details on the software are presented in the Appendix. It comes in two components, the acquisition program PyCamUV.exe and its counterpart PostProcess.exe for post-processing data. The former is primarily designed for acquiring PiCam data, providing a camera interface to control important

settings and displaying captured images; the latter, as its name suggests, makes it possible to post-process data acquired previously, to generate SO_2 images and corresponding emission rate time series. Of particular importance here is PyCamUV, which enables relatively easy user control of the PiCam and visualisation of the UV camera data in the field. Whilst PostProcess provides a good accompaniment to PyCamUV, allowing the rapid generation of emission rates with a number of processing options, it is of less critical importance. This is because a number of extremely detailed SO_2 camera codes already exist (Gliß et al., 2017; Campion et al., 2015; Tamburello et al., 2011c) which have had a great amount of time dedicated to them and incorporate an extraordinary amount of functionality; the work of Gliß et al. (2017) is particularly noteworthy here. The principal goal of the work presented here has been to facilitate simple, low-cost acquisition of UV camera images; once collected, the researcher may choose to process them in whichever way they prefer.

As a result of the recent user-friendly PiCam updates, the unit has already been utilised a number of times outside of work specifically for this thesis, facilitating work which may have previously been precluded by the cost of typical SO_2 camera systems. To date, PiCam measurements of SO_2 emissions have been made on: Stromboli and Mt. Etna, Italy; Masaya Volcano, Nicaragua (Pering et al., 2019); Sabancaya and Ubinas, Peru; Villarrica, Chile (Liu et al., 2019); Lascar, Chile ; Yasur, Vanuatu. In addition to this, due to the low cost of the PiCam, it has been possible to provide 5 research groups with free units. These cameras are now located in Chile, Costa Rica, Ecuador, Mexico and Peru.

3.6 Summary

This chapter presented the development of a low-cost UV camera, the PiCam, by modifying a R-Pi Camera Module (v1.3). The camera hardware was based on an Omnivision OV5647 sensor which was primarily designed for the smartphone market and, thus, has benefited from high consumer demand driving costs down. This was modified by chemical removal of its Bayer filter, producing a uniform sensor with greatly heightened UV sensitivity. The camera was completed by rebuilding the optical system with 3D prints housing a UV transmissive lens. Here, the UV camera was deployed as an SO_2 camera, measuring emissions both from a power station in the UK and from Mount Etna, an active volcano on Sicily. At the latter field tests, a scientific-grade UV camera (JAI) was deployed alongside the PiCam for comparison. In a range of tests, the PiCam was shown to perform remarkably well considering that its build price is an order of magnitude cheaper than the cost of the JAI ($\approx$ 800 USD vs $\approx 10,000$ USD). From this, it is suggested that the PiCam could support widespread proliferation of SO_2 camera systems in volcanology, especially since a large number of the world's active volcanoes are located in the Global South, where limited funding can preclude access to vital monitoring and

research equipment. Furthermore, the PiCam's utility can extend beyond volcanology, into a much broader range of applications where UV cameras are employed.

It may be poignant to note that all of the research and development of the PiCam presented in this chapter, which included many broken camera sensors and a number of iterations of the system itself, was performed on a budget which would not have enabled purchase of a single SO_2 camera system based on commercial scientific-grade UV cameras. In a sense, this research has therefore already paid for itself in terms of allowing SO_2 measurements to be made where previously the instrument costs would have been prohibitive.

Chapter 4

PiSpec: Development of a 3D-printed ultraviolet spectrometer and its application in differential optical absorption spectroscopy (DOAS)

This chapter is associated with two bodies of published work (Wilkes et al., 2017b; Wilkes et al., 2019). It details the design, construction and application of a low-cost UV spectrometer, assembled with 3D prints, off-the-shelf optical components and the Raspberry Pi camera module sensor discussed in Chapter 3; the instrument is thus named the "PiSpec". The reported work spans from the inception of the spectrometer, through ray tracing, to the application of the spectrometer in remote sensing of volcanic SO_2 using differential optical absorption spectroscopy. The spectrometer has a spectral resolution of $\approx$ 1 nm and spectral range of $\approx$ 280-340 nm; however, I propose that this general methodology could be adapted to design and build a wide range of bespoke spectrometers spanning from UV to NIR wavelengths.

4.1 Introduction

Ultraviolet (UV) differential optical absorption spectroscopy (DOAS) is a technique which enables accurate retrievals of volcanic SO_2 for deriving emission rates from volcanoes; it was discussed in detail in Section 2.3. Most prominently in volcanology, the Network for Observation of Volcanic and Atmospheric Change (NOVAC) project has deployed a large number of scanning-DOAS spectrometers at volcanoes across the

globe, monitoring SO_2 emissions along with other gas species (Galle et al., 2010). These installations have been invaluable to both researchers and volcano observatories for investigating and monitoring volcanic unrest (e.g., Hidalgo et al., 2015; Coppola et al., 2017; Aiuppa et al., 2018; Primulyana et al., 2018).

Whilst the distribution of DOAS systems worldwide has improved notably in the past decade, the cost of a commercial UV spectrometer is still a limiting factor to the further deployment of such systems on active volcanoes. In this chapter I therefore set out to develop a low-cost spectrometer, named the PiSpec, which could be of great utility to the volcanology community. Utilising the debayered sensor and camera module presented in Section 3.2.2, this spectrometer also comprises a 3D-printed housing and off-the-shelf optical components, with a resulting single-build cost of $\approx$ 500 USD; with mass production this price could be driven down further. I detail the PiSpec's development, testing, and subsequent deployment for DOAS retrievals of SO_2 on Masaya and Kīlauea volcanoes.

4.2 Designing, building and testing the PiSpec

4.2.1 Ray tracing

Ray tracing is the process of geometrically tracking rays of light through an optical system. In simple terms, the angle a ray leaves a boundary between two media depends upon the angle of incidence with the boundary and the refractive indices of both the medium the ray is travelling from and the medium the ray is travelling into. Ray tracing software allows the user to simulate complex optical systems extremely rapidly, following the above principles; here, OpticStudio (Zemax LLC) was used for such modelling.

Tang et al. (2015) provide a good summary of the Czerny-Turner spectrometer format, presenting the geometrical principals which govern the PiSpec's design. This format provides a compact layout, and is therefore suitable for a miniature 3D printed spectrometer. Using OpticStudio it was relatively straightforward to model the Czerny-Turner spectrometer, without needing to delve significantly into the details of Tang et al. (2015)'s model for instance. Off-the-shelf optical components and the geometry of the Raspberry Pi (R-Pi) camera module discussed in Section 3.2.2 were used as a starting point for the OpticStudio model. In particular, 2 UV enhanced aluminium-coated mirrors of 12.7 mm diameter and 50 mm focal length (CM127-050-F01; Thorlabs, Inc.) were chosen, due to their small size and relatively short focal length allowing a compact spectrometer design. From this model, a diffraction grating and entrance slit were chosen and arranged in OpticStudio to provide the desired spectral range and resolution for DOAS measurements of SO_2, i.e., a spectral resolution of $\approx$ 1 nm and spectral range of $\approx$ 280-340 nm. In this case the diffraction grating was a 1200 lines/mm UV-reflective holographic grating

(GH13-12U; Thorlabs, Inc.) and the entrance aperture was a 30 μm $\times$ 3 mm slit aperture (S30R; Thorlabs, Inc.). These components, along with the sensor's dimensions as the imaging plane, were arranged in OpticStudio such that light of a particular wavelength was focussed onto the sensor, effectively imaging the slit. The diffraction grating causes dispersion of light such that each wavelength is focussed at a different distance along one dimension of the imaging plane. Due to spherical aberrations and the off-axis nature of the spectrometer, focussing on the detector is not perfect; these effects therefore limit the performance of the instrument.

Results of the ray tracing are displayed in Figure 4.1, superimposed on top of a photo of the final spectrometer. This highlights the simplicity of the spectrometer design, which has the advantage of being quite accessible to non-expert researchers who generally focus on the application of spectrometers rather than their design and manufacture.

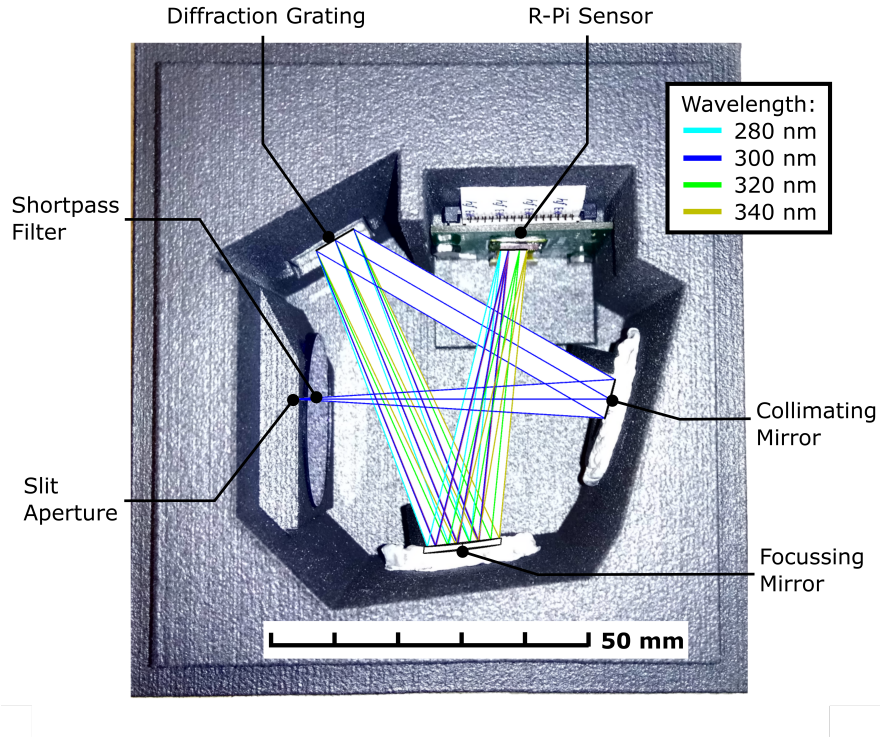

Figure 4.1: An image of the PiSpec. Overlain is the ray tracing output from OpticStudio, for a variety of wavelengths. Light enters through the slit aperture, a short-pass filter then blocks much of the visible radiation, to reduce stray light. The light is collimated by a spherical mirror, dispersed by the diffraction grating, and then focused onto the R-Pi sensor by a second spherical mirror.

4.2.2 3D design and printing

Following the original design of the spectrometer, this information needed to be transferred into a tangible model that could be manufactured. To do this, the OpticStudio design was exported as a STEP (.stp) file, a computer aided design (CAD) format, which

contained the surfaces of all of the modelled optical surfaces. SolidWorks®, a CAD software, was then used to design the spectrometer casing. First, models of the optical components (openly provided by Thorlabs in the proprietary SolidWorks® format) were mated to their respective surfaces in the .stp file, to create a model of floating optics. A 3D model was then simply built around these components in SolidWorks®, to create the spectrometer housing design (Fig. 4.2). At this stage, a mount for a short-pass filter was incorporated into the spectrometer design, to minimise stray light; furthermore, baffling was integrated into the optical mounts, to further reduce stray light. Around each optical component a tolerance of 0.2 mm was incorporated into the housing, to account for inaccuracies in the 3D printing procedure used to manufacture the spectrometer.

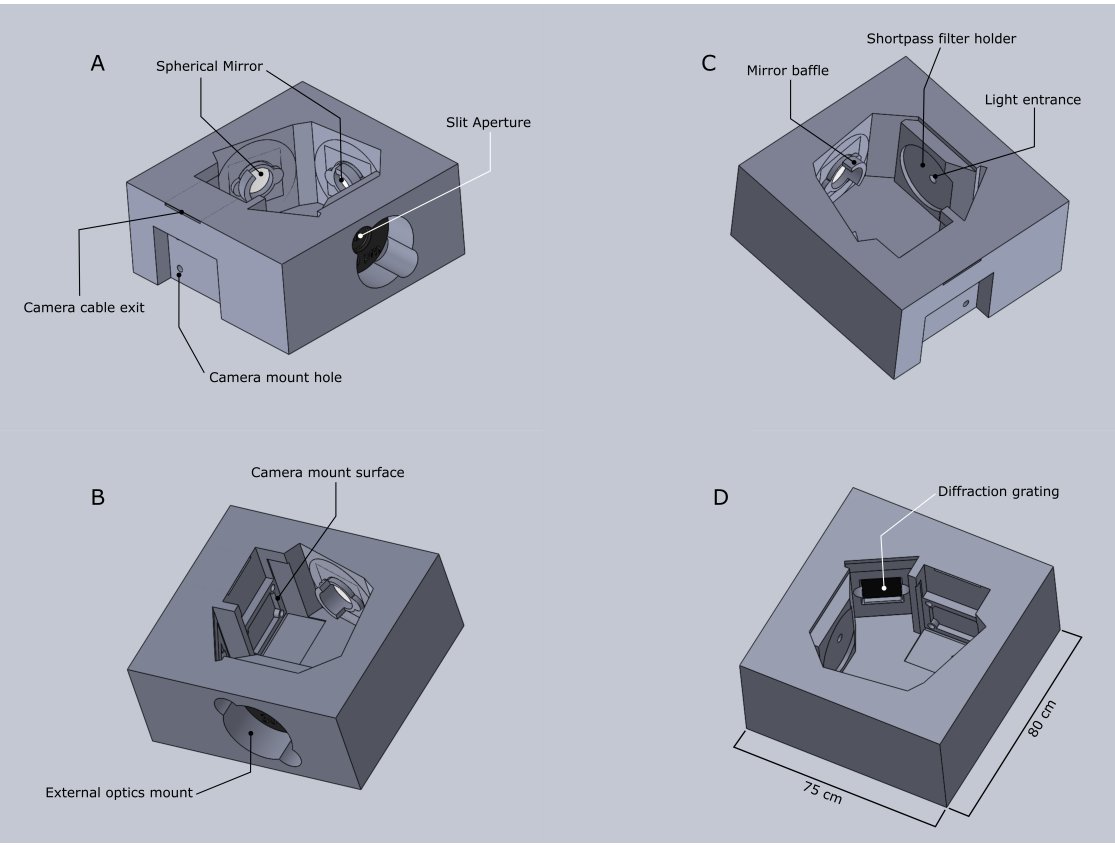

Figure 4.2: 3D models of the PiSpec taken from the SolidWorks® design. The vertical profile here has been slightly cropped, for improved visibility of the PiSpec interior and its components.

In front off the entrance slit aperture, a region for mounting exterior optics was created. This was preferred to a built in SMA connector for optical fibre compatibility, since it provides a little more system flexibility for fore-optics. Furthermore, on initial design it was not clear exactly what exterior optical setup would be implemented. This design allowed more freedom for testing; however, for improved robustness in later iterations a fixed design for exterior optics may be preferred.

As in Section 3.2.3, the instrument model was manufactured using a third party public

3D printing service, https://3dprintdirect.co.uk/, which provides selective laser sintering (SLS) manufacturing in graphite-reinforced nylon. This technique and material was chosen since the quoted build precision ($\pm$ 0.2 mm) far exceeds that of the typical fused filament fabrication procedure. This precision is of particular importance for a spectrometer, since small misalignments in optical components can result in significant changes in instrument performance. Once printed, the optical components were carefully placed into their respective mounts and secured in place with further 3D printed parts and/or glue. Prior to glueing it was important to check that the system was performing adequately and, if not, some small adjustments to the positions of parts may be afforded by the tolerances in the mounts. To date, only one PiSpec has been built, and it was found that the components' positions almost immediately provided an acceptable performance after mounting. Initially mounting the diffraction grating rotated 90° from its required orientation did, however, highlight the need for testing.

As in Chapter 3, the R-Pi camera module was attached to a R-Pi 3 Model B for controlling sensor acquisitions. Here, the camera flex cable was passed through the spectrometer via a thin cut-out in the housing design. This cut-out was then plugged with Blu Tack to prevent stray light from entering the spectrometer via this pathway.

4.2.3 Acquiring spectra

Code for acquiring spectra from the PiSpec was similar to the PyCamUV code presented in Appendix A. Indeed, it is possible to directly use PyCamUV for spectral acquisitions. Since acquisitions are still 2-dimensional arrays coming from the sensor, they will still be referred to here as "images" or "spectral images"; spectra are then extracted from the images by post-processing, which here was performed in MATLAB.

As with the PiCam in Chapter 3, images were software binned to 648 $\times$ 486 to increase the signal-to-noise ratio (SNR) of the spectra. A spectrum, which is dispersed across the columns of the sensor, was then extracted from an image by co-adding 11 rows of the image, typically in a region where signal is greatest. This further increases the SNR of the resulting spectrum, the advantages of which are highlighted in Section 4.2.5. Each spectrum therefore contains 648 data points (the number of columns in the image). Prior to spectrum extraction, the initial image is dark image subtracted, using an acquisition where light is blocked from entering the spectrometer. Figure 4.3 shows a spectral image and resulting spectrum acquired from a Hg-Ar light source (HG-1, Ocean Optics, Inc.), demonstrating how UV radiation is dispersed across the focal-plane array (FPA).

Although ideally the ray tracing output would allow calibration of the spectrometer, in reality the inability to mechanically reproduce the ray tracing model perfectly means that the spectrometer's performance will always deviate somewhat from the ideal case. To calibrate, therefore, the Hg-Ar lamp was used to identify the locations of known

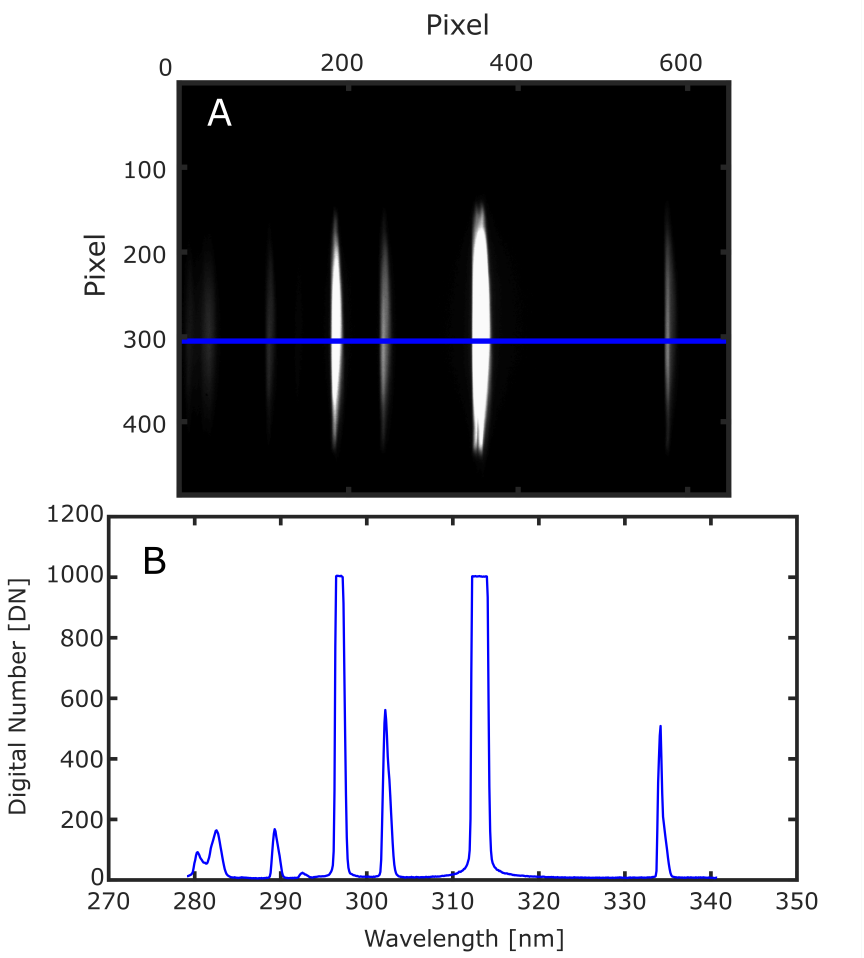

Figure 4.3: (A) PiSpec image of Hg-Ar lamp input, from which the calibrated spectrum (B) was generated by co-adding 11 of the brightest rows (300-310). The blue line in (A) indicates the location of these rows. The FWHM of the 302.150 nm spectral line provides a $\approx$ 1.0 nm constraint on spectral resolution.

emission lines and subsequently perform pixel-wavelength mapping from these points. These emission lines, which may be thought of as infinitesimally thin relative to the spectrometer's spectral resolution, can also then be used to define the spectral resolution of the instrument. This is defined as the full width at half maximum of the instrument's line shape, i.e., a single emission line from the lamp. Using the 302.150 nm spectral line in the spectrum displayed in Figure 4.3B, since this line is located within the typical wavelength fit window for SO_2 DOAS retrievals, the spectral resolution was found to be $\approx$ 1.0 nm.

4.2.4 Thermal Stability

Volcanoes can be located in a range of extreme environments, often found at low temperatures due to their altitude, or in hot conditions from direct sun exposure at low latitudes. Since spectrometers can be sensitive to changes in thermal conditions, shifting

and warping the line function (e.g., Platt and Stutz, 2008), it is important to address this issue as part of evaluating the PiSpec's utility in volcano surveillance operations.

These tests were performed by acquiring spectra from the Hg-Ar lamp, coupled to the PiSpec by an optical fibre. This setup was placed in an incubator (Panasonic MIR-254-PE), set on Low Humidity Mode, to expose it to temperatures between ≈ 0 and 50 °C. The PiSpec was further placed inside a plastic pouch containing silica gel, to reduce humidity and prevent condensation; within this pouch the lowest temperature actually achieved was 2.5 °C. Temperature was logged every minute using a LogTag® HAXO-8 recorder. At each temperature setting a stabilisation period of ≈ 1 hour was applied before acquiring spectra, to allow the pouch to equilibrate with the incubator temperature. The tests spanned two days, 19-20 June 2018.

Here, thermally induced changes in instrument line shape (ILS) and spectral calibration are discussed using the 313.155 nm emission line from the Hg-Ar lamp, in order to investigate the system robustness to variations in ambient conditions during field operations. This peak is located within typical fit windows for SO_2 DOAS retrievals, which are generally somewhere in the 300 - 325 nm range. The results suggest that the spectrometer calibration has a generally linear dependence on temperature (Fig. 4.4); however, a few notable deviations from this trend are also apparent. Firstly, there appears to be no change in peak location between 20 and 25 °C. This may partly be a result of the pixel discretisation of the signal. There is, however, some change in ILS, in keeping with the general trend (see Fig. 4.5). The second effect is apparent at the highest temperature measurements, ≈ 50 °C. Here, there is a large shift in the peak, which jumps ≈ 1 nm from the 45 °C spectrum. This notable displacement may be caused by a significant mechanical movement in one of the PiSpec's components, for example, the detector, via some release mechanism activated above a particular temperature threshold. The similarity in line shape between the 45 °C and 50 °C spectra would corroborate this argument (Fig. 4.5). The detector and associated Pi Camera board are currently mounted to the spectrometer with nuts and bolts which may allow movement, especially under changing thermal conditions. Securing this part more stringently, with glue for instance, may prevent such issues in the future; it should be emphasised that the current hardware is very much a first version of this instrument. As this issue is believed to be independent of the general thermal stability characteristics of the PiSpec, these data points are omitted from the line position versus temperature regression analysis (Fig. 4.4). It may then be proposed that above 45 °C the PiSpec could become unstable; however, since only one instrument was tested, it is not clear if this will be a persistent factor, or was simply associated with this specific PiSpec instrument.

The linear dependence, omitting the high temperature data as discussed above, indicates that the PiSpec displayed wavelength shifts of ≈ 0.046 nm/°C between ≈ 2.5 - 45 °C; the coefficient of determination, $r^2 = 0.97$, indicates that this linear model fits the wavelength shifts well across this temperature range. This thermal stability is in extremely good

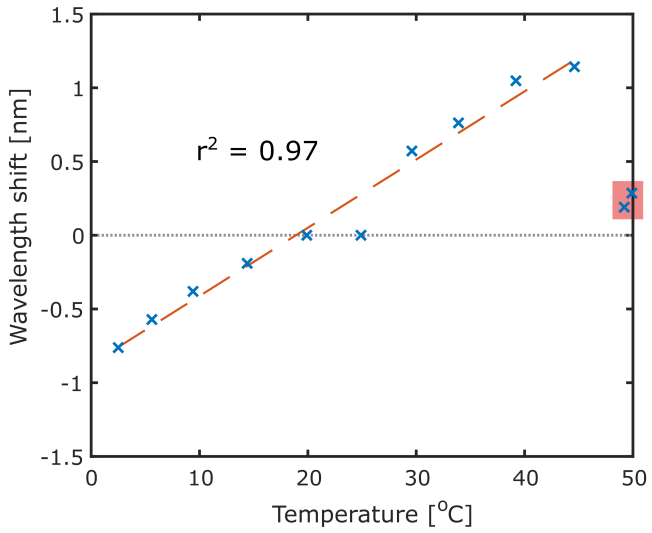

Figure 4.4: Thermal stability of the spectrometer displayed as wavelength change of the 313.155 nm mercury emission line with temperature. Shifts are shown relative to the peak location at 25 °C. A linear regression model indicates a wavelength shift dependence of 0.046 nm/°C, with a good model fit of $r^2 = 0.97$. The two high-temperature points, boxed in red, do not follow the linear trend, and may be caused by a larger scale shift in one of the optical components in the PiSpec. These data are not included in the regression analysis, since they are clearly associated with a different mechanism. Nevertheless, they should not be ignored, and suggest that at high temperatures (>45 °C) the PiSpec may begin to become unstable. In general, such high temperatures should be easily avoidable by keeping the instrument out of direct sunlight.

agreement with shifts in some commercial spectrometers, quoted by Platt and Stutz (2008) as 0.05 nm/°C, indicating that in this sense there is no trade off in using this lower cost PiSpec unit.

In addition to a directional shift of all wavelengths, thermal instabilities can also cause a stretch/squeeze of wavelength dispersion across the sensor (e.g., McGonigle, 2007; Platt and Stutz, 2008). This effect was investigated by tracking two widely separated emission lines (296.728 nm and 334.148 nm) through the acquired spectra. For every spectrum acquired below 40 °C, the peaks of these two emission lines were separated by exactly 393 pixels, indicating that no observable stretch/squeeze of spectra was occurring. The pixel separation moved to 392 pixels for the three temperatures above 40 °C. A single pixel in a PiSpec spectrum represents a spectral band of ≈ 0.095 nm; therefore, a shift from a separation of 393 pixels to 392 pixels still represents a relatively insignificant squeeze, considering that the emission lines are separated by 37.42 nm. In general, this analysis indicates that the PiSpec's thermal instability causes all wavelengths to shift simultaneously in the same direction, at the rate determined above of 0.046 nm/°C.

There was, however, also a change in ILS across the studied temperature range (see Fig. 4.5). In particular, at cooler temperatures the PiSpec's ILS was notably wider, with the

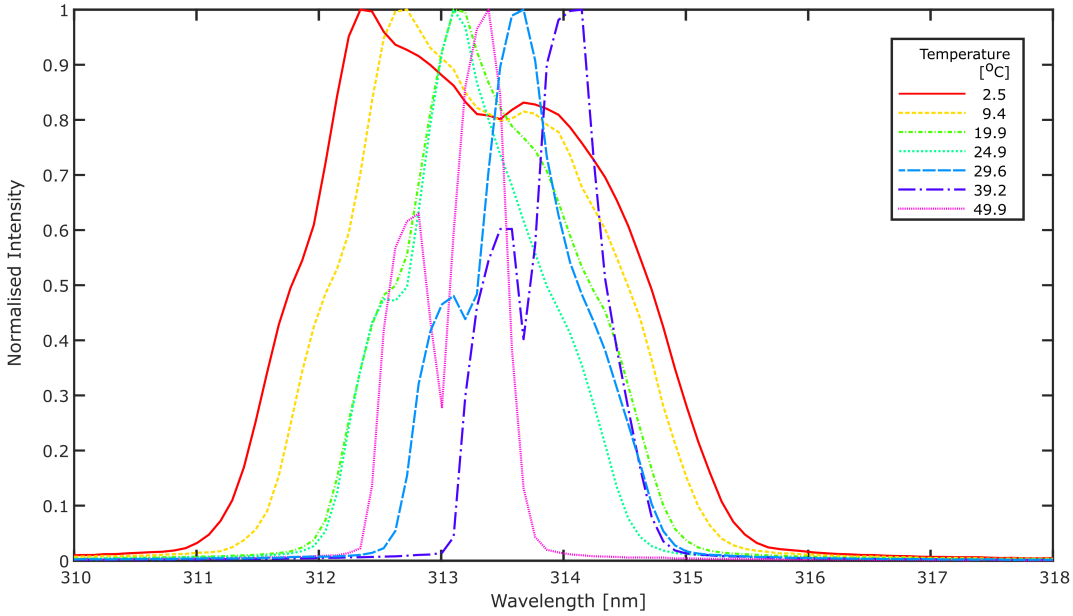

Figure 4.5: Normalised instrument line shapes for a number of temperatures displayed in Figure 4.4. At low temperatures the line shape becomes quite broad, possibly preventing DOAS retrievals from being performed. Towards higher temperatures a double peak begins to form.

spectral resolution, defined as the FWHM of an emission line, increasing markedly. At 2.5 °C this increased to 2.9 nm, which would almost certainly be too broad to enable conventional SO_2 DOAS measurements. At 25 °C the spectral resolution measured in these tests was $\approx$ 1.1 nm. Kantzas et al. (2009) showed that the spectral resolution of commercial units (USB2000, Ocean Optics) is also impacted by changing ambient temperatures; however, the temperature range considered therein was not as extreme as that presented here. Kantzas et al. also highlighted that the line widths and thermal responses vary between individual spectrometers, even for the same model, and the same should therefore be expected of the PiSpec; as already mentioned, to date, only one PiSpec instrument has been built and tested. Indeed, all of the above analyses should be interpreted cautiously, as they apply solely to the tested instrument. Whilst it is possible that future PiSpec instruments could display similar thermal characteristics to those of the instrument tested here, to what extent such an assumption is valid cannot be concluded from this work.

As discussed by Platt and Stutz (2008), thermostating a spectrometer is the best means of preventing thermal instabilities from affecting DOAS retrievals. As with commercial spectrometers, the tests presented here show that the PiSpec would similarly benefit from such measures. Nevertheless, DOAS measurements with commercial instruments are frequently made without such controls in place. Similarly, it is shown here that the PiSpec does appear to work adequately, at least within the range of conditions encountered in this study, without thermal stabilisation. To some extent post processing

of spectra, by wavelength shifting and squeezing the differential optical density array such that it better fits the SO_2 reference spectrum, can account for calibration error caused by thermal instability, as can measurements of gas cells containing known column amounts of SO_2, and/or regular calibration with mercury lamps under the conditions encountered in the field. However, the change in ILS is more difficult to correct for, unless the change is well characterized. Inspecting the changes in ILS in Figure 4.5, it is therefore suggested that the PiSpec could function acceptably within $\approx \pm 5$ °C of its calibration temperature; although this will still result in some error in retrieved column densities. Alternatively, Meroni et al. (2010) present a method for calibrating spectrometers using Fraunhofer lines and atmospheric absorption features, therefore providing a possible means of recalibration without the need for a calibration lamp in the field.

4.2.5 Performing DOAS retrievals

The PiSpec's ability to perform DOAS retrievals of SO_2 was first tested using quartz calibration cells filled with known column densities of the gas. These cells do, however, decrease in SO_2 concentration through their lifetime, possibly due to photochemical reaction, adsorption onto the cell wall, or leaking through the cell walls (personal communication with Robin Campion and Andrew McGonigle). This means that DOAS measurements need to be used to quantify the column density of gas in the cell; this was somewhat of a Catch-22 scenario for the PiSpec, since the aim of the test was to determine how accurately the instrument could perform SO_2 measurements. Therefore, measurements were also made with a USB2000 spectrometer, which is routinely used in remote sensing of SO_2; these measurements were then used as a standard on which the PiSpec could be assessed. Control of the USB2000 and subsequent SO_2 retrievals were performed using volcanoSO2.exe (McGonigle, 2007). The DOAS retrieval procedure was outlined in Section 2.3.1.

Measurements were made of 2 different SO_2 cells (referred to as A and B), with both spectrometers performing 10 retrievals of each. Average column densities of 296 $\pm$ 12 ($\pm 1\sigma$) ppm·m and 1184 $\pm$ 30 ppm·m for cell A and B, respectively, were recorded using the USB2000; the PiSpec measured values of 304 $\pm$ 31 ppm·m and 1257 $\pm$ 58 ppm·m, respectively. Example fits for the PiSpec are displayed in Figure 4.6. For both cells, the results overlap within the range of the two devices' standard deviations, validating the PiSpec's performance for DOAS retrievals of SO_2. The standard deviations of the PiSpec retrievals are, however, somewhat larger than those of the USB2000, suggesting that the signal-to-noise ratio of the former is lower. This would be expected given the lower cost of the PiSpec instrument.

The agreement between the two systems is also limited by errors inherent in the DOAS retrieval itself, rather than purely being a function of the instrument. For instance, the fitting window used in the retrieval can have a significant impact on the returned column

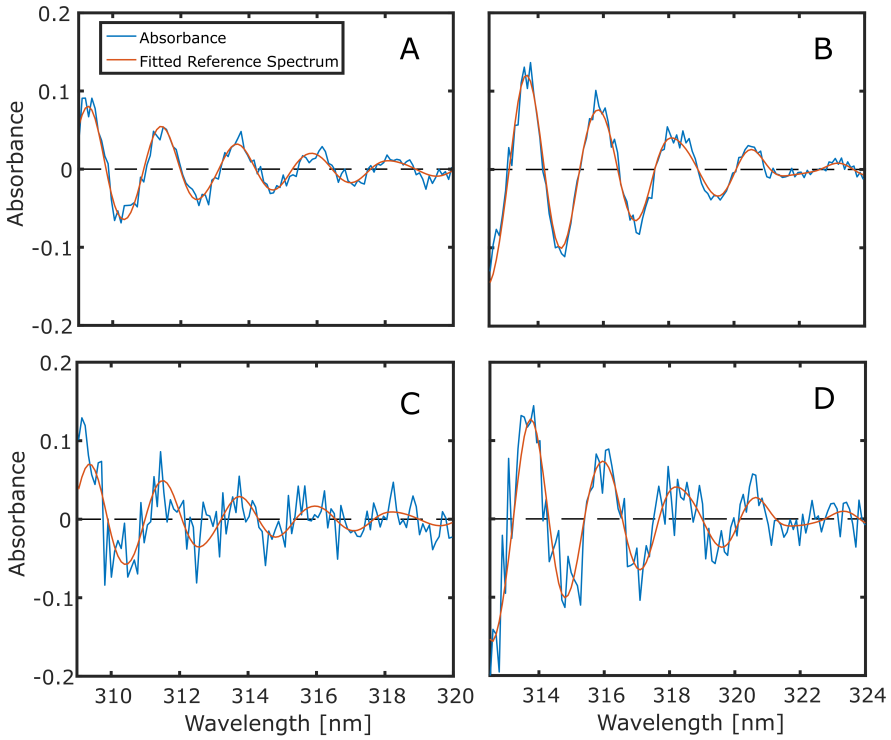

Figure 4.6: Example processed PiSpec absorbance spectra calculated for gas filled SO_2 cells, and fitted reference spectra using data from Vandaele et al. (1994). Column densities of (A) 316 ppm·m and (B) 1187 ppm·m were found for the two cells, when co-adding 11 rows. (C) and (D) are as (A) and (B), respectively, but with no co-adding of rows. Increased noise levels are evident in the absorbances, and respective column densities of 290 and 1278 ppm·m were found in this case.

density (Vogel et al., 2013; Fickel and Delgado Granados, 2017). Due to differences in instrument responses and retrieval softwares, the fit windows for the two instruments were not standardised, with the optimal window for each instrument being selected manually. Nevertheless, the mean cell measurements of the two instruments are well within the 15 % error quoted by (McGonigle, 2007) for volcanoSO2.exe retrievals.

It is important to note here that the integration times used for the PiSpec were considerably longer than those used for the USB2000 in these tests. PiSpec integration times were 6 seconds, the longest possible exposure on the R-Pi camera module, whilst the USB2000 times were 1.5 seconds. This was to be expected, since the sensor employed in the PiSpec is not UV specific. Conversely, the USB2000 spectrometer contains a CCD which has been specifically designed for UV sensitivity, with the photodetector being coated in a fluorescent coating which down-converts UV radiation to visible, where the silicon detector is more sensitive. Furthermore, the USB2000 optical bench contains a cylindrical lens which focusses light from the entire entrance slit height onto the linear CCD detector, increasing the UV irradiance. It should be noted, however, that the experiment was performed on an overcast day in the United Kingdom and, therefore, in other areas of the world the PiSpec may require integration times significantly shorter

than 6 seconds. Use of a larger slit would also improve the sensitivity of the PiSpec by increasing light throughput; however, this would come with the trade off of degraded spectral resolution.

Another option for increasing the SNR of the PiSpec, and thus decreasing required integration times, is the co-adding of rows on the sensor. This is somewhat equivalent to the USB2000's use of a cylindrical lens to focus light onto its linear CCD. It is also similar to co-adding individual spectra, with one main disparity: it adds in the spatial domain, rather than the temporal domain. Indeed, the vertical direction of a PiSpec spectral image represents a spatial dimension in the field-of-view of the instrument, as discussed further in Section 6.3.2 in regard to hyperspectral imaging. Figure 4.6 highlights the improvement in the quality of the DOAS fit resulting from co-adding 11 rows. Column amounts of SO_2 for cell A estimated from spectra generated by just single rows of the 648 $\times$ 486 image (1314 $\pm$ 95 ppm·m) differ considerably from the USB2000 measurements; furthermore, they have a notably larger standard deviation than the co-added PiSpec retrievals.

Whilst co-adding in the spatial domain could cause issues when viewing a scene which changes rapidly in the FOV of the instrument, there is another significant issue with this co-adding mechanism which may restrict the number of rows it is feasible to co-add. Due to possible non-orthogonal alignment of the optical components in the PiSpec, such as the sensor and the slit, the pixel-wavelength mapping calibration is not perfectly consistent across the entire height of the sensor. Co-adding rows could therefore alter the lineshape and general calibration of the resultant spectrum. By mounting components on high-precision adjustable mounts, it may be possible to align each optical component more accurately; however, this added complexity and cost detracts from the core design principles of the PiSpec: low-cost and simple manufacturing. It may also be possible to generate a calibration specific to each row of the sensor, therefore allowing these artefacts to be eradicated in software; co-adding could subsequently be performed on the adjusted spectra.

4.2.6 Detection Limit

The detection limit of a scattered skylight DOAS spectrometer is difficult to objectively define, since it is dependent on the measurement conditions and spectrometer acquisition settings. Figure 4.7 highlights this, displaying retrievals of relatively low SO_2 column densities both for a traverse (Fig. 4.7A) and scan (Fig. 4.7B) at Masaya volcano, Nicaragua (see Section 4.3.1 for details of this field work). It is apparent that noise levels in the two spectra are different, with the scan spectrum having a notably lower SNR (higher noise level). This results from lower signal levels during the scan, with the clear-sky spectra having DN values of 326 and 50 at 311 nm, for the traverse and scan respectively. The lower SNR in the scan clear-sky spectrum is then propagated to the

absorbance spectrum of the DOAS retrieval. Both the scan and traverse spectra were acquired with a shutter speed of 6 seconds, therefore the difference in signals was likely caused by either the time of day (≈ 11am for traverse vs. ≈ 3pm for scan), different meteorological conditions, and/or different viewing orientations.

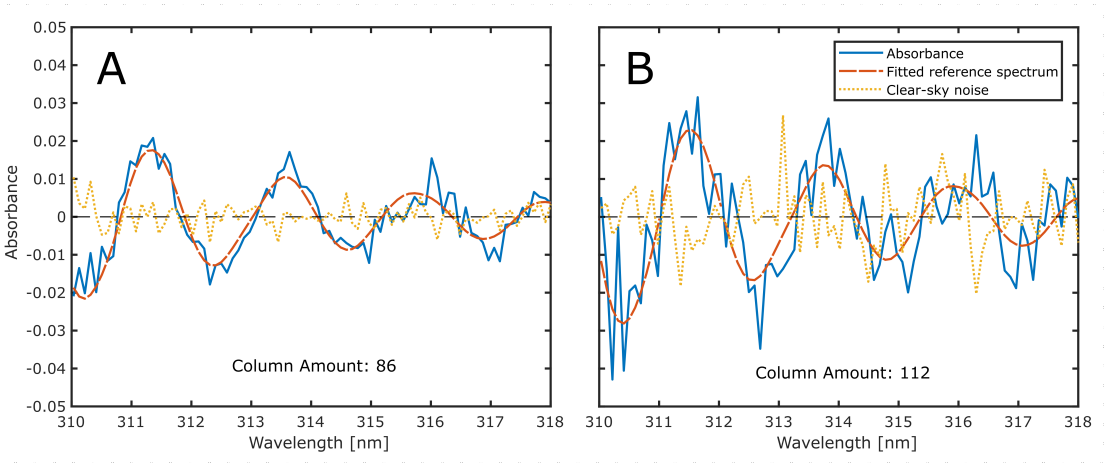

Figure 4.7: Relatively low column density DOAS fits for (A) traverse and (B) scan modes on Masaya volcano. Also shown are noise spectra generated using a second clear-sky spectrum as $I(\lambda)$, as opposed to an in-plume spectrum. Differences in noise levels results from different viewing geometries and conditions for the traverse and scan measurements.

The PiSpec's detection limit, which is associated with this noise level, was estimated following Stutz and Platt (1996), by analysing the noise in an absorbance spectrum generated from two clear-sky spectra:

$$\overline{D}_{limit} \approx \sigma_{abs} \times \frac{6}{(n-1)^{1/2}} \tag{4.1}$$

where σ_{abs} is the standard deviation of an absorbance spectrum generated from two spectra containing no absorbing species (i.e., two clear-sky spectra) and n is the number of pixels in the spectrum. $\overline{D}_{limit}$ is the detection limit of the average optical density, which itself is defined by Stutz and Platt as three times the standard deviation of the reference spectrum. Stutz and Platt (1996) and Platt and Stutz (2008) also discuss a more complex and rigorous Monte Carlo model for determining an instrument's detection limit; however, they show that the more simplistic algorithm above provides a relatively accurate estimation (within 10-20 %).

From clear sky spectra acquired in Masaya (June 2017) on the end of a traverse sequence, the absorbance noise, σ_{abs}, was 3.10×10^{-3}. In a fitting window of 85 pixels, such as that used in the DOAS fits in Figure 4.7, this noise corresponded to a detection limit, $\overline{D}_{limit}$, of 2.03×10^{-3}. In the presence of residual structures, from unknown gas species or the instrument itself, the detection limit must be scaled by a correction factor of 3-4 (Platt

and Stutz, 2009). Here, I conservatively used 4, therefore, the average optical density detection limit was 8.11×10^{-3}, with a resulting column density detection limit of 26 ppm·m of SO_2. Following the same methodology for the scan associated with Figure 4.7B, a detection limit of 50 ppm·m was estimated. As can be seen, these values are case-specific and it is not possible to generate a single detection limit for the PiSpec instrument for all scenarios. Indeed, $\overline{D}_{limit}$ will depend on field conditions, PiSpec acquisition settings and the DOAS fitting procedure.

The PiSpec detection limits are an order of magnitude larger than the 2.5 ppm·m quoted by Galle et al. (2003) for a mini-DOAS instrument; however, it is not clear how they defined the limit in their work. The limits discussed for the PiSpec are quite conservative, since they include a factor of four increase in $\overline{D}_{limit}$ associated with the potential presence of residual structures in the spectra, following Platt and Stutz (2008). Omitting this factor, the detection limit for the traverse discussed above would be 6.5 ppm·m, which is quite similar to the mini-DOAS. I suggest, however, that the more conservative estimate, 26 ppm·m in this case, is likely to be more realistic. Nevertheless, this performance is still quite reasonable, and should be adequate for the majority of volcanological DOAS applications.

4.2.7 Retrieval linearity

At large optical densities of SO_2 the DOAS retrieval can become non-linear, due to the instrument's line shape not being able to perfectly resolve the high frequency variations in the SO_2 absorption cross section, and the fact that the natural logarithm and convolution with ILS are not commutative operations (Frankenberg et al., 2005; Wenig et al., 2005; Bobrowski et al., 2010). Whilst it is preferable to use a system with a linear response across the range of column densities expected to be encountered during measurements, an accurate model of an instrument's response can be used to correct retrievals for non-linearity (Wagner et al., 2003; Kern et al., 2017).

The linearity of PiSpec DOAS retrievals was modelled following Wagner et al. (2003) and Kern et al. (2017). First, an assumed SO_2 column density was used to generate an absorption spectrum, using a high-resolution absorption cross section (Vandaele et al., 2009) and the Beer-Lambert law. This absorption spectrum was convolved with the PiSpec's ILS and the natural logarithm taken; the resultant spectrum was then down-sampled to the pixel resolution of the PiSpec. Finally, a typical DOAS fit procedure was applied to this spectrum, using the ILS-convolved high-resolution absorption cross-section spectrum.

Figure 4.8 shows the model results between 0 and 10000 ppm·m, in increments of 1000 ppm·m. A fit window of 314-324 nm was used in this case, which represents a relatively typical window for SO_2 retrievals. The response was extremely linear up to 4000 ppm·m

, with a retrieved SO_2 column density of 3957 ppm·m at a true column density of 4000 ppm·m ($\approx$ 1 % error). For the majority of volcanic applications, this indicates that the PiSpec will perform linearly (see Section 4.3.2 for an example of where this was not the case). Since non-linearity becomes more pronounced at higher optical densities, shifting to a fitting window of longer wavelengths, where SO_2 has a weaker absorption cross-section, is one method which could account for this saturation effect above 4000 ppm·m (Bobrowski et al., 2010); alternatively, the modelled response presented here can be used to correct retrievals (Wagner et al., 2003; Kern et al., 2017). If the latter correction is used, it is of course critical that the fit window used in the DOAS retrieval is the same as that used in the modelled response.

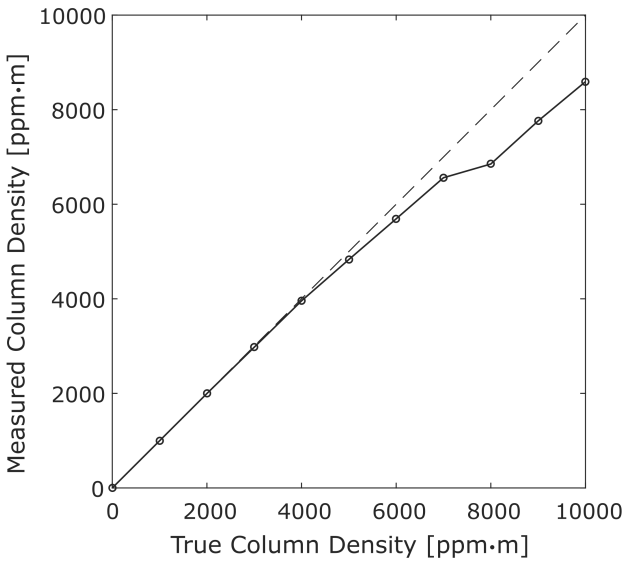

Figure 4.8: A plot of the PiSpec's deviation from a linear response to SO_2 column densities. The model is described in detail in the text. Up to $\approx$ 4000 ppm·m the PiSpec retrievals are extremely linear. Beyond this, the response deviates from the true column densities, and therefore a correction would be required for accurate retrievals; this becomes especially critical above $\approx$ 7000 ppm·m.

4.3 Volcanic applications

4.3.1 Masaya Volcano

Whilst the SO_2 cell test confirmed that the PiSpec had the ability to perform DOAS retrievals of SO_2, field deployments can be more challenging; for example, involving road traverses over bumpy roads or large changes in ambient temperature (as investigated in Section 4.2.4). It was therefore important to deploy the instrument under real-world conditions, by quantifying SO_2 emissions from an actively emitting volcano. The first deployment was performed on Masaya volcano, Nicaragua, where both scanning and

traverse DOAS modes were implemented.

Masaya volcano is an active basaltic caldera located in western Nicaragua. In its active vent, the Santiago Crater, a lava lake became visible in late 2015, and at the time of field work (June 2017) the lake was vigorously overturning; the thermal characteristics of this lake are detailed in Chapter 5. The volcano is currently one of the largest emitters of SO_2 in the world, with Carn et al. (2017) listing it as the 18th highest passive volcanic source between 2005-2015, measured from the Ozone Monitoring Instrument (OMI). Over this period, the average emission rate was 10.0 $\pm$ 4.2 (1σ) kg s^{-1}. Aiuppa et al. (2018) quoted emissions between 0-50 kg s^{-1} measured with NOVAC DOAS instruments from March 2014 to March 2017, whilst a slightly more recent study by Stix et al. (2018) (May 2017), using Drone-borne DOAS (DROAS), measured 9-27 kg s^{-1}. The effects of this large plume on local vegetation and communities are exacerbated by Masaya's low lying summit, which sits at just $\approx$ 560 m above sea level whilst much of the surroundings are at a similar or greater elevation (Delmelle et al., 2002; Francis et al., 2018; Sebastien et al., 2018).

The PiSpec scans and road traverses were performed on two separate days, 14^{th} and 16^{th} June 2017, respectively (see Fig. 4.9 for locations). Scans were performed relatively close to the vent, by manually scanning horizontally through the buoyantly rising plume. Contemporaneous visible video was acquired with a DSLR camera from the same location, allowing plume speed estimation via the cross-correlation technique commonly used in both spectroscopic and image-based SO_2 measurements (McGonigle et al., 2005b; Mori and Burton, 2006). Indeed, this work highlights that in settings where the volcanic plume is persistently condensed, visible imagery can provide a low-cost means of estimating plume speeds for DOAS instruments.

Traverses were performed by car, supporting the PiSpec out of the window in a zenith-looking orientation. Each spectral acquisition was geo-referenced by a GPS module (Adafruit Ultimate GPS breakout) attached to the R-Pi that was simultaneously controlling the PiSpec; locations were logged in an ASCII-format text file alongside the file name of the spectral image, such that in post-processing the spectra could be mapped to the location. Traverses followed La Carretera a Masaya, located north east of Masaya and running generally in an east to south-east direction. This road was optimally positioned for traverses at this time, since the plume was blowing from the south-south-west, under rather rare conditions for the region; prevailing wind typically blows from the east, as evidenced by the considerably stunted vegetation to the west of the Santiago crater. At times overhanging tree branches along the road may have interfered with the acquired spectra; however, large obstructions were avoided by delaying acquisitions when approaching such areas. In general, the quality of the fitted SO_2 spectra suggested that significant issues from overhanging vegetation were avoided. As with the scans, plume speeds were estimated from visible video of the condensed plume, which was acquired prior to the traverses (see Fig. 4.9 for location). Traverse emission rates were then

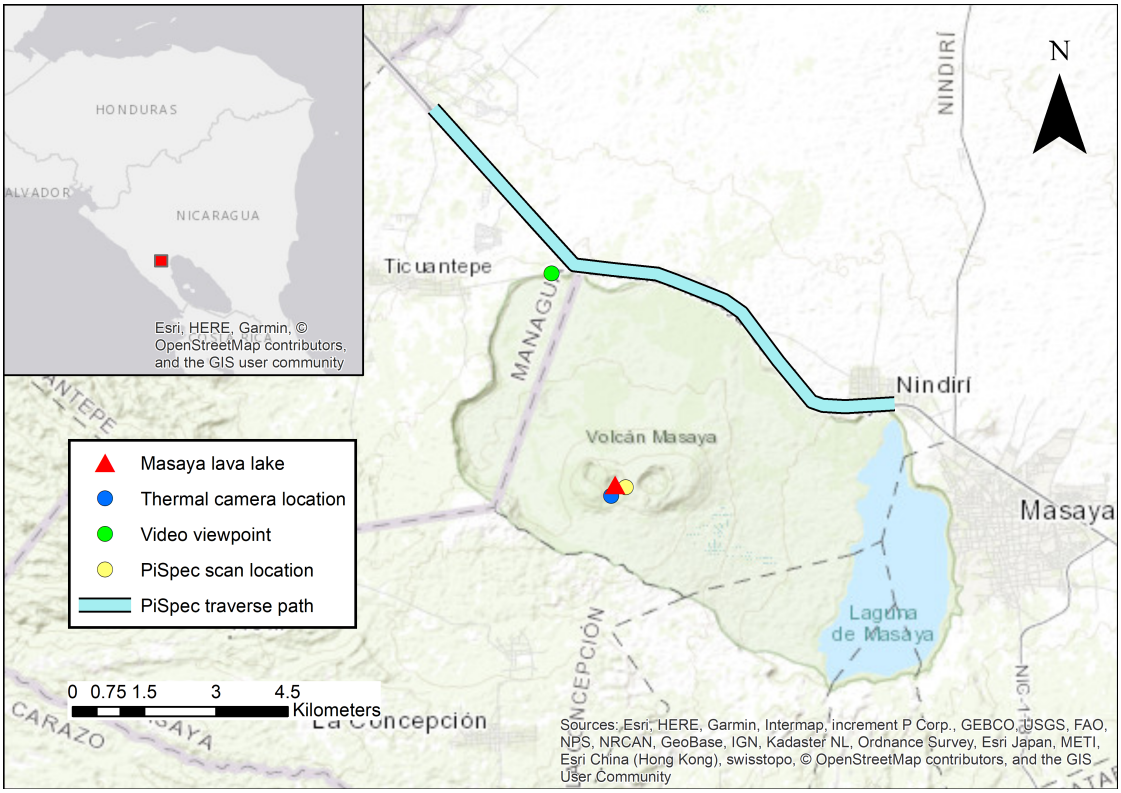

Figure 4.9: A map of locations of field work operations during the campaign to Masaya volcano, Nicaragua, in June 2017. Both PiSpec scans and traverses (this Chapter) and Thermal PiCam measurements (Chapter 5) were made over the course of a week.

estimated following the methodology outlined by McGonigle (2007).

The PiSpec measurements are summarised in Table 4.1. Seven scans were performed on the rim of the Santiago crater. A typical scan and example DOAS fit are shown in Figure 4.10. The plume, which was buoyantly rising from the crater, was estimated to have a speed of 3.9 m s^{-1}, through cross-correlation of the visible video. Resulting emission rates ranged between 3.2 and 7.3 kg s^{-1}, and had a mean of 5.1 kg s^{-1}. The road traverses, which were performed two days later, yielded notably larger emission rates, with a mean of 23.1 kg s^{-1}(range of 11.3 to 45.6 kg s^{-1}); two typical traverses are displayed in Figure 4.11. Here, the plume speed was estimated as 5.3 m s^{-1}. Considering both data sets together, the mean emission rate from Masaya was 13.4 $\pm$ 12.3 (1σ) kg s^{-1}.

In general, the PiSpec data are comparable to the emission rates from Aiuppa et al. (2018) and Stix et al. (2018), which were captured in the same activity period in which Masaya's crater contained the lava lake. Notwithstanding the potential for changes in degassing between the three observation periods, the datasets do compare rather favourably, with all bar two of the PiSpec fluxes falling within the range 0 - 25 kg s^{-1}, which encompassed the majority of the Aiuppa et al. (2018) fluxes; all emission rates herein fall below their quoted maximum flux of 50 kg s^{-1}. The PiSpec traverse values are also in quite good agreement with the traverses of Stix et al. (2018), with mean values

Table 4.1: A summary of scan and traverse emission rates measured with the PiSpec

Start Time (UTC)	End Time	Retrieval Mode	Plume Speed ($m\ s^{-1}$)	Emission rate ($kg\ s^{-1}$)
19:22:25	19:32:27	Scan	3.9	3.2
19:33:50	19:41:05	Scan	3.9	4.0
19:43:08	19:51:01	Scan	3.9	4.6
19:51:59	20:01:31	Scan	3.9	3.6
20:02:30	20:07:37	Scan	3.9	5.6
21:04:22	21:15:42	Scan	3.9	7.3
21:16:37	21:25:47	Scan	3.9	7.1
16:42:26	16:54:37	Traverse	5.3	45.6
17:02:39	17:12:18	Traverse	5.3	17.8
17:28:11	17:35:27	Traverse	5.3	20.5
17:46:01	17:54:33	Traverse	5.3	16.3
17:55:10	18:03:27	Traverse	5.3	27.2
18:08:21	18:17:39	Traverse	5.3	11.3

of 23 and 18 $kg\ s^{-1}$, respectively.

The PiSpec scan data correspond to the quoted Aiuppa et al. (2018) emission rates rather better than the traverse data, with 4 of 7 scans falling within one standard deviation of their quoted mean; the further 3 are comfortably within 2 standard deviations. Since their work also employed scanning spectrometers, albeit in a different location to the PiSpec measurements, it is possible that the good agreement stems somewhat from this similarity in method. Similarly, the PiSpec traverse data are in best agreement with the traverses of Stix et al. (2018), with both datasets containing notably larger average fluxes than the average of scans from the PiSpec and Aiuppa et al. (2018). The disparity in PiSpec scan and traverse emission rates could be simply a manifestation of rapid (timescales of hours to days) variation in emission rate from the volcano, which is also apparent in the NOVAC fluxes reported in Aiuppa et al. (2018). However, recently Moor et al. (2017) also found that a scanning-DOAS system systematically retrieved

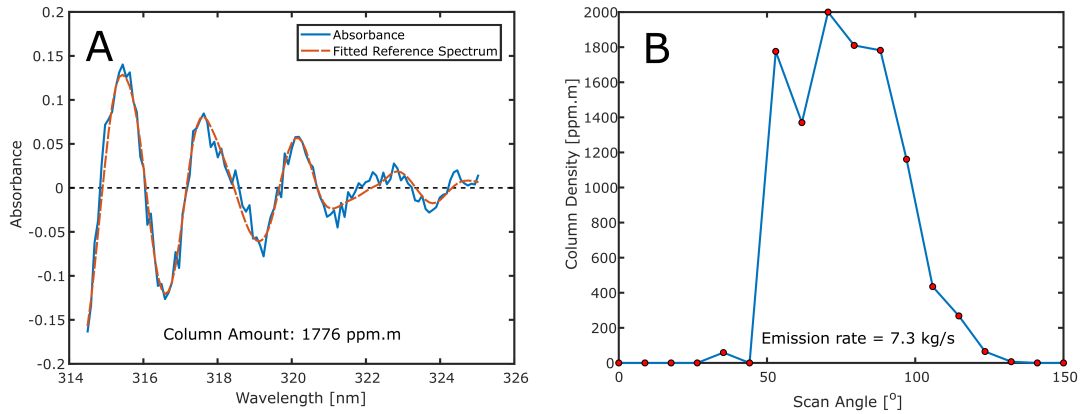

Figure 4.10: (A) Example DOAS retrieval (fit window of 314.5-325 nm) from the scan presented in (B). (B) A full PiSpec scan taken from the Santiago crater rim between 21:04 UTC and 21:15 UTC, on 14 June 2017. The resulting emission rate computed from the scan was 7.3 kg s^{-1}.

lower SO_2 fluxes than traverses, when studying emissions from Turrialba in Costa Rica. It is not clear whether this is simply coincidental or whether it is caused by fundamental differences in how the scan/traverse retrieval modes are performed and processed. In their supplementary information, Moor et al. (2017) provide a good discussion of possible causes for discrepancies, such as ash on the optics or sub-optimal scanning position; for a permanent station the latter is of course impossible to always prevent since wind direction is changeable. Some systematic over-/under-estimation in the PiSpec data may also come from the plume speed scalar, since all scan emission rates were derived from a single plume speed and, likewise, all traverse emission rates were derived from a separate single plume speed. Any error in this calculated speed will therefore have been propagated through all emission rates of that retrieval mode.

As discussed in Section 4.2.5, it is important to note that the PiSpec does require relatively long shutter speeds to achieve an acceptable SNR for DOAS retrievals, due to the relatively modest UV sensitivity of the Omnivision sensor. With the 30 μm entrance slit in place, shutter speeds of 6 seconds were required. Due to large overheads on the camera board, this resulted in acquisition times of 30 - 40 seconds. Although a software fix may be able speed up this process, scans on Masaya took $\approx$ 10 minutes to complete; of course, this time will vary depending on the viewing geometry and angular resolution of the scanner. Traverse durations will be unaffected by this issue, however, for a given traverse speed the spatial resolution will be notably lower for the PiSpec, relative to a commercial spectrometer with a faster acquisition rate.

One prospect for reducing the PiSpec acquisition time is using a larger entrance slit. This will allow higher light throughput, although it will simultaneously decrease the spectral resolution of the instrument; this is therefore an important trade-off to consider. A configuration with a 50 μm in place was tested for the final three Masaya traverses

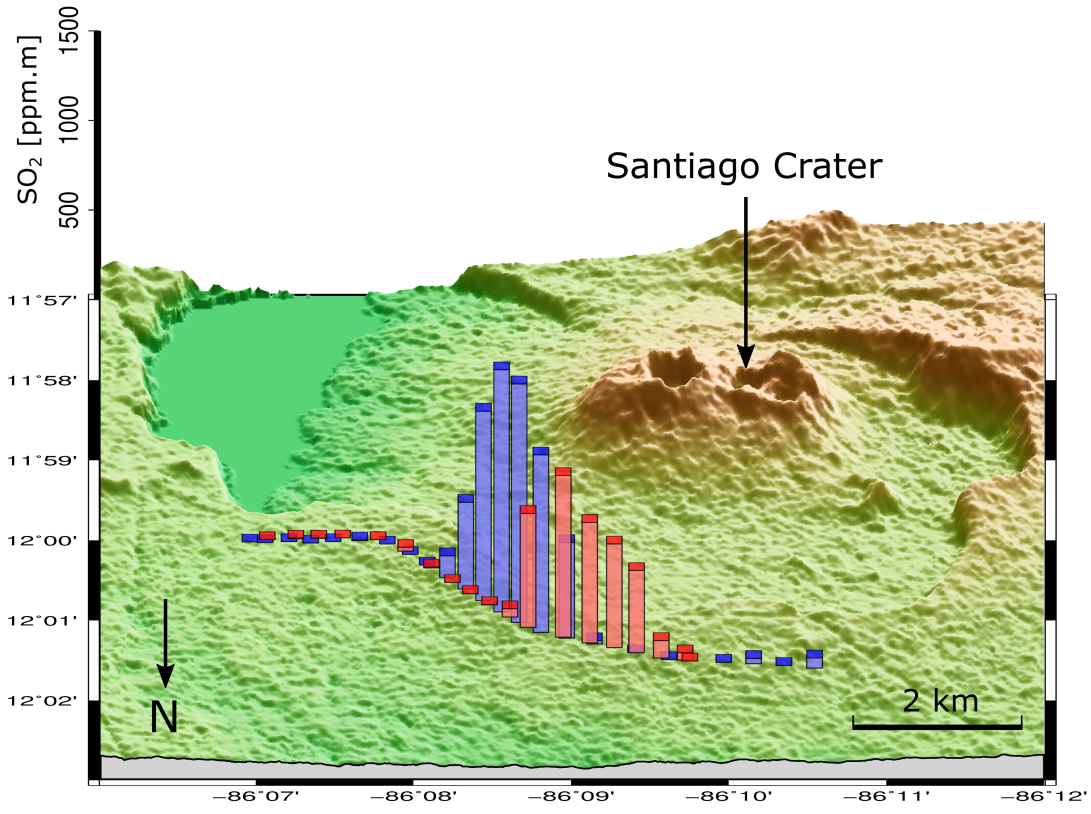

Figure 4.11: Traverse SO_2 column densities (ppm·m) plotted in bars for two traverses started at 17:46:01 UTC (red) and 17:55:10 UTC (blue); emission rates were 16.3 and 27.2 kg s^{-1}, respectively. Traverses were performed along La Carretera a Masaya. Base map topographic data retrieved from USGS (2018). Map created using the Generic Mapping Tool (Wessel et al., 2013).

on 16th June. This allowed shutter speeds to be reduced from 4.5-6.0 seconds to 2.5-4.5 seconds, whilst maintaining $\approx$ 70 % sensor saturation at the peak of the DOAS fit window. The PiSpec then required 15-20 seconds per acquisition. Emission rates with this configuration were comparable to those traverses made with the 30 μm in place, with no systematic over- or under-estimation resulting from the larger aperture. This suggests that, in this context at least, use of a larger aperture could reduce the acquisition rate issue. As discussed in Section 4.2.5, a further solution could be to co-add more rows of the sensor when generating the spectrum. This would enable higher SNRs to be achieved at lower levels of sensor saturation, therefore allowing shorter shutter speeds to be used. However, the complications associated with this method have been discussed previously, and would require further investigation.

4.3.2 Extremely high emissions on Hawai'i

On 3 May 2018 a period of vigorous activity began in the East Rift Zone of Kīlauea volcano, Hawai'i. A series of fissures opened up, with lava flows stretching to the sea and destroying over 600 homes (Global Volcanism Program, 2018a). Following approximately a month of numerous fissures opening up, Fissure 8 became a well developed vent, with lava fountaining and a continuous rapidly moving lava flow leaving the area. SO_2 emission rates at this time were incredibly high for a persistent non-explosive eruption, reaching in excess of 50,000 t day^{-1} (Neal et al., 2019). The extremely high optical density of SO_2 meant that standard SO_2 cameras were not working, since absorption in the on-band filter was beginning to saturate and become non-linear, whilst the typical off-band images (330 nm) were recording significant SO_2 absorption (inferred from PiCam images taken during this period of activity).

On 31 July 2018, the PiSpec was used to measure emissions from Fissure 8 by traversing highway 130; a total of 4 traverses were performed. When traversing underneath the plume, signal from the PiSpec was seen to decrease considerably, caused by substantial attenuation of radiation by SO_2 and aerosols. Due to the large column densities of SO_2, reaching over 10,000 ppm·m at times, the fitting window used in the retrievals was often moved to quite long wavelengths ($\approx 322-332$), making use of weaker absorption features that are less susceptible to saturation at high column densities. Nevertheless, the column densities still required a correction for non-linearity, employing the methodology outlined in Section 4.2.7. A reasonable amount of manual fitting was required to determine the optimal wavelength window for each acquisition, as a result of the broad range of SO_2 column densities. Such procedures have been proposed before by Vogel et al. (2013) and Fickel and Delgado Granados (2017); in particular, the latter is also in relation to high column densities of SO_2 associated with degassing volcanoes.

A wind speed estimate was retrieved from the National Oceanic and Atmospheric Administration (NOAA) Global Data Assimilation System (GDAS), providing 1° of latitudinal/longitudinal resolution. For the time of the traverses this speed was estimated to be 6.5 m s^{-1}. Emission rates from the traverses ranged between 320 and 630 kg s^{-1}(27,000 - 54,000 t day^{-1}). These are quite consistent with the measurements of Neal et al. (2019), who quoted only a rough value of greater than 50,000 t day^{-1}. The PiSpec emission rates, however, vary quite considerably over a short period of time. It is not clear whether this is a result of changing fissure emissions, changeable wind speeds which are not captured in the low-resolution GDAS data, or other sources of error. Unfortunately, Neal et al. (2019) do not quote a more comprehensive database of SO_2 flux measurements during this period; therefore, a more detailed comparison, which could further evaluate the integrity of the PiSpec traverses, was not possible here.

Overall, in concordance with the comparison with a USB2000 spectrometer presented in Section 4.2.5, the deployments on Masaya and Hawai'i, and comparisons to relevant sec-

Table 4.2: A summary traverse emission rates measured with the PiSpec on Hawai'i on 31st July 2018 (1st August 2018 UTC)

Start Time (UTC)	End Time	Plume Speed (m s^{-1})	Emission rate (kg s^{-1})
01:23:25	01:41:00	6.5	630 (54,000 t day^{-1})
01:45:03	02:00:03	6.5	320 (27,000 t day^{-1})
02:01:53	02:11:26	6.5	410 (36,000 t day^{-1})
02:24:25	02:38:35	6.5	400 (34,000 t day^{-1})

ondary datasets, suggest that the PiSpec can quite effectively perform DOAS retrievals of volcanic SO_2.

4.4 Summary

This chapter presented the development of a relatively low-cost, 3D printed, UV spectrometer, specifically designed for application in differential optical absorption spectroscopy (DOAS) retrievals of SO_2. The spectrometer's sensor was the modified R-Pi camera module presented in Chapter 3. The work first identified the relative ease with which a spectrometer can be designed and manufactured, with the use of ray tracing software, computer aided design (CAD), and 3D printing technology. The resulting spectrometer, named the PiSpec, exhibited a spectral range and resolution of $\approx 280 - 340$ nm and 1 nm, respectively. The spectrometer was rigorously tested for its ability to accurately perform DOAS retrievals of SO_2. Subsequently, the PiSpec was deployed on Masaya volcano (scan and traverse modes) and on Hawai'i (traverse mode) during a substantial fissure eruption. In each case, PiSpec measurements of SO_2 emission rates were relatively consistent with independent measurements made by groups using scientific-grade commercial spectrometers that are routinely used for such measurements. The PiSpec therefore shows great promise for providing a lower-cost alternative to commercial spectrometers in volcanology, as well as possibly in other fields.

Beyond the PiSpec presented in this chapter, to redesign the spectrometer for a different application, with a new spectral range and resolution, it would be relatively straightforward to edit the OpticStudio model and create a new instrument. For instance, in volcanology, it may be useful to design a visible spectrometer ($\approx$ 715-735 nm) to measure H_2O in a volcanic plume, as in Kern et al. (2017). Of course, the cost of such an instrument would need to be considered, to determine whether the PiSpec could provide an economically feasible alternative to a commercial visible spectrometer. Alternatively,

in this case it may be possible to design a novel spectrometer with two spectral bands, one in the UV for SO_2 retrievals, and one in the visible for H_2O retrievals. By inserting a second sensor into the current PiSpec model this may be quite easily done, although this is dependent on whether it is possible to get two Pi Camera modules close enough together that these two bands would be measured (the boards are relatively large, whilst the active sensor itself is just a small region). This design would be extremely low-cost, since only one set of optical components would be required. Furthermore, the ability to measure both species in a single spectrometer, without the need for a bifurcated optical fibre attaching to two separate spectrometers, could be an attractive proposal.

Chapter 5

Accurate measurements of Masaya lava lake temperatures using a novel low-cost near-infrared thermal imager

This chapter is associated with the work presented in Wilkes et al. (2018). It details another use for the modified Raspberry Pi camera module that was introduced in Chapter 3. Here, the sensor was purposed for near-infrared measurements of high temperature sources, enabling accurate retrieval of the emitting body's temperature. This low-cost thermal camera was deployed to retrieve lava lake temperatures at Masaya volcano (Nicaragua). A detailed consideration of measurement uncertainties is also presented, to ensure that the integrity of retrievals could be evaluated.

5.1 Introduction

Thermal imaging cameras have a range of useful applications in volcanological research and monitoring, as Section 2.4.2 discussed in detail. In general, the instruments used are based on medium-wavelength/long-wavelength infrared (MWIR/LWIR) detectors that are sensitive to radiation within one of two atmospheric windows: 3-5 μm or 8-14 μm. Typically, such instruments are expensive (1000-10000s USD), since they have a relatively low demand and therefore have not benefited from the economy of scale driving costs down.

Conversely, the cost of silicon CMOS detectors, such as the Omnivision OV5647 (see previous chapters) which was designed primarily for smartphone cameras, has been driven down considerably by high consumer demand. Such detectors can be sensitive up to

wavelengths of ≈ 1.1 μm, corresponding to the silicon band gap (Darmont, 2009), therefore NIR imaging with these sensors is theoretically possible. For NIR detectors to be useful in thermal imaging applications the target object must produce a large enough NIR radiant flux for the resulting irradiance on the sensor to produce a signal well above the sensor's internal noise. Equations 2.8-2.10 and Figure 2.3 show that at lower temperatures peak emission of radiation is at longer wavelengths and the associated total radiant flux is lower than at higher temperatures. Therefore, for adequate NIR irradiance at the silicon detector, larger temperatures are required, indicating that a thermal camera based on low-cost silicon detectors will only be be able to detect higher temperatures (typically ≥ 450 °C) than MWIR/LWIR systems (Dixon, 1988).

In volcanology, high temperature objects ($\approx$ 100-1000 °C) are commonly encountered, especially where molten lava/magma is exposed. This makes utilising low-cost silicon NIR detectors for thermal measurements not only feasible, but possibly preferable to MWIR/LWIR detectors. Indeed, a number of relatively recent articles have presented the utility of consumer instruments for temperature measurements on volcanoes (Saito et al., 2005; Furukawa, 2010; Radebaugh et al., 2016). However, these studies have, to date, had some limitations, predominantly due to limited user control of the sensor or the calibration procedure. The earliest of these works, by Saito et al. (2005), used a Sony digital camcorder, which worked with automatic shutter speed and gain control. This resulted in small hot objects often saturating the sensor if the rest of the image scene was considerably cooler; therefore, in such cases accurate temperatures could not be retrieved. Furthermore, non-linearity of sensor response was introduced by post-processing of the RAW image frames, which was performed within the camera and could not be bypassed. A correction for this was therefore required; however, it is possible that such corrections introduced some error into the images. Overall, for scientific applications it is preferable to work directly with the RAW sensor data from the outset.

Later work by Furukawa (2010) improved on the earlier research by using an instrument which allowed greater user control of the camera system. In particular, the Canon EOS 300D allowed exposure time and aperture size to be set manually. The calibration scheme involved heating volcanic rock, sourced from the target region (Aso volcano), in an electric furnace, then plotting normalised intensity (scaled for shutter speed, aperture and ISO) against temperature. Whilst this calibration procedure can be accurate, care needs to be taken to ensure that internal reflections are not affecting the radiant flux from the furnace, which will affect the calibration. Furthermore, the authors do not discuss a dark current correction, which would account for the dark offset and provide some level of non-uniformity correction.

The most recent work in this area was presented by Radebaugh et al. (2016), who used the Raspberry Pi (R-Pi) camera module (as already presented in Chapters 3 and 4) and a photometric calibration scheme to retrieve temperatures at Marum lava lake, Vanuatu. Considerable limitations to this calibration procedure, which involved solar illumination

of white and grey card (90 % and 18 % reflectance, respectively), were noted by the authors, who stated that it was "challenging to establish an absolute calibration to the instrument". Furthermore, the use of the camera's video port prevents fixing of camera gains, which can introduce further errors: the gain amplifies a signal, making a calibration obsolete if gain is not accurately corrected for (e.g., as in Saito et al., 2005). Additionally, reversing the gamma correction, which is applied as a part of image post-processing on the camera board, can be difficult, since the value of gamma was only estimated. Conversely, work presented in Chapter 3, and corroborated later in Section 5.2.2, has shown that the RAW PiCam sensor data has a linear relationship to irradiance, since this format avoids post-processing effects found in the JPEG images.

An additional advantage to the RAW sensor data is that it provides 10-bit quantization (1024 levels) as opposed to all other previous low-cost thermal imaging systems which worked with 8-bit (256 levels) images. This higher bit depth considerably increases the temperature resolution of the instrument. It must be acknowledged here that the instruments discussed above did have the capability to provide higher bit depth images, but this functionality was not exploited by the researchers.

Finally, all previous instruments have utilised non-modified visible imaging instruments, other than removing the external NIR filter to extend sensitivity beyond visible wavelengths. The sensitivity of visible imaging cameras to NIR radiation will be further limited by the colour filter array (e.g., Bayer filter), which is specifically designed to provide Red-Green-Blue sensitivity (or some other combination of visible wavelengths). Furthermore, if the RAW sensor data is extracted, the advantages of which were highlighted above, the Bayer filter introduces a non-uniform pixel response, in a mosaic pattern, which must be corrected for (e.g., Gunturk et al., 2005, and Chapter 3). Work presented here follows Chapter 3, removing the Bayer filter, therefore producing a camera without mosaicking complications and with heightened NIR sensitivity.

This Chapter therefore presents the development of a new low-cost thermal imaging system which is believed to be more precise and accurate than previous NIR thermal imaging instruments. In particular, the instrument, which is based on the Pi Camera module as in previous chapters, has 10-bit quantization, fixed analog gain and a black body furnace calibration. Furthermore, the uncertainties associated with this instrument's temperature measurements are discussed in detail, going beyond the previous work on low-cost NIR thermal imaging instruments, where such discussions have been quite limited. Many of these discussions also serve to emphasise the issues faced when attempting to retrieve accurate temperatures remotely; often in volcanology these limitations are neglected, with thermal imaging systems being used without due consideration of the errors involved.

The new instrument was deployed on Masaya volcano, Nicaragua, to image the lava lake which had been active in the Santiago crater since late 2015 (Global Volcanism Program,

2018b; Aiuppa et al., 2018). Recent work by Aiuppa et al. (2018) presented a detailed investigation into this latest phase of activity, using both ground-based and satellite instruments to better understand the evolution of this interesting volcanic system. The thermal data presented therein, however, was relatively low spatial resolution (1 km from MODIS observations) and low temporal resolution (4 returns per day). In addition to the presentation of a novel instrument, this work therefore also presents the first evaluation of the thermal characteristics of Masaya's lava lake. It also aided the development of a more holistic interpretation of this recent phase of activity at Masaya, which was presented by Pering et al. (2019).

5.2 Developing a low-cost thermal imaging system

5.2.1 Camera Hardware

The thermal camera was based on the R-Pi Camera Module (v1.3), with the Omnivision OV5647 sensor debayered as detailed in Section 3.2.2. As with the UV camera, this process was important in that it created a uniform sensor free from a mosaic response structure; furthermore, the Bayer filter removal enhanced NIR sensitivity, which is important for thermal imaging since a system working at longer wavelengths is able to detect cooler temperature objects.

The optics for this camera were more complex than that of the UV camera. This is because high image quality across the entire FOV of the system was particularly important in this application. A triplet lens system, shown in Figure 5.1A, was modelled in OpticStudio to provide a FOV of 10°; this had been determined to be an optimal FOV based on the viewing geometry at Masaya lava lake (see Fig. 5.2). The optics consisted of three off-the-shelf lenses (Ross Optical, L-BCX011; Thorlabs, LD4797; Optosigma, SLSQ-07B-08P), a 3mm diameter aperture and a long-pass 850 nm filter (Thorlabs, RG850) which restricts the instrument's response to only NIR radiation. The filter was located behind the triplet whilst the aperture was positioned between the LD4797 and SLSQ-07B-08P lenses. As in Chapters 3 and 4, the lens holder was designed in Solidworks® and 3D printed in graphite reinforced nylon using the SLS method (https://3dprintdirect.co.uk/); the final optical system is displayed in Figure 5.1B.

As with Chapters 3 and 4, image acquisition was controlled by a R-Pi 3 Model B, which in turn was controlled by a laptop computer. The laptop connected to the R-Pi wirelessly via the Pi's built-in wireless hotspot capabilities. Images were acquired using a version of the PyCamUV software, allowing real-time display of the captured images on the laptop. However, calibration was performed later, therefore there was no real-time display of temperatures in this field deployment. Incorporation of real-time calibration could be developed in the future, and would be relatively simple to implement if the

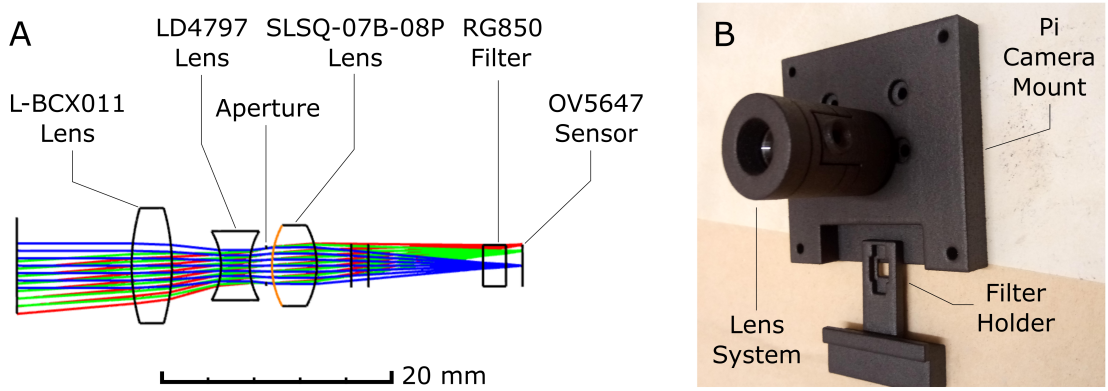

Figure 5.1: (A) The OpticStudio model of the thermal camera triplet optical system, indicating the location of each optical part in the design. The coloured lines represent rays originating from different angles in the camera field of view. (B) The optical system housed inside its 3D printing. The filter holder slides into the camera mount whilst the lens holder is threaded and can therefore be focussed (on infinity) in the field.

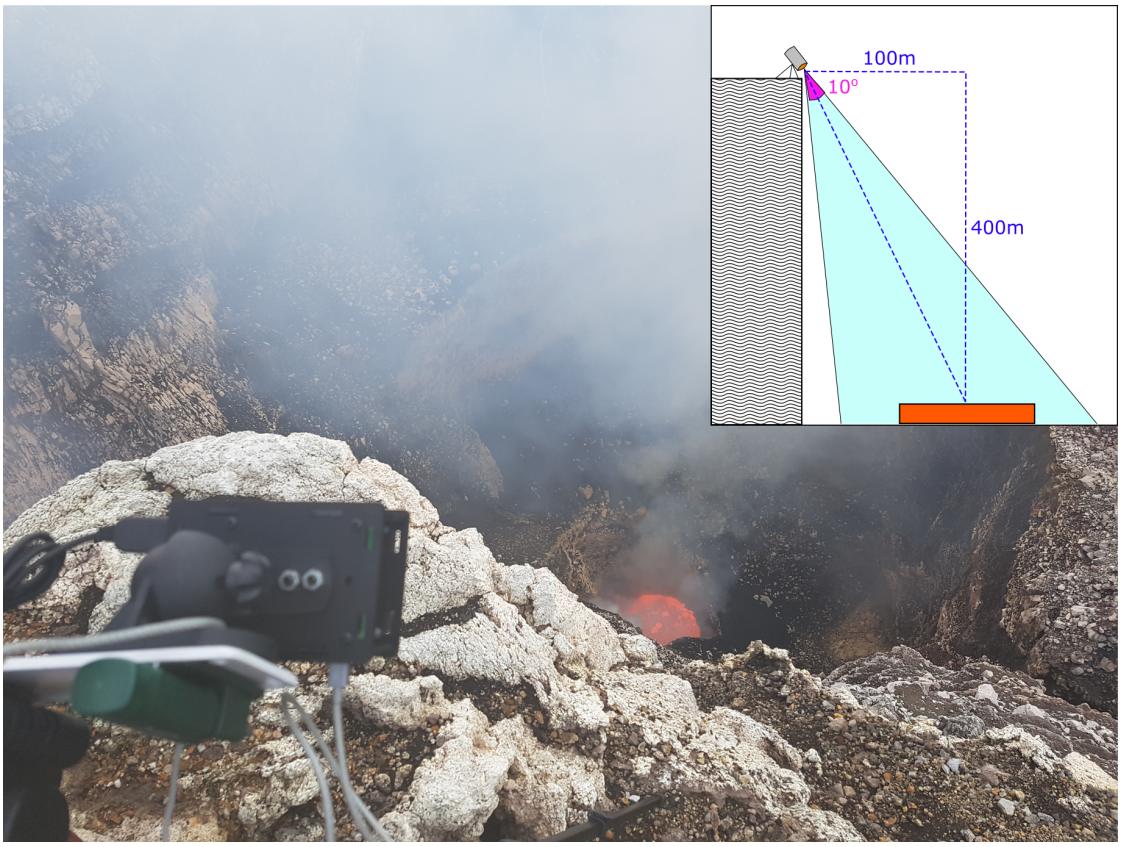

Figure 5.2: An image of the PiCam thermal camera deployed on the Santiago Crater rim on Masaya volcano, to image the active lava lake. Inset: A schematic of the associated viewing geometry provided by Instituto Nicaragüense de Estudios Territoriales (INETER; Personal Communication, 2017); figure is not drawn to scale.

calibration steps are performed prior to field work. This could be extremely useful for volcano monitoring and hazard assessments, where tracking temperatures in real-time could highlight changes in the volcanic system (Walter et al., 2013; Patrick et al., 2014; Patrick et al., 2016).

5.2.2 Sensor Response Linearity

Section 3.2.4 explored the response of the OV5647 sensor to UV radiation, to test linearity. Whilst it is likely that this linearity is observed for other spectral bands, it is useful to confirm this, since the thermal imaging instrument was based on NIR detection rather than UV. Furthermore, here, using a black body furnace, the sensor's response was tested more robustly, since the furnace irradiance should vary much less than the diffuse sky radiation used for the UV tests.

Linearity was tested using the images taken as part of the calibration, which will be presented in Section 5.2.3. This involved looking at a black body furnace, which will be introduced further therein. At each furnace temperature, a range of shutter speeds were used to acquire images, with 30 images taken for each temperature-shutter speed pair; a dark image for the respective shutter speed was first subtracted from each image to correct for dark current offset. Figure 5.3 displays the 30 image average digital number (DN) for a range of shutter speeds and temperatures. Clearly, the sensor response to NIR radiation was extremely linear, with all regressions having very high r^2 values ($r^2 > 0.99$). However, not all regressions passed through the origin as would have been expected. At 950 °C particularly, for an unknown reason the dark image subtraction caused the regression to intersect 0 μs shutter speed at a DN of -8.6. The regression quality was then degraded if the model was forced through the origin. It is likely that this error caused the greater uncertainty found in the second calibration method presented in Section 5.2.3, whereby all image signals were scaled to a 1 μs signal; this is discussed further in that section.

5.2.3 Calibration

Calibration and uncertainty analyses were performed with significant support from Leigh Stanger (Department of Electronic Engineering, University of Sheffield).

In order to retrieve meaningful information from the NIR images, calibration of the system must be performed such that pixel intensities can be mapped to specific temperatures. This was implemented using a black body furnace (Landcal P1200B) with a thermocouple providing UKAS (https://www.ukas.com/) certified temperature measurements of the source. If the cavity is isothermal, the quoted furnace effective emissivity is 0.998. Images were taken of the furnace with the PiCam, at temperatures between 500 °C and 1000 °C, in 50 °C increments; this was done at a range of shutter speeds

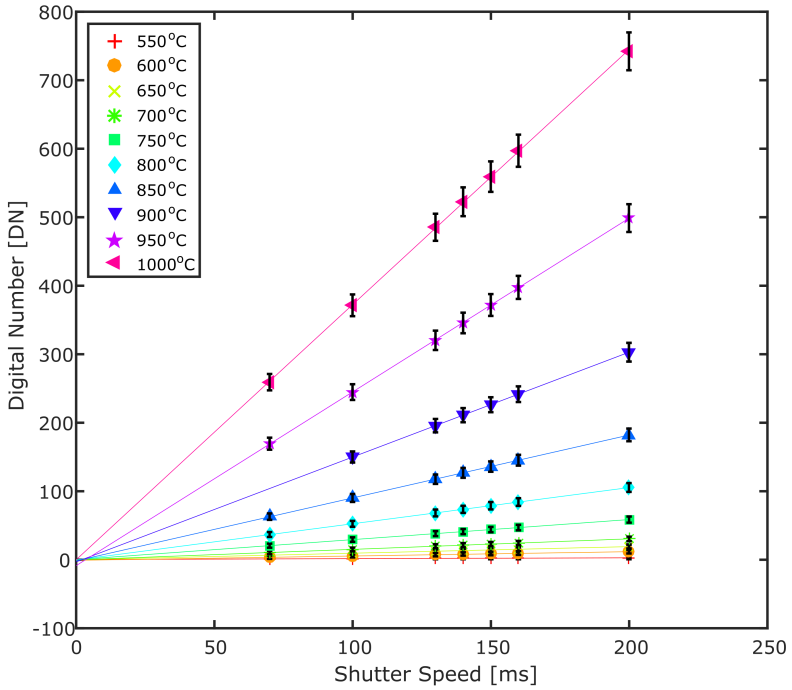

Figure 5.3: A plot of Digital Number (DN) vs. shutter speed (ms), where the DN is found from an average of 30 images taken imaging a black body furnace at the specified temperature. Error bars represent the associated uncertainty of this 30-member mean. The optical system used for this test had the 1080 nm band-pass filter mounted to the fore of the system, as well as the 850 nm long pass filter mounted behind the lens triplet.

which were predetermined by those used in the deployment on Masaya volcano. Whilst it is preferable to cover the range of observed field temperatures during the calibration ($\approx$ 1100 °C at Masaya lava lake), issues with the furnace meant that the calibration was limited to a maximum of 1000 °C. Nevertheless, the calibration fit was extremely good, with a standard error of 1.08 °C, suggesting that extrapolating to $\approx$ 1100 °C should be acceptable.

At each temperature and shutter speed 30 images were taken. These images were first dark image subtracted, and then averaged spatially and temporally, to provide a single digital number (DN) representative of that temperature and shutter speed. Although a single calibration was applied to every pixel on the sensor here, it would be possible to derive a calibration for each pixel individually, to account for pixel non-uniformity (Lane and Whitenton, 2015).

The sensor's response to temperature is not linearly related, therefore a non-linear model must be used to fit the measured signal (DN), S_{meas}, to the object temperature in Kelvin, T_K. The model applied here was the Planckian form of the Sakuma-Hattori equation (e.g., Saunders and White, 2003), with three fitting coefficients, A_1, A_2, A_3:

$$S_{meas} \approx \varepsilon\beta S_{SH} = \frac{\varepsilon\beta A_0}{\exp\left(\frac{c_2}{A_1 T_K + A_2}\right) - 1} \tag{5.1}$$

where ε is the object emissivity, β is the path transmission coefficient and c_2 is the second radiation constant ($1.43877736 \times 10^{-2}$ m K). If the instrument's response is well known, parameters A_1, A_2 and A_3 can be estimated by specific characteristics of the system (Saunders and White, 2003); however, here the fit parameters were determined through a least-squares fit to measured data, which provides a more robust method of characterisation.

Table 5.1 shows the calibration parameters for a 1 ms shutter speed, along with uncertainty fit parameters which are discussed in Section 5.2.5. It is important to note that this calibration is specific to the instrument and cannot be used for other PiCam thermal cameras. Each camera system should have specific calibration parameters empirically derived for that instrument, since each detector will have a different sensitivity. It is possible that calibrations for different PiCam instruments could be substantially different to those presented here.

Table 5.1: Calibration and uncertainty fit parameters for a shutter speed of 1 ms

Parameter	Value	Used in equation
A_1	1.35×10^{-8}	5.1-5.3
A_2	8.6697×10^{-7}	5.1-5.3
A_3	3.90586×10^{-5}	5.1-5.3
σ_{fit}[°C]	1.08	5.5
B_0	0.6966	5.6
B_1	0.002594	5.6
C_0	0.1098	5.7
C_1	0.1545	5.7

To retrieve temperatures from a given signal and known fit parameters, equation 5.1 can be rearranged to give:

$$T_K \approx \frac{c_2}{A_1 \ln\left(\frac{\varepsilon\beta A_0}{S_{meas}} + 1\right)} - \frac{A_2}{A_1} \tag{5.2}$$

Equation 5.1 can also be differentiated as follows:

$$\frac{\partial S_{meas}}{\partial T} = \frac{\varepsilon\beta\partial S_{SH}}{\partial T} = \frac{\varepsilon\beta \left[S(T_K)\right]^2 A_1 c_2}{A_0 \left(A_1 T_K + A_2\right)^2} \cdot \exp\left(\frac{c_2}{A_1 T_K + A_2}\right) \tag{5.3}$$

This derivative will be used in the uncertainty analysis presented in Section 5.2.5. It should be noted here that since $S(T_K)$ is monotonic, $\frac{\partial T}{\partial S} = \left(\frac{\partial S}{\partial T}\right)^{-1}$.

From the Sakuma-Hattori model, two methods of calibration were attempted. First, the calibration fit parameters were determined individually for every shutter speed used during acquisitions; since only a small number of shutter speeds were used in the deployment on Masaya, this was relatively straightforward. However, this method would become increasingly time consuming as more shutter speeds were used in the field, and therefore may not always be so convenient to perform. The advantage of this method is that it ensures high integrity of the resulting calibration. Although the sensor response is very linear with changing shutter speed, considerable uncertainty is incorporated into the calibration if pixel DNs are simply linearly scaled to the shutter speed. This is the second attempted calibration method, where only a single calibration was performed at a shutter speed of 1 μs. All acquisitions were then scaled to a 1 μs signal by dividing by the shutter speed of that acquisition; for example, a DN of 1000 at a shutter speed of 100 μs would become a DN of 10 for a 1 μs shutter speed, assuming perfect linearity. As shown in Section 5.2.2, although the sensor responds very linearly to incident NIR radiation, in some tests this response does not pass through the origin of DN vs shutter speed, possibly due to the dark current subtraction not perfectly accounting for the offset in an image. This calibration experiment was therefore not as successful as the previous method, with a standard uncertainty in the Sakuma-Hattori fit (standard deviation of fit residuals) of 9.35 °C; the standard uncertainty for 1 ms using the first calibration method was just 1.08 °C.

5.2.4 Extinction and Emissivity

As shown by Equation 5.2, accurate retrievals of temperature require knowledge of two further parameters along with the measured signal and fit parameters: the path transmissivity, β, and the object emissivity, ε. The former pertains to the extinction of radiation between the plume and observer, whilst the latter accounts for the deviation of an object from a perfect black body emitter. Both parameters can have considerable effects on the apparent temperature of an object observed by an instrument; therefore, if they are not correctly accounted for they can lead to large errors in temperature measurements.

There are two forms of atmospheric extinction: absorption and scattering of radiation by particles between the object and instrument. Neglecting re-emission of radiation, extinction and transmission must sum to unity; thus, understanding extinction allows the calculation of β in Equation 5.2. Scattering, which involves Rayleigh, Mie, and Raman (inelastic) components, is a considerably more complex radiative transfer problem than absorption, making accurate temperature retrievals difficult (e.g., Ball and Pinkerton, 2006; Spampinato et al., 2011). In general, avoiding imaging through an optically thick path will help to mitigate scattering issues, as will imaging as close to the emitting source as is safely feasible. Developing an accurate model for correcting scattering processes was beyond the scope of the work presented here; therefore, imaging through an atmosphere with a low scattering coefficient is preferable.

It is possible that in cases where scattering is significant, MWIR/LWIR thermal cameras may perform more favourably than a NIR instrument such as that presented here (Patrick et al., 2014). Conversely, it is possible that an NIR system may be less affected by absorption processes than MWIR/LWIR instruments (Furukawa, 2010; Radebaugh et al., 2016), since even in the atmospheric windows of MWIR/LWIR bands H_2O and CO_2 have significant absorption cross-sections. Absorption has been covered comprehensively for MWIR/LWIR systems by Sawyer and Burton (2006), whilst for NIR instruments it was discussed by Radebaugh et al. (2016). However, although the latter did give good consideration to this issue, they did not correct their temperatures for absorption effects. Herein, the estimation of absorption across the viewing path was used to correct the temperature retrievals, with the aim of providing more accurate final measurements.

One advantage of using a NIR detector is that within the spectral band of the instrument's sensitivity ($\approx 850 - 1100$nm) only H_2O exhibits significant absorption. This simplifies the correction to a single species, whilst in other spectral ranges other species (predominantly CO_2 and SO_2) must also be considered. Since high-resolution absorption/transmission spectra are well defined for all common gaseous species (e.g., via the HIgh resolution TRANsmission database; HITRAN; Gordon et al., 2017), it is relatively straightforward to quantify radiation attenuation due to absorption. Details of this correction are provided in the paragraphs below.

During the field work on Masaya volcano, relative humidity (RH) and temperature data were logged at the location of the thermal camera. Using an estimated atmospheric pressure and distance to the source (lava lake), these data were used to estimate the column density of H_2O in the viewing path. Transmission spectra were generated using bytran (Pliutau and Roslyakov, 2017), an application based on the HITRAN Application Programming Interface (HAPI; Kochanov et al., 2016), to extract and manipulate H_2O molecular line intensities, which were scaled by the H_2O column densities. Rather than taking into account temporal variations in these parameters, which would involve much more intensive data processing, the two extremes of logged values were used as bounds to estimate the effect of H_2O; these extremes were 26.5 °C and 82 % RH, and 31.9 °C and

60 % RH, respectively. This work relied on the assumption that conditions measured at the thermal camera's location accurately represented the average conditions over the entire path length. In reality, close to the surface of the lava lake conditions would have been considerably different to those at the measuring site, due to high temperatures and strong gaseous emissions from the lake, therefore limiting the applicability of this assumption. In lieu of a more sophisticated approach, however, these logged data should have provided a reasonable estimation of absorption effects.

Using the transmission spectrum along with the spectral response of the PiCam with the long-pass filter in place (determined using a monochromator), the effect of H_2O on observed temperature was determined by integrating the spectral irradiance at a given temperature with these two filters applied (e.g., see Figure 5.4 for visualisation). The ratio of this signal to the signal calculated without the H_2O spectrum applied then provided the path transmission coefficient, β, which would be used for temperature retrievals in Equation 5.2. The path transmission coefficient is dependent on temperature, since the shape of the black body curve changes with temperature (Figs. 2.3 and 5.4) and therefore the proportion of absorption by each H_2O line relative to the total radiant flux changes with the shifting distribution of spectral radiance. This means that if all atmospheric parameters remained constant, the transmission coefficient would still be a non-constant scalar, dependent on the temperature of the emitting body. For this work, lava lake temperatures ranged between $\approx 800 - 1200°C$; therefore, path transmission coefficients were calculated in 100 °C increments within this temperature range and then averaged. Similarly, β was also averaged between the two extremes of atmospheric conditions. This resulted in a single value for β of 0.8789, which was used throughout the entirety of this work. Uncertainty related to this value, associated with differing temperature and atmospheric conditions, was then considered, and is discussed in Section 5.2.5.

It may be possible to almost entirely remove the effect of H_2O absorption, within the spectral response of the PiCam thermal imager, by using a second optical filter that has minimal transmission within the H_2O absorption band centred at ≈ 950 nm. This could be done using either a bandpass filter centred outside of this absorption zone, or a notch filter which cuts out transmission within the H_2O absorption band.

As with the path transmission coefficient, the emissivity, ε, of an object can result in large measurement errors if it is not well defined. Unfortunately, this parameter is complex and dependent on a number of parameters, including: chemical composition, surface roughness, viewing angle and porosity (Vollmer and Möllmann, 2017). Indeed, to date, a broad range of emissivities for basalt rock have been quoted for the NIR spectral band, ranging between 0.5 and 1.0 (Pinkerton et al., 2002, and references therein). However, much of this range was determined by Rothery et al. (1988), who inferred emissivity using reflectivity data from satellite, rather than more direct measurement approaches, finding values between 0.5 and 0.9. Atmospheric effects can introduce errors into such satellite

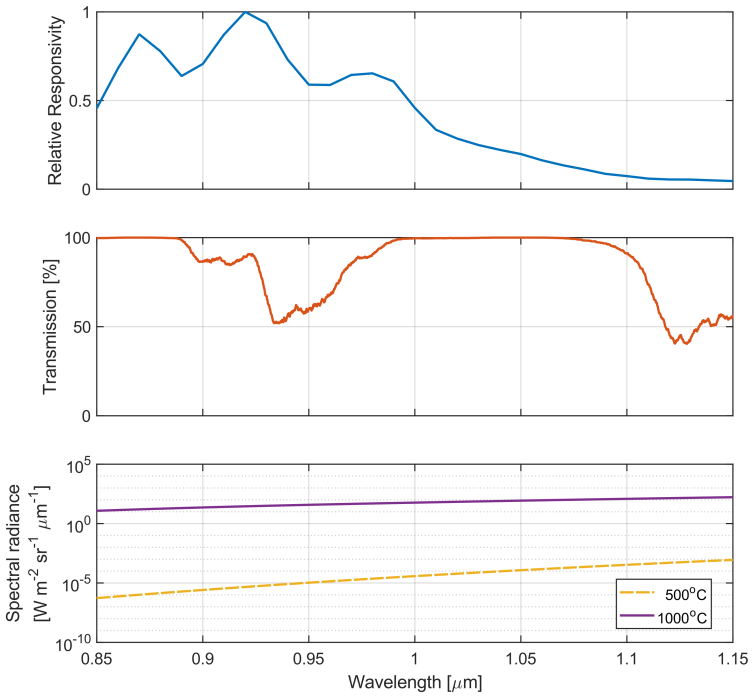

Figure 5.4: PiCam responsivity (top), H_2O transmission (middle) and spectral radiance of black bodies (bottom) all plotted within the band response of the PiCam. The transmission is plotted for a 412 m path length (as in the Masaya viewing geometry) through atmospheric conditions of 26.5 °C, 82 % relative humidity and a pressure of 94300 Pa. H_2O absorption lines have been smoothed with a running mean for clarity. The black body curves are shown for both 500 °C and 1000 °C.

estimations (e.g., Zhang et al., 2014). Ideally, for each application the emissivity of an object would be determined by taking a sample and making laboratory measurements. In the work presented here, the emissivity was assumed to be 0.95, disregarding the estimates of Rothery et al. (1988), and thus assuming that generally basalt emissivities lie between 0.9 and 1.0.

Although accurately measuring the emissivity of an object, such as the Masaya lava lake, is difficult in practice, it may be reasonable to assume that its emissivity is relatively constant through time. Therefore, whilst retrieval of extremely accurate absolute temperature may be difficult, the thermal characteristics from temporal and spatial temperature variations should be well defined by the thermal camera measurements. Indeed, poor characterisation of emissivity should only result in a systematic under- or over-estimation of the object's temperature. Conversely, the path transmission coefficient, β, which is dependent on atmospheric conditions, and in this case also volcanic emissions, could vary quite considerably over short time periods. This could result in masking thermal signals (such as periodicities) with unwanted effects from changing atmospheric transmissivity. In volcanology in particular, the interest lies predominantly in thermal signatures involving changes in temperature, which may relate to changes in volcanic

activity (e.g., Ripepe et al., 2005; Spampinato et al., 2011; Patrick et al., 2014), rather than performing extremely accurate absolute temperature measurements. Section 5.2.5 shows that for the conditions experienced on Masaya, the variations in β have a negligible effect on retrieved temperatures; therefore, the observed changes in temperature could predominantly be attributed to changing lava lake conditions (excluding periods of significant aerosol influence).

Figure 5.5 displays the effects of both emissivity and H_2O on retrieved temperatures, for the calibration at a 1 ms shutter speed. Given the estimated range of emissivities (0.9-1.0), it can be seen that at a DN of 750 assuming an emissivity of 1.0 would lead to an underestimation in temperature of $\approx$ 12 °C, were the object's true emissivity 0.9. This error is relatively modest, but still significant enough to indicate that emissivity should not be neglected. Similarly, at the close viewing distance of $\approx$ 412 m on Masaya, H_2O absorption effects were relatively modest; typically there was approximately 30 °C of temperature error between a totally dry (RH=0 %) and saturated (RH=100 %) viewing path. Of course, such extremes are very unrealistic, although near to the lake surface a RH of close 100 % may occur. Again, this indicates that the corrective parameter β should not be neglected in thermal imaging applications.

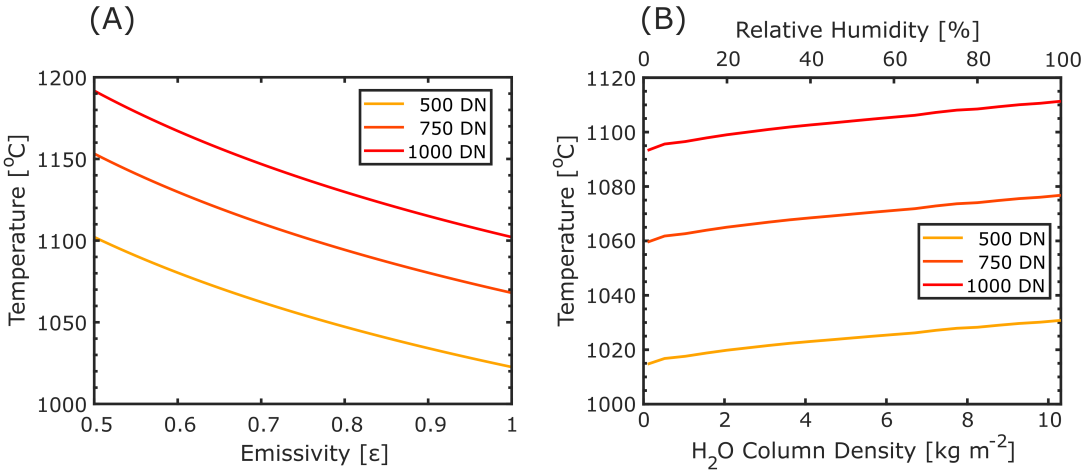

Figure 5.5: (A) Temperature vs emissivity, indicating the effect of estimated emissivity on the retrieved temperature. Three different digital numbers (DN) were modelled, for a shutter speed of 1 ms; a path transmission coefficient of 0.8789 was used. (B) Temperature vs H_2O loading in the atmosphere, again modelled for a shutter speed of 1 ms at three DN levels; an emissivity of 0.95 was assumed. For larger assumed water vapour columns the retrieved temperature rises due to more absorption of radiation assumed to have occurred in the atmosphere. For each modelled temperature the path transmission coefficient was calculated as the mean between 800-1200 °C, under atmospheric conditions of 26.5 °C and 94300 Pa. Relative humidity is quoted assuming a uniform distribution of H_2O along the 412 m path length from object to instrument.

5.2.5 Uncertainties

It is important to understand and quantify the broad range of uncertainties involved in radiometric temperature retrievals. Furthermore, quantifying the uncertainty associated with the thermal PiCam, specifically, was a crucial aspect of assessing this new instrument's performance. In general, in volcanology quite often a number of these uncertainties are neglected or poorly constrained; however, when critically analysing a dataset it is crucial that these limitations are considered. In this section, therefore, a detailed analysis of uncertainty is provided, with much of the work covered here following the comprehensive work of Lane et al. (2013).

In general, the standard uncertainty of temperature, ΔT, associated with the uncertainties of any number of measurands, x_i, can be calculated with:

$$\Delta T^2 = \sum_i \left(\Delta x_i \cdot \frac{\partial T}{\partial x_i} \right)^2 \tag{5.4}$$

where Δx_i is the standard uncertainty of measurand x_i. $\frac{\partial T}{\partial x_i}$ is termed the sensitivity coefficient. The uncertainties are added in quadrature, under the assumption that all uncertainties x_i are uncorrelated.

First, the calibration uncertainty was considered, which stems from the four individual sources shown in Table 5.2. Since these sources are independent, they were added in quadrature to provide a total calibration uncertainty, σ_{cal}. For a 95 % confidence interval, this value was multiplied by two:

$$\Delta T_{cal} = 2\sigma_{cal} = 2\sqrt{\sigma_{TcBB}^2 + \sigma_{TBB}^2 + \sigma_{\varepsilon BB}^2 + \sigma_{fit}^2} \tag{5.5}$$

Table 5.2: Calibration uncertainties

Uncertainty	Symbol	Quantification
Thermocouple Uncertainty	σ_{TcBB}	0.4 °C
Black body cavity temperature uncertainty	σ_{TBB}	1.0 °C
Black body emissivity uncertainty	$\sigma_{\varepsilon BB}$	$0.04 \times S_{meas} \times \left(\frac{\partial S_{meas}}{\partial T}\right)^{-1}$
Fit uncertainty	σ_{fit}	Standard error of Sakuma-Hattori fit (Table 5.1 for value at 1 ms)

Since the uncertainty of the black body furnace's emissivity was dependent on its temper-

ature, the total calibration uncertainty was also a function of temperature. By plotting the standard uncertainty against temperature it was apparent that a linear regression was a suitable model, therefore, ΔT_{cal} could be generated at any temperature T_K by:

$$\Delta T_{cal}(T) = B_0 + B_1 T_K \tag{5.6}$$

where B_0 and B_1 were determined by a least-squares fit. These values are displayed in Table 5.1 for a 1 ms exposure time.

Measurement noise, which is associated with the detector, is another important source of uncertainty in measurements. To quantify this noise, a 4 $\times$ 4 block of pixels was analysed (a small area was used to avoid non-uniform pixel illumination effects which are discussed shortly) in a number of images, and the root-mean-square (RMS) noise, σ_{noise}, calculated. If dominated by shot noise, a detector's noise shows approximately a square-root dependency on signal. Indeed, for the thermal PiCam a square root dependence of RMS noise with signal was observed as such:

$$\sigma_{noise} = C_0 \sqrt{S_{meas}} + C_1 \tag{5.7}$$

Here, the coefficients C_0 and C_1 were determined to be 0.109768 and 0.15447, respectively. For each signal level this was converted to a temperature uncertainty, again at 95 % confidence interval, using:

$$\Delta T_{noise} = 2\sigma_{noise} \cdot \frac{\partial S^{-1}}{\partial T} \tag{5.8}$$

As mentioned earlier, non-uniform pixel illumination was another issue that needed to be considered. As opposed to shot noise, it is possible to correct for this effect with a flat field correction. This involves capturing an image of a uniformly illuminated object (a clear sky image is adequate for some applications), and using this image to correct subsequent images for non-uniform response; this accounts for variation in sensitivity across the field of view of the sensor, which can result from optical effects and from characteristics of the sensor itself. Here, a flat field correction was not applied, but the uncertainty associated with it was quantified to assess the effects of this phenomenon. An image of a flat field was produced and the fractional standard deviation, SD_f, was calculated by dividing the standard deviation across the image by the image's mean pixel value. This could be used to find the flat field uncertainty at the 95 % confidence interval, ΔT_{flat}, for any given signal, S_{meas}, as follows:

$$\Delta T_{flat} = 2\sigma_{flat} \cdot \frac{\partial S^{-1}}{\partial T} = 2SD_f \cdot S_{meas} \cdot \frac{\partial S^{-1}}{\partial T} \tag{5.9}$$

where σ_{flat} is the flat field standard uncertainty. In this case $SD_f = 0.03$ was empirically derived. To determine this value, all other sources of sensor noise must be removed from the flat field image. This was done by averaging 30 images on a pixel-by-pixel basis, therefore effectively eliminating shot noise. The standard deviation of the resulting image was therefore almost entirely due to deviation of the sensor's response from a perfect flat field.

As mentioned in Section 5.2.4, there are two uncertainties associated with the path transmission coefficient, β. These relate to atmospheric variability and the object's temperature. For the atmospheric conditions, it was assumed that the extreme values of atmospheric parameters presented in Section 5.2.4 provided the limits of a uniform distribution function. The standard deviation, σ_β, of such a function could then be calculated by the general equation:

$$\sigma_x = \sqrt{\frac{1}{12}\left(x_{max} - x_{min}\right)^2} \tag{5.10}$$

where x_{max} and x_{min} are the upper and lower limits of variable x, which in this case is the path transmission coefficient β.

Secondly, β is dependent on the object temperature. Two extremes of temperature were chosen (800 and 1200 °C) and, again, a uniform distribution between these two limits was simply assumed. Therefore, the standard deviation of β with respect to temperature could be calculated with Equation 5.10. The final uncertainty of β was then calculated by summing the two standard deviations in quadrature, since they are independent of each other.

The temperature uncertainty of any scalar to the Sakuma-Hattori model may be calculated by first using the chain rule to find the associated sensitivity coefficient (see Equation 5.4):

$$\frac{\partial T}{\partial x} = \frac{\partial T}{\partial S_{meas}} \cdot \frac{\partial S_{meas}}{\partial x} \tag{5.11}$$

where $\frac{\partial S_{meas}}{\partial x} = \gamma \cdot S_{SH}$. γ represents the product of any further Sakuma-Hattori scaling factors from Equation 5.1, which is simply the emissivity, ε, when $x = \beta$.

Finally, therefore, the temperature uncertainty for scalars, $x = \{\beta, \varepsilon\}$, may be calculated by combining Equation 5.11 with the measured uncertainty of parameter x:

$$\Delta T_x = \Delta x \cdot \gamma \cdot S_{SH} \cdot \left(\frac{\partial S_{meas}}{\partial T}\right)^{-1} \tag{5.12}$$

where $\Delta x = 2\sigma_x$ for uncertainty at 95 % confidence level of variable x.

Extinction through scattering processes was not included in the uncertainty associated with β, just as it was not included in the calculation of β itself, due to its considerable complexity making it difficult to constrain. It is acknowledged, however, that this process could have significant effects on retrieved temperatures and their associated uncertainty, an issue which is discussed further in Section 5.3.

The uncertainty associated with emissivity, ε, was calculated following the same steps as with β. Again, a uniform distribution was assumed, between the values 0.9-1.0, which are the limits of emissivity in the literature; values presented by Rothery et al. (1988) were disregarded, since they were inferred from satellite reflectance values, rather than from more directly measured experiments, and have a range much larger than the other sources (Pinkerton et al., 2002, and references therein). Due to the paucity of data here, a uniform distribution between these values was believed to be a best estimate; however, due to the dependence of emissivity on composition, drawing data from the literature, which presents values from other volcanoes, comes with notable caveats. The standard deviation σ_ε was calculated from Equation 5.10 and subsequently the standard uncertainty ΔT_ε from Equation 5.12; in the latter, γ was this time equal to β.

Each uncertainty presented above was considered to be independent of the other uncertainties, therefore, the total uncertainty of the system could be calculated by adding all independent uncertainties in quadrature, as shown in Equation 5.4. The specific calculation for the thermal PiCam uncertainties was therefore:

$$\Delta T_{total}^2 = \Delta T_{cal}^2(T) + \Delta T_{noise}^2(S_{meas}) + \Delta T_{flat}^2(S_{meas}) + \Delta T_\beta^2(T) + \Delta T_\varepsilon^2(T) \qquad (5.13)$$

All discussed uncertainties are dependent on the temperature of the object or the measured signal. Figure 5.6 displays how these uncertainties vary with object temperature and the resulting total uncertainty for a 1 ms shutter speed calibration. At low temperatures, the sensor noise dominates, since this was approaching a DN of 0, and therefore the SNR would be extremely low. Above these lower temperatures, the total uncertainty was predominantly comprised of flat-field and emissivity uncertainties. For the former, this shows that a flat-field correction would be highly beneficial to the performance of this thermal PiCam instrument. Poor knowledge of the lava lake emissivity also limits the accuracy of the instrument; however, as discussed in Section 5.2.4, this uncertainty will likely result in a systematic error in measurements rather than affecting the instrument's precision.

Significantly, for the range of conditions experienced during the Masaya field campaign, the uncertainty related to H_2O (path transmission uncertainty) was negligible. It therefore seems adequate to use a single path transmission coefficient for the entire period, rather than varying this parameter temporally by following changing atmospheric con-

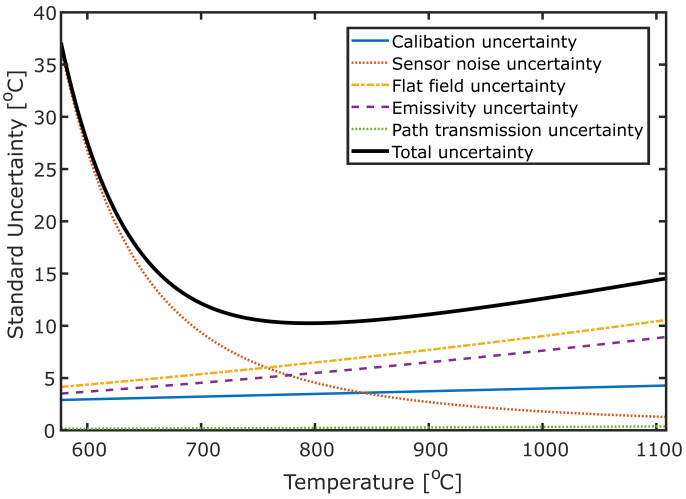

Figure 5.6: Thermal PiCam uncertainties and their relationship with the object temperature.

ditions and estimated source temperatures. Such corrections would require much more processing to implement. Figure 5.5B highlights, however, that, whilst a variable β may be less critical, lack of any water correction whatsoever would lead to significant underestimation of the object's temperature. In general, these results somewhat corroborate the work of Furukawa (2010) and Radebaugh et al. (2016), who suggest that NIR silicon detectors are relatively insensitive to fluctuations in atmospheric absorption through the instrument's viewing path. This is due to the weaker absorption cross section of common gas species within the responsivity of the PiCam instrument, when compared to MWIR/LWIR systems where both H_2O and CO_2 have quite strong absorption features. Nevertheless, for the retrieval of accurate object temperatures, the use of at least a single path transmission coefficient for the thermal PiCam is strongly advised.

The total uncertainty presented here is likely a lower limit on the real uncertainty in the measurements. This is due to other contributors to uncertainty which are more difficult to quantify, and therefore were neglected here. For instance, the size of source effect (e.g., Du and Voss, 2004; Lane et al., 2013), which relates the sensitivity of the system to radiance from outside of the intended pixel instantaneous field of view (IFOV), was not characterised here. A recent study by Stanger et al. (2018) has, however, quantified this for the thermal PiCam instrument, finding a measurement field of view (MFOV) of 1.27°. This means that the instrument will not be able to perfectly resolve the temperatures of objects with spatial frequencies larger than an imaging ratio of 1:45 (object size:object distance). Similarly, there may be considerable uncertainties associated with solar reflection of radiation, as well as attenuation from aerosols, as previously mentioned. Whilst the former is given more comprehensive consideration in Section 5.2.6, an associated uncertainty is not presented, since this would be difficult to accurately define without further instrumentation on the volcano.

Herein, the lower limit of temperature which the PiCam was able to detect was not assessed directly, since defining such a limit is complex and dependent on a number of factors. Indeed, this minimum detectable temperature will change significantly depending on the conditions of deployment. Furukawa (2010) suggested that their silicon photodetector-based thermal camera was imaging temperatures of just a little over 300 °C. Since the thermal PiCam is similarly based on a silicon focal-plane array (FPA), it would be reasonable to expect that a similar detection limit is achievable. However, given the temperature uncertainty associated with sensor noise at 600 °C in Figure 5.2.5, a more conservative estimate of $\geq$ 500 °C is suggested here as the minimum detectable temperature. To reach such a temperature, a longer shutter speed would be required, to increase the SNR, which will decrease the associated temperature uncertainty. Furthermore, at lower temperatures more consideration needs to be given to the effects of solar radiation, since this signal can exceed the radiance of the object itself. The work of Furukawa (2010) was performed at night, to avoid such effects, and Section 5.2.6 gives a detailed consideration of this issue.

5.2.6 Solar reflection

As mentioned previously, solar radiation reflected by the surface of the imaged object can contribute significantly to the irradiance at the detector. This is particularly the case when an object's temperature is relatively low and/or when the object is illuminated by direct sunlight, particularly at low-latitudes close to solar noon. Furthermore, since the emissivity and reflectivity of an object sum to unity, an object with low emissivity will reflect a large proportion of energy from its surface; therefore, such objects will cause greater solar reflection effects.

To model the effect of solar radiation, the solar spectral irradiance was taken from the American Society for Testing and Materials (ASTM) G173-03 reference air mass 1.5. This models spectral irradiance at the Earth's surface using the Simple Model for Atmospheric Transmission of Sunshine (SMARTS v2.9.2) developed by Gueymard (2001). The model represents irradiance on a plane inclined towards the sun at 37°, at a solar zenith angle of 48.19°. It assumes a cloudless sky, therefore, results presented here will provide a worst-case scenario for atmospheric conditions. Nevertheless, in some scenarios, where the air mass is $\approx$ 1 and with direct normal object illumination, it is feasible that the solar contribution to signal could be larger than that modelled here. This would, however, be quite a rare scenario.

Assuming Lambertian reflectance over a hemisphere, the reflected spectral radiance, $L_R(\lambda)$, can be calculated from:

$$L_R(\lambda) = \frac{\alpha I_s(\lambda)}{\pi} \tag{5.14}$$

where α is the surface reflectance (1 - ε) and $I_s(\lambda)$ is the solar spectral irradiance incident on the surface. The emitted spectral radiance of the object for a given temperature, $L_E(\lambda, T)$, was calculated using Planck's law for black body emission (Equation 2.8), and scaled by emissivity ε.

The spectral radiances were filtered by the responsivity of the PiCam instrument, which was determined using a monochromator (as in Section 5.2.4), then integrated to calculate the radiant flux of reflected (M_R) and emitted (M_E) radiation. The proportion of signal incident on the detector resulting from solar reflection, P_R, was then simply calculated with:

$$P_R = \frac{M_R}{M_R + M_E} \tag{5.15}$$

Using Equation 5.1, the signal measured for a range of pertinent temperatures was retrieved. The proportion of this signal associated with both reflected solar radiation and emitted radiation from the object was then determined. From this, the true temperature of the object, or the temperature error associated with solar reflection, was derived with Equation 5.2. The latter, error associated with solar reflection, is presented in Figure 5.7, with all calculations performed for $\beta = 0.8789$, following Section 5.2.4.

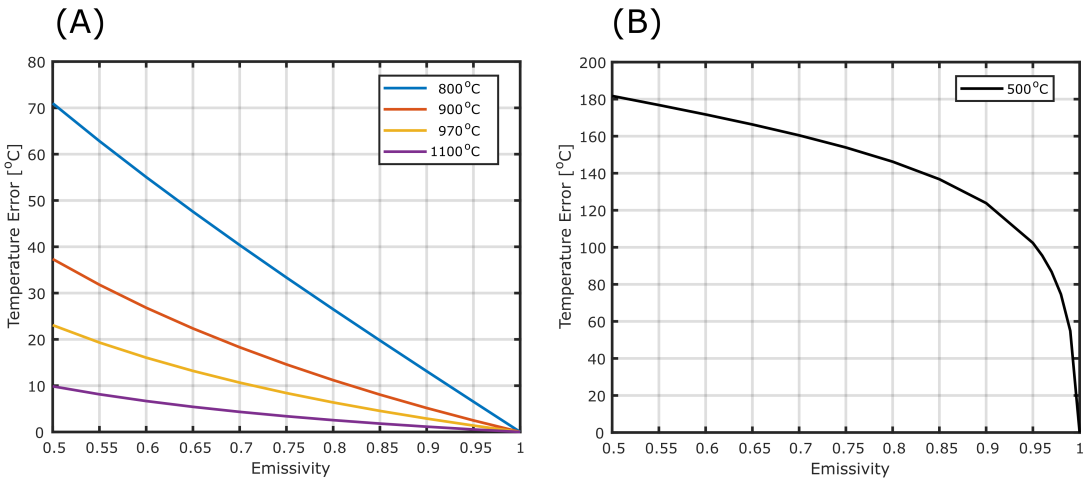

Figure 5.7: Temperature errors associated with reflected solar radiation incident on the hot object. Both plots are the same, with (B) presenting a much lower object temperature of 500 °C (note the differing scales).

Later, Section 5.3 will highlight that the majority of Masaya lava lake temperatures were $\geq$ 900 °C. From Figure 5.7, it can be seen that such temperatures will result in a relatively small error associated with solar reflection ($\leq$ 6 °C) for an emissivity $\geq$ 0.9. For higher temperatures ($\geq$ 1100 °C), the temperature error remains less than 10 °C even at extremely low emissivities ($\geq$ 0.5), which fall at the lower limit of basalt NIR emissivity values quoted by Rothery et al. (1988).

For lower temperature applications, such as that presented by Furukawa (2010), the solar contribution is found to be considerable. Figure 5.7B shows that at a temperature of 500 °C, an error of at least 100 °C will be introduced for all objects with emissivities less than 0.95. The error remains significant until emissivity approaches 1, where by definition the reflectivity reduces to 0 and no solar contribution is present. This result indicates that applications involving lower temperatures would benefit considerably from being performed at night, and in some cases this may be a critical requirement. For other cases, solar effects may be minimal as long as direct sunlight is not incident on the object. Of course, this model does not identify contributions from diffuse sky radiation, or sunlight through clouds, therefore, it is difficult to provide a detailed discussion on imaging under such conditions. Nevertheless, it is important to emphasise that this model represents clear sky conditions at an air mass factor of 1.5, therefore, this scenario is close to worst-case conditions. Thus, in most applications the solar contribution should be notably less than those displayed in Figure 5.7.

In applications where sunlight is considered to be a considerable problem, it may be possible to correct for such effects. This could enable imaging of relatively low temperature targets even in direct sunlight. Such a correction scheme may involve characterising the spectral irradiance close to the hot object, which should allow a relatively straightforward correction if the emissivity/reflectivity of the object can be estimated. Alternatively, a more general correction using the SMARTS model, or similar, to estimate the spectral irradiance for any time of day/year at any global location could provide an acceptable approximation.

5.3 Retrieving accurate temperatures of Masaya lava lake

5.3.1 Methods

The thermal PiCam was deployed at Masaya volcano in June 2017, to image the active lava lake in the Santiago crater. The volcano and that phase of activity were described in Section 4.3.1. In brief, Masaya is a basaltic caldera located in the south west of Nicaragua. In late 2015, a lava lake appeared in the floor of the Santiago Crater, which was seen to be vigorously overturning at the time of the thermal PiCam deployment. The formation of this lake was tracked and discussed in some detail by Aiuppa et al. (2018). However, whilst thermal characteristics were evaluated therein, this was done using satellite data (Moderate Resolution Imaging Spectrometer; MODIS), therefore, they were not able to spatially resolve thermal characteristics of the lake in any way.

The thermal PiCam was positioned on the Santiago Crater rim (Fig. 4.9, approximately 400 m above the lake's surface, with a vantage point that is displayed in Figure 5.2. Due to the geometry of the crater and the position of the lava lake, whose level was 10s

of metres below the main crater floor and visible through a skylight or small vent, it was not possible to image the entire lava lake. It should therefore be noted that results presented here do not represent measurements of the entire exposed surface of the lake. It is not clear how much of the lava lake was not visible, but it is possible it was 25-50 %, based on the circular shape of its visible portion.

Data presented here was acquired on 12 June between 18:12:20 to 18:44:48 UTC. Images were acquired at a frame rate of 0.5 Hz, which is at the upper limit of frame rates currently achievable with the PiCam. Previous thermal imaging with a Pi Camera Module by Radebaugh et al. (2016) used the video port, allowing much higher frame rates to be achieved; however, a number of issues with this method were highlighted in Section 5.1.

The camera was set to acquire with an analog gain of 1; an optimal shutter speed, such that maximum pixel saturation of $\approx$ 80 % was achieved, was then found experimentally. This ensured that the SNR of the system was optimised. Furthermore, images were binned to a resolution of 648 $\times$ 486 to improve the SNR of the system. Here, it is important to note that maintaining a higher spatial resolution could be advantageous for accurate temperature retrievals of small objects. In such a scenario, the 5 MP (2592 $\times$ 1944) capability of the PiCam could result in improved performance relative to commercial MWIR/LWIR thermal cameras, which typically have FPAs with much fewer pixels. For the application on Masaya lava lake, however, it was decided that detecting small features on the lake would be less important than improving the SNR of the system; thus, pixel binning was implemented. Furthermore, limitations of the instrument's MFOV caused by the optics, as discussed by Stanger et al. (2018), could mean that the full resolution images are somewhat redundant.

To accurately interrogate the lava lake and its thermal features it was important to isolate the lake from its surroundings in each image. This lake extraction could be performed in a number of ways. The two methods explored here were: defining a region of interest (ROI) in the image, which remained constant throughout the video sequence (manual picking of each individual video frame would be too labour intensive); or, setting a threshold temperature above which all pixels in the image were considered part of the lava lake.

For the former method, issues were encountered due to windy conditions creating substantial camera shake (see Supplementary Video S4). Therefore, in each image frame the lava lake was located in a slightly different position. To correct this issue, video stabilisation was attempted using the Lucas-Kanade image registration algorithm (Baker and Matthews, 2004), implemented with the Image Alignment Toolbox (Evangelidis, 2013) in MATLAB. After this correction, a single polygon was used to define the extent of the lava lake across all images. Possibly due to the fast flowing lava or intermittent aerosol presence, the image registration was not always perfect; this may also have been a result

of the difficulty in finding optimal input parameters for the Lucas-Kanade algorithm. The resulting stabilised video therefore still contained some camera shake (see Supplementary Video S5); whilst larger shifts have been predominantly removed, this method appears to increase the amount of small shake.

As a result of difficulties in stabilising the video, threshold pixel extraction was also attempted. The lava lake was manually determined to correspond to pixels of temperatures ≥ 850 °C, therefore, in each image all pixels above this threshold were extracted for analysis. This threshold mask tracked the movement of the lake, and therefore was not dependent on video stabilisation (see Supplementary Video S6); however, at the edges of the lake, where significant spattering occurred and/or the crater wall was significantly heated, the threshold can over-define the true lake surface. In Masaya's turbulent lake this was quite a significant issue, and was also observed by Radebaugh et al. (2016) for thermal imagery of Marum lava lake in Vanuatu. Furthermore, when aerosols are present the lake becomes significantly under-defined by thresholding; arguably, however, pixels affected by this aerosol attenuation are somewhat redundant in analyses and their removal may be desirable.

Data discussed here was analysed using the first method of stabilising the video and then defining a polygonal ROI to be extracted from all frames. In most cases this is expected to be the most robust method, especially since it can be improved by better video stabilisation or simply with a more secure mounting system such that camera shake is minimised. There are, however, a number of scenarios in which thresholding could be extremely valuable. For instance, for examining the extent of cooled plates on a lava lake surface, or where effects from spattering and aerosols are minimal, such that the boundary of the lava lake can be well defined by a temperature contrast with the surrounding wall rock.

5.3.2 Thermal characteristics of Masaya lava lake

Figure 5.8 shows an example thermal PiCam image of Masaya's lava lake. Overall, the image quality is quite high, with both cooled plates and bubble bursts being well resolved; this indicates that the triplet lens and 3D-printed optical housing performed well. As was the case with all acquired imagery, in this image parts of the crater wall display extremely high temperatures (750-850 °C). This, however, is quite clearly erroneous, and stems from reflection/scattering of radiation either by the wall rock itself or by aerosols in the volcanic plume. These errors highlight the difficulty in accurately retrieving temperatures through thermal imaging in a single spectral band, due to the complex radiative transfer involved.

The mean lava lake temperature, across the time series from 18:12:20 to 18:44:48 UTC (Fig. 5.9), was ≈ 970 °C, averaged in both space and time. Whilst the uncertainty of

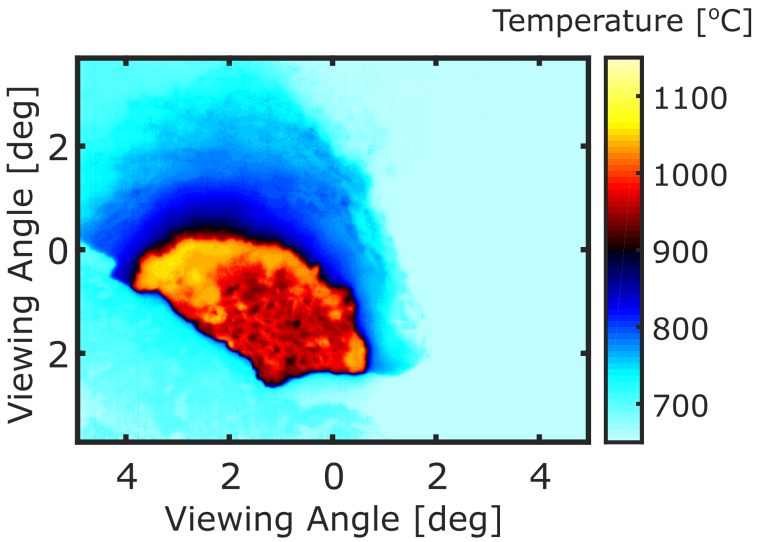

Figure 5.8: A thermal PiCam image of Masaya lava lake taken on 12 June 2017 at 18:12:20 UTC. Here, a maximum temperature of 1059 ± 14 °C was found. Cooling plates on the lake surface are clearly visible, as is the turbulent edge of the lake as it collides with the crater wall. Erroneously high temperature retrievals above the lake are due to reflection/scattering of the lake's radiation, either by the crater wall or aerosols.

a pixel at this temperature is not directly applicable, since this represents an average of many data points, it is useful to note that a pixel of this temperature carries with it an uncertainty of ± 12 °C. Freshly exposed magma, which may have resulted from a bubble burst or collision of the rapidly moving lake with the crater wall, reached a maximum temperature of 1104 ± 14 °C. This value is quite consistent with independent measurements of molten basalt at other lava lakes (Oppenheimer and Yirgu, 2002; Spampinato et al., 2013; Carling et al., 2015; Radebaugh et al., 2016).

The effects of aerosols on temperature retrievals are clearly observable in Figure 5.9 as the sharp decreases in minimum temperature, often with a concomitant decrease in mean temperature. It may, therefore, be possible to implement a minimum temperature threshold, whereby frames with minimum ROI temperatures below this value are discarded or flagged as containing aerosol. Since detailed analysis/interpretation of the lake dynamics is beyond the scope of this research, this procedure was not required here. Beyond this, it is difficult to identify when aerosols are affecting the temperature retrievals. Interrogation of individual image frames or temperature histograms, which are presented later, may provide further insight into the presence of aerosols. Overall, however, it must be assumed that aerosol effects are negligible other than at times highlighted above. Whilst it is possible that MWIR/LWIR thermal imaging systems are less susceptible to aerosol attenuation, such assumptions must also routinely be made with these instruments. Indeed, without more detailed information about conditions along an instrument's viewing path, general assumptions about aerosols are unavoidable.

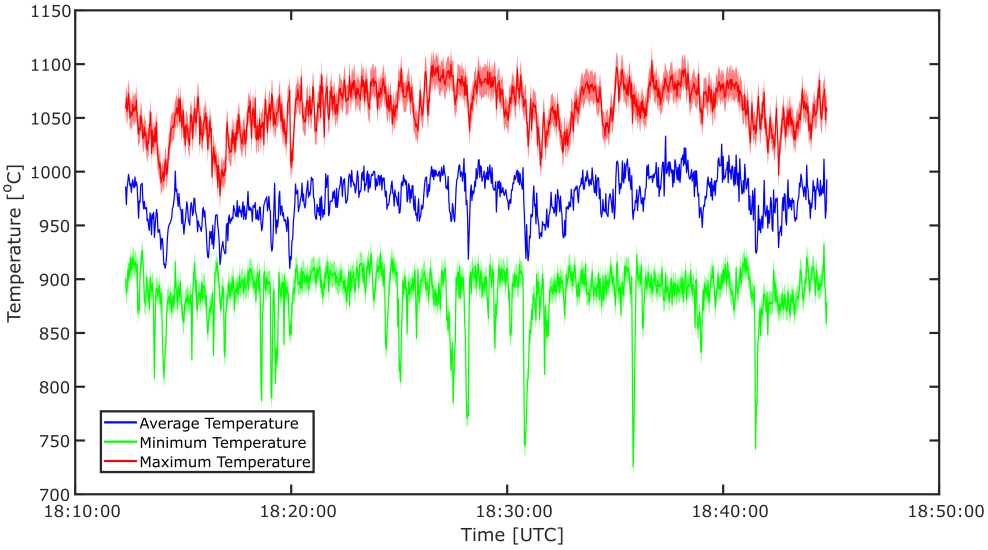

Figure 5.9: Maximum, minimum and mean lava lake temperatures for 18:12:20 to 18:44:48 UTC on 12 June 2017. Temperatures are calculated from the defined lava lake region of interest. The associated temperature uncertainties are displayed as shaded regions for the maximum and minimum datasets.

The radiative power output of a lava lake is a useful quantity for comparison both with other lava lakes and with perhaps more tangible anthropogenic systems such as power stations. The radiative power output, Q (Watts), was calculated with:

$$Q = \varepsilon\sigma \sum_{i=0}^{n} A_i T_i^4 \tag{5.16}$$

where the area, A_i, of the i^{th} pixel was determined with the estimated viewing geometry and the camera field of view; the total lake area was estimated to be 280 m^2. T_i is then the temperature (K) of the i^{th} pixel, σ is the Stefan-Boltzmann constant (5.67×10^{-8} W m^{-2} K^{-4}) and ε is the emissivity.

The average radiative power output of Masaya lava lake was estimated to be 37 MW (Fig. 5.10). This value is approximately 1-10 % of common power station outputs. Aiuppa et al. (2018) collected MODIS measurements made of Masaya between May 2016 and March 2017, finding an average radiant flux of 60.8 MW with the Middle Infrared Observation of Volcanic Activity (MIROVA) evaluation. Measurements here were made 3 months after their last measurements, therefore changes in activity could account for the slight disparity in values; however, the radiant fluxes are within the same order of magnitude, which somewhat corroborates the measurements presented herein. Furthermore, since it is estimated that ≈25-50 % of the lava lake was not visible with the thermal PiCam viewing geometry, these two values may be remarkably similar. Since the MODIS retrievals have very poor spatial resolution relative to a ground-based camera, it

is also possible that their measurements carry quite large uncertainties, as the lava lake would cover less than one pixel in a MODIS scene. Direct comparison should therefore be performed with due caution.

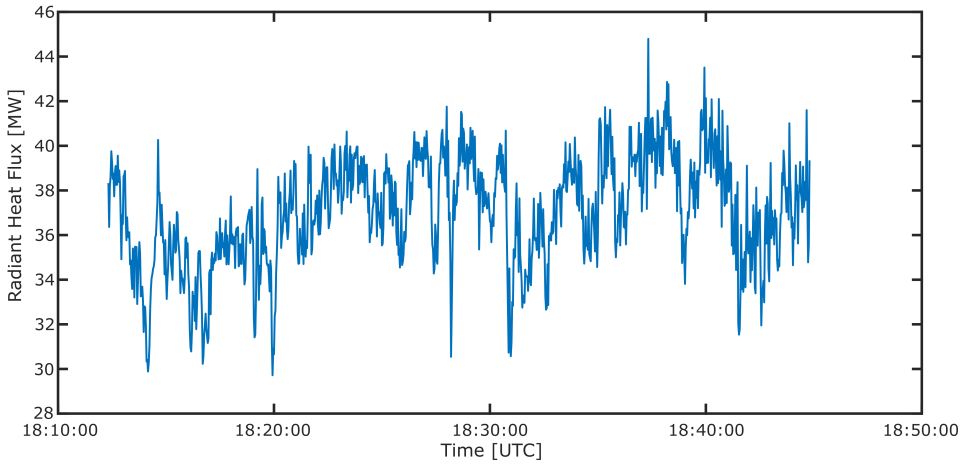

Figure 5.10: Radiant power output from Masaya lava lake between 18:12:20 and 18:44:48 UTC on 12 June 2017. Values are relatively stable, ranging from 30 to 45 MW.

The results presented here are also comparable to radiant fluxes from a number of other lava lakes measured previously with both ground-based and satellite instruments (Table 5.3). From measurements presented here, on 12 June 2017 Masaya had a particularly similar radiative power output to Erebus and Erta 'Ale; however, the lakes were characteristically quite different. This similarity resulted from Masaya's markedly higher temperatures, but much smaller surface area. The radiant fluxes were significantly lower than at Nyiragongo, which has an extremely large radiating surface, often many 10,000 m^2, whilst the visible portion of Masaya's lava lake was just $\approx$ 280 m^2 (the total area may have been $\approx$ 500 m^2).

It must be acknowledged that there was a considerable uncertainty in the lava lake area at Masaya, since the viewing geometry that was used to calculate the lake size was a rough estimate provided by INETER. To calculate the lake area more accurately, the path length from the instrument to the lake would need to be more accurately determined; this could be retrieved by using LiDAR, for example. As a result, the radiant flux accuracy would be commensurate with the improved lake area estimate. It should further be noted that, as previously highlighted, a portion of the lake was obscured from the thermal PiCam by crater walls. It is therefore likely that the lake area was larger than estimated here and, likewise, the radiant flux presented here is likely an underestimation of the total. Furthermore, as a result of the turbulent nature of the lake and frequent bubble bursts, it is likely that the lake had a larger surface area than that estimated from a flat surface assumption; again, this would result in a greater radiant flux than that estimated here.

Table 5.3: Assimilation of lava lake radiant powers from a number of studies. Instruments where the lava lake is sub-pixel scale are omitted form this summary, such that only spatially resolved measurements are included.

Volcano Year	**Instrument**	**Area (m^2)**	**Radiant Power (MW)**	**Reference**
Masaya				
2017	GB NIR Camera	280	30-45	This work
Erebus				
1985	Landsat TM	180	12-18	Harris et al. (1999)
1985	Landsat TM	300	8-15	Harris et al. (1999)
2004 (Ray Lake)	GB MWIR Camera	1400	20-40	Calkins et al. (2008)
2004 (Werner Lake)	GB MWIR Camera	1000-1200	20	Calkins et al. (2008)
2004 (Total)	GB MWIR Camera	2400-2600	40-60	Calkins et al. (2008)
Erta 'Ale				
1973	Landsat TM	3800	3546	Le Guern et al. (1979) and Harris et al. (1999)
1986	Landsat TM	2960	11-22	Harris et al. (1999)
2001	GB MWIR Camera	6200	70-150	Oppenheimer and Yirgu (2002)
2003	GB MWIR Camera	910	5-30	Oppenheimer et al. (2004)
2006	GB LWIR Camera	2500	45-76	Spampinato et al. (2008)
Kīlauea				
1991 (Pu'u 'O'o)	Landsat TM	4000	322-327	Harris et al., 1999
2009 (Halema'uma'u)	ARTEMIS	Not quoted	15-24	Cipar et al. (2012)
Nyiragongo				
1959	Landsat TM	Unclear	540	Le Guern (1987) and Harris et al. (1999)
1972	Landsat TM	45,200	1220	Le Guern (1987) and Harris et al. (1999)
1987	Landsat TM	25	0.1-0.3	Harris et al. (1999)
2012	GB LWIR Camera	31,400	600-1200	Spampinato et al., 2013

GB - Ground-based
TM - Thematic Mapper

Variation of the lava lake's thermal distribution through time was assessed by plotting a histogram time series, similar to the RadTherm plots of Coppola et al. (2007); this is displayed in Figure 5.11. Here, histograms have been assimilated such that the frequency of pixels in each temperature bin is displayed on the colour axis, and subsequent frames are therefore stacked along the x-axis. This can be a useful way of interrogating thermal changes through time, and may help to identify significant changes in a volcanic system or images of particular interest.

Figure 5.11B highlights that during periods of high activity the modal temperature shifted to considerably higher temperatures, as the large bubble bursts and/or increased turbulence at the lake edges exposed fresh hot magma. Periods of slightly lower activity showed a bimodal temperature distribution (Fig. 5.11A), where some bubble bursts and/or turbulence punctuated the otherwise steadily cooling surface. Figure 5.11C then shows a relatively stable surface, which was steadily cooling and forming plates. Bubble bursts were ever-present at the lake, therefore giving these stable conditions a slight positive skew as fresh magma was exposed. In periods where aerosols had significant impact on temperature retrievals, the temperature distribution was much less structured,

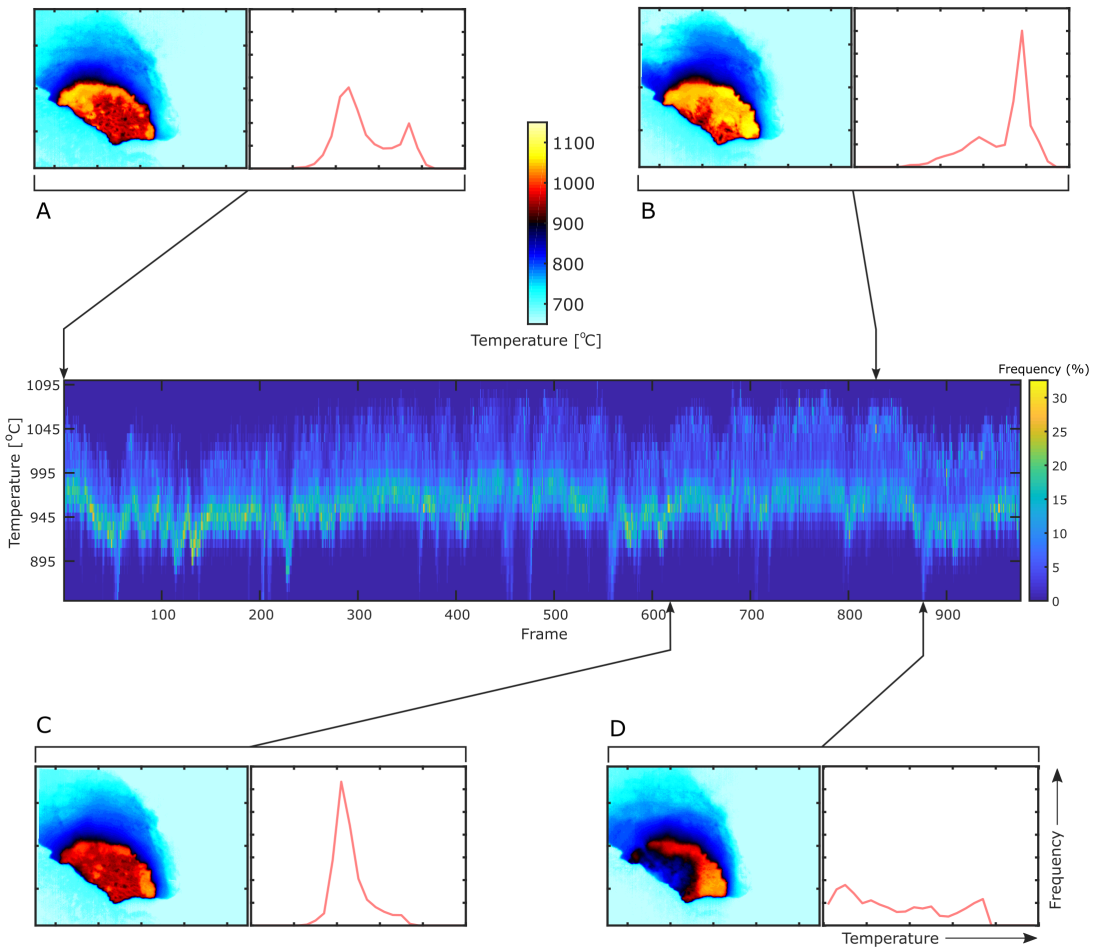

Figure 5.11: A time series of temperature histograms for Masaya lava lake (central pane) between 18:12:20 and 18:44:48 UTC on 12 June 2017. Subplots show example lava lake imagery and associated temperature histograms from a range of characteristic lake states; all subplots are plotted to the same scale, following that of Figure 5.12 for ease of comparison. The central temperature colour scale relates to the lava lake images, whilst the frequency colour scale relates to the histogram time series. (A) Bimodal temperature distribution caused by the exposure of some fresh hot magma at the lake edge as the lake collides with the crater wall; (B) Large bubble bursts and spattering causes extremely high temperatures for a large proportion of the lake; (C) Typical, quasi-normal distribution of lake temperatures caused by steady cooling of the lake crust; the week positive skew is caused by some small bubble bursts; (D) Aerosol extinction causing a large reduction in temperature across much of the lava lake.

and considerably lower temperatures were retrieved (Fig. 5.11D). There are a number of places in the histogram time series where such dips can be found.

Overall, Figure 5.12 shows that the mean distribution of lake temperatures within the observed time period was a weak positive skew, with a modal temperature very similar to that of Figure 5.11C. This suggests that the majority of the time the lake was relatively stable, with the steadily cooling crust disrupted by some bubble bursts and turbulence towards the crater walls. These punctuated the normally distributed crustal temperature with the higher temperature freshly exposed magma.

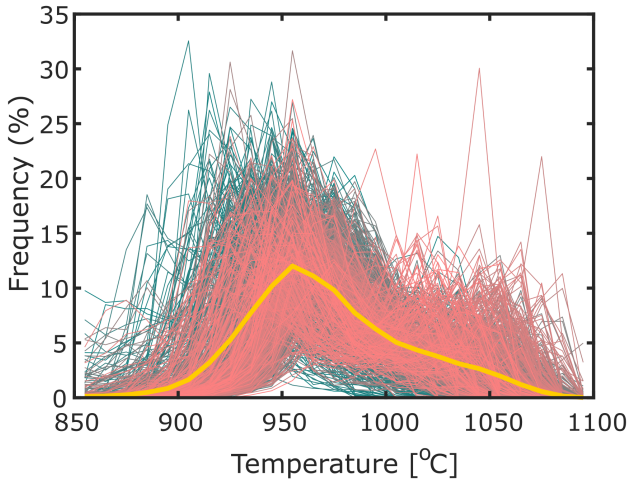

Figure 5.12: A stack of histograms between 18:12:20 and 18:44:48 UTC on 12 June 2017. Histograms are coloured such that more blue lines represent earlier images whilst more red lines represent later frames. The bold yellow line indicates the mean distribution, which is slightly positively skewed.

The positively skewed mean temperature distribution has been previously found at other lava lakes. Specifically, Erta 'Ale (Oppenheimer and Francis, 1997; Oppenheimer and Yirgu, 2002; Spampinato et al., 2008), Mt Erebus (Calkins et al., 2008) and Nyiragongo (Spampinato et al., 2013) have all displayed similar distribution shapes; however, all of these had considerably cooler modal temperatures, typically between 400-600 °C, as opposed to ≈ 950 °C on Masaya. Of the three, Nyiragongo displayed temperatures closest to Masaya, with modal temperatures reaching ≈ 800 °C. The difference in temperatures is likely due to the rapid motion on the surface of the Masaya lava lake, which prevented the formation of a thick cooled crust that covers much of the surfaces of the other lava lakes discussed here.

The Masaya lava lake, however, also displayed a characteristic which has not previously been presented in the albeit relatively limited literature on lava lake thermal properties. During times of high activity at the lake's surface, temperatures rose to extremely high temperatures across most of the lake, with a negatively skewed distribution and a modal temperature in excess of 1000 °C.

Overall, these results suggest that the Masaya lava lake was, at the time of the study, fundamentally quite different to many of the other lava lakes which have been observed and studied on Earth. Whilst each volcanic system is different, and indeed each lava lake differs from all other lava lakes, the Masaya lava lake shows characteristics which differ quite dramatically from any other. The surface was extremely turbulent and fast moving, which prevented the formation of a cooler crust that is common in other lava lakes. Some cooled plates were present and are visible in the Masaya imagery; however, they typically did not cover a large proportion of the lake surface. Pering et al. (2019) studied this lava lake in some detail, including data from the thermal PiCam, suggesting that this lake displayed the highest velocities ever recorded at a lava lake, of 13.7-16.4 m s^{-1}. Therein, they highlight in more detail the curious nature of this lava lake, which appeared to be rapidly convecting at an unprecedented rate.

5.4 Summary

This chapter presented the development of a low-cost, high temperature, thermal camera working in the NIR spectral band. The thermal PiCam was based on a modified R-Pi camera module, as in previous chapters, where the Bayer filter was removed from the silicon detector to produce a uniform sensor with heightened NIR sensitivity. The optical system was based on off-the-shelf optical components and a 3D printed housing, and was shown to perform well, producing high quality imagery. The camera was calibrated using a black body furnace and a Sakuma-Hattori model. Measurements uncertainties were quantified and shown to be quite reasonable at higher temperatures ($< \pm 15$ °C at temperatures >700 °C for a 1 ms shutter speed).

The camera system was deployed to image the active lava lake of Masaya volcano in Nicaragua, which emerged in late 2015. Temperatures of up to 1104 ± 14 °C were retrieved, with a mean lake temperature of ≈ 970 °C. These temperatures are relatively consistent with molten basalt temperatures quoted in the literature, providing some credence to the performance of this camera system. Aerosols were, however, seen to affect the retrievals significantly, and at times they prevented any accurate measurements from being made. In general, the lake displayed a positively skewed mean temperature distribution, associated with a steadily cooling crust which was punctuated with hot freshly exposed molten lava through both bubble bursts and collisions with the crater walls. The rapid motion of the lava lake, combined with frequent bubble bursts, makes it quite a unique system, which differs quite considerably from other studied lava lakes.

This camera system could provide a low-cost alternative to commercial MWIR/LWIR thermal cameras, which can cost 1000s-10000s USD. Importantly, however, due to the spectral band of the thermal PiCam, it is only able to image high temperature targets. Tentatively, it is suggested that objects ≥ 500 °C may be observed with this system;

however, under certain circumstances it may be possible to work at lower temperatures, following the work of Furukawa (2010) who imaged fumaroles at ≈ 300 °C with a silicon NIR detector. Such an instrument could have great use in volcano monitoring and research, as well as in a range of applications outside of volcanology.

Chapter 6

Discussion and Concluding Remarks

6.1 Discussion

This thesis has presented on the development and application of three low-cost remote sensing devices, primarily designed for volcanological applications. These are: an ultraviolet (UV) SO_2 camera (PiCam), a UV spectrometer for differential optical absorption spectroscopy (DOAS) retrievals of SO_2 (PiSpec), and a near-infrared (NIR) imaging system for the accurate retrieval of high temperature sources (thermal PiCam). Tests of each instrument in a volcanic setting have highlighted that they perform well, in some cases comparably to commercial instruments which may be an order of magnitude more expensive. All of the instruments presented herein are based on a modified Raspberry Pi (R-Pi) Camera Module (v1.3), which houses an Omnivision OV5647 sensor. This sensor was primarily designed for the smartphone market, benefiting from high consumer demand driving costs of its production down; the R-Pi camera module therefore retailed for just $\approx$ 20 USD.

Chapter 3 first details the modification of the R-Pi camera module, specifically by the removal of the OV5647 sensor's Bayer filter. The filter is utilised in visible imagery as the means of forming RGB composite images; however, it attenuates UV radiation, lowering the quantum efficiency of the sensor at these wavelengths, as well as creating a mosaicked non-uniform response that is undesirable here. Following this modification, the chapter presents the rebuilding of the camera's optical system for UV applications, using an off-the-shelf fused silica lens and 3D printed lens holder. Finally, the chapter presents tests of the camera system, most notably in a side-by-side comparison with a commercial UV camera unit (JAI) on Mount Etna. These tests found that the PiCam performed quite similarly to the JAI system, with SO_2 emission rate retrievals from the two units showing a strong linear relationship ($r^2 = 0.92$). The JAI system (or equivalent

models) is routinely deployed for such retrievals in volcanology (e.g., Kern et al., 2015b; D'Aleo et al., 2016), therefore suggesting that the PiCam could provide a reasonable low-cost alternative.

Chapter 4 utilises the modified R-Pi camera module presented in Chapter 3 for a second application in UV instrumentation. This work utilised the sensor as the detector within a UV spectrometer (the PiSpec), designed for DOAS retrievals of SO_2. The chapter steps through the design and manufacture of the spectrometer and subsequent rigorous testing of the instrument. The instrument was based on off-the-shelf optical components and a 3D-printed housing, making it possible for researchers to replicate the design, or quite simply modify it for alternative applications. In the setup presented here, the PiSpec had a spectral range and resolution of $\approx 280 - 340$ nm and ≈ 1 nm, respectively. Tests of the instrument alongside a USB2000 (Ocean Optics Inc.) spectrometer, retrieving SO_2 column densities from gas-filled quartz cells, found that whilst the USB2000 did outperform the PiSpec (lower standard deviation of retrieval values), the PiSpec generally made quite similar retrievals. Furthermore, emission rates measurements performed on Masaya volcano (June 2017) were comparable to measurements made by others (Aiuppa et al., 2018; Stix et al., 2018) during a similar stage of its activity (early 2017).

Chapter 5 again utilised the modified R-Pi camera module presented in Chapter 3, here working at the upper limit of the detector's spectral sensitivity, in the NIR. The work presents on the development of a thermal imaging system capable of retrieving accurate temperatures of high-temperature objects. This work built on earlier studies that have utilised NIR imaging systems for temperature retrievals in volcanology (Saito et al., 2005; Furukawa, 2010; Radebaugh et al., 2016). Most pertinently, Radebaugh et al. (2016) also used the R-Pi camera module for their novel thermal imaging system. Their photometric calibration scheme, however, was potentially quite inaccurate; therefore, the work presented in this chapter introduced a number of improvements to temperature retrievals using a NIR detector. In particular, this thermal PiCam was calibrated using a black body furnace and a Sakuma-Hattori model (e.g., Saunders and White, 2003). The chapter also presents a detailed consideration of measurement uncertainties, which can often be somewhat neglected in volcano science literature.

Overall, this body of work has presented three novel low-cost instruments which could have utility in volcano science and monitoring, as well as potentially more broadly. The low-cost nature of these instruments could promote widespread proliferation of monitoring and research instrumentation across the globe. This is particularly pertinent since a large number of the world's active volcanoes are located in developing countries, where funding for monitoring and research is more limited. Indeed, Aspinall et al. (2011) studied 441 active volcanoes in 16 developing countries, finding that 384 had little or no monitoring; of those, 65 were defined as posing high risk to large populations (summarised by Sparks et al., 2012). Perhaps another important aspect of this work is to highlight the relative ease with which scientists could develop their own instrumentation,

primarily due to the current costs and capabilities of consumer electronics; indeed, this is already being done elsewhere in volcanology (e.g., Tortini et al., 2014; Moure et al., 2015).

6.2 Future Work

6.2.1 Testing the v2 Raspberry Pi camera module

It is unfortunate that the Omnivision OV5647 chip is no longer in production, and as a result the R-Pi Camera Module v1.3 has limited availability while stocks last. The v2.1 sensor was released in 2016, housing an 8-megapixel (2464 × 3280) Sony IMX219 back-illuminated CMOS detector. In principle, this sensor should provide an improvement to the older technology in the OV5647. However, removal of the Bayer filter on this sensor, via the method present in Chapter 3, has proven difficult, therefore posing a considerable barrier to the camera's use as a UV/NIR camera. Scratching tests show that the sensor has the potential to produce UV images, and that the Bayer filter removal still results in significantly enhanced UV sensitivity (Fig. 6.1).

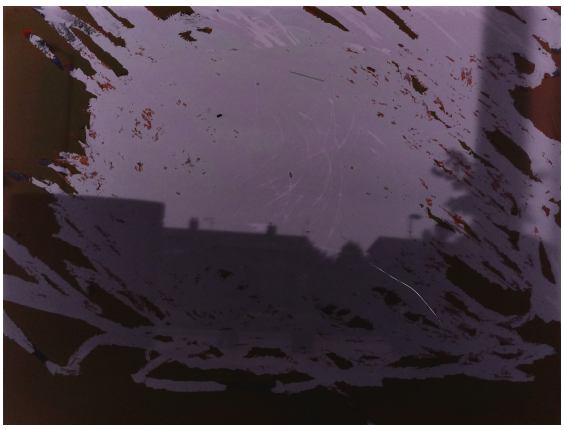

Figure 6.1: Image of buildings and clear sky taken with the Raspberry Pi Camera Module v2.1, through a 310 nm bandpass filter (10 nm FWHM). The Sony IMX219 sensor has been scratched to remove the Bayer filter in the centre of the image. A clear improvement in UV sensitivity can be seen in this region.

Recently, tests of Bayer filter removal with hydrofluoric acid (HF) have been performed, showing promising results. HF is extremely aggressive and hazardous, therefore it is important that care is taken both for the user's safety and in order to avoid breaking the camera module. The HF indeed can remove the Sony sensor's Bayer filter if dropped onto the sensor for approximately 5 seconds. Subsequently, the sensor is washed with isopropyl alcohol and then rubbed with a cotton bud to remove the filter. The sensor is then cleaned again in isopropyl alcohol.

Tests of this methodology have found that a working camera module can be produced,

with heightened UV/NIR sensitivity due to removal of the Bayer filter. However, producing a perfectly clean sensor is somewhat difficult, perhaps due to the HF attacking the sensor in a non-uniform manner. With further refinement of the methodology, however, it should be possible to perfect this etching process such that the resulting sensor quality is on par with that of the debayered Omnivision OV5647 chip.

It should now follow that rigorous testing of a modified v2.1 camera module should be performed, investigating its use for both UV and NIR applications. Recently, Pagnutti et al. (2017) have performed a detailed study of this camera's performance, focussing solely on visible imaging with the unmodified camera module. They found that the small number of cameras they tested displayed consistent, repeatable results during radiometric characterisation. This is a promising starting point upon which tests of the debayered sensor could build.

6.2.2 PiCam

Whilst the instruments developed during this thesis have been shown to perform quite well, as with any emerging technology there is still room for improvements to the designs. The following sections discuss possible next steps for each instrument, in an attempt to identify where future work could be focussed.

To reduce aberrations in the PiCam images, the optical system may be improved. This would likely involve the development of a triplet lens, similar to that employed in Chapter 5, which is designed specifically to reduce spherical aberrations present in simple optics. This addition to the PiCam would, however, almost certainly increase the overall cost of the system, since multiple lenses would be required for each camera. The price-rise is likely to only be a few hundred USD, and it may be decided that the improvement in PiCam performance, especially towards the edges of the image, would be worthwhile.

Similar to the improved lens system, the bandpass filters could be improved by spending a little more money. The 310 nm Edmund Optics filter has quite a low peak transmission of 17 %. Asahi Spectra USA Inc. provide a 310 nm filter with a much greater peak transmission of 67 %, which would cause a marked increase in light throughput. Since the PiCam has a relatively modest UV sensitivity, due to the non-specialist design of the sensor, increasing light throughput would be extremely beneficial. This would allow much shorter shutter speeds to be used in image acquisition, which can sometimes currently reach $\approx$ 1 second for the 310 nm filter. Such long exposures lead to blurring, and therefore can cause errors in the final measurements, as the 310 nm and 330 nm images don't perfectly match; furthermore, the long exposures reduce the maximum achievable frame rate of the system. Changing filters does, however, come at a cost, with Edmund Optics and Asahi filter prices of $135 and $280, respectively; this is largely due to the Asahi filters having a 25 mm diameter, whilst Edmund Optics provide a 12.5 mm filter

option. With the primary advantage of the PiCam being its low price-point, whether the anticipated increased in performance with the Asahi filter outweighs the extra cost would need to be considered. Due to the higher peak transmission of the Edmund Optics 330 nm filter (39 %), along with larger 330 nm diffuse sky signal and sensor quantum efficiency relative to at 310 nm, the above issue is more pronounced with the 310 nm camera. This adaptation would therefore only be necessary for the one filter, thus minimising the increase in costs.

6.2.3 PiSpec

To date, only one PiSpec has been built. As was discussed in Chapter 4, the repeatability of this instrument should therefore be tested, since its performance relies quite heavily on the quality of the 3D printing procedure. The selective laser sintering process is quoted to have an accuracy of approximately ± 0.2 mm (https://3dprintdirect.co.uk/). Prints may, however, contract after printing, which would affect the design of the instrument if this is significant.

Tests of the PiSpec highlighted that there may be some significant motion of parts afforded by the current design when under certain stresses (see Section 4.2.4). This should be prevented in order to ensure that the PiSpec can perform well under a range of conditions. Further consideration could be given to the mounting of optical components, including the detector, which may improve the robustness of this instrument.

6.2.4 Thermal PiCam

One of the most significant issues with temperature retrievals from the thermal PiCam is the effect of H_2O absorption along the light path (see Section 5.2.4). To mitigate this issue, a notch filter could be used to remove the significant absorption cross-section centred at ≈ 950 nm (see Fig. 5.4). By blocking the camera's response to these wavelengths H_2O effects will be minimised, such that the need for a transmissivity correction may be removed. Of course, this will lower the camera's sensitivity in general, meaning that longer shutter speeds would be needed. Furthermore, this will not reduce sensitivity to aerosol scattering, since this is a broadband effect.

It may be interesting to test a number of thermal PiCam units, or just the sensors themselves, to determine how standardised their responses are. If it is possible to form a generic calibration, or simplify the calibration procedure, such that cameras could be widely disseminated without the need for individual calibrations, this would be extremely beneficial for the speed and ease of distribution. As highlighted in Section 6.2.2, Pagnutti et al. (2017) have shown that the Sony IMX219 housed within the v2.1 R-Pi camera module is quite repeatable across units, therefore that instrument would be extremely suitable for this dissemination process. From their work, it may not be unreasonable to

suggest that the Omnivision OV5647 sensor could also have such repeatability; however, tests to confirm this would be needed.

6.3 Extended applications

As with the majority of instruments found in volcanology today, the instruments developed and presented in this thesis could have numerous applications outside of volcanology. Here, a few such applications are briefly presented, along with some preliminary experiments.

6.3.1 UV camera images for assessing human exposure to sunlight

Human skin exposure to UV radiation can have both positive and negative effects on health. It is broadly accepted that a lack of exposure to sunlight is a principle cause of vitamin D deficiency in a large number of humans (Kimlin et al., 2003; Holick and Chen, 2008). This deficiency has been associated with a number of issues, such as increased cancer risk, hypertension and autoimmune diseases (Holick and Chen, 2008). Conversely, over exposure to UV radiation is well known to cause sun burn, and ultimately can increase the risk of developing non-melanoma skin cancer (Urbach, 1997).

UV imagery has previously been used to enhance visualisation of sun damage on human skin (Fulton, 1997b). The low-cost PiCam provides a new quite accessible instrument for such measurements, or associated studies. During a field campaign on Hawai'i's Main Island (19^{th} July to 2^{nd} August), where a broad UV survey was conducted, the UV PiCam was used to augment an investigation into UV exposure of the head/face throughout the day. UV sensors were placed on a mannequin head, on the cheek, eyes, ears and forehead. Whilst these sensors were used to provide a quantitative assessment of UV intensity (in terms of UV index) incident on the face, here the UV images were used as a more qualitative and visual representation of the scene; although quantitative studies would be possible with such equipment. Figure 6.2 shows example imagery of the mannequin head taken on Kailua Beach, captured with a 300 nm (40 nm FWHM) filter placed to the fore of the lens. The images highlight the most vulnerable parts of the head to the sun, in particular the forehead and nose. Furthermore, two of the images identify the high reflectivity of white ocean surf, which is a particularly important phenomenon for surfers and swimmers. As previously stated, this work was part of a larger project which is detailed by Mims et al. (2019).

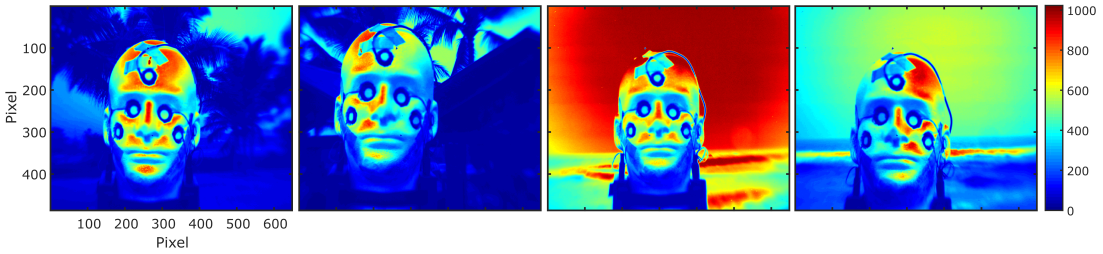

Figure 6.2: UV images (300 nm filter; 40 nm FWHM) of a mannequin head taken in Hawai'i on 23 July 2018. From left to right the camera viewing direction is East (at 14:28:28 HST), North (at 14:33:40 HST), West (at 14:41:46 HST), South (at 14:48:32 HST); in each image the head is then facing towards the opposite cardinal direction. At this mid-afternoon time, the sun was at a zenith angle of $\approx 25°$and approximately to the west.

6.3.2 Hyperspectral Imaging with the PiSpec

As was briefly discussed in Chapter 4, the use of a 2-dimensional imaging sensor inside the PiSpec means that it is in fact possible to retrieve spatial as well as spectral information from each acquisition, as long as the correct fore-optics are chosen; of course, if an optical fibre is used to transmit light to the PiSpec entrance slit any spatial information will be lost. Figure 6.3 shows the principles of using the PiSpec to retrieve spatial information along the height of the sensor.

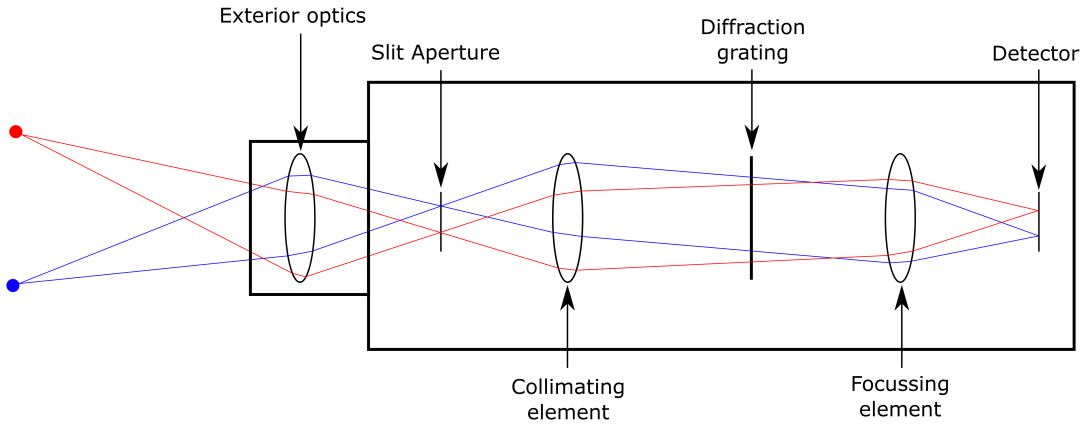

Figure 6.3: A drawing of the imaging optical plane in the PiSpec. The optics have been unfolded and here are represented as lenses for clarity; however, the same principle applies to the mirrors within the PiSpec. Light is focussed onto the entrance slit, then collimated; the focussing element then refocusses the light onto the detector. The colours represent rays originating from different field heights. The diffraction grating causes dispersion in the direction perpendicular to the plane of this drawing, theoretically having no effect on the optical system in the plane displayed here. Note, the rays are simply for visualisation of the general theory and are not drawn with any true ray tracing accuracy.

If the PiSpec is then made to scan across the second dimension, a 2-dimensional hyper-

spectral image can be iteratively built up. This method was employed by Bobrowski et al. (2006), who used an Imaging-DOAS (IDOAS) system to retrieve 2D images of SO_2 distributions on Mt. Etna, Italy.

Preliminary tests of the PiSpec, simply looking through slats on a park bench, indicate that the spectral images do contain spatial information along the rows of each image (Fig. 6.4). Dark regions can be seen where the bench blocks the Fraunhofer spectrum of diffuse sky radiation. Using the slats and trigonometry, the field of view with this lens in place was estimated to be $\approx 3°$. More recently, a shorter focal length lens has been used, to increase the field of view to $\approx 15°$.

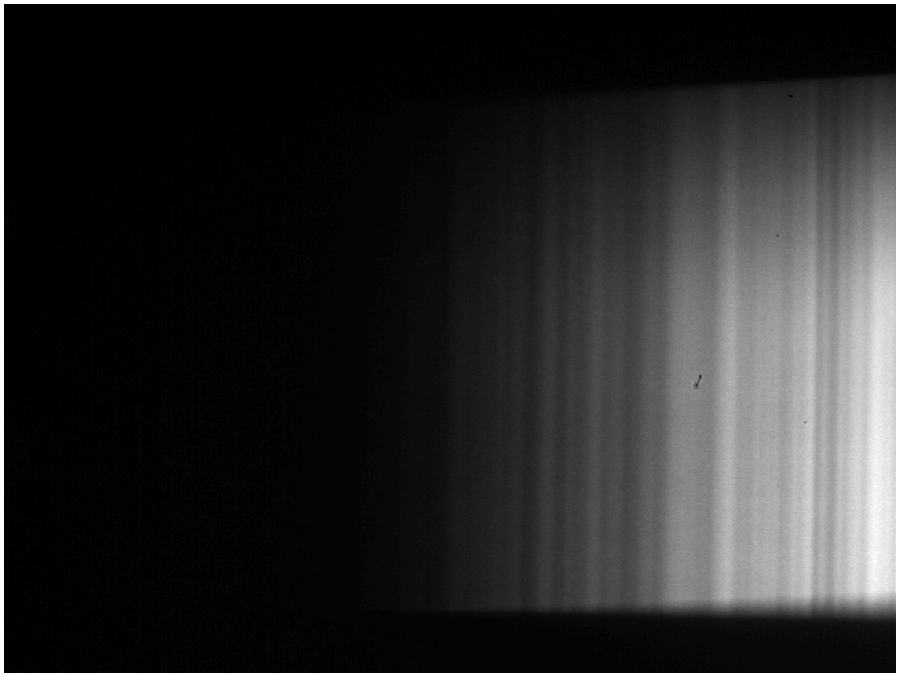

Figure 6.4: A hyperspectral line acquired looking at the sky through bench slats. The dark regions at the top and bottom of the spectral image show the slat locations, whilst the central portion displays the Fraunhofer lines of diffuse sky radiation.

This proof of concept image has highlighted some issues with the instrument, however. Firstly, the onset of the darker section does not track horizontally across the image. This is likely a result of non-orthogonal alignment of optical components (including the sensor) in the PiSpec; however, a further complication can be seen since the lines from two slats do not run parallel to each other. This suggests a more complex optical issue is also affecting the spectra, which would need to be well characterised before good hyperspectral images could be generated. Furthermore, the spectral dispersion does appear to be approximately horizontal, as evidenced by the quite vertical orientation of Fraunhofer lines. This indicates that there are some quite considerable complexities to this instrument, since the spatial and spectral dimensions are non-orthogonal.

Tests of the PiSpec's utility as an IDOAS instrument have been performed on Stromboli,

Hawai'i and Cotopaxi (Ecuador); however, at present no successful IDOAS images have been made. This is likely to be a combination of both poor measuring conditions in many cases, and issues with the instruments functionality in this application.

6.3.3 Ozone measurements with the PiSpec

Atmospheric ozone measurements have been made for many decades, typically involving a Langley calibration method (e.g., Komhyr et al., 1989; Morys et al., 2001; Staehelin et al., 2018). This is based on the principle of measuring the sun's spectral irradiance through the day, at different zenith angles, therefore making measurements for different light path lengths through an absorbing medium; in this case, the path length through the ozone layer in the stratosphere is the important variable. The Beer-Lambert law (Equation 2.1) can then be used to determine an ozone vertical column density from the measurements.

PiSpec tests were performed on the island of Hawai'i on the 25 June 2018 at Royal Kona Resort. Between approximately 13:45 and 16:30 local time, the PiSpec was used to acquire spectral images of direct sunlight, capturing several images every $\approx$ 10 minutes. The shutter speed was set during the first acquisitions at 13:45 such that $\approx$ 80 % image saturation was achieved at $\approx$ 320 nm, with signal then diminishing towards shorter wavelengths. As a result, longer wavelengths were saturated, but they were not required for this work. The entire sequence of acquisitions was performed with this shutter speed, to ensure integrity of results, although it has previously been shown that the sensor responds linearly to changing shutter speeds (Sections 3.2.4 and 5.2.2). This meant that with increasing air mass (later afternoon) the signal was much lower; if the experiment had continued later into the evening the shutter speed would have been changed, to ensure the signal-to-noise ratio remained at a tolerable level.

Throughout the experiment, the sun was tracked manually, with the aid of a long thin stick mounted to the PiSpec, which allowed rough alignment of the instrument to the sun by minimising the shadow of the stick. Since the PiSpec's sensor response may be non-uniform, care was taken to attempt to align each spectral image such that the direct sun spectra were all located on similar rows of the image array throughout the tests. An example direct sunlight spectral image is displayed in Figure 6.5.

Ozone retrievals were performed by extracting the signal at a specific wavelength from all spectra. This wavelength was located in a region where O_3 has a significant absorption cross-section (313.5 nm). According to the Beer-Lambert law, this signal should decrease proportionally to the exponent of the path length through the atmosphere. By plotting the natural logarithm of the signal against the air mass at that time, the Langley plot should therefore show a linear trend (Komhyr et al., 1989; Morys et al., 2001). By extrapolating to an air mass of zero, the extraterrestrial constant L_0 can be determined,

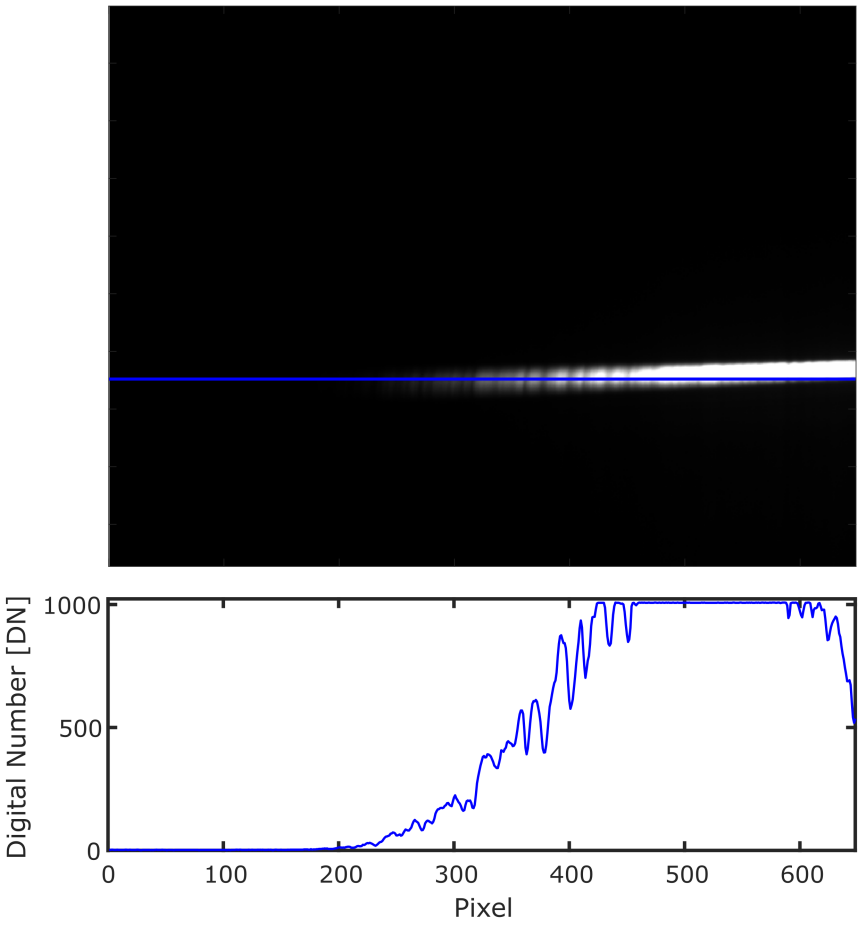

Figure 6.5: A PiSpec spectral image of direct sunlight. The sun covers approximately 20 rows of the image, highlighting again the hyperspectral imaging capabilities of the PiSpec instrument. An associated spectrum extracted from a single row of the image is also shown, with the blue line indicating where this spectrum was extracted from in the image. Slight non-orthogonal alignment of components in the instrument is apparent through the non-orthogonal distribution of spectra across the image.

which is used in quantifying total column ozone. Whilst such a plot showed some promise with the PiSpec (Fig. 6.6), with a coefficient of determination (r^2) of 0.990, hazy and somewhat changeable conditions meant that accurate ozone retrievals were not possible in this instance. Furthermore, typically it is beneficial to span as large an airmass range as possible. Here an air mass of 1.76 was reached; extending the measurements beyond 2 would make the Langley retrieval more robust. Future work with the PiSpec for this application could therefore prove more fruitful.

6.4 Concluding Remarks

This thesis has presented the development of a number of low-cost remote sensing instruments, all of which could have a variety of applications; here, they were primarily

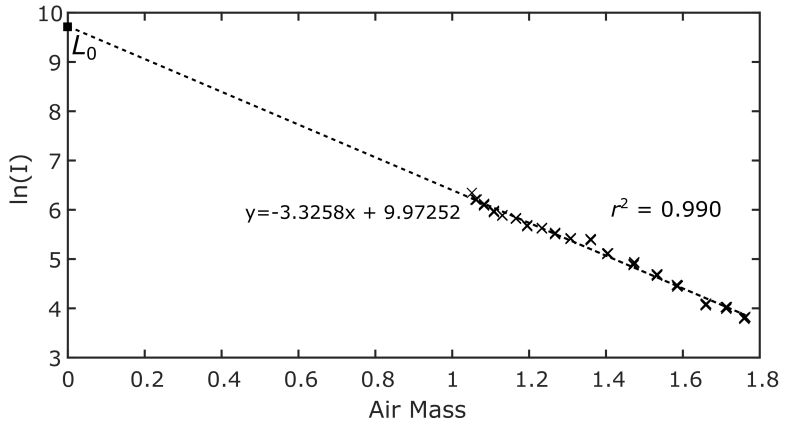

Figure 6.6: A Langley plot generated from PiSpec data at 313.5 nm, showing relative linearity between the natural logarithm of signal (I) and air mass. An r^2 value of 0.990 shows promise, although hazy conditions prevented accurate ozone determination in this case. L_0 represents the extraterrestrial constant, here estimated to be 9.97.

designed and deployed for application in volcanology.

Specifically, I have outlined the design and testing of: the PiCam, an ultraviolet (UV) imaging camera; the PiSpec, a UV spectrometer; a near-infrared (NIR) thermal imaging PiCam, for imaging high temperature sources. All were based on the Raspberry Pi camera module (v1.3), which houses an Omnivision OV5647 sensor. This sensor was modified by the removal of its Bayer filter, a layer which both attenuates light, particularly light outside of the visible waveband, and causes a non-uniform mosaic response from the sensor.

On discrete field campaigns, each of these instruments has been shown to perform quite reasonably for their respective retrievals. In the case of the UV PiCam and PiSpec, instrument tests alongside commercial alternatives found that their performances were generally quite comparable to their commercial counterparts; this gives credence to promoting their use in volcanology. In all cases, future work on both hardware and software could further improve the instruments and their utility to volcanologists. Beyond this, a number of applications outside of volcanology have also been suggested for these instruments (in this chapter), with further exploration of such avenues also suggested as future work.

Supplementary Material

Supplementary material is available online at https://doi.org/10.15131/shef.data.5164795.v3, *hosted by the University of Sheffield Online Research Data (ORDA) repository.*

Video S1: A video of PiCam SO_2 retrievals performed at Drax power station smokestack on 15 August 2016. The camera frame rate was 0.25 Hz.

Video S2: A video of JAI SO_2 retrievals performed on Mt. Etna on 19 July 2016, imaging Etna's North East Crater plume. Images have been sub-sampled to achieve a frame rate of 0.25 Hz, in concordance with the PiCam acquisitions.

Video S3: A video of PiCam SO_2 retrievals performed on Mt. Etna on 19 July 2016, imaging Etna's North East Crater plume. The camera frame rate was 0.25 Hz.

Video S4: A video of Masaya lava lake temperatures captured with the PiCam thermal imager on 12 June 2017. The camera frame rate was 0.5 Hz.

Video S5: A stabilised version of Video S4. The video was stabilised using the Lukas-Kanade method discussed in Section 5.3.1. Whilst small-scale shake is still present, if not enhanced, in this video, larger frame shifts have been minimised by this stabilisation.

Video S6: A video of the lava lake mask produced by thresholding temperatures from Video S4. Maroon pixels are identified as the lava lake, exhibiting a temperature of ≥ 850 °C.

Bibliography

Aiuppa, A. et al. (2007) Forecasting Etna eruptions by real-time observation of volcanic gas composition. *Geology* **35**(12), 1115–1118. DOI: 10.1130/G24149A.1.

Aiuppa, A. et al. (2008) Total volatile flux from Mount Etna. *Geophysical Research Letters* **35**(24), L24302. DOI: 10.1029/2008GL035871.

Aiuppa, A. et al. (2009) The 2007 eruption of Stromboli volcano: Insights from real-time measurement of the volcanic gas plume CO2/SO2 ratio. *Journal of Volcanology and Geothermal Research* **182**(3-4), 221–230. DOI: 10.1016/j.jvolgeores.2008.09.013.

Aiuppa, A. et al. (2010) Unusually large magmatic CO2 gas emissions prior to a basaltic paroxysm. *Geophysical Research Letters* **37**(17), L17303. DOI: 10.1029/2010GL043837.

Aiuppa, A. et al. (2015) New ground-based lidar enables volcanic CO2 flux measurements. *Scientific Reports* **5**, 13614. DOI: 10.1038/srep13614.

Aiuppa, A. et al. (2018) Tracking Formation of a Lava Lake From Ground and Space: Masaya Volcano (Nicaragua), 2014-2017. *Geochemistry, Geophysics, Geosystems* **19**(2), 496–515. DOI: 10.1002/2017GC007227.

Allard, P., Burton, M., and Muré, F. (2005) Spectroscopic evidence for a lava fountain driven by previously accumulated magmatic gas. *Nature* **433**, 407–410. DOI: 10.1038/nature03246.

Ambrosino, F. et al. (2014) The MU-RAY project: Detector technology and first data from Mt. Vesuvius. *Journal of Instrumentation* **9**(2). DOI: 10.1088/1748-0221/9/02/C02029.

Aspinall, W. P. et al. (2011) Volcano Hazard and Exposure in GFDRR Priority Countries and Risk Mitigation Measures. *NGI report* **20100806**.

Baker, S. and Matthews, I. (2004) Lucas-Kanade 20 years on: A unifying framework. *International Journal of Computer Vision* **56**(3), 221–255. DOI: 10.1023/B:VISI.0000011205.11775.fd.

Balagizi, C. M., Kasereka, M. M., Cuoco, E., and Liotta, M. (2017) Rain-plume interactions at Nyiragongo and Nyamulagira volcanoes and associated rainwater hazards, East Africa. *Applied Geochemistry* **81**, 76–89. DOI: 10.1016/j.apgeochem.2017.03.018.

Ball, M. and Pinkerton, H. (2006) Factors affecting the accuracy of thermal imaging cameras in volcanology. *Journal of Geophysical Research: Solid Earth* **111**(11), 1–14. DOI: 10.1029/2005JB003829.

Barnie, T., Bombrun, M., Burton, M. R., Harris, A. J. L., and Sawyer, G. M. (2015) Quantification of gas and solid emissions during Strombolian explosions using simultaneous sulphur dioxide and infrared camera observations. *Journal of Volcanology and Geothermal Research* **300**, 167–174. DOI: 10.1016/j.jvolgeores.2014.10.003.

Birnie, R. W. (1973) Infrared radiation thermometry of guatemalan volcanoes. *Bulletin Volcanologique* **37**(1), 1–36. DOI: 10.1007/BF02596879.

Blackett, M. (2017) An Overview of Infrared Remote Sensing of Volcanic Activity. *Journal of Imaging* **3**(2), 13. DOI: 10.3390/jimaging3020013.

Bluth, G., Shannon, J., Watson, I. M., Prata, A. J., and Realmuto, V. (2007) Development of an ultra-violet digital camera for volcanic SO2 imaging. *Journal of Volcanology and Geothermal Research* **161**(1-2), 47–56. DOI: 10.1016/j.jvolgeores.2006.11.004.

Bobrowski, N., Hönninger, G., Galle, B., and Platt, U. (2003) Detection of bromine monoxide in a volcanic plume. **423**(May), 273–276. DOI: 10.1038/nature01625.

Bobrowski, N., Hönninger, G., Lohberger, F., and Platt, U. (2006) IDOAS: A new monitoring technique to study the 2D distribution of volcanic gas emissions. *Journal of Volcanology and Geothermal Research* **150**(4), 329–338. DOI: 10.1016/j.jvolgeores.2005.05.004.

Bobrowski, N. et al. (2007) Reactive halogen chemistry in volcanic plumes. *Journal of Geophysical Research Atmospheres* **112**(6), 1–17. DOI: 10.1029/2006JD007206.

Bobrowski, N., Kern, C., Platt, U., Hörmann, C., and Wagner, T. (2010) Novel SO2 spectral evaluation scheme using the 360-390 nm wavelength range. *Atmospheric Measurement Techniques* **3**(4), 879–891. DOI: 10.5194/amt-3-879-2010.

Boichu, M., Oppenheimer, C., Tsanev, V., and Kyle, P. R. (2010) High temporal resolution SO2 flux measurements at Erebus volcano, Antarctica. *Journal of Volcanology and Geothermal Research* **190**(3-4), 325–336. DOI: 10.1016/j.jvolgeores.2009.11.020.

Brown, S. K., Jenkins, S. F., Sparks, R. S. J., Odbert, H., and Auker, M. R. (2017) Volcanic fatalities database: analysis of volcanic threat with distance and victim classification. *Journal of Applied Volcanology* **6**(1). DOI: 10.1186/s13617-017-0067-4.

Burton, M., Allard, P., Mure, F., and La Spina, A. (2007) Magmatic Gas Composition Reveals the Source Depth of Slug-Driven Strombolian Explosive Activity. *Science* **317**, 227–230. DOI: 10.1126/science.1141900.

Burton, M. R., Caltabiano, T., Murè, F., Salerno, G. G., and Randazzo, D. (2009) SO2 flux from Stromboli during the 2007 eruption: Results from the FLAME network and traverse measurements. *Journal of Volcanology and Geothermal Research* **182**(3-4), 214–220. DOI: 10.1016/j.jvolgeores.2008.11.025.

Burton, M. R., Prata, F., and Platt, U. (2015) Volcanological applications of SO2 cameras. *Journal of Volcanology and Geothermal Research* **300**, 2–6. DOI: 10.1016/j.jvolgeores.2014.09.008.

Calkins, J. A., Oppenheimer, C., and Kyle, P. R. (2008) Ground-based thermal imaging of lava lakes at Erebus volcano, Antarctica. *Journal of Volcanology and Geothermal Research* **177**(3), 695–704. DOI: 10.1016/j.jvolgeores.2008.02.002.

Calvari, S. et al. (2018) Satellite and Ground Remote Sensing Techniques to Trace the Hidden Growth of a Lava Flow Field: The 2014-2015 Effusive Eruption at Fogo Volcano (Cape Verde). *Remote Sensing* **10**(7), 1115. DOI: 10.3390/rs10071115.

Campion, R., Delgado Granados, H., and Mori, T. (2015) Image-based correction of the light dilution effect for SO2 camera measurements. *Journal of Volcanology and Geothermal Research* **300**, 48–57. DOI: 10.1016/j.jvolgeores.2015.01.004.

Campion, R. et al. (2018) Breathing and Coughing: The Extraordinarily High Degassing of Popocatépetl Volcano Investigated With an SO2 Camera. *Frontiers in Earth Science* **6**(October). DOI: 10.3389/feart.2018.00163.

Carling, G. T. et al. (2015) Temperatures, thermal structure, and behavior of eruptions at Kilauea and Erta Ale volcanoes using a consumer digital camcorder. *GeoResJ* **5**, 47–56. DOI: 10.1016/j.grj.2015.01.001.

Carn, S. A., Fioletov, V. E., McLinden, C. A., Li, C., and Krotkov, N. A. (2017) A decade of global volcanic SO2 emissions measured from space. *Scientific Reports* **7**, 44095. DOI: 10.1038/srep44095.

Chen, Z., Wang, P., and Yu, B. (2008) Research of UV detection System Based on Embedded Computer. *2008 World Automation Congress*.

Chiodini, G. et al. (2015) Evidence of thermal-driven processes triggering the 2005-2014 unrest at campi flegrei caldera. *Earth and Planetary Science Letters* **414**, 58–67. DOI: 10.1016/j.epsl.2015.01.012.

Choubey, B. and Collins, S. (2007) "Fixed pattern noise correction for wide dynamic range linear-logarithmic pixels". In: *2007 50th Midwest Symposium on Circuits and Systems*. IEEE, pp. 1169–1172. DOI: 10.1109/MWSCAS.2007.4488763.

Cipar, J. J., Anderson, G. P., and Cooley, T. W. (2012) Temperature and power output of the lava lake in Halema'uma'u crater, Hawaii, using a space-based hyperspectral imager. *IEEE Journal of Selected Topics in Applied Earth Observations and Remote Sensing* **5**(2), 617–624. DOI: 10.1109/JSTARS.2012.2184086.

Coppola, D., Laiolo, M., and Cigolini, C. (2016) Fifteen years of thermal activity at Vanuatu's volcanoes (2000-2015) revealed by MIROVA. *Journal of Volcanology and Geothermal Research* **322**, 6–19. DOI: 10.1016/j.jvolgeores.2015.11.005.

Coppola, D., Staudacher, T., and Cigolini, C. (2007) Field thermal monitoring during the August 2003 eruption at Piton de la Fournaise (La Réunion). *Journal of Geophysical Research: Solid Earth* **112**(5). DOI: 10.1029/2006JB004659.

Coppola, D. et al. (2017) Shallow system rejuvenation and magma discharge trends at Piton de la Fournaise volcano (La Réunion Island). *Earth and Planetary Science Letters* **463**, 13–24. DOI: 10.1016/j.epsl.2017.01.024.

D'Aleo, R. et al. (2016) Spatially resolved SO 2 flux emissions from Mt Etna. *Geophysical Research Letters* **43**(14), 7511–7519. DOI: 10.1002/2016GL069938.

Darmont, A. (2009) Spectral Response of Silicon Image Sensors. *Aphesa White Paper*, 1–13.

Delle Donne, D. et al. (2016) Gas Mass Derived by Infrasound and UV cameras: implications for Mass Flow Rate. *Journal of Volcanology and Geothermal Research* **325**, 169–178. DOI: 10.1016/j.jvolgeores.2016.06.015.

Delle Donne, D. et al. (2017) Exploring the explosive-effusive transition using permanent ultraviolet cameras. *Journal of Geophysical Research: Solid Earth* **122**(6), 4377–4394. DOI: 10.1002/2017JB014027.

Delle Donne, D. and Ripepe, M. (2012) High-frame rate thermal imagery of Strombolian explosions: Implications for explosive and infrasonic source dynamics. *Journal of Geophysical Research: Solid Earth* **117**(B9), n/a–n/a. DOI: 10.1029/2011JB008987.

Delmelle, P., Stix, J., Baxter, P., Garcia-Alvarez, J., and Barquero, J. (2002) Atmospheric dispersion, environmental effects and potential health hazard associated with the low-altitude gas plume of Masaya volcano, Nicaragua. *Bulletin of Volcanology* **64**(6), 423–434. DOI: 10.1007/s00445-002-0221-6.

Dinger, F. et al. (2018) Periodicity in the BrO SO2molar ratios in the volcanic gas plume of Cotopaxi and its correlation with the Earth tides during the eruption in 2015. *Solid Earth* **9**(2), 247–266. DOI: 10.5194/se-9-247-2018.

Dixon, J. (1988) Radiation thermometry. *Journal of Physics E: Scientific Instruments* **21**(5), 425–436. DOI: 10.1088/0022-3735/21/5/001.

Doocy, S., Dick, A., Daniels, A., and Kirsch, T. D. (2013) The Human Impact of Volcanoes: a Historical Review of Events 1900-2009 and Systematic Literature Review. *PLOS current disasters*, 1–34. DOI: 10.1371/currents.dis.2664354a5571512063ed29d25ffbce74.Abstract.

Drax (2013) *Annual review of Environmental Performance*. Available online at:http://www.pfpi.net/wp-content/uploads/2016/12/Environmental-Performance-Review-2013.pdf (Accessed on 29-08-2018).

Du, H. and Voss, K. J. (2004) Effects of Point-Spread Function on Calibration and Radiometric Accuracy of CCD Camera. *Applied Optics* **43**(3), 665. DOI: 10.1364/AO.43.000665.

Edmonds, M. (2008) New geochemical insights into volcanic degassing. *Philosophical Transactions of the Royal Society A: Mathematical, Physical and Engineering Sciences* **366**(1885), 4559–4579. DOI: 10.1098/rsta.2008.0185.

Esse, B. et al. (2018) Quantification of ash sedimentation dynamics through depolarisation imaging with AshCam. *Scientific Reports* **8**(1), 2–10. DOI: 10.1038/s41598-018-34110-6.

Evangelidis, G. (2013) *IAT: A matlab toolbox for image alignment.* Available online: https://sites.google.com/site/imagealignment/.

Feuillard, M. et al. (1983) The 1975-1977 crisis of La Soufriere de Guadeloupe (F.W.I.): A still-born magmatic erutpion. *Journal of Volcanology and Geothermal Research* **16**, 317–334. DOI: https://doi.org/10.1016/0377-0273(83)90036-7.

Fickel, M. and Delgado Granados, H. (2017) On the use of different spectral windows in DOAS evaluations: Effects on the estimation of SO2 emission rate and mixing ratios during strong emission of Popocatépetl volcano. *Chemical Geology* **462**, 67–73. DOI: 10.1016/j.chemgeo.2017.05.001.

Fish, D. J. and Jones, R. L. (1995) Rotational Raman scattering and the ring effect in zenith-sky spectra. *Geophysical Research Letters* **22**(7), 811–814. DOI: 10.1029/95GL00392.

Fiske, R. S. (1984) Volcanologists, journalists, and the concerned local public: a tale of two crises in the eastern Caribbean. *Explosive Volcanism: Interception, Evolution, and Hazard*. Ed. by F. Boyd, 170–176.

Francis, H., Nobert, S., Leiva, X. H., and Bellanger, H. R. (2018) "We used to grow more crops here; now we can only grow pineapples and dragon fruit": impacts of persistent volcanic emissions on agriculture in Nicaragua. *EGU General Assembly Abstracts* **20**, 8199.

Frankenberg, C., Platt, U., and Wagner, T (2005) Iterative maximum a posteriori (IMAP)-DOAS for retrieval of strongly absorbing trace gases: Model studies for CH4 and CO2 retrieval from near infrared spectra of SCIAMACHY onboard ENVISAT. *Atmospheric Chemistry and Physics* **5**, 9–22. DOI: 10.5194/acpd-4-6067-2004.

Fulton, J. E. (1997a) Utilizing the ultraviolet (UV Detect) camera to enhance the appearance of photodamage and other skin conditions. *Dermatologic surgery official publication for American Society for Dermatologic Surgery et al* **23**(3), 163–169. DOI: 10.1111/j.1524-4725.1997.tb00013.x.

Fulton, J. E. (1997b) Utilizing the ultraviolet (UV Detect) camera to enhance the appearance of photodamage and other skin conditions. *Dermatologic surgery official publication for American Society for Dermatologic Surgery et al* **23**(3), 163–169. DOI: 10.1111/j.1524-4725.1997.tb00013.x.

Furukawa, Y. (2010) Infrared thermography of the fumarole area in the active crater of the Aso volcano, Japan, using a consumer digital camera. *Journal of Asian Earth Sciences* **38**(6), 283–288. DOI: 10.1016/j.jseaes.2010.02.001.

Galle, B. et al. (2003) A miniaturised ultraviolet spectrometer for remote sensing of SO2 fluxes: a new tool for volcano surveillance. *Journal of Volcanology and Geothermal Research* **119**(1-4), 241–254. DOI: 10.1016/S0377-0273(02)00356-6.

Galle, B. et al. (2010) Network for Observation of Volcanic and Atmospheric Change (NOVAC)A global network for volcanic gas monitoring: Network layout and instrument description. *Journal of Geophysical Research* **115**(D5), D05304. DOI: 10.1029/2009JD011823.

Ganci, G., James, M. R., Calvari, S., and Negro, C. D. (2013) Separating the thermal fingerprints of lava flows and simultaneous lava fountaining using ground-based thermal camera and SEVIRI measurements. *Geophysical Research Letters* **40**(19), 5058–5063. DOI: 10.1002/grl.50983.

Garcia, J. E., Dyer, A. G., Greentree, A. D., Spring, G., and Wilksch, P. A. (2013) Linearisation of RGB camera responses for quantitative image analysis of visible and UV photography: A comparison of two techniques. *PLoS ONE* **8**(11). DOI: 10.1371/journal.pone.0079534.

Gaudin, D et al. (2016) Mass and heat flux balance of La Soufrière volcano (Guadeloupe) from aerial infrared thermal imaging. *Journal of Volcanology and Geothermal Research* **320**, 107–116. DOI: 10.1016/j.jvolgeores.2016.04.007.

Gliß, J. et al. (2017) Pyplis - A Python Software Toolbox for the Analysis of SO2 Camera Data. Implications in Geosciences. *Geosciences* **7**(4), 134. DOI: 10.3390/geosciences7040134.

Global Volcanism Program (2018a) Report on Kilauea (United States). In: Sennert, S K (ed.), Weekly Volcanic Activity Report, 6 June-12 June 2018. Smithsonian Institution and US Geological Survey.

Global Volcanism Program (2018b) Report on Masaya (Nicaragua). In: Venzke, E (ed.), Bulletin of the Global Volcanism Network, 43:6. Smithsonian Institution.

Gordon, I. E. et al. (2017) The HITRAN2016 molecular spectroscopic database. *Journal of Quantitative Spectroscopy and Radiative Transfer* **203**, 3–69. DOI: 10.1016/j.jqsrt.2017.06.038.

Grgić, G. and Pušnik, I. (2011) Analysis of thermal imagers. *International Journal of Thermophysics* **32**(1-2), 237–247. DOI: 10.1007/s10765-011-0932-z.

Grutter, M et al. (2008) SO2 emissions from Popocatépetl volcano: emission rates and plume imaging using optical remote sensing techniques. *Atmos. Chem. Phys. Atmospheric Chemistry and Physics* **8**(December 1994), 6655–6663. DOI: 10.5194/acp-8-6655-2008.

Gueymard, C. A. (2001) Parameterized transmittance model for direct beam and circumsolar spectral irradiance. *Solar Energy* **71**(5), 325–346. DOI: 10.1016/S0038-092X(01)00054-8.

Gunturk, B. K., Glotzbach, J., Altunbasak, Y., Schafer, R. W., and Mersereau, R. M. (2005) Demosaicking: Color filter array interpolation. *IEEE Signal Processing Magazine* **22**(1), 44–54. DOI: 10.1109/MSP.2005.1407714.

Harris, A. J. L. and Maciejewski, A. J. (2000) Thermal surveys of the Vulcano Fossa fumarole field 1994-1999: Evidence for fumarole migration and sealing. *Journal of Volcanology and Geothermal Research* **102**(1-2), 119–147. DOI: 10.1016/S0377-0273(00)00184-0.

Harris, A. J. L. and Stevenson, D. S. (1997) Thermal observations of degassing open conduits and fumaroles at Stromboli and Vulcano using remotely sensed data. *Journal*

of Volcanology and Geothermal Research **76**(3-4), 175–198. DOI: 10.1016/S0377-0273(96)00097-2.

Harris, A. J. L., Flynn, L. P., Rothery, D. A., Oppenheimer, C., and Sherman, S. B. (1999) Mass flux measurements at active lava lakes: Implications for magma recycling. *Journal of Geophysical Research* **104**(10), 7117–7136. DOI: 10.1029/98JB02731.

Harris, A. J. L., Lodato, L., Dehn, J., and Spampinato, L. (2009) Thermal characterization of the Vulcano fumarole field. *Bulletin of Volcanology* **71**(4), 441–458. DOI: 10.1007/s00445-008-0236-8.

Hidalgo, S. et al. (2015) SO2 degassing at Tungurahua volcano (Ecuador) between 2007 and 2013: Transition from continuous to episodic activity. *Journal of Volcanology and Geothermal Research* **298**, 1–14. DOI: 10.1016/j.jvolgeores.2015.03.022.

Holick, M. F. and Chen, T. C. (2008) Vitamin D deficiency: a worldwide problem with health consequences. *The American Journal of Clinical Nutrition* **87**(4), 1080S–1086S. DOI: 10.1093/ajcn/87.4.1080S.

Holland, A. S. P., Watson, I. M., Phillips, J. C., Caricchi, L., and Dalton, M. P. (2011) Degassing processes during lava dome growth: Insights from Santiaguito lava dome, Guatemala. *Journal of Volcanology and Geothermal Research* **202**(1-2), 153–166. DOI: 10.1016/j.jvolgeores.2011.02.004.

Hönninger, G., Friedeburg, C. von, and Platt, U. (2004) Multi axis differential optical absorption spectroscopy (MAX-DOAS). *Atmospheric Chemistry and Physics* **4**(1), 231–254. DOI: 10.5194/acp-4-231-2004.

Iwabuchi, S et al. (2006) A Back-Illuminated High-Sensitivity Small-Pixel Color CMOS Image Sensor with Flexible Layout of Metal Wiring. *Solid-State Circuits Conference, 2006. ISSCC 2006. Digest of Technical Papers. IEEE International*, 1171–1178. DOI: 10.1109/ISSCC.2006.1696162.

James, M. R., Robson, S., Pinkerton, H., and Ball, M. (2006) Oblique photogrammetry with visible and thermal images of active lava flows. *Bulletin of Volcanology* **69**(1), 105–108. DOI: 10.1007/s00445-006-0062-9.

Johnson, J. B. (2004) Volcanic eruptions observed with infrasound. *Geophysical Research Letters* **31**(14), L14604. DOI: 10.1029/2004GL020020.

Kantzas, E. P., McGonigle, A. J. S., Tamburello, G., Aiuppa, A., and Bryant, R. G. (2010) Protocols for UV camera volcanic SO2 measurements. *Journal of Volcanology and Geothermal Research* **194**(1-3), 55–60. DOI: 10.1016/j.jvolgeores.2010.05.003.

Kantzas, E. P., McGonigle, A. J. S., and Bryant, R. G. (2009) Comparison of Low Cost Miniature Spectrometers for Volcanic SO2 Emission Measurements. *Sensors* **9**(5), 3256–3268. DOI: 10.3390/s90503256.

Kazahaya, R., Mori, T., Takeo, M., Ohminato, T., and Urabe, T. (2011) Relation between single very-long-period pulses and volcanic gas emissions at Mt . Asama , Japan. *Geophysical Research Letters* **38**, 3–7. DOI: 10.1029/2011GL047555.

Kazahaya, R., Shinohara, H., Mori, T., Iguchi, M., and Yokoo, A. (2016) Pre-eruptive inflation caused by gas accumulation: Insight from detailed gas flux variation at

Sakurajima volcano, Japan. *Geophysical Research Letters* **43**(21), 11,219–11,225. DOI: 10.1002/2016GL070727.

Kern, C. et al. (2010a) Radiative transfer corrections for accurate spectroscopic measurements of volcanic gas emissions. *Bulletin of Volcanology* **72**(2), 233–247. DOI: 10.1007/s00445-009-0313-7.

Kern, C., Kick, F, Vogel, L., and Platt, U. (2010b) Theoretical description of functionality, applications, and limitations of SO2 cameras for the remote sensing of volcanic plumes. *Atmospheric Measurement Techniques* **3**, 733–749. DOI: 10.5194/amt-3-733-2010.

Kern, C. et al. (2012) Improving the accuracy of SO2 column densities and emission rates obtained from upward-looking UV-spectroscopic measurements of volcanic plumes by taking realistic radiative transfer into account. *Journal of Geophysical Research: Atmospheres* **117**, D20302. DOI: 10.1029/2012JD017936.

Kern, C., Werner, C., Elias, T., Sutton, a. J., and Lübcke, P. (2013) Applying UV cameras for SO2 detection to distant or optically thick volcanic plumes. *Journal of Volcanology and Geothermal Research* **262**, 80–89. DOI: 10.1016/j.jvolgeores.2013.06.009.

Kern, C. et al. (2015a) An automated SO2 camera system for continuous, real-time monitoring of gas emissions from Kilauea Volcano's summit Overlook Crater. *Journal of Volcanology and Geothermal Research* **300**, 81–94. DOI: 10.1016/j.jvolgeores.2014.12.004.

Kern, C. et al. (2015b) Intercomparison of SO2 camera systems for imaging volcanic gas plumes. *Journal of Volcanology and Geothermal Research* **300**, 22–36. DOI: 10.1016/j.jvolgeores.2014.08.026.

Kern, C., Masias, P., Apaza, F., Reath, K. A., and Platt, U. (2017) Remote measurement of high preeruptive water vapor emissions at Sabancaya volcano by passive differential optical absorption spectroscopy. *Journal of Geophysical Research: Solid Earth* **122**(5), 3540–3564. DOI: 10.1002/2017JB014020.

Khokhar, M. F. et al. (2005) Satellite observations of atmospheric SO2 from volcanic eruptions during the time-period of 1996-2002. *Advances in Space Research* **36**(5), 879–887. DOI: 10.1016/j.asr.2005.04.114.

Kimlin, M. G., Downs, N. J., and Parisi, a. V. (2003) Comparison of human facial UV exposure at high and low latitudes and the potential impact on dermal vitamin D production. *Photochemical & Photobiological Sciences* **2**(4), 370. DOI: 10.1039/b211830k.

Kochanov, R. V. et al. (2016) HITRAN Application Programming Interface (HAPI): A comprehensive approach to working with spectroscopic data. *Journal of Quantitative Spectroscopy and Radiative Transfer* **177**, 15–30. DOI: 10.1016/j.jqsrt.2016.03.005.

Komhyr, W. D., Grass, R. D., and Leonard, R. K. (1989) Dobson spectrophotometer 83: A standard for total ozone measurements, 1962-1987. *Journal of Geophysical Research* **94**(D7), 9847. DOI: 10.1029/JD094iD07p09847.

Krauss, T and Warlen, S (1985) The Forensic Science Use of Reflective Ultraviolet Photography BT - The Forensic Science Use of Reflective Ultraviolet Photography. *Journal of Forensic Sciences* **30**(1), 262–268. DOI: http://dx.doi.org/10.1520/JFS10991J.

La Spina, A. et al. (2015) Open-path FTIR spectroscopy of magma degassing processes during eight lava fountains on Mount Etna. *Earth and Planetary Science Letters* **413**, 123–134. DOI: 10.1016/j.epsl.2014.12.038.

Lane, B and Whitenton, E. P. (2015) Calibration and Measurement Procedures for a High Magnification Thermal Camera. *National Institute of Standards and Technology*. DOI: 10.6028/NIST.IR.8098.

Lane, B, Whitenton, E, Madhavan, V, and Donmez, A (2013) Uncertainty of temperature measurements by infrared thermography for metal cutting applications. *Metrologia* **50**(6), 637–653. DOI: 10.1088/0026-1394/50/6/637.

Langmann, B. (2014) On the Role of Climate Forcing by Volcanic Sulphate and Volcanic Ash. *Advances in Meteorology* **2014**, 1–17. DOI: 10.1155/2014/340123. arXiv: 340123.

Le Guern, F. (1987) Mechanism of energy transfer in the lava lake of Niragongo (Zaire), 1959-1977. *Journal of Volcanology and Geothermal Research* **31**(1-2), 17–31. DOI: 10.1016/0377-0273(87)90003-5.

Le Guern, F., Carbonnelle, J, and Tazieff, H (1979) Erta'ale lava lake: heat and gas transfer to the atmosphere. *Journal of Volcanology and Geothermal Research* **6**(1-2), 27–48. DOI: 10.1016/0377-0273(79)90045-3.

Lee, C. T. A., Luffi, P., Plank, T., Dalton, H., and Leeman, W. P. (2009) Constraints on the depths and temperatures of basaltic magma generation on Earth and other terrestrial planets using new thermobarometers for mafic magmas. *Earth and Planetary Science Letters* **279**(1-2), 20–33. DOI: 10.1016/j.epsl.2008.12.020.

Lin, D.-L., Wang, C.-C., and Wei, C.-L. (2010) Quantified Temperature Effect in a CMOS Image Sensor. *Electron Devices, IEEE Transactions on* **57**(2), 422–428. DOI: 10.1109/TED.2009.2037389.

Liu, E. J. et al. (2019) Dynamics of Outgassing and Plume Transport Revealed by Proximal Unmanned Aerial System (UAS) Measurements at Volcán Villarrica, Chile. *Geochemistry, Geophysics, Geosystems* **20**(2), 730–750. DOI: 10.1029/2018GC007692.

Liu, Z., Xu, J., Wang, X., Nie, K., and Jin, W. (2015) A fixed-pattern noise correction method based on gray value compensation for TDI CMOS image sensor. *Sensors (Switzerland)* **15**(9), 23496–23513. DOI: 10.3390/s150923496.

Lopez, T. et al. (2015) Volcanic plume characteristics determined using an infrared imaging camera. *Journal of Volcanology and Geothermal Research* **300**, 148–166. DOI: 10.1016/j.jvolgeores.2014.12.009.

Lübcke, P. et al. (2013) On the absolute calibration of SO2 cameras. *Atmospheric Measurement Techniques* **6**(3), 677–696. DOI: 10.5194/amt-6-677-2013.

Lübcke, P. et al. (2014) BrO/SO2 molar ratios from scanning DOAS measurements in the NOVAC network. *Solid Earth* **5**(1), 409–424. DOI: 10.5194/se-5-409-2014.

Magnan, P. (2003) Detection of visible photons in CCD and CMOS: A comparative view. *Nuclear Instruments and Methods in Physics Research, Section A: Accelerators, Spectrometers, Detectors and Associated Equipment* **504**(1-3), 199–212. DOI: 10.1016/S0168-9002(03)00792-7.

McCormick, M. P., Thomason, L. W., and Trepte, C. R. (1995) Atmospheric effects of the Mt Pinatubo eruption. *Nature* **373**(6513), 399–404. DOI: 10.1038/373399a0. arXiv: arXiv:1011.1669v3.

McElhoe, H. B. and Conner, W. D. (1986) Remote Measurement of Sulfur Dioxide Emissions Using an Ultraviolet Light Sensitive Video System. *Journal of the Air Pollution Control Association* **36**(1), 42–47. DOI: 10.1080/00022470.1986.10466043.

McGonigle, A. J. S. (2007) Measurement of volcanic SO2 fluxes with differential optical absorption spectroscopy. *Journal of Volcanology and Geothermal Research* **162**(3-4), 111–122. DOI: 10.1016/j.jvolgeores.2007.02.001.

McGonigle, A. J. S., Oppenheimer, C., Galle, B., Mather, T. A., and Pyle, D. M. (2002) Walking traverse and scanning DOAS measurements of volcanic gas emission rates. *Geophysical Research Letters* **29**(20), 46–1–46–4. DOI: 10.1029/2002GL015827.

McGonigle, A. J. S., Thomson, C., Tsanev, V., and Oppenheimer, C. (2004a) A simple technique for measuring power station SO2 and NO2 emissions. *Atmospheric Environment* **38**(1), 21–25. DOI: 10.1016/j.atmosenv.2003.09.048.

McGonigle, A. J. S. et al. (2004b) SO2 depletion in tropospheric volcanic plumes. *Geophysical Research Letters* **31**(13), 2–5. DOI: 10.1029/2004GL019990.

McGonigle, A. J. S. et al. (2004c) Sulphur dioxide fluxes from Papua New Guinea's volcanoes. *Geophysical Research Letters* **31**(8), 1–4. DOI: 10.1029/2004GL019568.

McGonigle, A. J. S., Inguaggiato, S., Aiuppa, A., Hayes, a. R., and Oppenheimer, C. (2005a) Accurate measurement of volcanic SO2 flux: Determination of plume transport speed and integrated SO2 concentration with a single device. *Geochemistry, Geophysics, Geosystems* **6**(1). DOI: 10.1029/2004GC000845.

McGonigle, A. J. S., Hilton, D. R., Fischer, T. P., and Oppenheimer, C. (2005b) Plume velocity determination for volcanic SO2 flux measurements. *Geophysical Research Letters* **32**(11), L11302. DOI: 10.1029/2005GL022470.

McGonigle, A. J. S., Aiuppa, A., Ripepe, M., Kantzas, E. P., and Tamburello, G. (2009) Spectroscopic capture of 1 Hz volcanic SO2 fluxes and integration with volcano geophysical data. *Geophysical Research Letters* **36**(21), L21309. DOI: 10.1029/2009GL040494.

McGonigle, A. J. S. et al. (2017) Ultraviolet Imaging of Volcanic Plumes: A New Paradigm in Volcanology. *Geosciences* **7**(3), 68. DOI: 10.3390/geosciences7030068.

Meroni, M. et al. (2010) Characterization of fine resolution field spectrometers using solar Fraunhofer lines and atmospheric absorption features. *Applied Optics* **49**(15), 2858. DOI: 10.1364/AO.49.002858.

Millan, M. M. (1980) Remote sensing of air pollutants. A study of some atmospheric scattering effects. *Atmos. Environ* **14**(1), 1241–1253. DOI: 10.1016/0004-6981(80)90226-7.

Mims, F. M. I. et al. (2019) Measuring and Visualizing Solar UV for a Wide Range of Atmospheric Conditions on Hawai'i Island. *International Journal of Environmental Research and Public Health* **16**(6), 997. DOI: 10.3390/ijerph16060997.

Moffat, A. J. and Millan, M. M. (1971) The applications of optical correlation techniques to the remote sensing of SO2 plumes using sky light. *Atmospheric Environment (1967)* **5**(8), 677–690. DOI: 10.1016/0004-6981(71)90125-9.

Mohammadnejad, S., Nasiri sarvi, M., Roshani, S., and Roshani, S. (2012) A Novel Fixed Pattern Noise Reduction Technique in Image Sensors for Satellite Applications. *Electrical and Electronic Engineering* **2**(5), 271–276. DOI: 10.5923/j.eee.20120205.05.

Moor, J. M. de et al. (2017) A New Sulfur and Carbon Degassing Inventory for the Southern Central American Volcanic Arc: The Importance of Accurate Time-Series Data Sets and Possible Tectonic Processes Responsible for Temporal Variations in Arc-Scale Volatile Emissions. *Geochemistry, Geophysics, Geosystems* **18**(12), 4437–4468. DOI: 10.1002/2017GC007141.

Mori, T. and Burton, M. (2006) The SO2 camera: A simple, fast and cheap method for ground-based imaging of SO2 in volcanic plumes. *Geophysical Research Letters* **33**(24), L24804. DOI: 10.1029/2006GL027916.

Mori, T. and Burton, M. R. (2009) Quantification of the gas mass emitted during single explosions on Stromboli with the SO2 imaging camera. *Journal of Volcanology and Geothermal Research* **188**(4), 395–400. DOI: 10.1016/j.jvolgeores.2009.10.005.

Mori, T. and Notsu, K. (1997) Remote CO, COS, CO2, SO2, HCl detection and temperature estimation of volcanic gas. *Geophysical Research Letters* **24**(16), 2047–2050. DOI: 10.1029/97GL52058.

Mori, T. et al. (2016) Volcanic plume measurements using a UAV for the 2014 Mt. Ontake eruption. *Earth, Planets and Space* **68**(1), 49. DOI: 10.1186/s40623-016-0418-0.

Morys, M. et al. (2001) Design , calibration and performance of MICROTOPS II handheld ozonometer. **106**. DOI: 2001JD9001035.

Moure, D. et al. (2015) Use of Low-Cost Acquisition Systems with an Embedded Linux Device for Volcanic Monitoring. *Sensors* **15**(8), 20436–20462. DOI: 10.3390/s150820436.

Murakami, Y. and Shingyouji, T. (1994) Separation and analysis of diffusion and generation components of pn junction leakage current in various silicon wafers. *Journal of Applied Physics* **75**(7), 3548–3552. DOI: 10.1063/1.356091.

Nadeau, P., Palma, J. L., and Waite, G. P. (2011) Linking volcanic tremor, degassing, and eruption dynamics via SO2 imaging. *Geophysical Research Letters* **38**(1), L01304. DOI: 10.1029/2010GL045820.

Nadeau, P. et al. (2015) Using SO2 camera imagery and seismicity to examine degassing and gas accumulation at Klauea Volcano, May 2010. *Journal of Volcanology and Geothermal Research* **300**, 70–80. DOI: 10.1016/j.jvolgeores.2014.12.005.

Neal, C. A. et al. (2019) The 2018 rift eruption and summit collapse of Kilauea Volcano. *Science* **363**(6425), 367–374. DOI: 10.1126/science.aav7046.

Newhall, C. G. and Punongbayan, R. S., eds. (1996) *Fire and Mud: Eruptions and Lahars of Mount Pinatubo, Phillipines*. University of Washington Press.

Oláh, L., Tanaka, H. K., Ohminato, T., and Varga, D. (2018) High-definition and low-noise muography of the Sakurajima volcano with gaseous tracking detectors. *Scientific Reports* **8**(1), 29–33. DOI: 10.1038/s41598-018-21423-9.

Oppenheimer, C. and Francis, P. (1997) Remote sensing of heat, lava and fumarole emissions from Erta 'Ale volcano, Ethiopia. *International Journal of Remote Sensing* **18**(8), 1661–1692. DOI: 10.1080/014311697218043.

Oppenheimer, C. and Kyle, P. R. (2008) Probing the magma plumbing of Erebus volcano, Antarctica, by open-path FTIR spectroscopy of gas emissions. *Journal of Volcanology and Geothermal Research* **177**(3), 743–754. DOI: 10.1016/j.jvolgeores.2007.08.022.

Oppenheimer, C. and Yirgu, G. (2002) Thermal imaging of an active lava lake: Erta 'Ale volcano, Ethiopia. *International Journal of Remote Sensing* **23**(22), 4777–4782. DOI: 10.1080/01431160110114637.

Oppenheimer, C., McGonigle, A. J. S., Allard, P., Wooster, M. J., and Tsanev, V. (2004) Sulfur, heat, and magma budget of Erta 'Ale lava lake, Ethiopia. *Geology* **32**(6), 509–512. DOI: 10.1130/G20281.1.

Oppenheimer, C., Lomakina, A. S., Kyle, P. R., Kingsbury, N., and Boichu, M. (2009) Pulsatory magma supply to a phonolite lava lake. *Earth and Planetary Science Letters* **284**(3-4), 392–398. DOI: 10.1016/j.epsl.2009.04.043.

Oppenheimer, C., Scaillet, B., and Martin, R. S. (2011) Sulfur Degassing From Volcanoes: Source Conditions, Surveillance, Plume Chemistry and Earth System Impacts. *Reviews in Mineralogy and Geochemistry* **73**(1), 363–421. DOI: 10.2138/rmg.2011.73.13.

Oppenheimer, C. (2003) Climatic, environmental and human consequences of the largest known historic eruption: Tambora volcano (Indonesia) 1815. *Progress in Physical Geography: Earth and Environment* **27**(2), 230–259. DOI: 10.1191/0309133303pp379ra.

Orr, T. R., Bleacher, J. E., Patrick, M. R., and Wooten, K. M. (2015) A sinuous tumulus over an active lava tube at Kilauea Volcano: Evolution, analogs, and hazard forecasts. *Journal of Volcanology and Geothermal Research* **291**, 35–48. DOI: 10.1016/j.jvolgeores.2014.12.002.

Osorio, M. et al. (2017) Plume Segmentation from UV Camera Images for SO2 Emission Rate Quantification on Cloud Days. *Remote Sensing* **9**(6), 517. DOI: 10.3390/rs9060517.

Pagnutti, M. et al. (2017) Laying the foundation to use Raspberry Pi 3 V2 camera module imagery for scientific and engineering purposes. *Journal of Electronic Imaging* **26**(1), 013014. DOI: 10.1117/1.JEI.26.1.013014.

Parcheta, C. E. et al. (2016) A robotic approach to mapping post-eruptive volcanic fissure conduits. *Journal of Volcanology and Geothermal Research* **320**, 19–28. DOI: 10.1016/j.jvolgeores.2016.03.006.

Patrick, M. R. (2007) Dynamics of Strombolian ash plumes from thermal video: Motion, morphology, and air entrainment. *Journal of Geophysical Research* **112**(B6), B06202. DOI: 10.1029/2006JB004387.

Patrick, M. R. et al. (2007) Strombolian explosive styles and source conditions: insights from thermal (FLIR) video. *Bulletin of Volcanology* **69**(7), 769–784. DOI: 10.1007/s00445-006-0107-0.

Patrick, M. R. et al. (2010) Evidence for gas accumulation beneath the surface crust driving cyclic rise and fall of the lava surface at Halema‘uma‘u, Kilauea Volcano. *AGU Fall Meeting Abstracts*, V21C–2339.

Patrick, M. R., Orr, T. R., Antolik, L., Lee, L., and Kamibayashi, K. (2014) Continuous monitoring of Hawaiian volcanoes with thermal cameras. *Journal of Applied Volcanology* **3**(1), 1. DOI: 10.1186/2191-5040-3-1.

Patrick, M. R., Orr, T. R., Lee, L., and Moniz, C. J. (2015) *A Multipurpose Camera System for Monitoring Kilauea Volcano, Hawai'i*. Tech. rep., 25 p. DOI: 10.3133/tm13A2.

Patrick, M. R., Orr, T. R., Fisher, G., Trusdell, F., and Kauahikaua, J. (2017) Thermal mapping of a pahoehoe lava flow, Kilauea Volcano. *Journal of Volcanology and Geothermal Research* **332**, 71–87. DOI: 10.1016/j.jvolgeores.2016.12.007.

Patrick, M. R., Swanson, D., and Orr, T. (2016) Automated tracking of lava lake level using thermal images at Kilauea Volcano, Hawai'i. *Journal of Applied Volcanology* **5**(1). DOI: 10.1186/s13617-016-0047-0.

Pering, T. D. et al. (2014) High time resolution fluctuations in volcanic carbon dioxide degassing from Mount Etna. *Journal of Volcanology and Geothermal Research* **270**, 115–121. DOI: 10.1016/j.jvolgeores.2013.11.014.

Pering, T. D. et al. (2016) Conduit dynamics and post explosion degassing on Stromboli: A combined UV camera and numerical modeling treatment. *Geophysical Research Letters* **43**(10), 5009–5016. DOI: 10.1002/2016GL069001.

Pering, T. D. et al. (2019) A Rapidly Convecting Lava Lake at Masaya Volcano, Nicaragua. *Frontiers in Earth Science* **6**, 1–11. DOI: 10.3389/feart.2018.00241.

Peters, N., Oppenheimer, C., Kyle, P. R., and Kingsbury, N. (2014) Decadal persistence of cycles in lava lake motion at Erebus volcano, Antarctica. *Earth and Planetary Science Letters* **395**, 1–12. DOI: 10.1016/j.epsl.2014.03.032.

Peters, N., Hoffmann, A., Barnie, T., Herzog, M., and Oppenheimer, C. (2015) Use of motion estimation algorithms for improved flux measurements using SO2 cameras.

Journal of Volcanology and Geothermal Research **300**, 58–69. DOI: 10.1016/j.jvolgeores.2014.08.031.

Pinkerton, H., James, M. R., and Jones, A. (2002) Surface temperature measurements of active lava flows on Kilauea volcano, Hawai'i. *Journal of Volcanology and Geothermal Research* **113**(1-2), 159–176. DOI: PiiS0377-0273(01)00257-8.

Pinto, J. P., Toon, O. B., and Turco, R. P. (1989) Self-limiting physical and chemical effects in volcanic eruption clouds. *Journal of Geophysical Research: Atmospheres* **94**, 11165–11174. DOI: 10.1029/JD094iD08p11165.

Platt, U. and Stutz, J. (2008) *Differential optical absorption spectroscopy (DOAS)*. Berlin, Heidelberg: Springer-Verlag.

Platt, U. et al. (2015) Quantitative imaging of volcanic plumes Results, needs, and future trends. *Journal of Volcanology and Geothermal Research* **300**, 7–21. DOI: 10.1016/j.jvolgeores.2014.10.006.

Platt, U., Bobrowski, N., and Butz, A. (2018) Ground-Based Remote Sensing and Imaging of Volcanic Gases and Quantitative Determination of Multi-Species Emission Fluxes. *Geosciences* **8**(2), 44. DOI: 10.3390/geosciences8020044.

Pliutau, D. and Roslyakov, K. (2017) Bytran - spectral calculations for portable devices using the HITRAN database. *Earth Science Informatics* **10**(3), 395–404. DOI: 10.1007/s12145-017-0288-4.

Porter, W. C., Kopp, B., Dunlap, J. C., Widenhorn, R., and Bodegom, E. (2008) "Dark current measurements in a CMOS imager". In: *Proc. SPIE 6816, Sensors, Cameras, and Systems for Industrial/Scientific Applications IX*. Ed. by M. M. Blouke and E. Bodegom, p. 68160C. DOI: 10.1117/12.769079.

Prata, A. J. (2014) Measuring SO2 ship emissions with an ultraviolet imaging camera. *Atmospheric Measurement Techniques* **7**(5), 1213–1229. DOI: 10.5194/amt-7-1213-2014.

Prata, A. J. and Bernardo, C. (2009) Retrieval of volcanic ash particle size, mass and optical depth from a ground-based thermal infrared camera. *Journal of Volcanology and Geothermal Research* **186**(1-2), 91–107. DOI: 10.1016/j.jvolgeores.2009.02.007.

Prata, A. J. and Bernardo, C. (2014) Retrieval of sulfur dioxide from a ground-based thermal infrared imaging camera. *Atmospheric Measurement Techniques* **7**(9), 2807–2828. DOI: 10.5194/amt-7-2807-2014.

Primulyana, S. et al. (2018) Gas and ash emissions associated with the 2010-present activity of Sinabung Volcano, Indonesia. *Journal of Volcanology and Geothermal Research*. DOI: 10.1016/j.jvolgeores.2017.11.018.

Pritchard, M. E. and Simons, M (2004) An InSAR-based survey of volcanic deformation in the southern Andes. *Geophysical Research Letters* **31**(15). DOI: 10.1029/2004GL020545.

Pyle, D. M., Mather, T. A., and Biggs, J. (2013) Remote sensing of volcanoes and volcanic processes: integrating observation and modelling - introduction. *Geological Society, London, Special Publications* **380**(1), 1–13. DOI: 10.1144/SP380.14.

Radebaugh, J., Lopes, R. M., Howell, R. R., Lorenz, R. D., and Turtle, E. P. (2016) Eruptive behavior of the Marum/Mbwelesu lava lake, Vanuatu and comparisons with lava lakes on Earth and Io. *Journal of Volcanology and Geothermal Research* **322**(March), 105–118. DOI: 10.1016/j.jvolgeores.2016.03.019.

Ramsey, M. S. and Harris, A. J. L. (2013) Volcanology 2020: How will thermal remote sensing of volcanic surface activity evolve over the next decade? *Journal of Volcanology and Geothermal Research* **249**, 217–233. DOI: 10.1016/j.jvolgeores.2012.05.011.

Ripepe, M., Harris, A. J. L., and Marchetti, E. (2005) Coupled thermal oscillations in explosive activity at different craters of Stromboli volcano. *Geophysical Research Letters* **32**(17), 1–4. DOI: 10.1029/2005GL022711.

Rix, M. et al. (2009) Satellite Monitoring of Volcanic Sulfur Dioxide Emissions for Early Warning of Volcanic Hazards. *IEEE Journal of Selected Topics in Applied Earth Observations and Remote Sensing* **2**(3), 196–206. DOI: 10.1109/JSTARS.2009.2031120.

Robock, A. (2000) Volcanic eruptions and climate. *Reviews of Geophysics* **38**(2), 191–219. DOI: 10.1029/1998RG000054.

Rothery, D. A., Francis, P. W., and Wood, C. A. (1988) Volcano Monitoring Using Short Wavelength Infrared Data from Satellites. *Journal of Geophysical Research* **93**(B7), 7993–8008. DOI: 10.1029/JB093iB07p07993.

Saito, T. et al. (2005) A new technique of radiation thermometry using a consumer digital camcorder: Observations of red glow at Aso volcano, Japan. *Earth, Planets and Space* **57**(2), e5–e8. DOI: 10.1186/BF03352550.

Salerno, G. G. et al. (2009) Three-years of SO2 flux measurements of Mt. Etna using an automated UV scanner array: Comparison with conventional traverses and uncertainties in flux retrieval. *Journal of Volcanology and Geothermal Research* **183**(1-2), 76–83. DOI: 10.1016/j.jvolgeores.2009.02.013.

Saunders, P. (2001) On the effects of temperature dependence of spectral emissivity in industrial radiation thermometry. *High Temperatures - High Pressures* **33**(5), 599–610. DOI: 10.1068/htjr016.

Saunders, P. and White, D. R. (2003) Physical basis of interpolation equations for radiation thermometry. *Metrologia* **40**(4), 195–203. DOI: 10.1088/0026-1394/40/4/309.

Sawyer, G. M. and Burton, M. R. (2006) Effects of a volcanic plume on thermal imaging data. *Geophysical Research Letters* **33**(14), L14311. DOI: 10.1029/2005GL025320.

Schoberl, M., Senel, C., Fößel, S., Bloss, H., and Kaup, A. (2009) Non-linear dark current fixed pattern noise compensation for variable frame rate moving picture cameras. *European Signal Processing Conference* (Eusipco), 268–272.

Sebastien, N., Leiva, X. H., and Ilyinskaya, E. (2018) Unseen but not unfelt : community resilience to persistent volcanic emissions . Case study from Masaya volcano , Nicaragua. *EGU General Assembly Abstracts* **20**, 19061.

Smekens, J.-F. and Gouhier, M. (2018) Observation of SO2 degassing at Stromboli volcano using a hyperspectral thermal infrared imager. *Journal of Volcanology and Geothermal Research* **356**(1), 75–89. DOI: 10.1016/j.jvolgeores.2018.02.018.

Smekens, J.-F. F., Burton, M. R., and Clarke, A. B. (2015) Validation of the SO2 camera for high temporal and spatial resolution monitoring of SO2 emissions. *Journal of Volcanology and Geothermal Research* **300**, 37–47. DOI: 10.1016/j.jvolgeores.2014.10.014.

Spampinato, L., Oppenheimer, C., Calvari, S., Cannata, A., and Montalto, P. (2008) Lava lake surface characterization by thermal imaging: Erta 'Ale volcano (Ethiopia). *Geochemistry, Geophysics, Geosystems* **9**(12), 1–14. DOI: 10.1029/2008GC002164.

Spampinato, L., Calvari, S., Oppenheimer, C., and Boschi, E. (2011) Volcano surveillance using infrared cameras. *Earth-Science Reviews* **106**(1-2), 63–91. DOI: 10.1016/j.earscirev.2011.01.003.

Spampinato, L. et al. (2013) Thermal insights into the dynamics of Nyiragongo lava lake from ground and satellite measurements. *Journal of Geophysical Research: Solid Earth* **118**(11), 5771–5784. DOI: 10.1002/2013JB010520.

Sparks, R. S. J. (2003) Forecasting volcanic eruptions. *Earth and Planetary Science Letters* **210**(1-2), 1–15. DOI: 10.1016/S0012-821X(03)00124-9.

Sparks, R. S. J., Biggs, J., and Neuberg, J. W. (2012) Monitoring Volcanoes. *Science* **335**(6074), 1310–1311. DOI: 10.1126/science.1219485.

Staehelin, J., Viatte, P., Stübi, R., Tummon, F., and Peter, T. (2018) Stratospheric ozone measurements at Arosa (Switzerland): History and scientific relevance. *Atmospheric Chemistry and Physics* **18**(9), 6567–6584. DOI: 10.5194/acp-18-6567-2018.

Stanger, L., Wilkes, T. C., Boone, N., McGonigle, A. J. S., and Willmott, J. (2018) Thermal Imaging Metrology with a Smartphone Sensor. *Sensors* **18**(7), 2169. DOI: 10.3390/s18072169.

Stebel, K., Amigo, A., Thomas, H. E., and Prata, A. J. (2015) First estimates of fumarolic SO2 fluxes from Putana volcano, Chile, using an ultraviolet imaging camera. *Journal of Volcanology and Geothermal Research* **300**, 112–120. DOI: 10.1016/j.jvolgeores.2014.12.021.

Stenchikov, G. L. et al. (1998) Radiative forcing from the 1991 Mount Pinatubo volcanic eruption. *Journal of Geophysical Research Atmospheres* **103**(D12), 13837–13857. DOI: 10.1029/98JD00693.

Stix, J. et al. (2018) Using Drones and Miniaturized Instrumentation to Study Degassing at Turrialba and Masaya Volcanoes, Central America. *Journal of Geophysical Research: Solid Earth* **123**(8), 6501–6520. DOI: 10.1029/2018JB015655.

Stutz, J. and Platt, U. (1996) Numerical analysis and estimation of the statistical error of differential optical absorption spectroscopy measurements with least-squares methods. *Applied Optics* **35**(30), 6041. DOI: 10.1364/AO.35.006041.

Surono et al. (2012) The 2010 explosive eruption of Java's Merapi volcano-A '100-year' event. *Journal of Volcanology and Geothermal Research* **241-242**, 121–135. DOI: 10.1016/j.jvolgeores.2012.06.018.

Tamburello, G., McGonigle, A. J. S., Kantzas, E. P., and Aiuppa, A. (2011a) Recent advances in ground-based ultraviolet remote sensing of volcanic SO2 fluxes. *Annals of Geophysics* **54**(2), 199–208. DOI: 10.4401/ag-5179.

Tamburello, G., Kantzas, E. P., McGonigle, A. J. S., Aiuppa, A., and Giudice, G. (2011b) UV camera measurements of fumarole field degassing (La Fossa crater, Vulcano Island). *Journal of Volcanology and Geothermal Research* **199**(1-2), 47–52. DOI: 10.1016/j.jvolgeores.2010.10.004.

Tamburello, G., Kantzas, E. P., McGonigle, A. J. S., and Aiuppa, A. (2011c) Vulcamera: A program for measuring volcanic SO2 using UV cameras. *Annals of Geophysics* **54**(2), 219–221. DOI: 10.4401/ag-5181.

Tamburello, G., Aiuppa, A., Kantzas, E. P., McGonigle, A. J. S., and Ripepe, M. (2012) Passive vs. active degassing modes at an open-vent volcano (Stromboli, Italy). *Earth and Planetary Science Letters* **359-360**, 106–116. DOI: 10.1016/j.epsl.2012.09.050.

Tamburello, G. et al. (2013) Periodic volcanic degassing behavior: The Mount Etna example. *Geophysical Research Letters* **40**(18), 4818–4822. DOI: 10.1002/grl.50924.

Tang, M. et al. (2015) General study of asymmetrical crossed CzernyTurner spectrometer. *Applied Optics* **54**(33), 9966. DOI: 10.1364/AO.54.009966.

Theys, N. et al. (2015) Sulfur dioxide vertical column DOAS retrievals from the Ozone Monitoring Instrument: Global observations and comparison to ground-based and satellite data. *Journal of Geophysical Research: Atmospheres* **120**(6), 2470–2491. DOI: 10.1002/2014JD022657.

Thomas, H. E. and Prata, A. J. (2018) Computer vision for improved estimates of SO2 emission rates and plume dynamics. *International Journal of Remote Sensing* **39**(5), 1285–1305. DOI: 10.1080/01431161.2017.1401250.

Tortini, R., Bonali, F. L., Corazzato, C., Carn, S. A., and Tibaldi, A. (2014) An innovative application of the kinect in earth sciences: Quantifying deformation in analogue modelling of volcanoes. *Terra Nova* **26**(4), 273–281. DOI: 10.1111/ter.12096.

Urbach, F. (1997) Ultraviolet radiation and skin cancer of humans. *Journal of Photochemistry and Photobiology B: Biology* **40**(1), 3–7. DOI: 10.1016/S1011-1344(97)00029-8.

USGS (2018) Advanced Spaceborned Thermal Emission and Reflection Radiometer 1 arc-second. ASTER DEM is a product of METI and NASA.

Vandaele, A. C., Simon, P. C., Guilmot, J. M., and Colin, R. (1994) SO2 absorption cross section measurement in the UV using a Fourier transform spectrometer. *Journal of Geophysical Research* **99**(D12), 25599–25605. DOI: 10.1029/94JD02187.

Vandaele, A. C., Hermans, C., and Fally, S. (2009) Fourier transform measurements of SO2 absorption cross sections: II. Temperature dependence in the 29 000-44 000 cm-1 (227-345 nm) region. *Journal of Quantitative Spectroscopy and Radiative Transfer* **110**(18), 2115–2126. DOI: 10.1016/j.jqsrt.2009.05.006.

Vogel, L. et al. (2011) Early in-flight detection of SO2 via Differential Optical Absorption Spectroscopy: A feasible aviation safety measure to prevent potential encounters with volcanic plumes. *Atmospheric Measurement Techniques* **4**(9), 1785–1804. DOI: 10.5194/amt-4-1785-2011.

Vogel, L., Sihler, H., Lampel, Johannes, Wagner, T., and Platt, U. (2013) Retrieval interval mapping : a tool to visualize the impact of the spectral retrieval range on differential optical absorption evaluations. *Atmospheric Measurement Techniques* **6**, 275–299. DOI: 10.5194/amt-6-275-2013.

Voight, B. (1990) The 1985 Nevado del Ruiz volcano catastrophe: anatomy and retrospection. *Journal of Volcanology and Geothermal Research* **42**(1-2), 151–188. DOI: 10.1016/0377-0273(90)90075-Q.

Vollmer, M. and Möllmann, K.-P. (2017) *Infrared thermal imaging: fundamentals, research and applications*. John Wiley & Sons.

Wagner, T., Heland, J., Zöger, M., and Platt, U. (2003) A fast H2O total column density product from GOME - Validation with in-situ aircraft measurements. *Atmospheric Chemistry and Physics* **3**(3), 651–663. DOI: 10.5194/acp-3-651-2003.

Waite, G. P., Nadeau, P., and Lyons, J. J. (2013) Variability in eruption style and associated very long period events at Fuego volcano, Guatemala. *Journal of Geophysical Research: Solid Earth* **118**(4), 1526–1533. DOI: 10.1002/jgrb.50075.

Walker, G. P. L. and McBroome, L. A. (1983) Mount St. Helens 1980 and Mount Pelee 1902Flow or surge? *Geology* **11**(10), 571. DOI: 10.1130/0091-7613(1983)11<571:MSHAMP>2.0.CO;2.

Walter, T. R., Legrand, D., Granados, H. D., Reyes, G., and Arámbula, R. (2013) Volcanic eruption monitoring by thermal image correlation: Pixel offsets show episodic dome growth of the Colima volcano. *Journal of Geophysical Research: Solid Earth* **118**(4), 1408–1419. DOI: 10.1002/jgrb.50066.

Waltham, N. R., Prydderch, M., Mapson-Menard, H., Pool, P., and Harris, A. (2007) Development of a thinned back-illuminated CMOS active pixel sensor for extreme ultraviolet spectroscopy and imaging in space science. *Nuclear Instruments and Methods in Physics Research, Section A: Accelerators, Spectrometers, Detectors and Associated Equipment* **573**(1-2), 250–252. DOI: 10.1016/j.nima.2006.10.259.

Wenig, M., Jähne, B., and Platt, U. (2005) Operator representation as a new differential optical absorption spectroscopy formalism. *Applied Optics* **44**(16), 3246. DOI: 10.1364/AO.44.003246.

Wessel, P., Smith, W. H., Scharroo, R., Luis, J., and Wobbe, F. (2013) Generic mapping tools: Improved version released. *Eos* **94**(45), 409–410. DOI: 10.1002/2013EO450001.

Whittam, A., Simpson, R., and McEvoy, H. (2014) "Performance tests of thermal imaging systems to assess their suitability for quantitative temperature measurement". In: *Proceedings of the 2014 International Conference on Quantitative InfraRed Thermography*. QIRT Council, pp. 0–9. DOI: 10.21611/qirt.2014.202.

Wilkes, T. C. et al. (2016) Ultraviolet Imaging with Low Cost Smartphone Sensors: Development and Application of a Raspberry Pi-Based UV Camera. *Sensors* **16**(10), 1649. DOI: 10.3390/s16101649.

Wilkes, T. C., Pering, T. D., McGonigle, A. J. S., Tamburello, G., and Willmott, J. R. (2017a) A Low-Cost Smartphone Sensor-Based UV Camera for Volcanic SO2 Emission Measurements. *Remote Sensing* **9**, 27. DOI: 10.3390/rs9010027.

Wilkes, T. C., McGonigle, A. J. S., Willmott, J. R., Pering, T. D., and Cook, J. M. (2017b) Low-cost 3D printed 1 nm resolution smartphone sensor-based spectrometer: instrument design and application in ultraviolet spectroscopy. *Optics Letters* **42**(21), 4323. DOI: 10.1364/OL.42.004323.

Wilkes, T. C. et al. (2018) The Development of a Low-Cost, Near Infrared, High-Temperature Thermal Imaging System and Its Application to the Retrieval of Accurate Lava Lake Temperatures at Masaya Volcano, Nicaragua. *Remote Sensing* **10**(3), 450. DOI: 10.3390/rs10030450.

Wilkes, T. C. et al. (2019) The PiSpec: A Low-Cost, 3D-Printed Spectrometer for Measuring Volcanic SO2 Emission Rates. *Frontiers in Earth Science* **7**. DOI: 10.3389/feart.2019.00065.

Wright, R. (2016) MODVOLC: 14 years of autonomous observations of effusive volcanism from space. *Geological Society, London, Special Publications* **426**(1), 23–53. DOI: 10.1144/SP426.12.

Wright, R., Flynn, L. P., Garbeil, H., Harris, A. J., and Pilger, E. (2004) MODVOLC: Near-real-time thermal monitoring of global volcanism. *Journal of Volcanology and Geothermal Research* **135**(1-2), 29–49. DOI: 10.1016/j.jvolgeores.2003.12.008.

Wright, T. L., Kinoshita, W. T., and Peck, D. L. (1968) March 1965 eruption of Kilauea volcano and the formation of Makaopuhi Lava Lake. *Journal of Geophysical Research* **73**(10), 3181–3205. DOI: 10.1029/JB073i010p03181.

Xu, J., Nie, H., Nie, K., and Jin, W. (2017) Fixed-pattern noise correction method based on improved moment matching for a TDI CMOS image sensor. *Journal of the Optical Society of America A* **34**(9), 1500. DOI: 10.1364/JOSAA.34.001500.

Zhang, C., Anzalone, N. C., Faria, R. P., and Pearce, J. M. (2013) Open-Source 3D-Printable Optics Equipment. *PLoS ONE* **8**(3), e59840. DOI: 10.1371/journal.pone.0059840.

Zhang, Y., Li, Z., and Li, J. (2014) Comparisons of emissivity observations from satellites and the ground at the CRCS Dunhuang Gobi site. *Journal of Geophysical Research: Atmospheres* **119**(22), 13,026–13,041. DOI: 10.1002/2014JD022216.

Appendix

The following pages contain the PyCamUV user manual. The manual is a relatively simple document which contains some general instructions for getting started with the PiCam and some troubleshooting advice.

PyCamUV v2.1 Instruction Manual

The PyCamUV software has two executables, PyCamUV.exe, and PostProcess.exe. The former is the main script, used for acquisition and real-time processing; the latter provides an environment in which subsequent processing can be performed, which may be useful if the initial acquisition script doesn't process the images correctly, or if you wish to change certain parameters and retry processing. PostProcess.exe also provides a number of options which aren't available in PyCamUV.exe, such as writing the absorbance images to a video, and cross-correlation plume speed estimation.

Disclaimer: This software is still under development, and may have a number of bugs. It would be greatly appreciated if any bugs can be reported to tcwilkes1@sheffield.ac.uk, where I will endeavour to fix and improve PyCamUV as soon as possible. Further functionality for the software can also be suggested to this email address, although time constraints may not make all suggestions feasible.

Requirements:

The exact specifications for computing power are not currently known, however, it is thought that this software is not too processor intensive, and thus may be able to work on relatively basic machines. Trial and error is unfortunately the only way to ascertain this at the moment. A few perquisite requirements are:

- Windows OS - the code could be adapted to work on other operating systems, such as Linux or Mac, however, this is not currently setup. On request I can look into this, it may be as simple as changing some file pathnames.
- PuTTY – this is not a strict requirement; however, it is very useful for troubleshooting the Raspberry Pi as it allows connection via SSH. https://www.putty.org/
- WinSCP – similarly to PuTTY, this may be useful for moving files to and from the Pi if necessary. https://winscp.net/
- OpenCV – this needs to be installed on the system. I am running v3.1.0.

PyCamUV

Quick Startup:

1. The Raspberry Pis should first be powered up, by connecting the USB power.
2. You then need to wait for a GPS fix, which is represented by the change from a rapidly flashing red LED on the GPS unit to a slow flash (one flash every ~15 seconds). A slow flashing LED represents that the GPS has a fixed to satellites, and therefore is receiving a reliable data stream. This is used to set the time of the Raspberry Pis, and so it is crucial that the fix has been obtained before running PyCamUV.exe. The code may not perform as expected if this step is not followed. Alternatively, if you do not wish to wait for this, or do not wish to sync the time to the GPS, you can change 'use_gps' in the config.txt file to 0. The times of the two pis will then be synced to each other – so that they both have the same time, but this time will not be synced to a gps time, so is likely to be incorrect.
3. Connect to the Pi wireless network. Password=raspberry

4. Now run PyCamUV.exe
5. The first image taken after opening PyCamUV is important. Ensure the lens caps are off both cameras and point them at a bright UV light source – preferably the sun, or the brightest part of the sky. This is important for the camera to choose a low analog gain, which will allow a higher signal-to-noise ratio (SNR) to be achieved before the sensor saturates.
6. Define a shutter speed for the first image. Arbitrarily setting to 100 ms for this is fine.
7. Click "Test Capture"
8. The first images should be taken – expect a delay for the first images as the camera is initialising.
9. Check the analog gain in the filenames of the images taken, which are displayed above the image. A value of one is preferable, but close to one is acceptable (see filename description for details).
10. Find a suitable shutter speed for acquisitions. Note that it is likely filter A will need notably longer shutter speeds than filter B due to lower detector quantum efficiency and lower skylight irradiance at this shorter wavelength.
11. Focus the image by rotating the lens holders. Use test images, or a sequence capture, to aid focussing. Once performed once this step should not have to be completed again, unless the system is knocked.
12. In the calibration tab perform a calibration, including: Dark images, clear sky images, SO_2 gas cell images.
13. Align the camera to the volcanic plume and take a test image. Ensure that some land is visible at the bottom of the image, to allow good image registration.
14. Select image registration technique and perform registration.
15. Select background region of clear sky, away from the plume, in both images.
16. Take another image.
17. In the Analysis tab, use the absorbance image, which was generated from the most recent image to define a cross-section across which plume column densities will be integrated. This should be perpendicular to the primary flow vector.
18. Select desired framerate.
19. **Start acquisition!** Note that the PiCam will attempt to achieve the defined framerate, however, overheads with image taking may mean it is unable to image as fast as requested. Please initally check the images as they update to ensure that timestamps represent the correct framerate and that no frames are dropped. If frames are dropped it may be from only one filter, and the real-time processing may subsequently fail. If this happens, stop the acquisition, select a lower framerate, and restart.
20. Stop and recalibrate every hour or so. When stopping, wait for two new images to appear on the screen and then press stop. Pressing stop as images arrive can cause the program to freeze, or subsequent capture commands to fail. If this happens restart PyCamUV. Raspberry Pi modifications may also be required (see troubleshooting for further explanation).
21. When closing the GUI, close it from the main GUI window rather than the Python console window. Closing from the console window can cause errors if trying to restart as it doesn't properly shut down the Pi code.

Calibration:

In the calibration tab the user can use gas cells of known SO_2 column densities to calculate a calibration for the system. It is recommended that a new calibration is performed every hour or so, since changing conditions can affect the calibration.

For a new calibration click 'New Calibration'. This will open options to calibrate the camera. The camera should be pointed away from the plume at this point, towards clear sky (or as best is possible). Direct sun should not be present in the camera field-of-views, and it is best to perform the calibration as close to the plume as possible without imaging it; this will hopefully ensure that background conditions are relatively similar to the acquisition conditions when viewing the plume. Dark and Clear (clear-sky) images can now be taken. When clicking the buttons both cameras will acquire images, so ensure that lens caps are placed on BOTH cameras when acquiring dark images, and removed from BOTH cameras when acquiring clear-sky images. Gas cells can then be held in front of each camera in turn and the Filter button pressed to acquire for that specific camera. The gas column density in the cell should be defined prior to acquisition. Cells can then be changed and further images acquired until a full calibration has been performed. Press End Calibration to complete the calibration. Results will then be plotted. For each acquisition, Dark, Clear and cells, it is recommended that multiple images are taken; average images will then be generated during the calibration, which will reduce noise in the measurement. If a mistake is made at any point in the calibration, end the calibration and restart the procedure again with a new calibration.

GUI description:

The following section briefly explains all of the GUI widgets in PyCamUV. The numbers refer to the stated figure.

Figure 1.

1. Shutter speed. This is defined in milliseconds, separately for each camera (filter A and filter B). Longer shutter speeds will produce brighter images, improving signal to noise ratio, however, if this is made too high image pixels can saturate, and this must be avoided.
2. Framerate. This is defined in Hz, and is only used when an acquisition sequence is acquired, using button 4. For example, 0.2 Hz will take an image every 1/0.2 = 5 seconds.
3. Test capture. A button to take a single capture, without beginning an acquisition sequence. This may be useful to shutter speeds for example, before beginning an acquisition sequence.
4. Start Acquisition. Begins the acquisition of a sequence of images. This will invoke image processing, and thus, absorbance images and fluxes (if absorbance images are calibrated) will be updated once imaging has begun.
5. Image registration. This box contains three options for registering images – warping the filter B image such that its image field matches that of the filter A image. **No registration** – filter B image will not be warped. **Control point** – control points are manually picked by the user on each image, and these are used to define a warp matrix by watch the filter B image is warped (Note: the CP select button (6.) must be selected in order to mark control points on the two images). **OpenCV ECC** – an automated OpenCV algorithm which automatically detects similar features in each image and thus generates a warp matrix to align these features. This comes with two options, the number of iterations this algorithm is allowed to

loop through to converge and the termination EPS. There is likely online material which better explains the effects of these parameters, should the user wish to experiment with changing them. The standard settings have been found to give good registration under a limited number of tested images.

6. CP select. When this button is selected, clicking on Image A or Image B will define control points which can be used for control point image registration (see 5.). This button is linked to the BG crop button (7.), such that only one option can be selected at a time.
7. BG crop. When this is selected, clicking and dragging on Image A or Image B will allow the user to define a background region, used in the absorbance image calculations. This region should be entirely out of the plume, and would ideally be position in clear blue sky, or if not, in a region of the image which is likely to best represent the sky conditions directly behind the plume.
8. Optical flow settings. Allows a number of optical flow parameters to be edited. The user will need to research how each of these parameters affects the output. The Peters et al. Plumetrack software has a good explanation of each parameter online. The same Farneback optical flow algorithm used by their software is employed here.
9. Plume distance. In metres, this defines the estimated distance to the plume, and is used in the flux calculations.
10. X-FOV. The field of view of the camera in the X-direction. This parameter should not be changed, unless you are advised to do so.
11. No. of pixels. Number of pixels in the X-direction. Again this parameter should not be changed, unless binning of images has been altered – this functionality is not currently available for the user.
12. Update. This button **must** be pressed to update the system configuration, such that the new plume distance is taken into account. Thus, every time the plume distance is changed, press this button afterwards.
13. Save control points. This button saves all of the current control points present in the image. If, once saved on both images, there are the same number of control points present in each image, the warp matrix will be calculated, and if Control Point registration is selected (6.) image B will be registered.
14. Reset control points. Removes all current control points on the image.
15. Messages. A message box which will display any important messages throughout PyCamUV's use.
16. Row. Defines the pixel row of the image in which to draw the cross section represented in the green subplot. This row is then displayed on the main image too.
17. Column. As 16, but for a specified column of the image.
18. Update plot. Updates the image and cross-section plots to represent new row and columns.
19. Save absorbance images. If selected, each absorbance image during sequence acquisition is saved to an 8-bit png.
20. PNG compression. Defines the compression of the PNG. A larger number means smaller files, but may have an undesired effect on the data.

Figure 2.

This tab contains 4 images, one displaying the current cell absorbance image, one plotting the calibration line, and two displaying the clear sky masks which will be used to vignette correct images.

1. New calibration. Clicking this opens the options to perform a new calibration, allowing you to take Clear (clear sky image for vignette correction), Dark (Dark image for dark current correction), and cell (SO_2 cell images) images which are all used in the calibration of the SO_2 camera. Ensure that the shutter speeds have been defined as you wish in the "Main" tab, before you take these images. All images should be taken at the shutter speeds you will use for the image sequence capture. I suggest calibrating about every hour, but this is up to the user to decide. You must perform calibration before starting your first image acquisition sequence, if you wish fluxes to be calculated.
2. Column density entry. This is to be used to tell the software what cell you are holding in front of the lens.
3. Choose directory. If you wish to load an old calibration, you can do this by clicking this button and navigating to the "Cal x" directory you wish to load.
4. Crop calibration region. Under some imaging conditions you may wish to calibrate the system using only a section of the image; for example, if there are patchy clouds in the image when calibrating, you may want to calibrate only within a region of blue sky, or only in a region of cloud, depending on what best represents the sky conditions directly behind the volcanic plume. Once this button is selected you can click and drag a box on the Cell Absorbance Image display, to define a crop region. You may then need to reload the calibration (using button 3.), to update the calibration output.
5. Add origin point to calibration. When selected, a point on the origin will be used when forming the calibration first order polynomial fit. There may be scenarios in which the user believes this to be appropriate, or they may find this inappropriate, so this is left to the user's discretion.
6. Vignette correct images. When selected, all images are corrected using their respective filter mask, prior to generating the absorbance image. In most scenarios we recommend that this is used, as it not only corrects for effects of the bandpass filter, but it also corrects for any inhomogeneities in the sensor. However, there may be scenarios, such as poor weather conditions, where patchy clouds in the mask image mean that the vignette correction does not seem to be beneficial, or rather, incorporates further error into the data, in which case deselecting this button may be appropriate.

Figure 3.

The Analysis tab contains 4 figures, displaying the output from image analysis. The first is an interactive figure which displays the **absorbance image**, or a calibrated SO_2 image if a calibration has been performed. By clicking on this figure, you can define a cross-section which is used to integrate the column densities between the two points to generate a flux. This line should be drawn perpendicular to the plume motion, and should be large enough to catch the entire plume, and perhaps account for any changes in plume size during acquisition. The figure below this displays the **cross section values**, either in ppm.m if calibrated, or in the dimensionless apparent absorbance if no calibration is present. The figure in the top right displays the **optical flow vectors**. It is important to check this, to know whether the optical flow algorithm is working. At times this may show no movement, or plume movement may not look realistic, in which case you either need to change the optical flow input parameters in the Main tab, or just post-process the images using the cross-correlation method of plume speed calculation; this can be done in PostProcess.exe. The final figure

displays **fluxes**, and will only be updated if a calibration is present, as it is not possible to calculate flux without calibration.

Filename description:

Image filenames are displayed above each image. It is important to understand their format so that you are able to check that everything is working correctly at any given time. Furthermore, if you wish to post-process the data using software other than that provided, understanding what each image represents will be important. Some example filenames are:

2017-09-11T121357_fltrA_63-8ag_700000ss_Plume.png

2017-06-13T163611_fltrB_1ag_75000ss_Dark.png

2017-06-13T163949_fltrB_1ag_75000ss_260ppm.png

In general, the filename format is:

<date>T<time>_<filter>_<analog_gain>_<shutter_speed>_<type>.png

Much of this is self-explanatory. First, the **data** and **time** are found. The data is in year-month-day format, and time in hour-minute-second. Then the **filter** is stated as either 'A' or 'B'. In the setup we provide, filter A represents a 310 nm (10 nm full-width-at-half-maximum) bandpass filter, and filter B represents a 330 nm (10 nm full-width-at-half-maximum) bandpass filter. The **analog gain** is then an important parameter to understand; it represents a scaling factor of signal for the detector (see 'Quick Startup' guide for discussion). A dash in this parameter represents a forward slash, and thus, denotes a fraction; the slash is not used since it represents directories in a file path. The lowest gain possible is 1. The **shutter speed**, which is always appended with "ss", is quoted in µs, since this is the unit the PiCamera works in. Note: the user defines shutter speed in ms, not µs. The final phrase relates to the **type** of image taken; image types are:

- Test – a test capture image. Taken during setup but not used after this.
- Dark – dark current image. Used for dark image subtraction.
- Clear – clear-sky image. Used for vignette correcting and as part of the calibration procedure.
- <>ppm – SO_2 gas cell image containing the quoted ppm·m column density of SO_2. For example, 260ppm is an image taken through a gas cell of column density 260 ppm·m. Used during calibration.
- Plume – part of a sequence acquisition. All Plume images should have contemporaneous filter A and B images and are the main images of the volcanic plume for processing.

Discussion:

The PyCamUV.exe and PostProcess.exe softwares are still under development, and currently only provide a few options for processing UV camera data. To this point I have kept the processing work

relatively simple, both for ease of use for any end-user, and also due to time constraints on developing these programs. For example, a number methods of defining a background sky intensity for each pixel in an image have been proposed, such as fitting a polynomial to a region of the clear-sky and expanding this across the image; here we use a single background and the assumption the that sky radiance is equal at all points in the image. More complex issues such as light dilution are also not currently addressed in this software. The user may, therefore, wish to perform their own analyses on the captured data. This would certainly be acceptable, in which case the provided code can be seen as more of a simple acquisition software rather than a complete suite for SO_2 camera processing. To facilitate such works, we have endeavoured to make all required data accessible to the user in logical a format. The filenames of each image describe its properties, as outlined earlier, and each set of images are packaged into a unique directory. We therefore suggest that the user should not feel restricted by the processing options provided.

Config.txt:

The configuration file, config.txt, can be used to set a number of useful parameters. It is read by the program on startup and will change the conditions of that instance of the program. The file can be sensitive to whitespace, so if editing it ensure that spaces remain the same i.e. do not insert whitespace after or before the = signs.

Importantly for display, on some laptops the GUI may be difficult to see, or may not fit on the screen. To change this, first I recommend editing the DPI (dots per inch) parameter. Increasing the dpi will cause the images to expand on the screen and vice versa. If this does not solve issues, figure sizes can also manually be edited in the file.

Shutdown:

In finishing acquisitions the system can be shutdown. First, close the PiCamUV application. In general, it seems that simply unplugging the Raspberry Pis from the camera boards is acceptable and in all experience has led to no issues. However, it may be sensible to shutdown the Pi systems properly. To do this, SSH into the Raspberry Pis using PuTTY and the associated Pi IP addresses. Once logged into the Pi, simply type:

sudo shutdown –h now

This should be performed on the client Pi first (the Pi with an IP which doesn't end in 1.1), since shutting down the host Pi will terminate the wireless connection and prevent any further interactions with either Pi. Secondly then shutdown the host Pi with the same command. The Pis can then be disconnected from the power bank.

Troubleshooting:

Raspberry Pi details:

1. **IP Addresses**: 172.24.1.1 (Host), 172.24.1.50-60 (Client)
2. **Username:** pi
3. **Password:** raspberry
4. **Wireless Network SSID:** Pi3-AP-<X>
5. **Wireless Network password:** raspberry

Pi IP address may be found in /var/lic/misc/dnsmasq.leases. Use sudo nano to open this file.

If the software freezes, it may leave programs running on the Pi which can then interfere with subsequent instances of PyCamUV. To ensure that this is not the case, the easiest thing to do is to restart the Pis, and begin again (unplug or restart via PuTTY). However, to save time, it may also be possible to kill the programs which can be left running on the Pi. To do this from the PuTTY command line, first search for all running processes with "ps axg", then find any process with mainPi.py and kill this process, by entering "kill x" where x is the process PID. This must be done for both Pis. You should now be fine to restart PyCamUV without any problems. If problems do persist, turn the Pis off and on.

A number of problems may be caused by having images, or filenames that end in .lock remaining on the Raspberry Pi. If you are experiencing problems, you should check that the Pi's imaging directory is clean, when the PyCamUV.exe program is NOT running. To do this, connect to the Pi using PuTTY (you should do this process for both Pis, as it may be just one Pi that is causing the problem). Then move into the UV_Cam directory by typing "cd UV_Cam". This is where some files to control the Pi are found, and where images are temporarily saved. Do not edit any of these files! Then move into the image directory with "cd Images". The list the files in the directory by typing "ls". This should then not display any files. If this command returns any files, either ending in .png or .lock, you should delete these files using "rm filename" where filename is the file you wish to delete. If it is a .png file, you may wish to move the file, rather than deleting it – to do this you need to us WinSCP software, connect to the R-Pi, and then move the file away from the Images folder.

If the Python console shows an error related to FTP timeout after first opening the GUI, close the GUI and restart. On a second attempt this error disappear since it is related to changing the system time on the Pi when syncing to the GPS. The FTP protocol doesn't like this sudden change in time and therefore throws an error.

If the GUI half loads and then freezes and the filter B image doesn't appear there may be an issue with your laptop's firewall blocking network connections. Either specifically allow PyCamUV.exe through the firewall, or just disable the firewall completely. This should solve the problem.

GPS wiring – Red (VIN), Black (GND), Green (RX), White (TX)

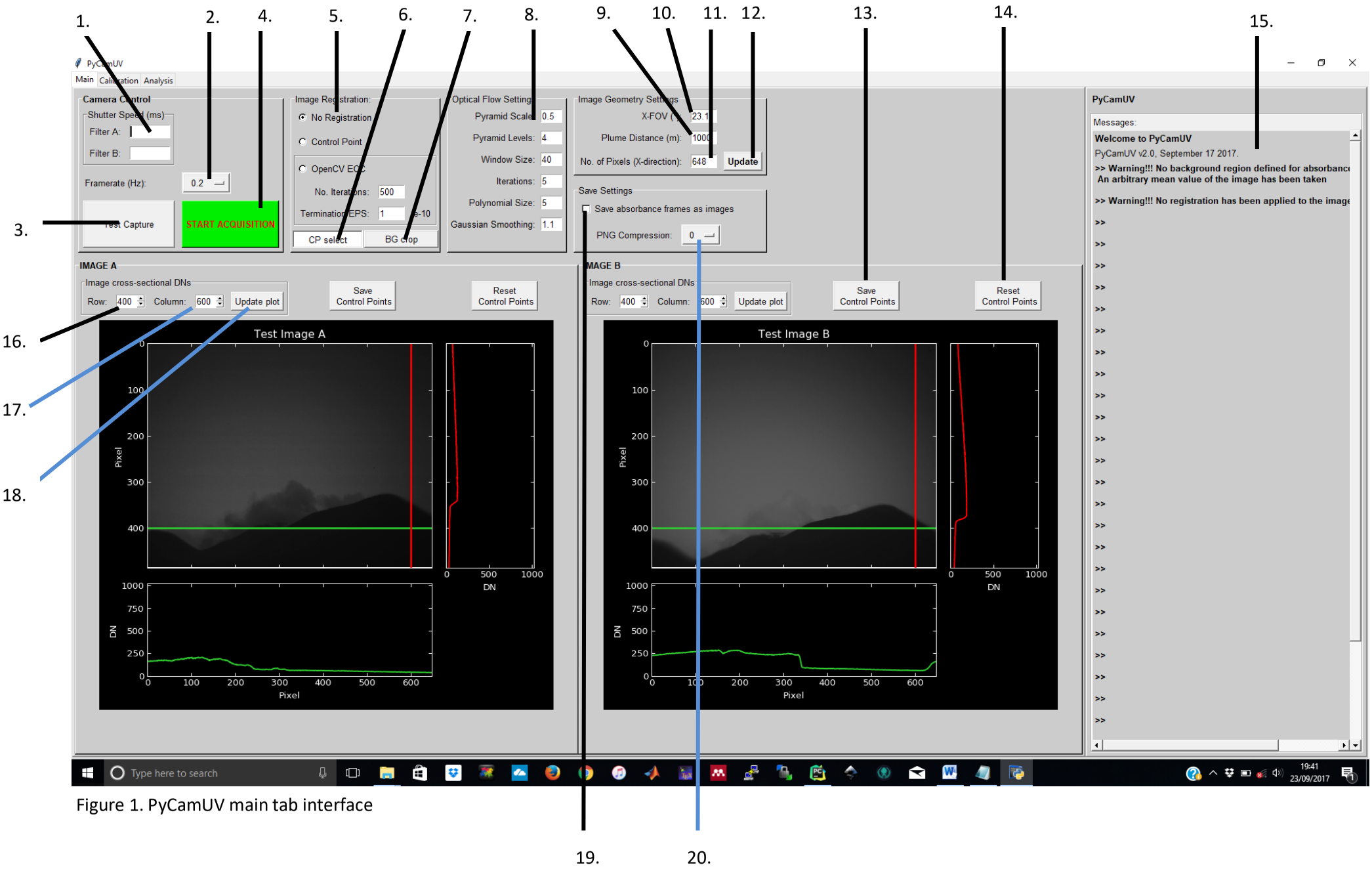

Figure 1. PyCamUV main tab interface

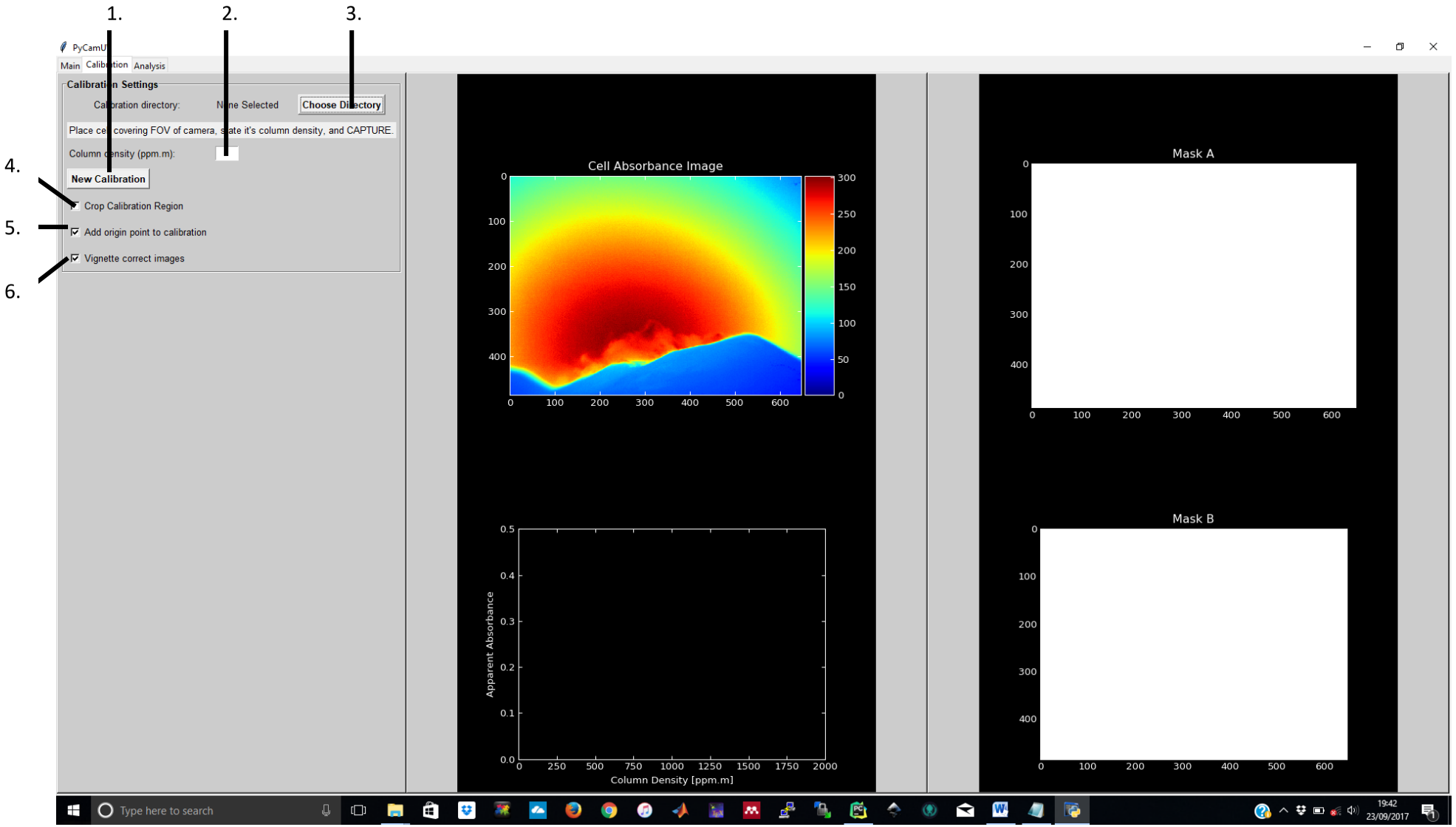

Figure 2. PyCamUV calibration tab interface.

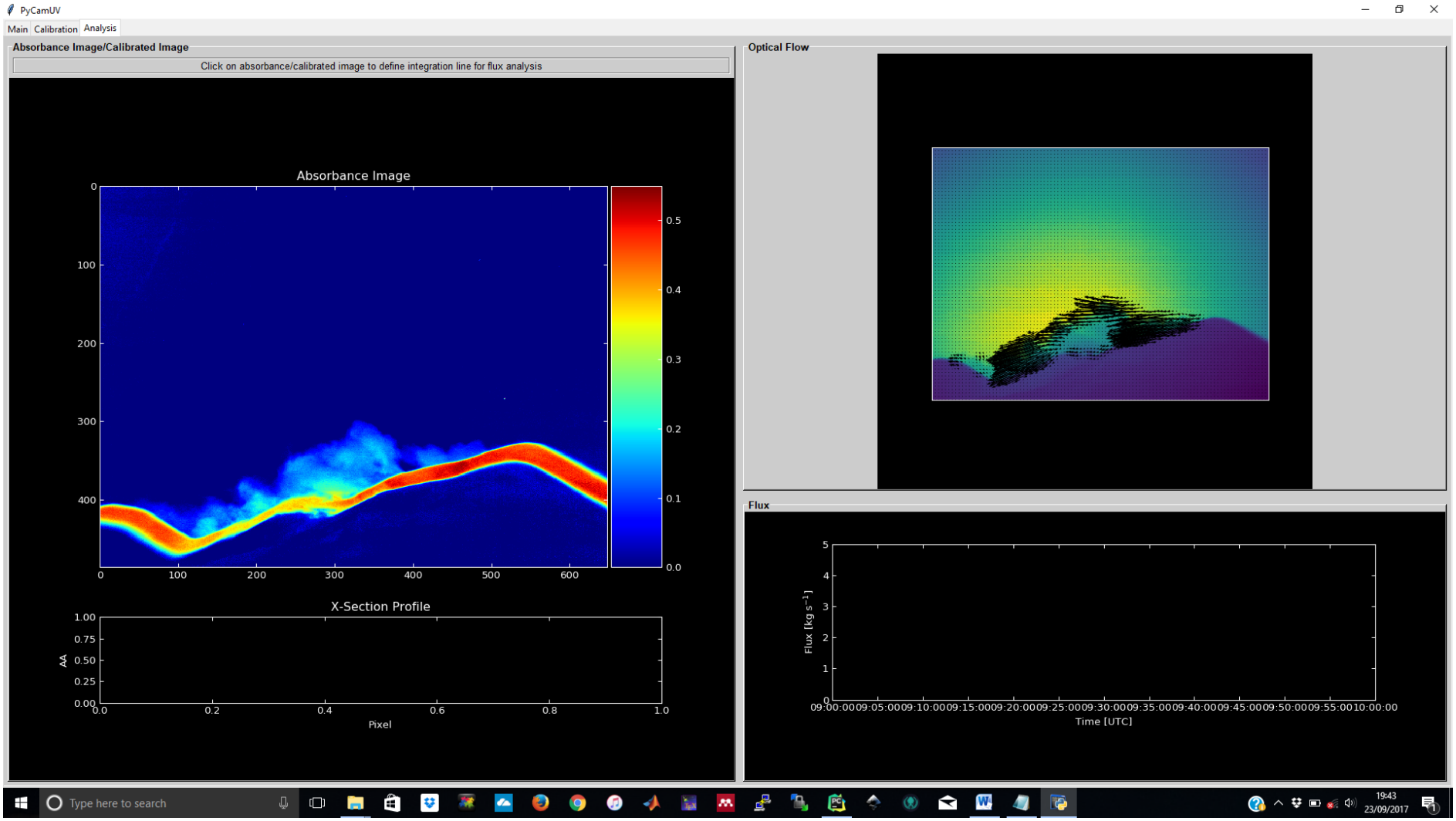

Figure 3. PyCamUV Analysis tab interface.